Thermalization of gluons in ultrarelativistic heavy ion collisions by including three-body interactions in a parton cascade

Inaugural-Dissertation
zur
Erlangung des Doktorgrades
der Naturwissenschaftlichen Fakultät
der Justus-Liebig-Universität Gießen
Fachbereich 7 – Mathematik, Physik, Geographie

vorgelegt von
Xu, Zhe
aus Tian Jin, V.R.China

Gießen 2004

Dekan: Prof. Dr. Volker Metag
I. Berichterstatter: Prof. Dr. Ulrich Mosel
II. Berichterstatter: Prof. Dr. Carsten Greiner

Contents

Chapter 1

Introduction

A nucleon is composed of *quarks* which are suggested to be elementary particles in nature. Quarks interact with each other by interchanging *gluons*. This *strong* interactions of quarks and gluons are described by the theory of *Quantum Chromodynamics* (QCD). In addition, quarks and gluons are normally confined within hadrons, and cannot be detected as free particles. This means that in a large nucleus being composed of nucleons, quarks and gluons in one nucleon cannot travel freely into the neighboring nucleons. This is the case for a normal nuclear matter. On the other hand, for high density matter, QCD predicts the existence of a deconfined phase of quarks and gluons, the so-called *Quark Gluon Plasma* (QGP) [CP 75]. Particularly, the numerical studies of QCD on the lattice [K 02] show that there is a rapid rise of the energy density of matter at the temperature $T \sim 170$ MeV, which indicates the occurrence of a phase transition from hadronic matter to QGP. The energy density at the critical temperature is ~ 1 GeV/fm^3 which is about an order of magnitude larger than that of atomic nuclei. QGP is presumed to have been present very shortly after the *Big Bang* in the early universe. In the laboratory, it is suggested that colliding large nuclei with each other at high energy will deposit a large amount of energy within a small volume, so that the required energy density for the transition between the confined and deconfined matter is achieved in such collision experiments. In the last thirty years, several experiments of nucleus-nucleus collisions are constructed and performed. The energy involved in the collision increases continuously from an experiment generation to the later one. The highest energy for the moment is $\sqrt{s} = 200$ AGeV (in the center of mass frame of colliding nuclei) at the Relativistic Heavy Ion Collider (RHIC) [RHIC 00] at Brookhaven National Laboratory, which began operation in 2000. At RHIC energy it is estimated using the Bjorken formula [B 83] that the initial energy density is about $20 - 30$ GeV/fm^3, which is high enough to produce a QGP. QCD predictions of new physics under extreme condition of high energy density and high temperature can be thus tested at RHIC. Experimental data collected until now show exciting novel phenomena. One of

them, the elliptic flow, will be discussed below. We note that in the future project at the Large Hadron Collider (LHC) at CERN, the collider energy will be one order magnitude larger than the RHIC energy. The situation for exploring QCD deconfined matter is even better at LHC.

Let us illustrate schematically what is expected to happen in a nucleus-nucleus collision. In the first moment after the collision, quarks and gluons originally confined in nucleons are liberated. The system of quarks and gluons is likely strongly coupled and might become thermalized very fast to a QGP. The formed QGP expands then hydrodynamically in space and time until the energy density or temperature decreases to the critical point. At this stage quarks and gluons begin to combine to form hadrons. This is a mixed phase of quarks, gluons and hadrons. When hadronization is completed, there exists a hadron gas. This phase expands further with hadronic interactions until the system falls apart and decouples. The single particles will then be detected. It shows that a nucleus-nucleus collision is a very complex process and a QGP (if it exists) appears only as a transient state of QCD matter in the collision. Therefore, the search for QGP has to be carried out by analysing certain proposed hadronic and electromagnetic signatures like the strangeness enhancement, J/ψ suppression or jet-quenching [M 86, S 80, MR 82, KMR 86, MS 86, KM 81, KLS 91, G 90]. These effects would appear when a thermal system of quarks and gluons, a QGP, exists. However, the possible signatures of the QGP may also come in part from the late time dynamics of a hadron gas formed after the phase transition [MSSG 89, GCG 98, GL 01, GGJ 88, VPKH 88, GGBCM 99, GGX 03]. In order to obtain a 'clean' signature, one has to look for novel phenomena developed at the early time in the collision. The elliptic flow v_2 is just one such 'early signature' of QGP. As seen in

$$\frac{dN_h}{dp_T^2 dy d\phi} = \frac{dN_h}{dp_T^2 dy}\,\frac{1}{\pi}\,(1 + 2\,v_1\,\cos\phi + 2\,v_2\,\cos 2\phi + \cdots)\,, \qquad (1.1)$$

v_2 is defined as the second harmonic coefficient of a Fourier expansion in the azimuthal angle ϕ of the measured hadron spectrum. The v_2 parameter denotes the quadrupole moment and is thus nonzero when an initial spatial anisotropy of the reaction zone exists, which is realized for semi-central collisions. The idea for studying v_2 is that if a QGP with high pressure is formed in a semi-central collision, there will be an azimuthal dependence of the pressure gradients and this will then push the particles to overcome the initial spatial asymmetry, so that this azimuthal anisotropy will be transferred into a momentum space anisotropy in the final state, which should be seen in the momentum dependence of v_2. The second point is that the elliptic flow v_2 is mainly generated at the early times, since at those times the spatial anisotropy is at maximum. v_2 will saturate if the spatial asymmetry disappears. Therefore, one does not expect a large generation of v_2 in the hadronic phase. Fig.1.1 shows the data of measured v_2 parameter for various hadronic particles at RHIC

[PHENIX 03, STAR 04], compared with the predictions based on simple ideal hydrodynamical models [KHHH 01]. The perfect agreements of the observed

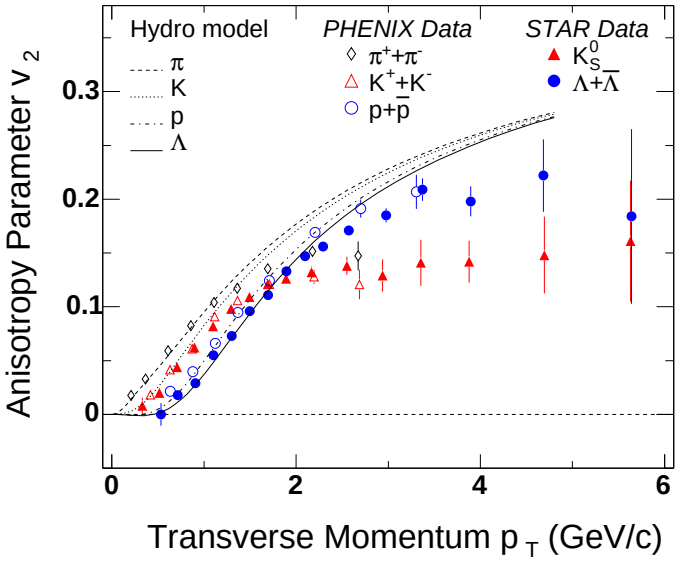

Figure 1.1: Differential elliptic flow $v_2(p_T)$. The data were collected by PHENIX [PHENIX 03] and STAR [STAR 04] collaborations at RHIC. The curves are hydrodynamic calculations [KHHH 01].

hadron mass dependence of the elliptic flow with the hydrodynamic calculatons below 1.5 GeV/c indicate that the evolving system of quarks and gluons builds up a sufficiently early pressure and potentially also achieves (local) equilibrium. Moreover, this suggests a strongly interacting (small viscosity) QGP. One can also see that the measured v_2 saturates at high p_T, while the hydrodynamic model predicts a continuous rise of v_2 with inceasing p_T. This shows that higher momentum particles do not behave hydrodynamically.

In spite of the success of the hydrodynamic model predicting the elliptic flow, one may ask for the timescale of thermalization of quarks and gluons, at which the hydrodynamic model starts to apply, since the system in the reaction is initially far from any (quasi-)equilibrium configuration. To address the crucial question of thermalization in the non-equilibrium dynamics, a number of QCD inspired theoretical analyses have been worked out either using the relaxation time approximation [B 84, HW 96, W 96, Wo 96] or performing full $3+1$ dimensional Monte Carlo cascade simulations based on the solution of the Boltzman equations for partons (quarks or gluons) [GM 92, Z 98, MG 00, BMGMN 00, BMS 03]. While the relaxation time method is only valid near equilibrium, Monte Carlo cascade simulations cover all situations, especially for the case far from equilibrium. Even the hydrodynamical behaviour of a thermal system can be, in principle, realized in such

simulations. Therefore, it is essential to use cascade simulations, inspired by QCD, to obtain quantitative predictions about the timescale of thermalization and about the behaviour of the further evolution of QGP in a nucleus-nucleus collision. In this thesis we develop a new cascade for on-shell partons to investigate the parton evolution in high-energy heavy ion collisions.

We first briefly review the already implemented parton cascade models developed by other groups. The first parton cascade, VNI, inspired by the perturbation QCD including binary elastic scatterings ($2 \leftrightarrow 2$) and gluon radiation and fusion ($1 \leftrightarrow 2$) was developed by Geiger and Müller [GM 92]. The partons are initially off-shell. They do not only propagate in space-time and in momentum space, but also propagate in their virtuality, the degree of the offshellness. In the simulation for a central Au+Au collision at RHIC energy [G 92] they concluded that a thermalized QGP will be formed at $\tau \approx$ 1.8 fm/c. However, the onset of potential hydrodynamical behaviour during the parton evolution was not demonstrated in their analyses. In addition, the treatment of the propagation of off-shell partons in their approach is not clear from a quantum kinetic point of view. Recently, Molnar and Gyulassy studied the buildup of elliptic flow at RHIC [MG 02] applying their on-shell parton cascade, MPC [MG 00] (an improved version of ZPC [Z 98]), in which up to now only elastic gluon interactions are included. In their analysis the early pressure can be achieved only if an unrealistic, much higher cross section than that dictated by pQCD is being employed. Furthermore, it is known that the elastic (and forward directed) $gg \leftrightarrow gg$ collisions cannot drive the system to kinetic equilibrium, as pointed out in [SS 01]. This would suggest, rather pessimistically, that the collective flow phenomena observed at RHIC cannot be described via pQCD. On the other hand, the possible importance of the inelastic pQCD interactions on overall thermalization was raised in the so-called 'bottom-up thermalization' picture [BMSS 01]. It is intuitively clear that gluon multiplication should not only lead to chemical equilibration [BDMTW 93], but also should lead to a faster kinetic equilibration [XS 94, BV 01]. This represents one (but not all) important motivation for developing a consistent algorithm to handle inelastic processes like $gg \leftrightarrow ggg$.

As a technical point in solving the transport equations, cross sections are interpreted geometrically in most of the cascades to model the collision processes. It turns out that in dense matter when the interaction length $\sqrt{\sigma/\pi}$ is not much smaller than the mean free path of particles, causality violation [KDCDN 84, KBHMP 95] will arise in these cascade models and will lead to numerical artifacts [ZGP 98]. One way to reduce these artifacts is to apply the common test particle method (or 'particle subdivisions') [W 82, WMGPS 89], in which the interaction length of the test particles is reduced by $\sqrt{N_{test}}$, while the mean free path is unchanged. N_{test} denotes the number of the test particles per real particle. However, the limitation of these transport models is obvious:

Inelastic collision processes with more than two incoming particles cannot be straightforwardly implemented since it is in general difficult to determine, for instance, a $3 \to 2$ process geometrically. Therefore, until now, the role of the inelastic processes in the formation of the QGP has not been studied fully quantitatively. To develop a consistent algorithm including $2 \leftrightarrow 3$ processes is a challenge and represents the technical part of the thesis.

An alternative collision algorithm suggested in [B 89, DB 91, L 93, C 02] dealt with the transition rate instead of the geometrical interpretation of cross section and determined proceeding collision processes in a stochastic manner by sampling possible transitions in a certain subvolume and time interval. This collision algorithm opens up the possibility to include the inelastic collision processes into transport simulations. In this thesis we will present a newly developed on-shell parton cascade using - for the first time - this sort of stochastic collision algorithm. Also the oftenly employed scheme based on the geometrical interpretation of cross section is discussed and compared with the stochastic algorithm. In particular, we concentrate on the study of the (unphysical) frame dependence. The new transport scheme will then be applied to simulate the parton evolution for a central ultrarelativistic heavy ion collision at highest RHIC energy. The emphasis is put on the investigation of gluon thermalization and their collective dynamics. For this investigation the initial conditions are assumed to be generated by independent minijets [KLL 87, EKL 89]. Other initial conditions, like the much discussed 'Color Glass Condensate' [MV 94], will also be implemented at the end. For the present study we consider quarks and gluons as classical Boltzmann particles throughout the thesis. The Pauli-blocking and Bose enhancement can, in principle, be taken into account.

The thesis is organized in the following way. In chapter 2 we present the stochastic collision algorithm for solving the on-shell Boltzmann equations and contrast this algorithm with the standard geometrical method. We explicitly show implementations of two-body collision processes and $2 \leftrightarrow 3$ collision processes in the transport simulations. As a first test, the dynamical evolution of a system within a fixed box is carried out to study global kinetic and chemical equilibration. Such calculations are mandatory to demonstrate the correct operation of the code and to look for the limitation of the algorithms.

Chapter 3 is concerned about the Lorentz invariance and the convergence of results extracted from cascade simulations. Numerical artifacts are discussed. We also make comparisons between the stochastic and geometrical collision algorithm in the connection with the frame dependence and the convergence.

In chapter 4 we give the initial distribution of partons in the first moment after a central Au+Au collision at RHIC energy. The initial partons are assumed to be generated via minijets production.

As a first application of the pQCD inspired parton cascade we study ther-

malization of a parton system in a fixed box in chapter 5. In chapter 6 we then finally present first results of cascade simulations for a central Au+Au collision at RHIC energy. Taking various initial conditions we predict relatively fast thermalization of partons: full kinetic equilibration at $1-2$ fm/c and full chemical equilibration at $1-4$ fm/c. The further expansion of the parton system shows (quasi-)hydrodynamical behaviour up to 4 fm/c. We summarize in chapter 7 and give an outlook for future studys.

In Appendix A and B more details of the geometrical collision algorithm are given. We list the pQCD partonic scattering cross sections in Appendix C for two-body processes and in Appendix D for $gg \leftrightarrow ggg$ processes. In Appendix E the numerical recipes for Monte Carlo samplings are presented. Some fomulas of relativistic hydrodynamics are given in Appendix F.

Chapter 2

Numerical solution of the Boltzmann equation

The Boltzmann equation is an equation of motion for $f(\mathbf{r}, \mathbf{p}, t)$, the average phase space density of particles with momentum $\mathbf{p}$ at the space-time point $(\mathbf{r}, t)$. For the case that there is no external force acting on the particles, the time derivative of f is computed by taking into account: 1) Particles with momentum $\mathbf{p}$ continually drift into and out of the volume element of space around $\mathbf{r}$; 2) Collisions that take place in this volume suddenly change the particle momenta. This results in the Boltzmann equation

$$\frac{\partial f}{\partial t} + \frac{\mathbf{p}}{E} \cdot \frac{\partial f}{\partial \mathbf{r}} = \mathcal{C} = \mathcal{C}_{22} + \mathcal{C}_{23} + \cdots , \tag{2.1}$$

where the second term of the left side expresses the drift of particles and $\mathcal{C}$ denotes the *collision term*, which can be classified into terms corresponding to two-body collision processes, $\mathcal{C}_{22}$, to $2 \leftrightarrow 3$ processes, $\mathcal{C}_{23}$, and so on. An essential assumption, absence of particle correlation, is postulated before each individual collision. Thus the number of collisions is proportional to the product of the phase space densities of the colliding particles and moreover to a transition rate, which is a measure for the probability of the collision process. The formulations of the collision terms will be given in the following sections.

One has to note that the Boltzmann equation is appropriate only for systems with weak, short-ranged forces. Strong collisions will lead to a fast variation of the particle density in space-time, which contradicts the basic condition for the Boltzmann equation that the possibility of a macroscopic description requires that changes of the particle density on microscopic scales of length and time are negligibly small. Furthermore, if the force is long-ranged, then the whole picture of local collisions breaks down completely.

The Boltzmann equation (2.1) is a non-linear equation for f. Therefore its solution is in general not straightfoward. In particular case that the system is in equilibrium, the equation (2.1) can be solved analytically, since in this case

the collision term is exactly zero. If the system is near equilibrium, one can linearize the collision term by employing the relaxation time approximation

$$\mathcal{C} \approx \frac{f - f_{eq}}{t_{rel}}\,, \tag{2.2}$$

where t_{rel} denotes the relaxation time of the particle density to that at equilibrium, f_{eq}. For the situation that the system is far from equilibrium, numerical facilities have to be applied, either performing the full $3+1$ dimensional computation on the lattice or making simulation of a real space-time evolution of particles by means of the Monte Carlo technique. In the latter the particle density in phase space is extracted to be

$$f(\mathbf{r},\mathbf{p},t) = \sum_i (2\pi)^3\,\delta^3(\mathbf{r}-\mathbf{r}_i(t))\,\delta^3(\mathbf{p}-\mathbf{p}_i(t))\,, \tag{2.3}$$

where the sum runs over all the particles. Particles evolve freely between two successive collisions. After collision new momentum will be determined statistically by employing the Monte Carlo technique. The buildup of such transport code is, in view of the numerical development, the main subject of this thesis and is also the 'cornerstone' for the future projects.

In this chapter we will present the numerical implementations simulating the individual collisions of on-shell particles in the course of their evolution. Especially, $2 \leftrightarrow 3$ processes are treated - for the first time - fully consistently within the stochastic method.

2.1 Numerical implementation of two-body collision processes

We consider a system consisting of classical, ultrarelativistic particles which are interacting via two-body collisions. The main emphasis is put on the numerical realization of such collision sequences in a relativistic transport simulation, which is theoretically based on the solution of the Boltzmann equations (2.1) with the following collision term given by

$$\begin{aligned}
\mathcal{C}_{22} \;=\; & \frac{1}{2E_1}\int\frac{d^3p_2}{(2\pi)^3 2E_2}\,\frac{1}{\nu}\int\frac{d^3p_1'}{(2\pi)^3 2E_1'}\,\frac{d^3p_2'}{(2\pi)^3 2E_2'} \\
& \times f_1' f_2' |\mathcal{M}_{1'2'\to 12}|^2\,(2\pi)^4\delta^{(4)}(p_1'+p_2'-p_1-p_2) \\
& -\frac{1}{2E_1}\int\frac{d^3p_2}{(2\pi)^3 2E_2}\,\frac{1}{\nu}\int\frac{d^3p_1'}{(2\pi)^3 2E_1'}\,\frac{d^3p_2'}{(2\pi)^3 2E_2'} \\
& \times f_1 f_2 |\mathcal{M}_{12\to 1'2'}|^2 (2\pi)^4\delta^{(4)}(p_1+p_2-p_1'-p_2')\,.
\end{aligned} \tag{2.4}$$

ν will be set to 2 when considering the double counting if $1'$ and $2'$ are identical particles. Otherwise ν is set to 1.

Since no mean field is considered throughout the present study, the evolution of particles is intuitively straightforward: Particles move along straight line between two collision events. After a particular collision the momenta of colliding particles are changed statistically according to the differential cross section. The determination of the collision sequence is, however, not unique and depends on the particular numerical implementation. We present in this section two numerical methods dealing with the realization of binary collisions. Comparisons between these two methods will be made in detail when investigating kinetic equilibration in a fixed box. We also study any potential (but unphysical) frame dependence of transport simulations within both schemes and how to minimize possible deficiencies. These results will be presented later in chapter 3.

2.1.1 The geometrical method

In the first method a collision happens when two incoming particles approach as close to each other that their closest distance is smaller than $\sqrt{\sigma_{22}/\pi}$, where σ_{22} denotes the total cross section for the colliding particles. In other words, the collision probability is either 1 or 0, depending on how close the collision partners come together. Since the total cross section is interpreted geometrically, we label this procedure the *geometrical method*. In this picture of the closest approach,which is already employed in parton cascade models like ZPC [Z 98], MPC [MG 00] and PCPC [BMGMN 00], collisions do happen one by one as time proceeds. If the initial positions and momenta of particles are given, the next collision event can be determined by comparing the individual times marking the occurrence of the various and possible collisions. Detailed numerical procedure can be found in Appendix A and B.

Unlike the total cross section the closest distance is, however, not invariant under Lorentz transformation. This may lead to the situation that a particle pair collides in one frame, but might not in another frame, which is unphysical. One faces here a violation of covariance, which is a historic problem in microscopic simulation within relativistic transport models. In the present scheme we define the closest distance in the center of mass frame of the individual particle pair and thus make it to be a Lorentz invariant quantity by hand. In spite of this definition the covariance of the Boltzmann equation is still not fulfilled, because the time ordering of collisions might be changed under Lorentz transformation [KDCDN 84, KBHMP 95]. Still, for a sufficiently dilute system the geometrical method works rather robust. We will continue discussing this problem of covariance violation later in this chapter and also in chapter 3. Besides the problem just mentioned, the *ordering time* of one particular collision itself which orders the occurrence of all collisions in a particular frame, called lab frame, is not well defined. Since we determine the closest distance of two

incoming particles in their center of mass frame, it is reasonable to define the collision points for the two particles also in this frame at the closest distance and at the same time. Consequently both particles, if they do collide, change their momenta at the same time in their center of mass frame, but generally at different times in the lab frame. (We now denote these individual two times by *collision times*.) One can now define the ordering time at some stage between these two collision times. There is, however, no unambiguous prescription. In general, different choices for the ordering time will lead to different collision sequences. This, as numerically verified, does not strongly affect the behaviours of physical (ensemble averaged) quantities shown below. In our simulation we choose the smaller one of the two collision times as the ordering time. For the clarity we note again that the ordering time marks the individual collision event and is needed for ordering the collision sequence and for looking for the next collision. If one collision happens, the two colliding particles do react to this interaction at their (different) collision times, i.e. particles move with their 'old' velocities to the space points at collision times, change the momenta suddenly and then move further with the 'new' velocities.

In order to demonstrate the correct operation of the numerical realization of the geometrical method, we will choose a situation when the outcome is known analytically. For this purpose we carry out 'box calculations', in which a particle ensemble with a none-quilibrium initial condition is enclosed in a fixed box and will evolve dynamically until an appropriate final time. The collisions of particles against the walls of the box are simply done via mechanical reflections. The times, at which particles collide with the walls, are uniquely determined and added into the time table of collisions among particles to find out next action, either a binary collision or a collision against wall. For sufficiently long times, the system should get kinetically equilibrated at the end. For a classical, ultrarelativistic ideal gas the energy distribution has the Boltzmann form

$$\frac{dN}{NE^2dE} = \frac{1}{2T^3}e^{-E/T}, \tag{2.5}$$

which guides as an analytical reference for the numerical results. The temperature T can be obtained from the simple relation between energy and particle density

$$\epsilon = 3nT\,, \tag{2.6}$$

where ϵ and n are solely given by the initial condition due to the energy and particle conservation. In the simulations particles are initially distributed homogeneously within the box and their momentum distribution is chosen highly anisotropic via

$$\frac{dN}{Ndp_Tdp_z} = \delta(p_T - 6\ \mathrm{GeV})\,\delta(p_z). \tag{2.7}$$

All particles have initially the same momentum and the energy per particle

is $\epsilon/n = 6$ GeV which leads to $T = 2$ GeV at equilibrium. In Fig.2.1 the final energy distribution from such box calculations for a system of $N = 2000$ massless particles is depicted. The size of the box is set to be 5 fm $\times$ 5 fm $\times$

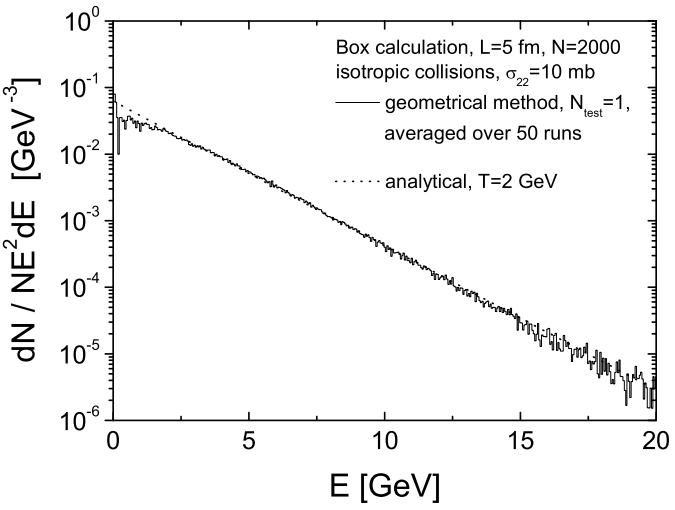

Figure 2.1: Energy distribution at final time ($t = 5$ fm/c) of a system consisting of $N = 2000$ massless particles in a fixed box. The initial energy distribution is set to be a delta-function at 6 GeV (2.7). The size of the box is 5 fm $\times$ 5 fm $\times$ 5 fm. We here apply the geometrical collision algorithm. The collisions are taken as isotropic and the total cross section is fixed to be a constant $\sigma_{22} = 10$ mb. The dotted line denotes the analytical result of temperature $T = 2$ GeV. The numerical distribution is obtained from an ensemble of 50 independent realizations.

5 fm. We consider collisions with isotropic differential cross section and take a constant total cross section of $\sigma_{22} = 10$ mb. The final time is set to be 5 fm/c. (As one will shortly realize, this chosen time is sufficient long for the system to become equilibrated.) To improve statistics we have collected particles from 50 independent realizations. The dotted line, depicted in Fig.2.1, denotes the analytical distribution (2.5) with temperature $T = 2$ GeV. We see a nice agreement between the numerical result and the analytical distribution except a slight, but characteristic deviation at low energies. We will come back to explain this discrepancy immediately.

Such a successful passing of the previous test is necessary for every collision algorithm, but it is still not a sufficient argument to guarantee whether the presented algorithm is operating correctly. One has to ask any numerical algorithm for its limitation of correctly describing the underlying problem. To be specific when considering the collision integral (2.4), it is not obvious whether

the geometrical interpretation of the total cross section is a reasonable choice to account for the Boltzmann process. In fact such a description has some shortcomings concerning causality violations which have been pointed out for example in [KBHMP 95]. Especially for the algorithm presented above we have to face the fact that the collision times of colliding particles are different in the lab frame. This will lead to a noticeable reduction of the collision rate compared to one given by the collision integral. Assume that the difference of the collision times is Δt_c. Consequently the particle with larger collision time should not collide again during this interval Δt_c, otherwise causality would be violated. As pointed out in Appendix A, for a system in equilibrium the ensemble averaged time delay $< \Delta t_c >$ depends only on the total cross section and increases with the increasing total cross section. This will lead to an increase of the mean free path and thus to a decrease of the collision rate. In other words, the collision rate decreases when noncausal collisions are forbidden. We can demonstrate this effect employing box calculations, in which we consider an initially kinetic equilibrated gas distributed homogenously within the box. The size of the box is taken to be the same as in Fig.2.1. We employ isotropic collisions with a constant cross section of $\sigma_{22} = 10$ mb. In Fig.2.2 collision rates are depicted as solid squares for several particle densities. The collision rate is obtained here as the time average of the collision number. While the box size is fixed, we vary the particle number to get different densities. The solid line shows the expected relationship between the collision rate and particle density in equilibrium $R = n\sigma_{22}$. We see a clear decrease of the collision rate when the expected mean free path $1/n\sigma_{22}$ is not much larger than the interaction length $\sqrt{\sigma_{22}/\pi}$. Such a numerical artifact would strongly slow down the kinetic thermalization of an initially highly non-equilibrium state, as, for instance, in case of ultrarelativistic heavy ion collisions. As also clearly seen from Fig.2.2, the collision rate tends to saturate at high density. The reason is that the collision rate has an upper limit which is exactly the inverse of the average collision time difference $< \Delta t_c > /2$ depending only on the total cross section as mentioned before. One can compute $< \Delta t_c > /2$ analytically. The detailed calculation is given in Appendix A. It turns out that $< \Delta t_c > /2 = 0.12$ fm/c for $\sigma_{22} = 10$ mb. This indicates that the saturation value of the collision rate would be 8.3 fm^{-1} at high density.

We now return to the slight discrepancy at low energy as noticed in Fig.2.1 and consider this as a consequence of the same effect of the relativistic time spread of collisions pointed out above, since in this particular situation the particle density is so high that the mean free path is one order smaller than the interaction length. To confirm this suspicion, we carry out similar calculations as in Fig.2.1, but with a tiny cross section of $\sigma_{22} = 0.1$ mb. The energy distribution, depicted as thick histogram, is shown in Fig.2.3 compared with the distribution (thin histogram) obtained by using $\sigma_{22} = 10$ mb. One does not see the artificial distortion in the spectrum at low energies any more when the

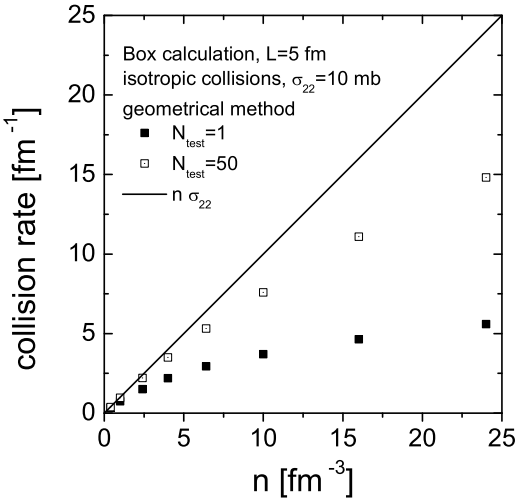

Figure 2.2: Collision rates for given particle densities. The size of the box is 5 fm $\times$ 5 fm $\times$ 5 fm. We apply here the geometrical collision algorithm. The collisions are isotropic and the total cross section is fixed to a constant of $\sigma_{22} = 10$ mb. The particle system is taken initially as thermal with a temperature of $T = 1$ GeV. The solid line shows the expected relationship between collision rate and particle density: $R = n\sigma_{22}$. The solid squares show the calculated collision rates without test particles ($N_{test} = 1$) and the open squares show the results with 50 test particles per real particle ($N_{test} = 50$).

cross section and hence the relativistic time spread is small. As a conclusion, the relativistic time spread effect not only decreases the collision rate, but also slightly distorts the system out of equilibrium.

To suppress this numerical artifact and hence to conserve Lorentz covariance we employ the widely used test particle, or 'subdivision', technique [W 82, WMGPS 89] based on the scaling

$$n \to n\, N_{test} \quad \text{and} \quad \sigma \to \sigma / N_{test}, \tag{2.8}$$

where N_{test} is the number of test particles belonging to one real particle. While the mean free path is unchanged by the scaling, the interaction length is reduced by a factor of $\sqrt{N_{test}}$. This consequently reduces the relativistic time spread which vanishes in the limit $N_{test} \to \infty$. The open squares in Fig.2.2 denote the results by using $N_{test} = 50$. The tendency of convergence towards the ideal limit is visible.

In Fig.2.4 we show the time evolution of the momentum anisotropy defined as the fraction of the average longitudinal momentum squared over the average transverse momentum squared. The initial conditions and parameters are set

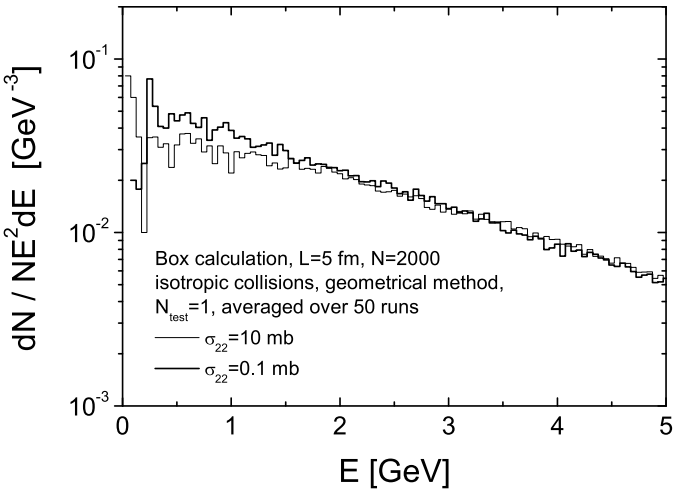

Figure 2.3: Energy distributions from box calculations. The thin histogram shows the same distribution as in Fig.2.1. The thick histogram shows the results with a smaller total cross section of $\sigma_{22} = 0.1$ mb.

to be the same as in Fig.2.1. The dotted line depicts the result without applying the test particle method ($N_{test} = 1$) and the dashed line shows the result with $N_{test} = 50$. The results confirm our reasoning that the relativistic effect of spreading of the two collision times for a colliding particle pair increases the relaxation time for achieving kinetic equilibrium.

2.1.2 The stochastic method

In the last section we have determined the collision probability of two incoming particles by means of the geometrical interpretation of the total cross section. Instead, one can also derive the collision probability of a chosen particle pair directly from the collision term of the Boltzmann equation [DB 91, L 93, C 02]. When assuming two particles in a spatial volume element $\Delta^3 x$ with momenta in the range $(\mathbf{p}_1, \mathbf{p}_1 + \Delta^3 p_1)$ and $(\mathbf{p}_2, \mathbf{p}_2 + \Delta^3 p_2)$, the collision rate per unit phase space for such particle pair can be read off from (2.4)

$$\frac{\Delta N_{coll}^{2\to 2}}{\Delta t \frac{1}{(2\pi)^3}\Delta^3 x \Delta^3 p_1} = \frac{1}{2E_1}\frac{\Delta^3 p_2}{(2\pi)^3 2E_2} f_1 f_2 \frac{1}{\nu}\int \frac{d^3 p_1'}{(2\pi)^3 2E_1'}\frac{d^3 p_2'}{(2\pi)^3 2E_2'} \times |\mathcal{M}_{12\to 1'2'}|^2 (2\pi)^4 \delta^{(4)}(p_1 + p_2 - p_1' - p_2'). \quad (2.9)$$

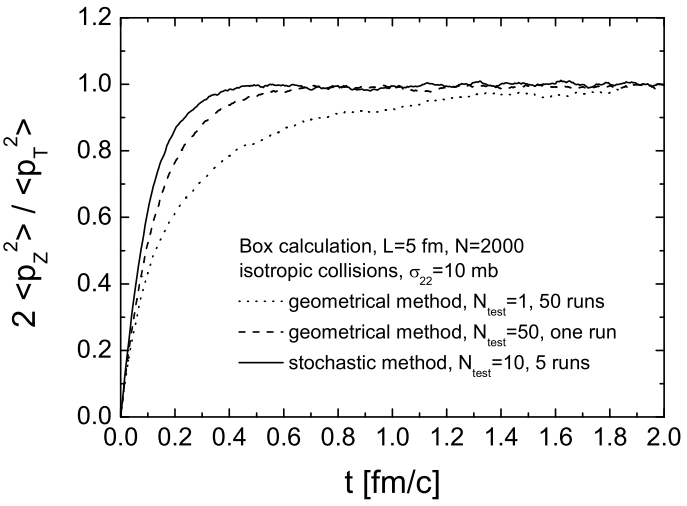

Figure 2.4: Time evolution of the momentum anisotropy from box calculations. The initial conditions and parameters are set to be the same as in Fig.2.1. The dotted (dashed) curve shows the results obtained by employing the geometrical method without test particles (with 50 test particles per real particle). The solid curve shows the result obtained by employing the stochastic method with 10 test particles per real particle.

Expressing distribution functions as

$$f_i = \frac{\Delta N_i}{\frac{1}{(2\pi)^3}\Delta^3 x \Delta^3 p_i}, \quad i = 1, 2, \tag{2.10}$$

and employing the usual definition of cross section [GLW 80] for massless particles

$$\sigma_{22} = \frac{1}{2s}\frac{1}{\nu}\int \frac{d^3p_1'}{(2\pi)^3 2E_1'}\frac{d^3p_2'}{(2\pi)^3 2E_2'}|\mathcal{M}_{12\to 1'2'}|^2(2\pi)^4\delta^{(4)}(p_1+p_2-p_1'-p_2')\,, \tag{2.11}$$

one obtains the absolute collision probability in a unit box $\Delta^3 x$ and unit time Δt

$$P_{22} = \frac{\Delta N_{coll}^{2\to 2}}{\Delta N_1 \Delta N_2} = v_{rel}\,\sigma_{22}\,\frac{\Delta t}{\Delta^3 x}\,. \tag{2.12}$$

$v_{rel} = s/2E_1E_2$ denotes the relative velocity, where s is the invariant mass of the particle pair. Unlike in the geometrical method where the collision probability is either 0 or 1, P_{22} now can be any number between 0 and 1. (Notice that, in practice, one should choose suitable $\Delta^3 x$ and Δt to make P_{22} to be consistently less than 1.) Whether the collision will happen or not is sampled

stochastically as follows: We compare P_{22} with a random number between 0 and 1. If the random number is less than P_{22}, the collision will occur. Otherwise there is no collision between the two particles within the present time step. Due to the stochastic nature of sampling the collision events we call this collision algorithm the *stochastic method*. If a particle pair collides, the collision time will be sampled uniformly within the interval $(t, t + \Delta t)$. The collision times for both colliding particles are here the same. The particle system propagates now from one time step to the next. This is different compared to the transport simulation scheme utilizing the geometrical method. Since in the limit $\Delta t \to 0$ and $\Delta^3 x \to 0$ the numerical solutions using the stochastic method converge to the exact solutions of the Boltzmann equation [B 89], we divide in practice the space into sufficient small spatial cells. For a true situation Δt and $\Delta^3 x$ have to be taken smaller than the typical scales of spatial and temporal inhomogeneities of the particle densities. We assume that only particles from the same cell can collide with each other. This and the choice of $\Delta^3 x$ are just the numerical treatments and will not be constrained by the interaction length $\sqrt{\sigma_{22}/\pi}$, since the interaction length is a scale based on the geometrical interpretation of the interaction and the stochastic method, which gives the correct realization of the transition rate, is conceptually completely different than the geometrical method.

In general we also might employ, in addition, the test particle technique in order to reduce statistical fluctuations of the collision events in cells. Accordingly the collision probability is changed to

$$P'_{22} = v_{rel} \frac{\sigma_{22}}{N_{test}} \frac{\Delta t}{\Delta^3 x} \tag{2.13}$$

by the scaling $\sigma \to \sigma / N_{test}$.

In the following we discuss the Lorentz invariance of the stochastic algorithm in the limit $\Delta x^3 \to 0$, $\Delta t \to 0$ and $N_{test} \to \infty$. Since $\Delta t \Delta^3 x$, $\Delta^3 p / \Delta E$, the distribution function f and the total cross section are Lorentz scalars, it is easy to realize from (2.9) that the collision number $\Delta N_{coll}^{2 \to 2}$ is a scalar under Lorentz transformations. Furthermore this is also true for ΔN_i, the particle number counted within a phase space interval at time t. Hence, the collision rate $\Delta N_{coll}^{2 \to 2} / \Delta N_i \Delta \tau$ as well as the collision probability P_{22} are scalars under Lorentz transformations. Therefore, in the limit $\Delta^3 x \to 0$, $\Delta t \to 0$ and $N_{test} \to \infty$ the stochastic method yields per se a Lorentz covariant algorithm. However, in practice, a non-zero subvolume $\Delta^3 x$ and non-zero timestep Δt disturb full Lorentz invariance explicitely. Any potential, but unphysical frame dependence will be discussed later in chapter 3.

To test and demonstrate the stochastic method we again pursue box calculations. The initial conditions are the same as in Fig.2.1. The size of the box is set as before to be 5 fm $\times$ 5 fm $\times$ 5 fm. Since we consider a spatially homogeneous initial situation of particles and this configuration will not change

very much during particle propagation, we choose a straightforward static cell configuration and divide the box into equal cells. The cell length is set to be 1 fm in the calculations. We consider isotropic collisions and use a constant total cross section of $\sigma_{22} = 10$ mb.

The implementation of the collisions against the walls of the box is not staightfoward when compared with the situation employing the geometrical method, since for particles in the cells near the walls there is no time order to decide whether they should experience collisions against the walls before or after potential collisions with other particles within one time step. However, this will not make strong effect on the rate of binary collisions and the rate of collisions against walls, if the time step is chosen to be appropriately small. In the simulations we choose the time step as the time span between next two potential collisions against walls.

Fig.2.5 shows the final energy distribution obtained by an average over 50 independent runs (with $N_{test} = 1$). One clearly recognizes that the stochastic

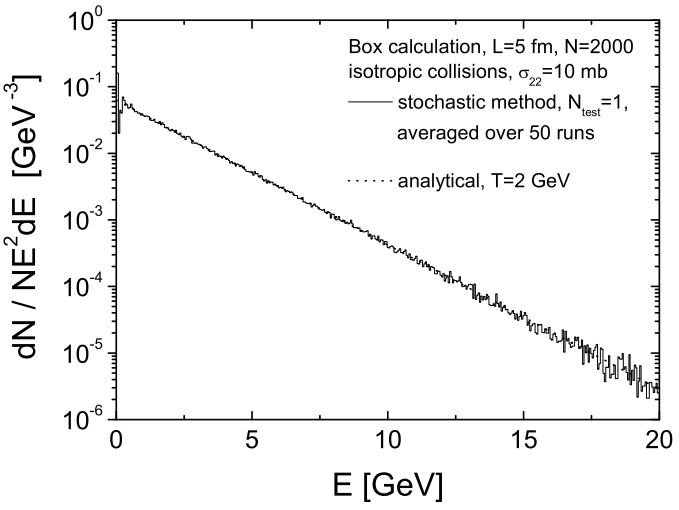

Figure 2.5: Energy distribution from box calculations. The initial conditions and parameters are set to be the same as in Fig.2.1. We apply here the stochastic collision algorithm. The box is divided into equal cells. The length of a cell is 1 fm.

collision algorithm also passes this basic test. The agreement between the numerical and analytical distribution is perfect and we do not see any distortion in the spectrum in contrast to the situation experienced in Fig.2.1.

Since the stochastic method is based directly on the formal collision rate, thus the numerically realized collision rate should be met in transport simulations if the sampled statistics in each cell is sufficiently high. We extract

the collision rates from box calculations employing the stochastic method and show the results in Fig.2.6 as solid squares. The box size and cell configu-

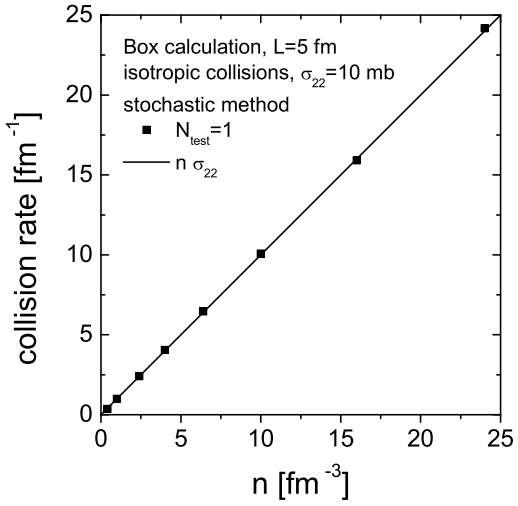

Figure 2.6: Collision rates for given particle densities. The initial conditions and parameters are set to be the same as in Fig.2.2. We apply here the stochastic collision algorithm. The cell configuration is the same as in Fig.2.5.

ration are set to be the same as in Fig.2.5. The system is taken at thermal equilibrium for the initial condition. One nicely recognizes that the squares lie on the expected line. (We do mention here that the box size is fixed and we vary the particle number to simulate different particle densities. For instance, a density of 1 fm^{-3} corresponds to a total particle number of 125, which means on average one particle per cell. For still lower densities not investigated, one would have to work in addition with a suitable amount of test particles.)

For a system which is initially out of equilibrium the lack of statistics in cells will affect the dynamical evolution of the system, since now all cells are correlated during the relaxation time. To study the effect we repeat the same simulations performed for Fig.2.5 starting with that particular non-equilibrium initial condition (2.7) and calculate the time evolution of momentum anisotropy. We use here the test particle method to control statistical fluctuations. Fig.2.7 shows the time evolution of the anisotropy for different test particle numbers N_{test}. We see that the lack of statistics in cells leads to a slight slowdown in the momentum relaxation. This effect is reduced by using larger values for N_{test}, which in turn results in lower statistical fluctuations. We also see the convergence of the momentum anisotropy for increasing N_{test}. It turns out that statistics with $20-30$ test particles per cell is sufficiently high to give the correct momentum relaxation.

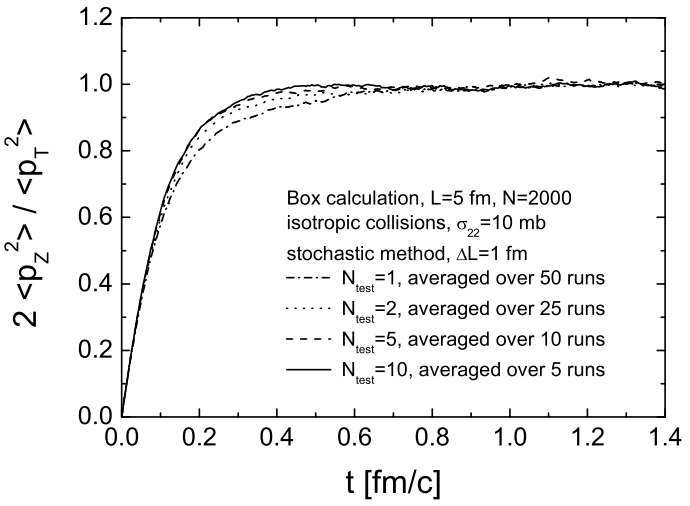

Figure 2.7: Time evolution of momentum anisotropy from box calculations. The initial conditions and parameters are set to be the same as in Fig.2.1 (or Fig.2.5). The stochastic method is used here. The cell configuration is the same as in Fig.2.5. The curves show the results with different test particles.

Let us summarize with some comparisons between the two simulation methods of treating collisions as presented in this section. In the simulation employing the stochastic method, the collision rate is correctly realized if the statistics in the individual cell is sufficiently high. In contrast, the collision rate will be numerically suppressed in the simulation using the geometrical method, when the mean free path is not much larger than the interaction length among test particles. In simulations with both algorithms the test particle technique has to be applied in addition in order to solve the Boltzmann equation with sufficient accuracy. For dense and strongly interacting system, convergence of the numerical results with increasing test particle number turns out to be more efficient in simulations employing the stochastic method than in simulations employing the geometrical method, as shown in Fig.2.4. In transport simulations applying the stochastic method we have to face the difficulty of dynamically configurating the space into smaller cells, which is not necessary in the geometrical method. Furthermore, the time step has to be chosen much smaller than the cell volume to avoid a strong change of the density distribution in cells. This, of course, reduces the computing efficiency. In general one should choose such a collision algorithm, so that numerical expense is small. However, the stochasic method offers an advanced technique when dealing with inelastic collision processes, which is the subject of the next section, whereas it is rather impossible to get a consistent geometrical picture for multi-particle

transition processes like $2 \leftrightarrow 3$ for instance. A further comparison between the two algorithms will be discussed in chapter 3 concerning any potential, but unphysical Lorentz frame dependence of the algorithms.

2.2 Numerical implementation of particle multiplication and annihilation processes

In this section we will now immediately *extend* the stochastic method to the more complicated particle multiplication and annihilation processes involving more than two particles. These processes are essential to drive the system towards chemical equilibrium and also do contribute to kinetic equilibration. The simplest processes are $2 \leftrightarrow 3$. In physical terms such processes will be specified then later in the thesis as gluon Bremsstrahlung and its back reaction. Now we will discuss their numerical implementations. The implementation of higher order processes is straightforward within the extended stochastic algorithm.

The collision term corresponding the $2 \leftrightarrow 3$ processes of identical particles is given by the expression

$$\begin{aligned}
\mathcal{C}_{23} \;=\; & \frac{1}{2E_1}\frac{1}{2!}\int \frac{d^3p_2}{(2\pi)^3 2E_2}\frac{d^3p_3}{(2\pi)^3 2E_3}\,\frac{1}{2!}\int \frac{d^3p_1'}{(2\pi)^3 2E_1'}\frac{d^3p_2'}{(2\pi)^3 2E_2'} \\
& \times f_1' f_2' \,|\mathcal{M}_{1'2'\to 123}|^2\,(2\pi)^4\,\delta^{(4)}(p_1'+p_2'-p_1-p_2-p_3) \\
& + \frac{1}{2E_1}\int \frac{d^3p_2}{(2\pi)^3 2E_2}\,\frac{1}{3!}\int \frac{d^3p_1'}{(2\pi)^3 2E_1'}\frac{d^3p_2'}{(2\pi)^3 2E_2'}\frac{d^3p_3'}{(2\pi)^3 2E_3'} \\
& \times f_1' f_2' f_3' \,|\mathcal{M}_{1'2'3'\to 12}|^2\,(2\pi)^4\,\delta^{(4)}(p_1'+p_2'+p_3'-p_1-p_2) \\
& - \frac{1}{2E_1}\frac{1}{2!}\int \frac{d^3p_2}{(2\pi)^3 2E_2}\frac{d^3p_3}{(2\pi)^3 2E_3}\,\frac{1}{2!}\int \frac{d^3p_1'}{(2\pi)^3 2E_1'}\frac{d^3p_2'}{(2\pi)^3 2E_2'} \\
& \times f_1 f_2 f_3 \,|\mathcal{M}_{123\to 1'2'}|^2\,(2\pi)^4\,\delta^{(4)}(p_1+p_2+p_3-p_1'-p_2') \\
& - \frac{1}{2E_1}\int \frac{d^3p_2}{(2\pi)^3 2E_2}\,\frac{1}{3!}\int \frac{d^3p_1'}{(2\pi)^3 2E_1'}\frac{d^3p_2'}{(2\pi)^3 2E_2'}\frac{d^3p_3'}{(2\pi)^3 2E_3'} \\
& \times f_1 f_2 \,|\mathcal{M}_{12\to 1'2'3'}|^2\,(2\pi)^4\,\delta^{(4)}(p_1+p_2-p_1'-p_2'-p_3')\,. \qquad (2.14)
\end{aligned}$$

The collision probability P_{23} for a particle multiplication process can be derived analogously to (2.12) as

$$P_{23} = v_{rel}\frac{\sigma_{23}}{N_{test}}\frac{\Delta t}{\Delta^3 x}, \qquad (2.15)$$

where the total cross section σ_{23} is defined as

$$\sigma_{23} = \frac{1}{2s}\frac{1}{3!}\int \frac{d^3p_1'}{(2\pi)^3 2E_1'}\frac{d^3p_2'}{(2\pi)^3 2E_2'}\frac{d^3p_3'}{(2\pi)^3 2E_3'}|\mathcal{M}_{12\to 1'2'3'}|^2(2\pi)^4\delta^{(4)}(p_1+p_2-p_1'-p_2'-p_3'). \qquad (2.16)$$

One can also extend the geometrical method to the multiplication processes. But it is in general impossible to obtain a unified scheme for the annihilation processes in a consistent geometrical picture. In contrast, the extension to $3 \to 2$ processes via the stochastic method is straightforward. We write the collision rate stemming from (2.14) per unit phase space in a form like (2.9)

$$\begin{aligned}\frac{\Delta N_{coll}^{3\to 2}/N_{test}}{\Delta t \frac{1}{(2\pi)^3}\Delta^3 x \Delta^3 p_1} &= \frac{1}{2E_1}\frac{\Delta^3 p_2}{(2\pi)^3 2E_2}\frac{\Delta^3 p_3}{(2\pi)^3 2E_3}\frac{f_1}{N_{test}}\frac{f_2}{N_{test}}\frac{f_3}{N_{test}} \\ &\times \frac{1}{2!}\int \frac{d^3p_1'}{(2\pi)^3 2E_1'}\frac{d^3p_2'}{(2\pi)^3 2E_2'}|\mathcal{M}_{123\to 1'2'}|^2 \\ &\times (2\pi)^4 \delta^{(4)}(p_1+p_2+p_3-p_1'-p_2')\,, \end{aligned} \tag{2.17}$$

where $f_i, i = 1, 2, 3$, denote now the phase space density of the test particles. Inserting (2.10) into (2.17) gives the collision probability of a $3 \to 2$ process

$$P_{32} = \frac{\Delta N_{coll}^{3\to 2}}{\Delta N_1 \Delta N_2 \Delta N_3} = \frac{1}{8E_1E_2E_3}\frac{I_{32}}{N_{test}^2}\frac{\Delta t}{(\Delta^3 x)^2} \tag{2.18}$$

for given momenta of the incoming particles in a particular space cell. I_{32} is defined as the integral $\frac{1}{2!}\int d^3p_1' d^3p_2' \cdots$ in (2.17) over the final states.

Danielewicz and Bertsch [DB 91] obtained a similar expression for P_{32}

$$P_{32} = v_{12}\frac{\sigma_{12}}{N_{test}}\frac{\mathcal{V}_3}{N_{test}}\frac{\Delta t}{(\Delta^3 x)^2}, \tag{2.19}$$

when investigating the production of deuterons in a non-relativistic transport model of low energy heavy ion reactions, where they approximately factorized the matrix element into a term describing a two-body collision and a term mimicing particle fusion. σ_{12} is the total cross section for the two-body collision and $\mathcal{V}_3$ can be interpreted as a volume: Once three particles are within this volume, a $3 \to 2$ transition may be considered to occur. The volume scales with $\mathcal{V}_3 \to \mathcal{V}_3/N_{test}$ when employing test particles. Therefore it is intuitively clear why the quantity I_{32} in (2.18) scales with $1/N_{test}^2$. In contrast to (2.19), expression (2.18) is a more general one formulated in a unified manner, and is correct for any given matrix elements without any approximations.

As an example, when considering isotropic $2 \leftrightarrow 3$ collisions for identical particles, integrals over momentum space for σ_{23} and I_{32} can be easily calculated analytically and one obtains

$$I_{32} = 192\pi^2 \sigma_{23}\,. \tag{2.20}$$

Applying the probabilities (2.15) and (2.18) we are now able to study kinetic and chemical equilibration in a box. We assume a system consisting of identical, massless particles and consider only isotropic $2 \leftrightarrow 3$ collisions. σ_{23}

is set to be 10 mb. As in the box calculations refering to Fig.2.1, initially the system is chosen to be strongly out of equilibrium according to eq. (2.7). The particles are distributed homogeneously in the box. The box has a volume of 5 fm $\times$ 5 fm $\times$ 5 fm and is divided into equal cells. The cell length is 1 fm. Initially the system contains $N_0 = 2000$ massless particles. Newly produced particles will be positioned randomly within the individual cells where the transitions occur. Before we come to the results, let us determine the final particle density and temperature to be expected when the system becomes thermally equilibrated. For an ultrarelativistic (one component) Maxwell-Boltzmann gas the following relations

$$\epsilon = 3 n_{eq} T \quad \text{and} \quad n_{eq} = \frac{T^3}{\pi^2} \tag{2.21}$$

hold in equilibrium. One can solve T and n_{eq} for an energy density given by the initial condition. In our case, according to eq. (2.7), we obtain $T = 1.248$ GeV and $n_{eq} = 25.64$ fm^{-3} which is larger than the initial particle density $n(t_0) = 16$ fm^{-3}. Fig.2.8 depicts the time evolution of the particle density obtained from the box calculation. The results are obtained by averaging 10 independent runs. We see that the particle density increases smoothly towards its final

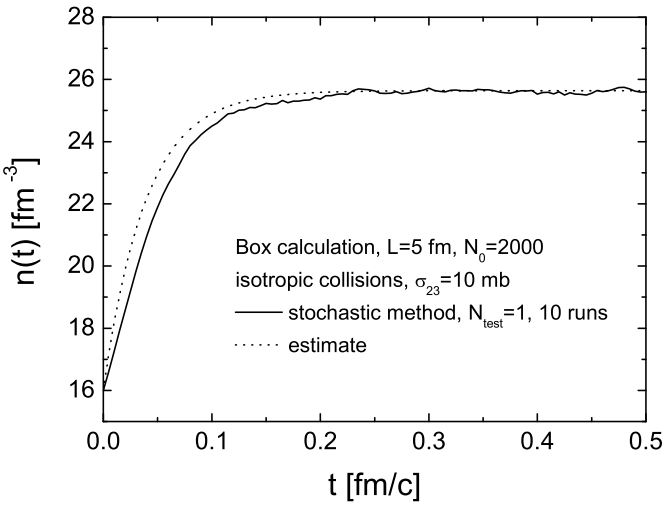

Figure 2.8: Time evolution of the particle density from box calculations. The initial conditions and parameters are set to be the same as in Fig.2.1 (or Fig.2.5). We consider isotropic inelastic collisions ($2 \leftrightarrow 3$) with a constant cross section of $\sigma_{23} = 10$ mb and employ the stochastic collision algorithm. The cell configuration is the same as in Fig.2.5. The dotted line denotes the estimate using a simple time relaxation approximation.

value which agrees fully with the analytical expectation. The dotted curve presents an estimate made by using the following relaxation approximation

$$n(t) = n_{eq} + (n(t_0) - n_{eq})\ e^{-\frac{t-t_0}{\theta}}, \tag{2.22}$$

where θ stands for the relaxation time. In general, for any complex equilibration, this quantity will be time dependent. For the estimate the relaxation time is taken by a simple fixed value at equilibrium $\theta = 1/n_{eq}\sigma_{23}$ which slightly overestimates the relaxation because of $n_{eq} > n_0$, as also seen in Fig.2.8. In Fig.2.9 the final energy distribution is depicted by the histogram. The dotted line

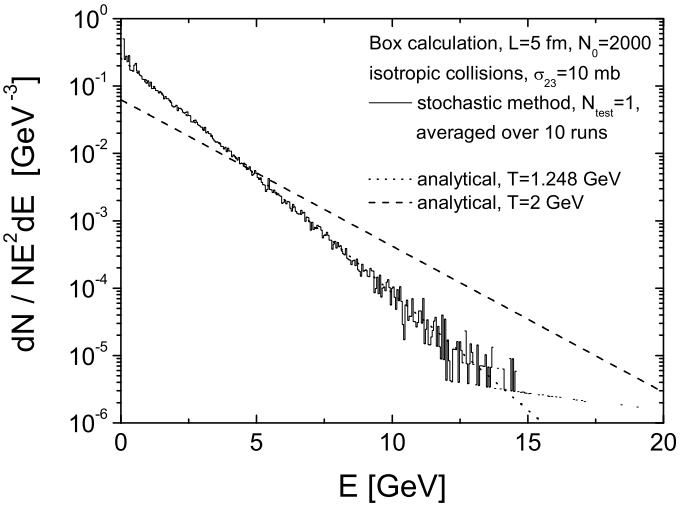

Figure 2.9: Energy distribution from the same calculations as in Fig.2.8. The histogram shows the numerical result. The dotted line shows the analytical expectation and the dashed line shows the analytical distribution (the same as in Fig.2.5) if the particle number would be conserved.

denotes the analytical distribution with the expected temperature $T = 1.248$ GeV. The numerical result agrees again perfectly with the analytical distribution. The fact that the final particle density and the final temperature obtained from the inverse slope of the energy spectrum are identical to the two analytical values demonstrates that detailed balance between the multiplication and annihilation processes is fully realized in our simulations. In Fig.2.10 we compare the time evolutions of the normalized particle density (the fugacity) and the momentum anisotropy. It turns out that for the given initial conditions the kinetic equilibration is slightly slower compared to the chemical equilibration.

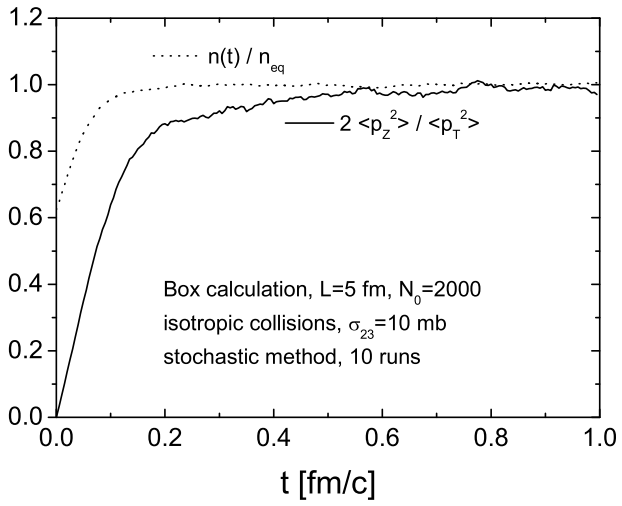

Figure 2.10: Time evolution of the fugacity $n(t)/n_{eq}$ versus the momentum anisotropy from the same calculation as in Fig.2.8.

Chapter 3

Testing the frame independence

The Boltzmann equation (2.1) is a relativistic kinetic equation. Multiplying eq. (2.1) by E gives

$$p^\mu \partial_\mu f = I_{coll} \,. \tag{3.1}$$

This is a Lorentz covariant expression. Therefore the covariance of its solution should not be affected by the choice of the frame, in which the many-body dynamics is actually described. Frame independence must also be fulfilled for any physical observables which can be expressed as Lorentz scalars. However, the equation (3.1) can not be solved exactly in practice by applying a transport algorithm. Strictly speaking, the frame independence is not fulfilled in any cascade-typ simulations. Our aim in this chapter is to study potential frame dependence in our description employing collision algorithms presented in chapter 2. We will also demonstrate the increasing insensitivity of the particularly chosen frame and the convergence of the numerical results when adding more and more test particles into the dynamics.

As explained in section 2.1, the geometrical method is based on the geometrical interpretation of the total cross section and the time ordering of the collision events is generally frame dependent when the mean free path of particles is in the same order as the mean interaction length. In contrast, in simulations employing the stochastic method, which deals with the transition rate, a time ordering of the collision sequence is not needed because collision events will be sampled stochastically within a time step. Still, one has to be aware that a non-zero subvolume of cells and a non-zero timestep disturb the Lorentz invariance. Zhang and Pang had studied already the frame dependence of parton cascade results in [ZP 97] applying a parton cascade code with a similar geometrical collision scheme as presented here. They argued that results from parton cascade simulations are not sensitive to the choice of the frame when the collision criterion is formulated in the center of mass frame of two incoming partons. We will demonstrate the issues in detail in the following considerations and calculations. Furthermore, we note that in

the Poincare-covariant parton cascade model [BMGMN 00] which is also classified to the transport model employing the geometrical method, the collision sequence is ordered by a so-called Poincare-scalar, s, instead of by the usual time, t. For this scheme the ordering of binary collisions and thus the evolution of the system are indeed frame independent. However, it is doubtful whether the space-time evolution, simulated in this model, preserves causality, especially for the extreme case when the mean free path of particles is less than the mean interaction length.

3.1 One dimensional expansion in a tube

For the purpose of studying the frame dependence we do not need consider a special situation. However, as emphasized in the introduction, the here presented cascade model will be applied to simulate the parton evolution in ultrarelativistic heavy ion collisions. Therefore it makes sense to consider a one dimensional expanding system as testing ground, since at the initial stage of an ultrarelativistic heavy ion collision the partonic system will undergo mainly a longitudinal expansion. For convenience, particles of the test system are classical Boltzmann particles instead of quarks and gluons. Furthermore, in the present chapter we will employ isotropic collisions and a constant cross section. In order to mimic a perfect longitudinal expansion we embed all particles into a cylindrical tube with infinite length. The reflections of particles against the tube wall are operated in a same way as performed in the box calculations.

Initially, particles are considered to be thermal in their local spatial element. We use a Bjorken-type boost invariant initial conditions [B 83]

$$f(\mathbf{x}, \mathbf{p}, \tau) = e^{-\frac{p_\perp \cosh(y-\eta)}{T(\tau)}}, \tag{3.2}$$

where τ is the proper time $\tau = \sqrt{t^2 - z^2}$ and y and η denote, respectively, momentum and space-time rapidity

$$y = \frac{1}{2} \ln \frac{E + p_z}{E - p_z} \quad , \quad \eta = \frac{1}{2} \ln \frac{t + z}{t - z}. \tag{3.3}$$

Due to the assumption of the boost invariance, quantities such as particle density n, energy density ϵ and temperature T depend only on the proper time τ. For an ideal, longitudinal and boost-invariant hydrodynamical expansion we obtain

$$n(\tau) = n(\tau_0) \frac{\tau_0}{\tau}, \tag{3.4}$$

$$\epsilon(\tau) = \epsilon(\tau_0) \left(\frac{\tau_0}{\tau}\right)^{4/3}, \tag{3.5}$$

$$T(\tau) = T(\tau_0) \left(\frac{\tau_0}{\tau}\right)^{1/3}. \tag{3.6}$$

Detailed calculations can be found in Appendix F. Besides the study of the frame dependence we also attempt to address the possibility of buildup of an approximately ideal hydrodynamical expansion in cascade simulations when the collision rate is considered to be very high. The time dependences (3.4), (3.5) and (3.6) then serve as ideal references when comparing them with results extracted from the numerical simulations.

To be able to apply the stochastic method, the tube needs to be subdivided into sufficient small cells. A static cell structure as configurated in the box calculations is not suitable any more for an expanding system. However, since the expansion is only one dimensional, we can still employ a static configuration in the transverse plane. Instead of a lattice structure (which will also work), we make use of the symmetry in the given situation and consider a spider web like structure in the transverse plane. Particularly we divide the polar angle ϕ and the radial length squared r^2 equally within the interval $[0, 2\pi]$ and $[0, R^2]$ respectively, where R denotes the radius of the cylindrical tube. This division gives a same transverse area $\Delta F = \Delta\phi\Delta r^2/2$ for all cells. Longitudinally we have to construct a comoving cell configuration which adapts to the expanding system, since, as a reminder, the spatial inhomogeneity of particles in the local cells should be small within any time step. With the thermal distribution function (3.2) it can be simply realized by employing the formula given in Appendix F that the particle number per unit space-time rapidity $dN/d\eta$ calculted at time t in a frame (and also at τ as well) is constant, i.e. time independent, when the system expands hydrodynamically. This gives us the guideline to divide the tube longitudinally into equal small η-bins. We mark the individual cells $[\eta_i, \eta_{i+1}]$ with the central value $\eta = (\eta_i + \eta_{i+1})/2$ and the size $\Delta\eta_c = \eta_{i+1} - \eta_i$. Then the longitudinal length of a particular cell reads

$$\Delta z(t) = t\ [\tanh(\eta + \Delta\eta_c/2) - \tanh(\eta - \Delta\eta_c/2)] \tag{3.7}$$

and increases linearly in time. At time t, when going outwards from the expansion center towards the front edges, the cells becomes more and more narrow. Since the particle diffusion within a time step should not destroy the homogeneity in the local cells very much, the time step has to be chosen smaller than the shortest longitudinal size among all cells. In simulations we set the time step to be half of the shortest Δz of the cell located at the front edge

$$\Delta t\,(t) = 0.5\,\Delta z_{min}(t) = 0.5\,t\ [\tanh(\eta_m + \Delta\eta_c/2) - \tanh(\eta_m - \Delta\eta_c/2)]\ , \tag{3.8}$$

where η_m denotes the outermost η-bin.

With (3.8) we obtain the collision probability for a two-body process in the central cell ($\eta = 0$)

$$P_{22} = v_{rel}\sigma_{22}\frac{\Delta t}{\Delta^3 x} = v_{rel}\sigma_{22}\frac{0.5\ [\tanh(\eta_m + \Delta\eta_c/2) - \tanh(\eta_m - \Delta\eta_c/2)]}{\Delta x_\perp\, 2\ \tanh(\Delta\eta_c/2)}\ . \tag{3.9}$$

For the parameters $\sigma_{22} = 10$ mb, $\Delta x_\perp = 2.5$ fm^2, $\eta_m = 3.0$ and $\Delta\eta_c = 0.2$, the collision probability P_{22} in the central region is expected to be a small value, $P_{22} < 0.004$. In order to make an estimate of the collision probability in the noncentral cells we go to their local comoving frames for convenience, since the collision probability is invariant under Lorentz transformations. The time in the local frame of a η-bin is $\tau = t/\gamma$, where $\gamma = \cosh\eta$ denotes the Lorentz factor. Suppose that the system undergoes one dimensional hydrodynamical expansion, the collision rate $R = n < v_{rel}\sigma_{22} >$ in the local frame of a moving noncentral cell is higher than that in the central cell by factor γ, since the particle density is just γ-times higher according to (3.4). (Note that the estimate becomes complicated when the total cross section depends on s instead of a constant, since the distribution of s is a function of the temperature and the temperatures in the central and noncentral cell are different at time t according to (3.6).) On the other hand, the transformed time step $\Delta\tau$ is γ-times smaller than Δt. Therefore the averaged collision number, which is a Lorentz scalar, is the same in all cells within a time step Δt. Furthermore, for the given cell configuration there are on average the same number of particles in each cell. This leads to the conclusion that for an approximate one dimensional hydrodynamical expansion and choosing a constant cross section, the mean collision probability of two incoming particles (for an ensemble average) is the same wherever the collision will occur. Due to the fact that the collision probability is small, we follow the scheme of [DB 91] and [L 93] to reduce the computing time: We choose randomly $\mathcal{N}$ collision pairs instead of $n(n-1)/2$ possible doublets (n being the particle number in a cell). In order to achieve the correct collision rate, we have to accordingly amplify the collision probability to be

$$P_{22} \to P_{22}\frac{n(n-1)/2}{\mathcal{N}}\,. \tag{3.10}$$

The choice of $\mathcal{N}$ is arbitrary. In the following simulations we set $\mathcal{N} = n$.

For the numerical simulations we consider a tube with a radius of $R = 5$ fm. All particles will be produced initially at $\tau_0 = 0.1$ fm/c and are distributed homogeneously within a space-time rapidity region $\eta \in [-3:3]$. The initial temperature at τ_0 is set to be $T_0 = 2.6$ GeV and thus the initial particle density is

$$\frac{dN}{d\eta}(\tau_0) = \pi R^2\,\frac{T_0^3}{\pi^2}\,\tau_0 = 1748\,. \tag{3.11}$$

We have chosen these parameters to achieve an initially dense system. For the cell configuration we set

$$\Delta\phi = 2\pi/8, \quad \Delta r^2 = R^2/4 \text{ fm}^2 \quad \text{and} \quad \Delta\eta_c = 0.2\,. \tag{3.12}$$

The transverse area of cells is thus about 2.5 fm^2 and the particle number in one cell is around 11.

The total cross section of the two-body collisions is set to be $\sigma_{22} = 10$ mb if only $2 \leftrightarrow 2$ processes are included. We also carry out calculations including both $2 \leftrightarrow 2$ and $2 \leftrightarrow 3$ processes. To be able to make comparisons between simulations without and with inelastic processes, we set the cross sections in the latter case to be $\sigma_{22} = 5$ mb and $\sigma_{23} = 5/2$ mb, which will lead to the same number of absolute transitions per unit time in both cases. The angular distributions of the transitions are considered to be isotropic.

To study the frame dependence we will simulate the expansion in a so-called lab frame (XYZ), whose origin agrees with the center of the expanding system and in a boosted reference frame (X'Y'Z'), which is moving relatively to the lab frame with velocity $\beta = -\tanh\eta_0$. The situation is illustrated in Fig.3.1. In the simulations we set $\eta_0 = 2$. Particles are initialized in the lab frame. The

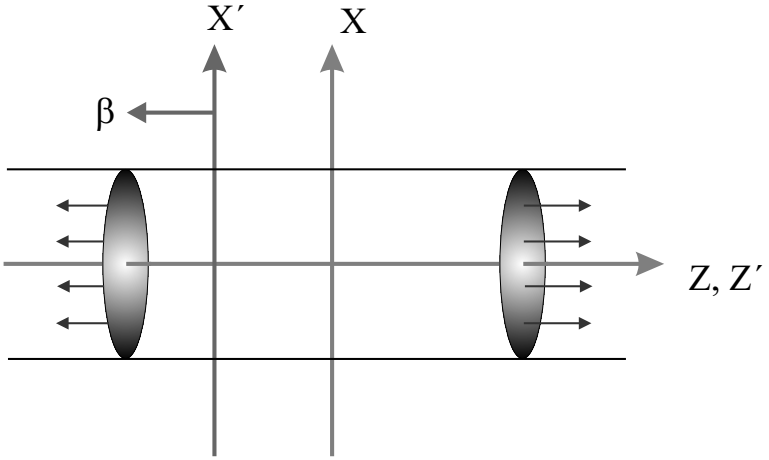

Figure 3.1: One dimensional expansion in a tube. The lab frame is labeled by X, Y and Z, the boosted frame by X', Y' and Z' which is moving with a velocity of β relative to the lab frame.

initial positions and momenta of particles in the boosted frame are obtained by Lorentz transformations from the lab frame. Since particles are initialized longitudinally within a limited spatial region in rapidity, the pictures of the expansion in the two frames will be quite different. The expansion in the lab frame is symmetric, while in the boosted frame the right part of the system expands faster than the left part at late times. Therefore the expansion itself is frame dependent at late times due to the limitation of the particle initialization. We will concentrate on a so-called central region which is a cylinder around $\eta = 0$ in the lab frame and correspondingly around η_0 in the boosted frame with a size of $\Delta\eta = 1$. The time evolutions of observables such as $n(\tau)$, $\epsilon(\tau)$, $T(\tau)$ and others will be extracted in this central region in the two frames and will be compared. We will present the results in section 3.3.

3.2 Improved cell configuration

Before we concentrate on the further analysis, we have to make sure that the cell configuration constructed in the previous section is really suitable for an expanding system simulated by employing the stochastic method. To demonstrate this we perform a one dimensional expansion in the lab frame with the parameters set in the previous section and extract $dN/d\eta$ distribution at time t. One expects that the distribution will be constant over a large region, since this was the basic motivation for the cell construction. Fig.3.2 shows the $dN/d\eta$ distribution within an interval of $\eta \in [-0.3 : 0.3]$ at time 0.11, 0.13, 0.16 and 0.2 fm/c. The dotted line depicts the initial value $dN/d\eta(\tau_0) = 1748$.

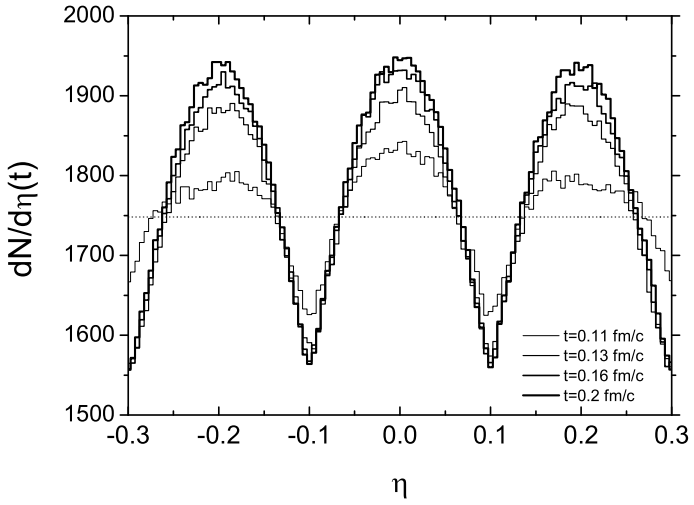

Figure 3.2: Space-time rapidity distributions at different times (t = 0.11, 0.13, 0.16 and 0.2 fm/c from histogram with smallest amplitude to histogram with largest amplitude) from a simulation of one dimensional expansion in a tube. We consider a thermal and boost-invariant initial condition for evolving particles: Particles are produced initially on a hyperbola of $\tau_0 = 0.1$ fm/c and are distributed homogenously within a space-time rapidity interval $\eta \in [-3 : 3]$, $dN/d\eta(\tau_0) = 1748$, which is depicted by the dotted straight line. The initial temperature is set to be $T(\tau_0) = 2.6$ GeV. The radius of the tube is $R = 5$ fm. We consider $2 \leftrightarrow 2$ collisions with isotropic cross section and a constant total cross section of $\sigma_{22} = 10$ mb. The stochastic method is used in the simulation. The η-bins of the cell configuration are set to be $\Delta\eta_c = 0.2$. No test particles ($N_{test} = 1$) are used in the simulation. The distributions are obtained by an average over 10^4 independent realizations.

Astonishingly, at first sight one notices a clear structure in the distribution

within the η-bins. (Remember that the size of the η-bins is set to be $\Delta\eta_c = 0.2$.) One can also realize that this structure approaches a characteristic final shape at late times. The meaning of the structure is that particles in a cell are spatially centered. This has no physical reason, but comes from a numerical artifact due to the finite size of the cell structure, which can be understood as follows: We concentrate on the central η-bin, $\eta \in [-0.1 : 0.1]$, and assume that the expanding system is in local thermal equilibrium. Any change of the $dN/d\eta$ distribution in the central η-bin is caused from collisions among the particles and from the ongoing particle diffusion. Even in the central η-bin the collective motion is still outwards in spite of the small flow velocity. There are more particles moving outwards than particles moving towards the center. Suppose two extreme cases of collision occurring in the central η-bin: In case 1 two particles are moving towards the center and are approaching each other. In case 2 two particles are moving outwards and back-to-back. Due to the considered isotropic scattering the momentum distribution of the particles after the collision is same in both cases. Since, on average, the case 2 happens more frequently than the case 1, one can draw the conclusion that collisions in a η-bin tend to bring more particles back into the center than to push them towards the outside when the collective flow in an η-bin is indeed directed outwards. This is the reason for the artificial structure of the $dN/d\eta$ distribution in the small η-bins. On the other hand, since the distribution of $dN/d\eta$ is no more constant, the particle diffusion from the center outwards is now stronger than the diffusion towards the center. The diffusion is thus counterbalancing the particle centralization and the $dN/d\eta$ distribution will approach a final shape when the balance between the diffusion and the centralization is fully established.

In Fig.3.3 we compare the $dN/d\eta$ distributions at time $t = 0.2$ fm/c from the simulations with $\Delta\eta_c = 0.2$ and with a smaller size of $\Delta\eta_c = 0.1$. In the simulation with $\Delta\eta_c = 0.1$ we employ 2 test particles per real particle in order to obtain the same statistics as in the case with $\Delta\eta_c = 0.2$ and $N_{test} = 1$. We see a weaking in the structure of $dN/d\eta$, though the structure does still exist. In the limit $\Delta\eta_c \to 0$, however, the characteristic substructure in the $dN/d\eta$ distribution will vanish, since the velocity of the *intrinsic* collective flow in the η-bins goes to zero. Therefore decreasing the size of the η-bins and using more test particles would be a natural way to reduce this numerical artifact. However, the more test particles, the longer will the computing time be. A more elaborate way which does not need further test particles is to move the cell configuration randomly from time to time. For instance, we move the central η-bin $\eta \in [-0.1 : 0.1]$ to $[-0.1 + \xi : 0.1 + \xi]$, where ξ is a random number distributed within $[0 : \Delta\eta_c = 0.2]$. Although particles in each η-bin will be still centered within each time step after collisions, but because of the random shift of the cell configuration the associated center of the bin for a particular particle is also moving, so that there is no absolute center for the

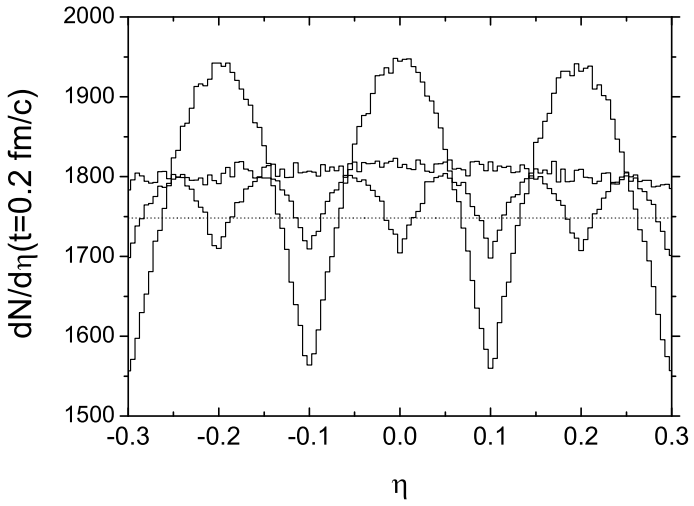

Figure 3.3: Space-time rapidity distributions at time $t = 0.2$ fm/c in tube calculations. The initial condition and collision cross section are the same as in Fig.3.2. The stochastic method is employed in the simulations. The result showing structure with larger(smaller) period is obtained from the simulation with $\Delta\eta_c = 0.2(0.1)$. In the simulation with $\Delta\eta_c = 0.1$ we use 2 test particles per real particle in order to achieve the same statistics in each cell as that in the simulation with $\Delta\eta_c = 0.2$ and $N_{test} = 1$. The histogram, which is nearly constant, is obtained from the simulation with improved moving cell configuration of $\Delta\eta_c = 0.2$ and $N_{test} = 1$. The dotted line shows the initial distribution $dN/d\eta = 1748$. All the distributions are received by an average over 10^4 independent realizations.

particle. Therefore, on average, the effect of the centralization will be washed out. In Fig.3.3 we depict the $dN/d\eta$ distribution from simulations employing the improved moving cell configuration with $\Delta\eta_c = 0.2$. We see that the distribution is nearly constant and does not show any unwanted substructure. In Fig.3.3 we also notice a tiny enhancement of the $dN/d\eta$ distribution when compared with the initial distribution $dN/d\eta = 1748$. We will come back to this further artifact in the next section.

3.3 Results

3.3.1 $2 \leftrightarrow 2$ processes without test particles

At first we present the results from simulations with the improved cell configuration and without introducing test particles. Fig.3.4 and Fig.3.5 show the time evolution of the particle density, energy density and temperature in the central space-time rapidity region in the two frames. The results are ex-

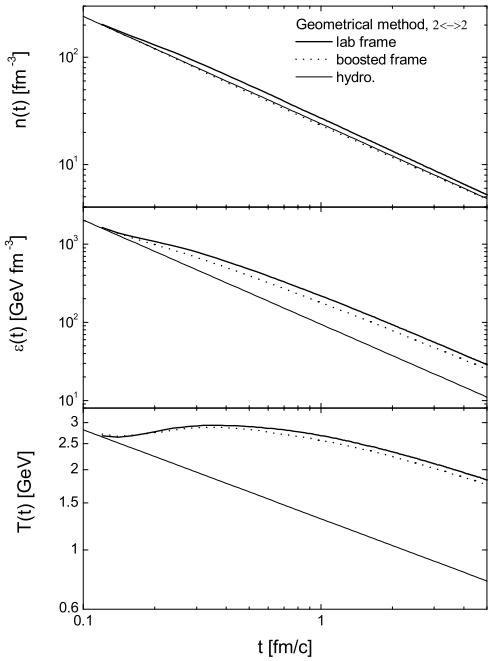

Figure 3.4: Time evolution of the particle density, energy density and temperature extracted in the central space-time rapidity region $\eta \in [-0.5 : 0.5]$ from simulations of one dimensional expansion in the lab and boosted frame of a tube. The geometrical method is employed in the simulations. The initial condition and collision cross section are the same as in Fig.3.2. No test particles ($N_{test} = 1$) are used. Only $2 \leftrightarrow 2$ processes are included. The results are obtained by an anerage over 20 independent realizations. The thin lines indicate time evolutions of the quantities in the hydrodynamical limit.

tracted from the simulations employing the geometrical and stochastic method respectively and are obtained by averaging 20 independent realizations. The effective temperature is defined as $T = \epsilon/3n$ and corresponds to the statistical temperature when the system is at local kinetic equilibrium. Otherwise T

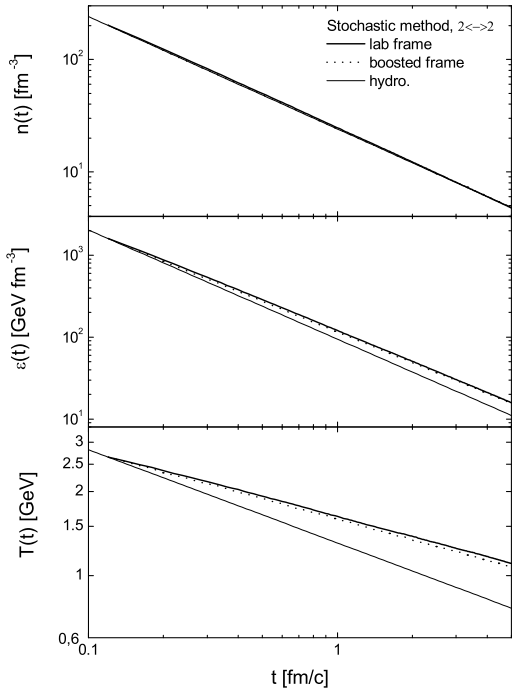

Figure 3.5: Time evolution of the particle density, energy density and temperature extracted in the central space-time rapidity region $\eta \in [-0.5 : 0.5]$ from simulations employing the stochastic method in the lab and boosted frame of a tube. The initial condition and collision cross section are the same as in Fig.3.2. No test particles ($N_{test} = 1$) are used. Only $2 \leftrightarrow 2$ processes are implemented. We apply the moving cell configuration with $\Delta\eta_c = 0.2$. The results are obtained by an average over 20 independent realizations.

can be regarded as the mean energy per particle. In the simulation with the stochastic method we set the size of the η-bins to be $\Delta\eta_c = 0.2$. The time scale in Fig.3.4 and Fig.3.5 denotes the time in the local frame of the central region. The solid and dotted curves depict the results achieved in the lab and boosted frame respectively. The thin solid lines show the ideal hydrodynamical limit calculated via a corresponding integral of the thermal phase space distribution (3.2). Please note that we have taken the size of the central region into account. Therefore the hydrodynamical results (3.4), (3.5) and (3.6) are modified by

$$n(t) \;=\; a_n \, n(\tau = t) \,, \quad a_n := \frac{\Delta\eta}{2 \, \tanh(\Delta\eta/2)} \tag{3.13}$$

$$\epsilon(t) = a_\epsilon\,\epsilon(\tau = t)\,, \quad a_\epsilon := \frac{1}{6\,\tanh(\Delta\eta/2)} \int_{-\Delta\eta/2}^{\Delta\eta/2} d\eta' \left(3 + (\tanh\eta')^2\right) \times (\cosh\eta')^{4/3} \tag{3.14}$$

$$T(t) = a_T\,T(\tau = t)\,, \quad a_T := \frac{a_\epsilon}{a_n}\,. \tag{3.15}$$

In the limit $\Delta\eta \to 0$ the additional factors go to 1. For $\Delta\eta = 1.0$ we obtain $a_n = 1.082$, $a_\epsilon = 1.1737$ and thus $a_T = 1.0848$.

From Fig.3.4 and Fig.3.5 we see that the frame dependence of the considered quantities is quite noticeable in the simulation when employing the geometrical method, while it is rather weak in the simulation employing the stochastic method. Moreover and astonishingly, the 'temperature' in the simulation with the geometrical method is increased at the beginning of the expansion. This 'reheating' is unphysical, since the isotropic initialization of the particle system does not give any reason for an introversive pressure. The gradient of the pressure is directed outward, so that in the further evolution the longitudinal work done by the pressure should lead to a cooling of the system. We also rule out any explanation based on a possible viscous effect which might bring some effective net energy flow into the local region, because there is no reheating in the simulation with the stochastic method. From the investigations within a static box we have realized that the collision rate obtained in the simulation with the geometrical method will be suppressed when the mean free path is in the same order as (or even smaller than) the interaction length. This is indeed the situation at the beginning of the expansion in the tube. The suppression of collisions will obviously slow down the cooling of the system, but this can not lead to any reheating. However, the fact that particles can interact with each other over a larger distance than the mean free path makes it reasonable that the pressure could be incorrectly built up. The effect of the 'anti-pressure' is thus a numerical artifact. We extract the collision rate and the difference of space-time rapidities of colliding particles per collision event $< \Delta\eta >_{coll}$ in the central region from the simulations carried out in the lab and boosted frame. The results are depicted in Fig.3.6. The collision rates are obtained by counting the collision events in the central region within a time interval of 0.02 fm/c. It is clearly seen that the collision rates in the simulation with the stochastic method agree well with the expectation. The slight discrepancy can be understood as the consequence of the relative large size of the η-bins ($\Delta\eta_c = 0.2$). In contrast, the collision rates in the simulation with the geometrical method are strongly suppressed at high densities due to the relativistic effect of the time spread of the two collision times, as explained in section 2.1.1. The results of the $< \Delta\eta >_{coll}$ show that particles interact in fact over very large distance at high densities in the simulation when employing the geometrical method. The decrease of the $< \Delta\eta >_{coll}$ at the highest densities corresponding to the very beginning of the expansion is due to the

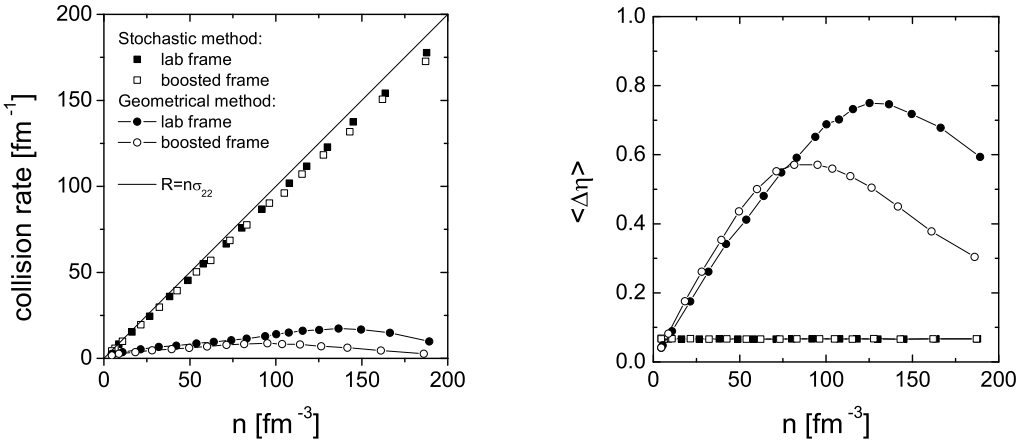

Figure 3.6: Collision rate (left panel) and averaged difference in space-time rapidity of colliding particles (right panel) in the central space-time rapidity region for various particle densities experienced during the expansion. The results are extracted from the same simulations performed for the extractions of $n(t)$ and $\epsilon(t)$ in Fig.3.4 and Fig.3.5. The solid line in the left panel shows the analytical expectation.

fact that at the early times particles with large η are still not formed. In the simulation employing the stochastic method the interaction length is, however, controlled by the cell structure. In summary, we suspect that the larger interaction distance (compared with the mean free path) may be the reason for the 'reheating'.

Fig.3.7 shows the space-time rapidity distributions at the proper time $\tau =$ 0.2 and 1.0 fm/c extracted from the simulations in the lab and boosted frame with the geometrical (upper panel) and the stochastic (lower panel) method respectively. The solid (dotted) curves depict the distributions in the lab (boosted) frame. The thin solid lines show the initial distribution $dN/d\eta(\tau_0) =$ 1748 within $\eta \in [-3 : 3]$. We see that the results obtained when employing the geometrical method show a strong frame dependence. A clear hump exists around the expansion center $\eta = 0$ in both frames and broadens gradually. (Note that the expansion center in the boosted frame is at $\eta = -2$ after the shift.) The humps indicate a net particle diffusion towards the expansion center, which again can be explained as a consequence of the 'anti-pressure' effect: The introversive pressure drives the particles back to the expansion center. In the distributions obtained when using the stochastic method we see a relative tiny hump at the expansion center which disappears at the later time. The slight enhancement has been also noticed in Fig.3.3. We recognize that the size of the cell bins $\Delta\eta_c = 0.2$ is not small enough to overcome the

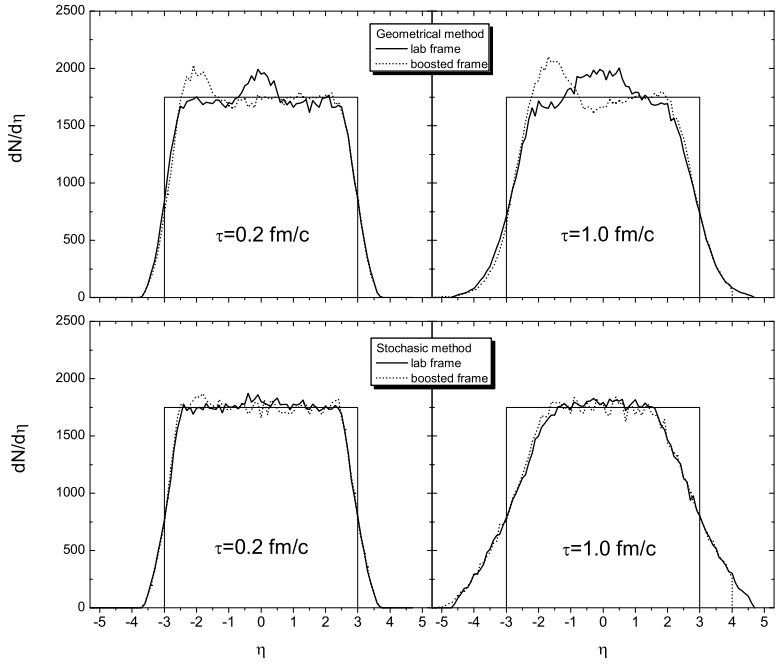

Figure 3.7: Particle distributions versus space-time rapidity at the proper time $\tau = 0.2$ and 1.0 fm/c extracted from simulations employing the geometrical and stochastic method in the lab and boosted frame. The initial condition and collision cross section (and cell configuration) are the same as in Fig.3.4 (and in Fig.3.5). In order to compare the distributions in the same physical regions directly, we have shifted the distributions in the boosted frame by $-\eta_0 = -2$. Except that the distributions extracted from the simulations in the boosted frame using the stochastic method are obtained by an average over 10 independent realizations, all other distributions are obtained from 20 independent realizations. The thin solid lines indicate the initial distribution $dN/d\eta(\tau_0) = 1748$.

numerical artifact completely. Moreover, we notice the cuts at $\eta = 4$ in the distributions at $\tau = 1.0$ fm/c for the expansion in the boosted frame. This is due to the fact that the end time of the simulation in the boosted frame is $t' = 210$ fm/c and thus particles with η being greater than 6 (or 4 after the shift) have smaller proper time than 1 fm/c.

In Fig.3.8 we depict the momentum rapidity distributions at proper times. The thin solid curves show the initial rapidity distribution

$$\frac{dN}{dy}(\tau_0) = \frac{R^2 T_0^3 \tau_0}{\pi} \frac{\sinh(2\eta_m)}{\cosh(2\eta_m) + \cosh(2y)}, \tag{3.16}$$

where η_m denotes the boundary of the initial system which has been set to be 3. In Fig.3.8 one also recognizes the particle diffusion towards the expansion

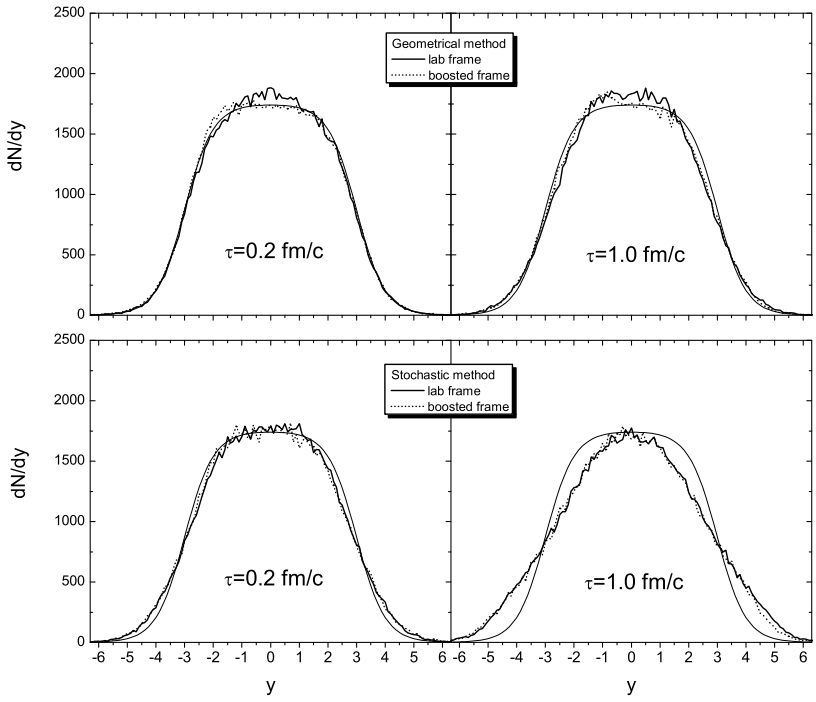

Figure 3.8: Particle distributions versus momentum rapidity at the proper time $\tau = 0.2$ and 1.0 fm/c extracted from simulations employing the geometrical and stochastic method in the lab and boosted frame. The results are obtained from the same simulations performed for the extractions of $dN/d\eta(\tau)$ in Fig.3.7. The thin solid curves indicate the initial distribution at $\tau_0 = 0.1$ fm/c.

center, though the effect is not strong. The disributions obtained when using the stochastic method show perfect 'no frame dependence' and a collective flow outwards to the higher rapidity at late times.

For an initially thermal system it seems reasonable that the system will be still locally in or close to kinetic equilibrium during the further expansion. On the other hand, we have also realized that numerical artifacts make strong effects at the beginning of the expansion, especially in the simulations applying the geometrical algorithm. Therefore it is essential to question whether the encountered numerical problem does affect the maintenance of the kinetic equilibrium in the cascade simulations of the one dimensional expansion. For this we extract the transverse momentum distributions at $y = 0$ within an interval $y \in [-0.5 : 0.5]$ at different proper times and compare them with the analytical thermal distributions. In Fig.3.9 and Fig.3.10 the p_T distributions extracted from the simulations in the lab frame are depicted. Fig.3.9 shows

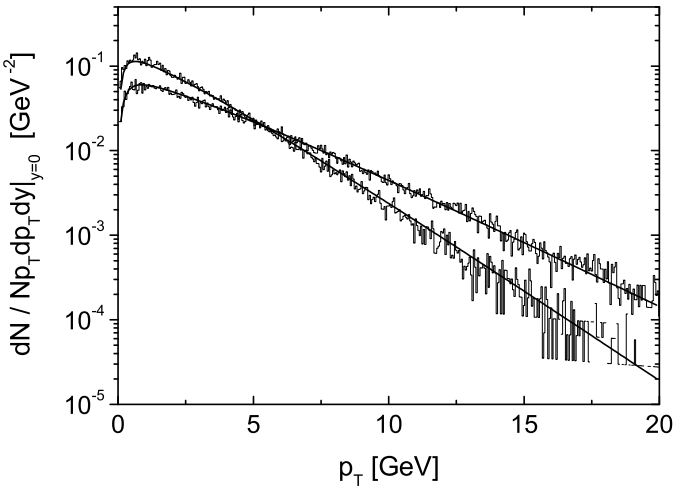

Figure 3.9: Distributions of the transverse momentum per unit rapidity at $y = 0$ at $\tau = 1.0$ and 4.0 fm/c (from upper to lower histogram) in a simulation employing the geometrical method in the lab frame. The solid lines show the analytical distributions (3.17) with the temperatures read off from Fig.3.4.

the results at $\tau = 1.0$ and 4.0 fm/c in the simulations with the geometrical method and Fig.3.10 shows the results at $\tau = 0.2$, 1.0 and 4.0 fm/c in the simulations with the stochastic method. The thermal distributions shown by the solid lines are obtained as integral of the thermal particle distribution function (3.2) by means of the Cooper-Frye formula [CF 74]

$$\left.\frac{1}{N}\frac{dN}{p_T\,dp_T\,\Delta y}\right|_{y=0}(\tau) = \frac{1}{N}\frac{2\,\pi^2 R^2}{(2\pi)^3}\frac{1}{\Delta y}\int_{-3}^{3} d\eta \int_{-\Delta y/2}^{\Delta y/2} dy\, p_T\,\tau\cosh(y-\eta)\, e^{-\frac{p_T\,\cosh(y-\eta)}{T(\tau)}}\,, \tag{3.17}$$

where $\Delta y = 1$ and the temperature $T(\tau)$ is read off from Fig.3.4 or Fig.3.5 at $t = \tau$. We see good agreements between the numerical and the analytical distributions, even for the case of the geometrical method. The analogous p_T distributions, extracted from the simulations in the boosted frame (at $y = \eta_0 = 2$), are also compared with the analytical spectra (both not shown in figures). The agreements are perfect as those presented in Fig.3.9 and Fig.3.10. As a conclusion, although the expansion does not proceed fully close to ideal hydrodynamics, the expanding system is still kinetically equilibrated at least until $\tau = 4$ fm/c in the simulations with the stochastic method as well as with the geometrical method, although in the latter case the cooling of the system occurs much slower.

As a last point, we show in Fig.3.11 the proper time evolution of the trans-

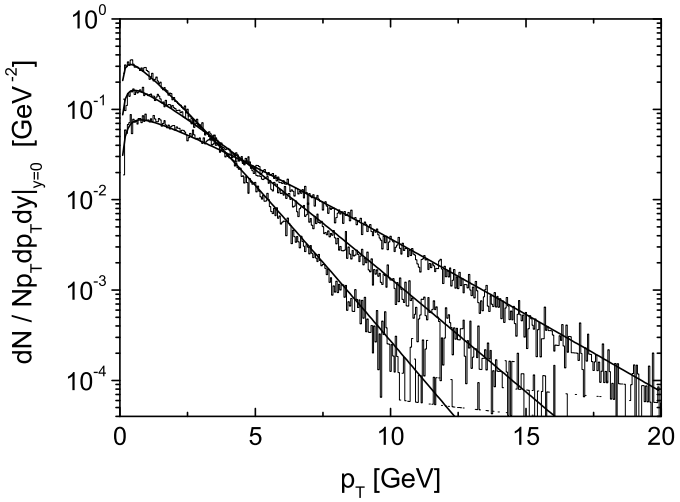

Figure 3.10: Distributions of the transverse momentum per unit rapidity at $y = 0$ at $\tau = 0.2$, 1.0 and 4.0 fm/c (from upper to lowest histogram) in a simulation employing the stochastic method in the lab frame. The solid lines show the analytical distributions (3.17) with the temperatures read off from Fig.3.5.

verse energy extracted at $y = 0$ per unit rapidity from both type of simulations in the lab and boosted frame respectively. The thin solid line depicts the result in the hydrodynamical limit

$$\begin{aligned} \left.\frac{dE_T}{dy}\right|_{y=0}(\tau) &= \frac{\pi R^2}{(2\pi)^3}\int d\eta\, d^2p_T\, p_T^2\, \tau \cosh(y-\eta)\, e^{-\frac{p_T\,\cosh(y-\eta)}{T(\tau)}} \\ &= \frac{3}{4}R^2\, T^4\, \tau = \frac{3}{4}R^2\, T_0^4\, \tau_0^{4/3}\, \tau^{-1/3}\,. \end{aligned} \tag{3.18}$$

The time evolutions of the transverse energy have similar shapes like that of the temperature shown in Fig.3.4 and Fig.3.5. We also recognize the unphysical 'reheating' occurring in the simulations with the standard geometrical method.

Summarying this section, we have studied the frame dependence of a one dimensional expansion in a tube by employing the two collision algorithms presented in this paper. The comparisons show that quantities extracted in the simulations with the geometrical method have a much pronounced and unphysical frame dependence. Numerical artifacts are very significant in these simulations, especially at the beginning of the expansion when the system is very dense. In contrast, the results obtained from the simulations when employing the stochastic method show almost 'no frame dependence'.

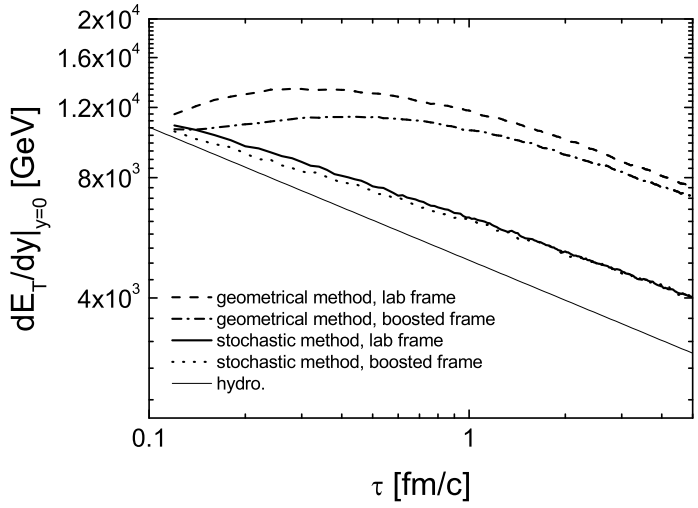

Figure 3.11: Proper time evolution of the transverse energy per unit momentum rapidity at $y = 0$ in the simulations employing the geometrical and stochastic method in the lab and boosted frame. The thin solid line shows the analytical evolution in the hydrodynamical limit.

3.3.2 $2 \leftrightarrow 2$ processes with test particles

The time evolutions of the particle density, energy density and temperature depicted in Fig.3.4 and Fig.3.5 demonstrate that simulated dynamics does not undergo an ideal hydrodynamical expansion. On the one hand, it is true that the ideal hydrodynamics can not be realized in simulations with finite collision rate. One has to take the finite viscosity into account. Thus it is interesting to make comparisons between the transport results and those calculated from viscous hydrodynamics [DG 85, GPZ 97, M 02]. This subject is, however, beyond the scope of this thesis. On the other hand, even the viscous expansion can not be solved exactly due to the limitation of the numerical implementations. Especially, as observed in the simulations with the geometrical method, the numerical artifacts make strong unphysical effects. In this subsection we introduce the test particle method into the dynamics to reduce this numerical uncertainty and to study the convergence of the transport solutions.

From the experiences in the box calculations, one realizes that the computing becomes more time-consuming when more and more test particles are added into the simulations. One way to reduce the computing time in the present case is to consider a tube with a smaller radius. The (real) particle density is however unchanged. In simulations with the geometrical method we set the radius of the tube to be $R' = R/\sqrt{N_{test}}$ with $R = 5$ fm. However, in

simulations with the stochastic method we instead keep the radius of 5 fm, in order to be able to refine the cell configuration.

Fig.3.12 depicts the relative frame dependence of the particle density, energy density and temperature extracted in the central region in the simulations with the geometrical method with $N_{test} = 1$, 4 and 25 respectively. The sim-

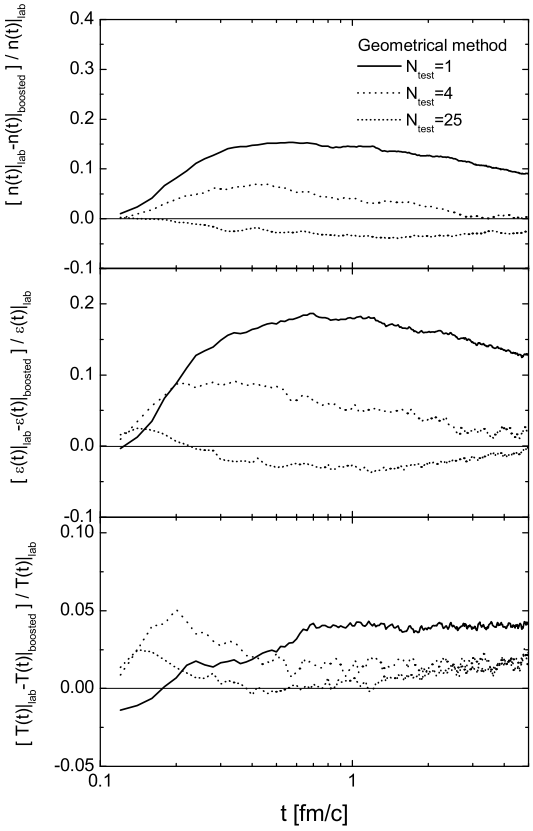

Figure 3.12: Relative frame dependence of the particle density, energy density and temperature in the simulations employing the geometrical method. The initial condition and collision cross section are the same as in Fig.3.4. The results are obtained by averaging 20, 2 and 20 independent realizations for increasing test particles $N_{test} = 1$, 4 and 25 respectively.

ulations are performed in the lab frame. We obtain the results by averaging 20, 2 and 20 independent realizations respectively. Note that the simulation with $N_{test} = 4$ is exceptionally carried out with the default radius of $R = 5$ fm. We see that the potential frame dependence is more and more reduced when more and more test particles are considered. The reduction of the frame

dependence is also clearly demonstrated in Fig.3.13. Here the distributions of

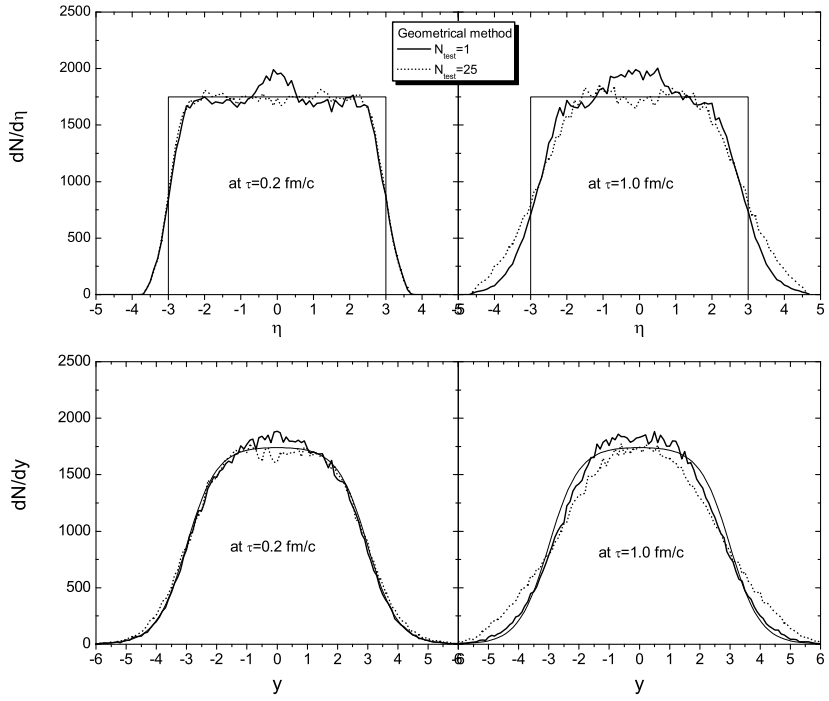

Figure 3.13: Comparison of the space-time and momentum rapidity distribution with $N_{test} = 25$ with the distribution without test particles at $\tau = 0.2$ and 1.0 fm/c. The distributions are extracted from the simulations employing the geometrical method in the lab frame by averaging 20 independent realizations. The thin solid lines indicate the initial distributions at $\tau_0 = 0.1$ fm/c.

the space-time and as well as momentum rapidity obtained with $N_{test} = 25$ (by dotted curves) are compared with the distributions without test particles (or $N_{test} = 1$ by solid curves) at $\tau = 0.2$ and 1.0 fm/c. The humps, which exist in the distribution without test particles due to the artificial back diffusion, do not occur with $N_{test} = 25$. Moreover, the shapes of the distributions obtained with $N_{test} = 25$ are almost the same as those obtained using the stochastic method with $N_{test} = 1$, shown in Fig.3.7 and Fig.3.8.

For the case employing the stochastic method it is not necessary to study the reduction of the frame dependence with the test particle method, since the frame dependence is actually very weak even without test particles (see Fig.3.5).

We also employ the test particle method to study the convergence of the transport solutions. Fig.3.14 shows the time evolution of the temperature ex-

tracted in the central region in the simulations with increasing test particles in the lab frame. In the simulations with the stochastic method the size of

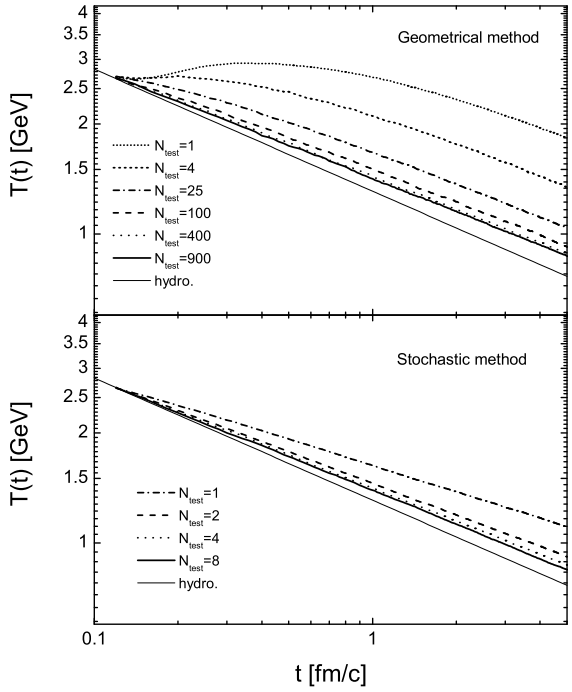

Figure 3.14: Convergence of temperature in the simulations in the lab frame with increasing test particles. The initial condition and collision cross section (and cell configuration) are the same as in Fig.3.4 (and in Fig.3.5). The results in the simulations employing the geometrical method are obtained by averaging 20, 2, 20, 5, 5 and 5 independent realizations for N_{test} = 1, 4, 25, 100, 400 and 900 respectively. The results in the simulations employing the stochastic method are obtained by averaging 20, 10, 2 and 1 independent realizations for $N_{test} = 1$, 2, 4 and 8 respectively.

the η-bins is refined to $\Delta\eta_c = 0.2/N_{test}$. There are on average 11 test particles in one cell. (We have also performed simulations with doubled test particle number in one cell to increase the statistics. The outcome shows almost no changes.) Since in the tube calculations the particle distribution in the transverse direction is absolutely homogeneous, there is no need to refine the cells transversely. In Fig.3.14 we see the clear tendency of convergence. The time evolution of the temperatures extracted from the simulations with the geometrical and stochastic method converge towards almost the same curve. It is obvious that the solution obtained with the stochastic method converges more

efficiently than the solution obtained with the geometrical method. Therefore, we do favour the stochastic method to be applied in transport simulations of system with high particle density. Furthermore, we see that the effect of the artificial reheating, appearing in the simulation with the geometrical method with $N_{test} = 1$, reduces and vanishes in the simulations when employing higher test particles.

In Fig.3.15 we depict the collision rate and the mean difference of the space-time rapidities of colliding particles per collision $< \Delta\eta >_{coll}$ in the simulations with the geometrical method with increasing test particles. We see

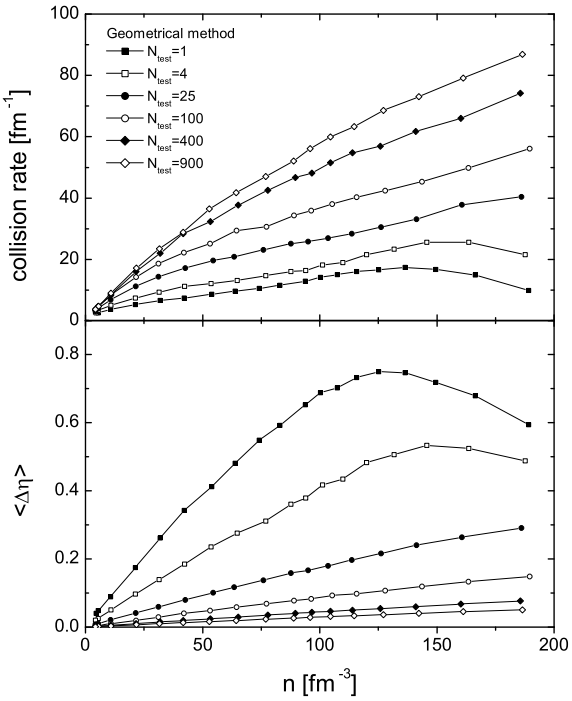

Figure 3.15: Collision rate and averaged difference in space-time rapidity of colliding particles. The results are extracted in the central space-time rapidity region $\eta \in [-0.5 : 0.5]$ for various particle densities experienced during the expansion. The simulations are the same as performed in the upper panel of Fig.3.14 when discussing the convergence of the temperature.

that the collision rate increases when using more test particles. However, even for $N_{test} = 900$ the collision rates at high densities are still suppressed. (Note that the interaction length decreases only with $1/\sqrt{N_{test}}$.) This is the reason why the temperature extracted from the simulation employing the geometrical method with $N_{test} = 900$ is slightly higher than that extracted from the

simulation employing the stochastic method with $N_{test} = 8$ (see Fig.3.14). We also see that the $< \Delta\eta >_{coll}$ decreases when the number of the test particles increases. Putting Fig.3.15 in relation to Fig.3.14 confirms our suspicion in the previous subsection that unwanted collisions over large distances may lead to the buildup of 'anti-pressure' which then influences the particle diffusion.

3.3.3 Including $2 \leftrightarrow 3$ processes

We now include the inelastic $2 \leftrightarrow 3$ processes into the dynamics of the one dimensional expansion in the tube and study the frame dependence and the convergence for the new situation. The stochastic method is applied to simulate the (in)elastic collisions whose cross sections are set to be $\sigma_{22} = 5$ mb and $\sigma_{23} = 2.5$ mb. These parameters lead to the same rate of the elastic and inelastic transitions. We consider isotropic collisions and set the size of the η-bins to be $\Delta\eta_c = 0.2/N_{test}$.

In Fig.3.16 we show the time evolutions of the particle density, energy

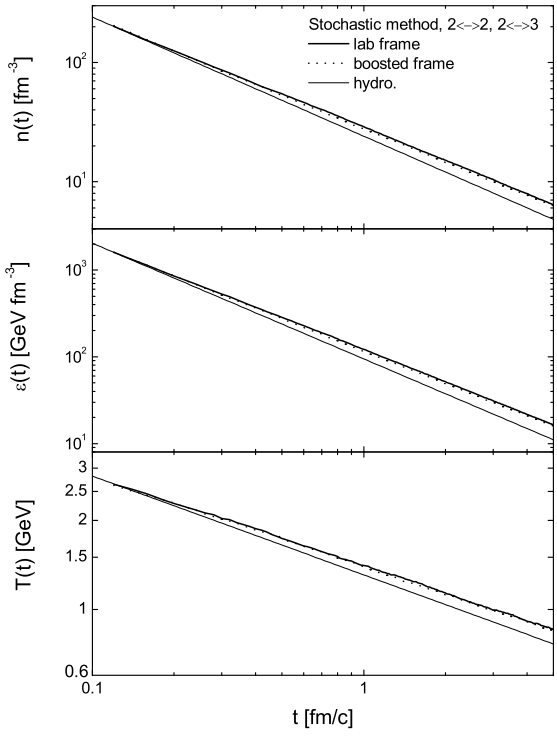

Figure 3.16: Time evolution of the particle density, energy density and temperature extracted in the central space-time rapidity region $\eta \in [-0.5 : 0.5]$ from the simulations with $N_{test} = 1$ employing the stochastic method in the lab and boosted frame. The initial conditions and cell configuration are the same as in Fig.3.5.

density and temperature extracted in the central space-time rapidity region from the simulations with $N_{test} = 1$ carried out in the lab and boosted frame. The results are obtained by an average over 10 independent realizations. The thin solid lines in Fig.3.16 indicate time evolutions in the hydrodynamical limit. We see that the results are absolutely frame independent. Comparing to the results with only two-body collisions shown in Fig.3.5, we notice that the particle density is slightly enhanced. This enhancement is not due to any numerical artifacts, but the consequence of the chemical equilibration: In the thermal equilibrium the particle density is related with the temperature by $n = T^3/\pi^2$. Since during the expansion the temperature is always higher compared to the ideal hydrodynamical limit due to finite viscosity, therefore, there have to be more particles being produced than annihilated in order to account for the undersaturated system and to achieve a new balance. To address the chemical equilibration we concentrate on the time evolution of the fugacity which is defined as $\lambda(t) = n(t)/n^{eq}(t)$, where

$$n^{eq}(t) = a_n\, n^{eq}(\tau) = a_n\, \frac{T^3(\tau)}{\pi^2} = \frac{a_n}{a_T^3}\, \frac{T^3(t)}{\pi^2}\,. \tag{3.19}$$

a_n and a_T are factors given in (3.13) and (3.15) taking the size of the central region into account. The $T(t)$ in (3.19) is just the extracted temperature from the simulation. Fig.3.17 depicts the time evolution of the fugacity. We see

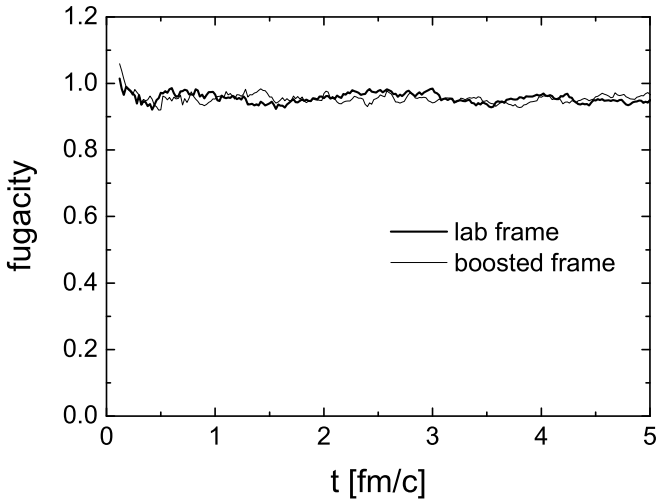

Figure 3.17: Time evolution of fugacity extracted from the same simulations performed for the extraction of $n(t)$ and $\epsilon(t)$ in Fig.3.16.

that the chemical equilibrium is almost achieved and maintained during the

expansion in both frames. We have also extracted the p_T distributions and compared with the analytical spectra at different times. The results show that the kinetic equilibrium is also maintained during the expansion.

The collision rates of $2 \leftrightarrow 2$, $2 \rightarrow 3$ and $3 \rightarrow 2$ processes, extracted from the simulation in the lab frame, are depicted in Fig.3.18. We see perfect

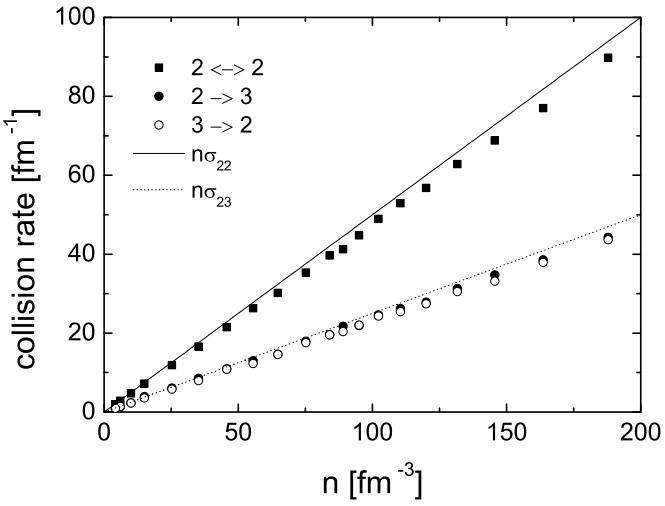

Figure 3.18: Collision rate in the central region for various particle densities experienced during the expansion. The results are extracted from the same simulations performed for the extractions of $n(t)$ and $\epsilon(t)$ in the lab frame in Fig.3.16. The solid squares, solid circles and open circles depict, respectively, the collision rates for $2 \leftrightarrow 2$, $2 \rightarrow 3$ and $3 \rightarrow 2$ transitions. The solid and dotted line show the analytical expectations.

agreements of the extracted collision rates with the expectations. Furthermore, the collision rates of $2 \rightarrow 3$ and $3 \rightarrow 2$ processes are almost identical, which demonstrates once more the maintenance of the chemical equilibrium in the expanding system.

We show in Fig.3.19 the particle distributions versus the space-time rapidity η and versus the momentum rapidity y at $\tau = 0.2$ and 1.0 fm/c, obtained from the simulations in the lab and boosted frame. The frame dependence is not noticeable and lies within the statistical errors. In Fig.3.19 we also see the enhancement in the particle number over a large range due to the slight particle production in the ongoing chemical equilibration.

Finally, when using more test particles, the results from the present simulations will converge to their exact forms. Due to the settings of $\sigma_{22} = 5$ mb and $\sigma_{23} = 2.5$ mb one would expect that the total collision rate including

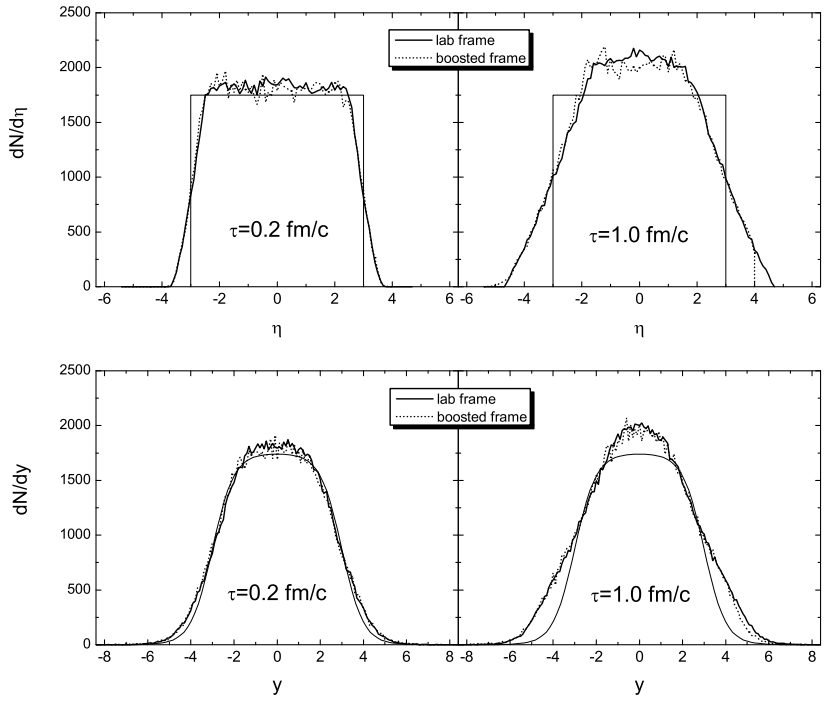

Figure 3.19: Particle distributions versus space-time rapidity and momentum rapidity at the proper time $\tau = 0.2$ and 1.0 fm/c, extracted from the simulations with $N_{test} = 1$ employing the stochastic method in the lab and boosted frame. The initial condition, collision cross section and cell configuration are the same as in Fig.3.16. The distributions extracted in the lab(boosted) frame are obtained by averaging 20(6) independent realizations. The thin solid lines indicate the initial distributions at $\tau_0 = 0.1$ fm/c.

elastic and inelastic processes is the same as that in the simulation with purely elastic collisions and $\sigma_{22} = 10$ mb. Therefore, the convergence with increasing test particles would be exactly the same in both cases. Still, as realized from the above comparison between Fig.3.16 and Fig.3.5, the temperatures (and the number densities as well) in the central space-time rapidity region are slightly different due to the new balancing as explained above. Therefore, the convergence of the temperature, for instance, will not be the same as that shown in the lower panel of Fig.3.14. On the other hand, the new balancing should not affect the time evolution of the energy density. This quantity is shown in Fig.3.20 in both cases with increasing N_{test}. We see the exactly same convergence of the energy density in the central region for the purely $2 \leftrightarrow 2$ and the $2 \leftrightarrow 2$, $2 \leftrightarrow 3$ case.

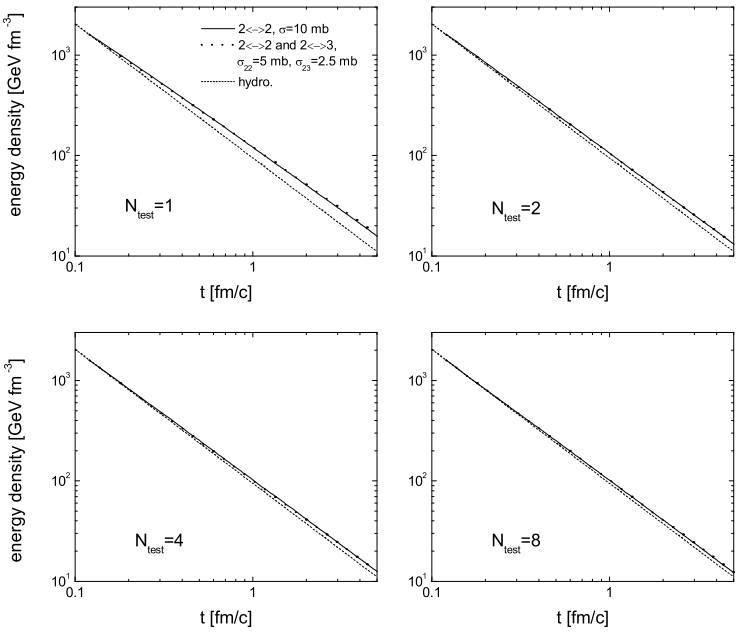

Figure 3.20: Convergence of energy density in the simulations in the lab frame with increasing test particles. The cascade simulations are performed employing the stochastic algorithm. The dotted lines depict the results with $\sigma_{22} = 5$ mb and $\sigma_{23} = 2.5$ mb, while the thin solid lines depict the results with purely elastic collisions and $\sigma_{22} = 10$ mb. The results are obtained by averaging 20, 10, 2 and 1 independent realizations for $N_{test} = 1$, 2, 4 and 8 respectively. The thin dashed lines show the hydrodynamical limit.

After this exhaustive discussion of testing the operation of the cascade, we now proceed to describe real heavy ion collisions.

Chapter 4

The initial conditions of partons in uRHIC

In heavy ion collisions at high collider energy like at RHIC and LHC, one assumes that when the two heavy ions go through each other, a large amount of partons (quarks and gluons) normally confined within hadrons will be liberated and overwhelm the wounded nucleons, especially in the midrapidity region. The picture of the very early stage of the collision, when potentialy the partons are freed from the two nuclear wave functions and do become on-shell particles, is crucial for all kinetic cascades which can only describe the further evolution. Hence, one has to incorporate a physical model for describing the very initial phase of liberated partons serving as initial conditions for cascades. These initial conditions will be discussed in this chapter.

One such physical picture is based on the idea of a free superposition of minijets being produced in the individual semi-hard nucleon-nucleon interactions. Minijets denote here partons with high transverse momentum. The creation of minijets can be well described by the perturbative QCD. It is estimated in [EKL 89] that partons with $p_T > 2$ GeV will carry off 50% (80%) of total transverse energy per unit rapidity at RHIC (LHC). These minijets are expected to undergo further collisions and become thermalized [KLL 87]. However, cascade simulations with this kind of initial condition and employing elastic $gg \to gg$ collisions failed to verify the achievement of thermalization. On the other hand, the inelastic $gg \leftrightarrow ggg$ interactions are expected to be efficient processes making the system thermalized. Therefore, it is our main interest to investigate thermalization under the initial condition of minijets production again, when using the new parton cascade including $2 \leftrightarrow 3$ processes. The results will be presented in chapter 6. The initial distributions of soft partons with smaller p_T can be solved in the classical effective field theory approach which is, in exact analogy to a spin glass, a Color Glass Condensate (CGC) [MV 94] and is characterized by Q_s, the momentum scale at

which gluon distributions saturate. At RHIC Q_s is estimated to be 1 GeV. The CGC model is based on the idea of gluon saturation of the QCD structure function of the nuclei at sufficiently low x. The so-called 'bottom-up' scenario [BMSS 01] of thermalization relies on these initial conditions, where in the leading order of the coupling constant α_s the various time scales of kinetic evolution is parametrically estimated. We will very briefly discuss the CGC initial conditions and show the corresponding results on thermalization at the end of chapter 6. Detailed analysis will follow in future investigations. At present, we concentrate on the description of the multiple minijets production at RHIC.

A 'jet' refers originally to a set of fairly well collimated hadrons observed in hadronic and also in e^+e^- reactions. One suggests, for example in a nucleon-nucleon collision, that large p_T events proceed via 'hard scattering' involving the collision of just one parton from each initial nucleon. This is in agreement with the whole philosophy of the parton model. The partons involved are scattered through large p_T and are supposed to fragment into showers of hadrons. It is thus accepted that high p_T jets are implied by perturbative QCD and that they are the simplest and perhaps best evidence supporting it.

We now redefine a jet to be a produced parton with high $p_T > p_0$ and compute the jet cross section by applying pQCD. In nucleon-nucleon collisions the differential jet cross section is given [WG 91] by

$$\frac{d\sigma_{jet}}{dp_T^2 dy_1 dy_2} = K \sum_{a,b} x_1 f_a(x_1, p_T^2) x_2 f_b(x_2, p_T^2) \frac{d\sigma_{ab}}{d\hat{t}}(\hat{s}, \hat{t}, \hat{u}) \,, \tag{4.1}$$

where the sum runs over all parton species, p_T is the transverse momentum and y_1 and y_2 are the momentum rapidities of the produced partons. x_1 and x_2 are the Feynman variables denoting the longitudinal momentum fractions carried by the partons respectively. These variables are related by

$$x_1 = \frac{x_T}{2}\left(e^{y_1} + e^{y_2}\right), \quad x_2 = \frac{x_T}{2}\left(e^{-y_1} + e^{-y_2}\right), \tag{4.2}$$

where $x_T = 2p_T/\sqrt{s}$. Note that the intrinsic transverse momentum of each colliding parton is zero. $d\sigma_{ab}$ stands for the leading order pQCD parton-parton cross sections which depend on the subprocess Mandelstam variables

$$\hat{s} = x_1 x_2 s \,, \quad \hat{t} = -p_T^2(1 + e^{y_2 - y_1}) \,, \quad \hat{u} = -p_T^2(1 + e^{y_1 - y_2}) \,. \tag{4.3}$$

$f(x, Q^2)$ denote the parton structure functions which are parametrizations based on experimental data from deep inelastic lepton- and neutrino-nucleon scatterings. Q^2 is the momentum transfer squred (with minus sign) in such reactions and serves as a kind of resolution scale for partons. The parton structure function $f_a(x, Q^2)$ gives the probability for finding parton species a at x and at Q^2 in a nucleon. In this study we employ the Glück-Reya-Vogt

parametrizations [GRV 95] for the parton structure functions, which are valid for $0.4 \leq Q^2 \leq 10^6$ GeV and $10^{-5} \leq x < 1$. They are sufficiently accurate for the RHIC energy, since the smallest x of minijets is estimated to be around $10^{-3} - 10^{-2}$ at RHIC. The scale Q^2 in hadronic reactions is ambiguous. We set it to be the transverse momentum of the produced parton $Q^2 = p_T^2$. The phenomenological factor K, set to be 2, accounts for higher-order pQCD corrections. It is straightfoward that the differential cross section $d\sigma_{jet}/d\hat{t}dx_1dx_2$ for a jet (or two back-to-back jets) production is equal the convolution of the corresponding parton structure functions and the elementary pQCD cross section $d\sigma/d\hat{t}$. A transformation from $d\hat{t}dx_1dx_2$ to $dp_T^2dy_1dy_2$ gives the additional factors x_1x_2 in eq. (4.1).

The total jet cross section with $p_T > p_0$ in a nucleon-nucleon reaction can be obtained for given $\sqrt{s}$ by integrating the differential cross section (4.1) over p_T^2, y_1 and y_2. The integration region is restricted by $p_0 < p_T < \sqrt{s}/2$, $x_1 < 1$, $x_2 < 1$ and $x_1x_2 > 4p_T^2/s$. This leads for a fixed p_T to the restriction

$$|y_1| \leq \ln(1/x_T + \sqrt{1/x_T^2 - 1}) \tag{4.4}$$

and for a fixed p_T and y_1 to

$$-\ln(2/x_T - e^{-y_1}) \leq y_2 \leq \ln(2/x_T - e^{y_1})\,. \tag{4.5}$$

At RHIC energy calculation gives $\sigma_{jet} = 38$ mb for $p_0 = 2$ GeV. To demonstrate agreements of the pQCD calculations with the measured data on jets production we show in Fig.4.1 the experimental data [UA1, UA2] of the jet cross section at very large p_T, measured by the UA1 and UA2 for $\bar{p}p \to jet + X$ at $\sqrt{s} = 540$ GeV (left panel) and at $\sqrt{s} = 200$, 500 and 900 GeV (right panel). The solid lines depict the pQCD calculations by integrating (4.1) over y_2 for fixed $y_1 = 0$. We see perfect agreements at smaller energies. However, at $\sqrt{s} = 900$ GeV one can recognize a relative large deviation of the pQCD calculation from the data. The reason is probably that the GRV parametrizations for the parton structure functions are inaccurate at this high energy. In addition, the next leading order pQCD partonic cross sections seem to be important correcting the distributions.

We now consider the jets or minijets (for small p_T) production in a heavy ion collision at high energy and assume that an ion-ion collision can be simply modeled as a sequence of binary nucleon-nucleon collisions [KLL 87, EKL 89]. Nuclear effects like the EMC effect or the shadowing effect at small x [EKS 99] are not taken into account. The averaged number of produced minijets is then just proportional to the number of binary nucleon-nucleon collisions

$$< N_{jet} > = \sigma_{jet}\, T_{AB}(\mathbf{b})\,. \tag{4.6}$$

$T_{AB}(\mathbf{b})$ denotes the nuclear overlap function for nucleus-nucleus collision at impact parameter of $\mathbf{b}$, which is given by

$$T_{AB}(\mathbf{b}) = \int d^2x_{T1}dz_1\, d^2x_{T2}dz_2\; n_A(\mathbf{r}_1)\, n_B(\mathbf{r}_2)\, \delta^2(\mathbf{b} - (\mathbf{x}_{T1} - \mathbf{x}_{T2}))\,, \tag{4.7}$$

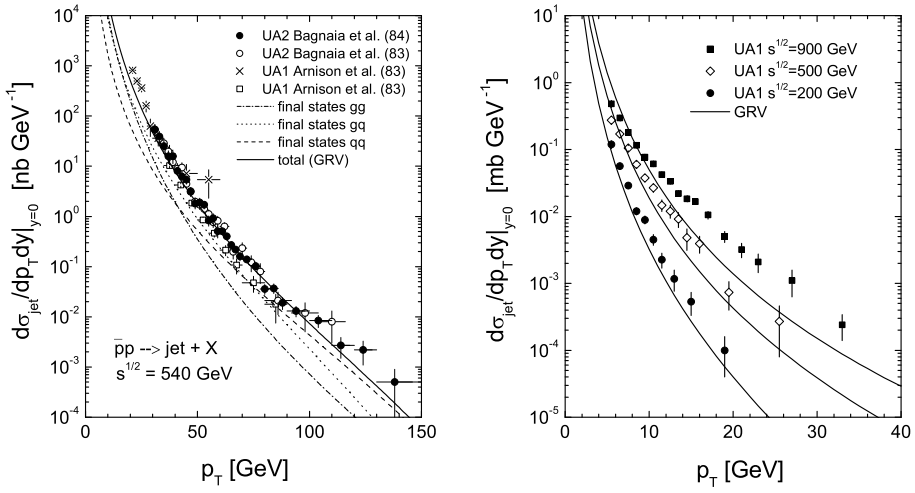

Figure 4.1: UA1 [UA1] and UA2 [UA2] data for $\bar{p}p \to jet + X$ process at $\sqrt{s} = 540$ GeV (left panel) and $\sqrt{s} = 200$, 500 and 900 GeV (right panel). The solid lines depict the pQCD calculation by integrating (4.1).

where $n_{A/B}(\mathbf{r})$ is the nuclear density. In physical terms, $\sigma T_{AB}(\mathbf{b})$, where σ denotes the total nucleon-nucleon cross section, gives roughly the number of binary semi-hard nucleon-nucleon collisions in an $A + B$ collision at impact parameter $\mathbf{b}$ [EKL 89]. The total jet cross section σ_{jet} with $p_T > p_0 = 2$ GeV in a nucleon-nucleon collision at $\sqrt{s} = 200$ GeV is calculated by integrating the differential jet cross section (4.1) und turns out to be 38 mb. Employing the Woods-Saxon distribution for the nuclear density of a Lorentz contracted nucleus

$$n_A(\mathbf{x}_{T1}, z_1) = \frac{\gamma\, n_0}{1 + Exp\left((\sqrt{x_{T1}^2 + (\gamma z_1)^2} - R_A)/d\right)}, \tag{4.8}$$

where $d = 0.54$ fm, $R_A = 1.12A^{1/3} - 0.86A^{-1/3}$ fm and n_0 is determined from the normalization $\int d^3r_1\, n_A = A$, one obtains $T_{AA}(b = 0) \approx 30/\text{mb}$ for a central Au+Au collision. We thus estimate that with a cutoff $p_0 = 2$ GeV about 1200 minijets will be produced in a central Au+Au collision at maximal RHIC energy. Note that this number does crucially depend on the cutoff p_0, which makes the minijet picture not so much promising. On the other hand, one might improve this by choosing some selfconsistent relation for this crucial parameter [EKRT 00]. In Fig.4.2 we show the momentum rapidity distributions of minijets produced at RHIC, which are computed by integrating (4.1) over p_T and y_2 and then multiplying the overlap function $T_{AA}(0)$. We see first that gluons are initially the dominant parton species. About 70% of the produced minijets are gluons. Second, when subtracting the

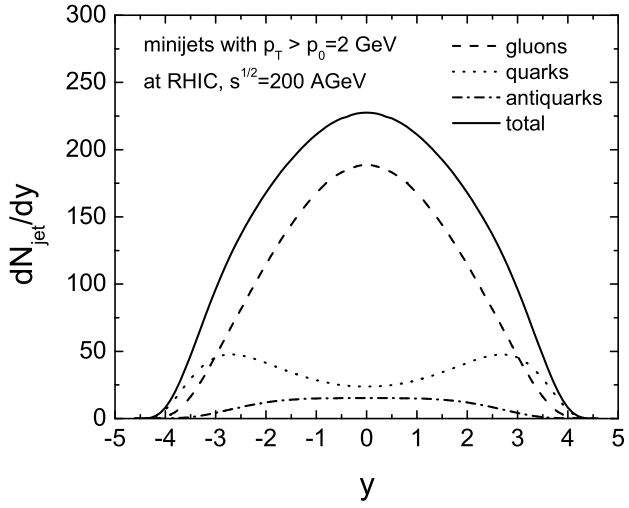

Figure 4.2: Momentum rapidity distributions of minijets produced at RHIC. The distribution for gluons, quarks and antiquarks are depicted separately. The solid curve shows the distribution of minijets in total.

distribution of the see quarks, which is equal to that of the antiquarks, from the total distribution of the quarks, one obtains the distribution of the valence quarks. It possesses peaks at larger rapidity, which corresponds the fact that the valence quarks take the most fraction of the momentum of the nucleon and have large x. At midrapidity the contribution of the valence quarks is very small. This shows that the heavy ions at RHIC energy indeed penetrate each other and leave almost a baryon free region behind them.

Since in a heavy ion collision minijets are assumed to be produced in independent binary nucleon-nucleon collisions, the initialization of the individual produced minijets in momentum space is straightforward: Minijets are sampled statistically according to the differential jet cross section (4.1) averaged over possible proton-proton, proton-neutron and neutron-neutron collisions. The space-time coordinates of the minijets are initialized within a simple geometrical picture when the two Lorentz contracted nuclei do overlap. For convenience for the moment, we set the zero point of the time scale to be the moment of the full overlap. Then the longitudinal positions of the two nucleus centers are at $\pm v\,t$, respectively, where v is the velocity of the nuclei. One now identifies the intrinsic coordinates z_1 and z_2 in (4.7) with the global space and time coordinate

$$z_1 = z - v\,t \qquad \text{and} \qquad z_2 = z + v\,t\,. \tag{4.9}$$

Changing from z_1 and z_2 to z and t yields for eq. (4.7) for $b = 0$ and $A = B$

$$\begin{aligned} T_{AA}(\mathbf{b}=0) &= \int d^2x_{T1}\, d^2x_{T2}\, 2\, v\, dt\, dz\; n_A(\mathbf{x}_{T1}, z - v\,t)\, n_A(\mathbf{x}_{T2}, z + v\,t) \times \\ &\qquad \times \delta^2(\mathbf{x}_{T1} - \mathbf{x}_{T2}) \\ &= \int d^2x_{T1}\, 2\, v\, dt\, dz\; n_A(\mathbf{x}_{T1}, z - v\,t)\, n_A(\mathbf{x}_{T1}, z + v\,t)\,. \end{aligned} \tag{4.10}$$

One thus receives the statistical distribution for sampling the space-time coordinates of the individual produced minijets

$$\frac{d < N_{jet} >}{d^2x_{T1}\, dz\, dt} \sim n_A(\mathbf{x}_{T1}, z - v\,t)\, n_A(\mathbf{x}_{T1}, z + v\,t)\,. \tag{4.11}$$

The probability for producing a parton at $(\mathbf{r}, t)$ is thus proportional to the convolution of the nuclear densities of the two overlapping nuclei at the individual space-time point. Due to the choice of the zero point in time, about half of the produced partons are liberated at negative times. Therefore, with this convention of the zero point in time the space-time rapidity η (3.3) is not a well-defined quantity. In order to correct this, we shift all the times to be larger than the absolute values of the corresponding longitudinal positions, i.e. $t \to t + t_s > |z|$, with a uniquely chosen t_s. This actually implies that $t_s \sim 0.5 R_A/\gamma$, i.e. half of the overlapping time. Since we apply Woods-Saxon distribution (4.8) for the nuclear density, we can not exactly specify when the first touch of the two colliding nuclei occurs. t_s is thus - strictly speaking - a parameter in our simulation. For a larger t_s particles pile up in the central space-time rapidity region and for a smaller t_s particles distribute within a wider rapidity range during the very early evolution. On the other hand, independently on the chosen t_s, most of the partons are in fact produced in the central rapidity region due to the geometry of the overlapping nuclei. In the simulations which will be presented later in chapter 6, we determine t_s with the assumption that the initial partons are distributed within a space-time rapidity range of $\eta \in [-5 : 5]$.

In the above picture concerning the implementation of the space-time production of minijets, it is assumed that partons become immediately on-shell when the (semi-)hard nucleon-nucleon collisions occur. Alternatively, one may introduce an additional *formation time* for every minijet, $\Delta t_f = \cosh y\, \Delta\tau_f \approx \cosh y \cdot 1/p_T$, which models the off-shell propagation of the freed partons. Within that time span, one assumes, for simplicity, that the still virtual parton does not interact and moves with speed of light. Fig.4.3 shows the space-time configurations of the initial partons without and with the formation time. We see two very different configurations. While the partons with no formation time gather in a small space-time region around ($z = 0$ fm, $t = 0.1$ fm/c), the partons with the formation time distribute widely. It looks that they are produced on hyperbolas around $\tau = \sqrt{t^2 - z^2} = 0.2$ fm/c with a width of 0.1 fm/c.

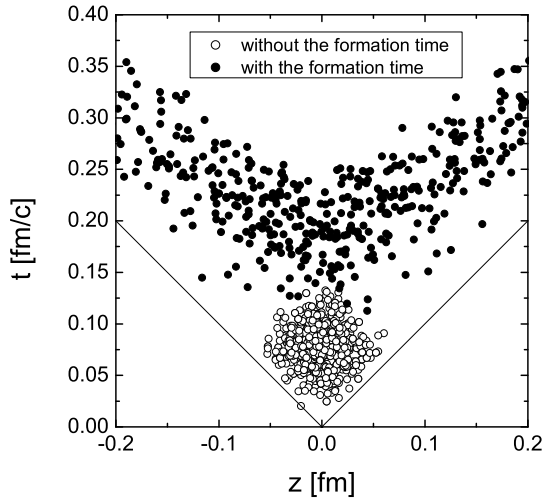

Figure 4.3: Space-time configurations of the initial partons without (open circles) and with (solid circles) the formation time.

In spite of the different pattern of the space-time distribution of the initial partons between without and with the formation time, we will realize, confirmed by numerical simulations presented in chapter 6, that the introduction of such a formation time does not affect our main findings too much.

Chapter 5

Quark Gluon Plasma in box

A quark gluon plasma (QGP) is suggested as a kineticly and chemically equilibrated system of deconfined quarks and gluons. Such state of matter is presumed to have been formed after the big bang and also expected to exist temporarily during the course of an ultrarelativistic heavy ion collision in the laboratory. The main goal of the heavy ion collision experiments at RHIC and of the future experiments at LHC is to find evidence of such a new state of matter, the existence of quark gluon plasma. From the theoretical point of view it is also very interesting to address the possibility of the formation of QGP under different theoretical assumptions of the initial conditions, and to investigate the further evolution of the quark gluon system in space and time. A cascade type transport simulation solving relativistic Boltzmann equations for quarks and gluons with Monte Carlo technique is just well suited for such a study. Whereas the current parton cascade models, MPC [MG 00], PCPC [BMGMN 00] and VNI/BMS [BMS 03], have not included the $2 \leftrightarrow 3$ processes, we can apply the extended stochastic collision algorithm presented in the last section to build up a parton cascade describing the space-time evolution of interacting quarks and gluons including $gg \leftrightarrow ggg$ within the framework of perturbative QCD. As a first application, we restrict ourselves in this chapter to investigate the formation of a quark gluon plasma in a fixed box. The convenience is that a thermalized parton system should be formed in any case after some time. Although this situation can not be given in reality, one can still address the way of equilibration for different particle species. Furthermore, box calculations offer an essential test for the numerical realization of detailed balance of $gg \leftrightarrow ggg$ and $gg \leftrightarrow q\bar{q}$ processes. A realistic space-time approach for the simulation of parton evolution during the early stage after an ultrarelativistic heavy ion collision will be presented in chapter 6.

The parton interactions include all two-body processes: (1) $gg \leftrightarrow gg$, (2) $gg \leftrightarrow q\bar{q}$ (3) $gq \leftrightarrow gq$, (4) $qq \leftrightarrow qq$, (5) $qq' \leftrightarrow qq'$, (6) $q\bar{q} \leftrightarrow q\bar{q}$, (7) $q\bar{q} \leftrightarrow q'\bar{q}'$ and three-body processes (8) $gg \leftrightarrow ggg$. The matrix elements squared in leading

order of the perturbative QCD are taken from [ORG 78] and [GB 82]. We regularize the infrared divergences by using the Debye screening mass [Wo 96] m_D^2 for gluons

$$m_D^2 = 16\pi\alpha_s \int \frac{d^3p}{(2\pi)^3}\frac{1}{p}(N_c f_g + n_f f_q) \tag{5.1}$$

and the quark medium mass m_q^2 for quarks

$$m_q^2 = 4\pi\alpha_s \frac{N_c^2-1}{2N_c}\int \frac{d^3p}{(2\pi)^3}\frac{1}{p}(f_g + f_q), \tag{5.2}$$

where $N_c = 3$ for SU(3) of QCD and n_f is the number of quark flavor. All formulas for the differential cross sections are listed in Appendix C and D. Here we write down only the differential cross sections (or the matrix element squared) of the dominant processes for achieving kinetic and chemical equilibration [W 96, BDMTW 93]:

$$\frac{d\sigma^{gg\to gg}}{dq_\perp^2} = \frac{9\pi\alpha_s^2}{(q_\perp^2 + m_D^2)^2}\,, \tag{5.3}$$

$$\frac{d\sigma^{gg\to q\bar{q}}}{dq_\perp^2} = \frac{\pi\alpha_s^2}{3s(q_\perp^2 + m_q^2)}\,, \tag{5.4}$$

$$|\mathcal{M}_{gg\to ggg}|^2 = \left(\frac{9g^4}{2}\frac{s^2}{(\mathbf{q}_\perp^2 + m_D^2)^2}\right)\left(\frac{12g^2\mathbf{q}_\perp^2}{\mathbf{k}_\perp^2[(\mathbf{k}_\perp - \mathbf{q}_\perp)^2 + m_D^2]}\right)\,, \tag{5.5}$$

where $g^2 = 4\pi\alpha_s$. The matrix element (5.5) describing the $gg \leftrightarrow ggg$ transitions is factorized into a part for elastic scattering and a part for gluon radiation (or gluon fusion). $\mathbf{q}_\perp$ and $\mathbf{k}_\perp$ denote, respectively, the perpendicular component of the momentum transfer and that of the momentum of the radiated gluon in the c.m. frame. In a dense medium the radiation of soft gluons is assumed to be suppressed due to the Landau-Pomeranchuck-Migdal (PLM) effect: The emission of a soft gluon should be completed before it scatters again. This leads to a lower cutoff of $k_\perp$ via a step function $\Theta(k_\perp\Lambda_g - \cosh y)$, where y is the rapidity of the radiated gluon in the c.m. frame and Λ_g denotes the gluon mean free path which is the inverse of the gluon collision rate $\Lambda_g = 1/R_g$. R_g is the sum of the rate of the following transitions: $gg \to gg$, $gg \to q\bar{q}$, $gq \to gq$, $gg \to ggg$ and $ggg \to gg$.

The collision rate is an important quantity governing the time scale of kinetic and chemical equilibration. In Fig.5.1 we depict the thermally averged cross section $< v_{rel}\sigma >$ and the gluon collision rates as function of temperature for $gg \to gg$, $gg \to q\bar{q}$, $gq \to gq$ and $gg \to ggg$ transitions. $< v_{rel}\sigma >$ are calculated numerically, for which we take the screening masses obtained at equilibrium ($f_g = f_q = e^{-E/T}$)

$$m_D^2 = (3+n_f)\frac{8}{\pi}\alpha_s T^2 \quad \text{and} \quad m_q^2 = \frac{16}{3\pi}\alpha_s T^2\,. \tag{5.6}$$

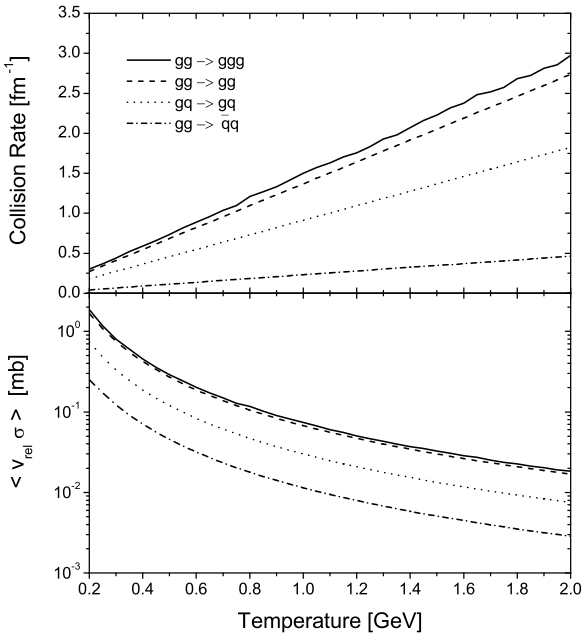

Figure 5.1: Gluon collision rates and thermally averaged $< v_{rel}\sigma >$ as function of temperature. The solid, dashed, dotted and dash-dotted line show the temperature dependence for $gg \to ggg$, $gg \to gg$, $gq \to gq$ and $gg \to q\bar{q}$ transitions respectively. We consider here two quark flavors and employ a constant coupling $\alpha_s = 0.3$ (for the cross sections and the screening masses).

In the calculations we consider two quark flavors ($n_f = 2$) and employ a constant coupling $\alpha_s = 0.3$. The corresponding collision rates are obtained by $R = n_g < v_{rel}\sigma >$, where $n_g = \nu_g T^3/\pi^2$ is the gluon density in thermal equilibrium. $\nu_g = 2{\times}8$ denotes the degeneracy of gluons. Because of our simple minded inclusion of the LPM effect, the cross section $\sigma_{gg\to ggg}$ depends on the sum of the rates $R_g = R_{gg\to gg} + R_{gg\to q\bar{q}} + R_{gg\to ggg} + R_{ggg\to gg}$, in which, however, $R_{gg\to ggg}$ and $R_{ggg\to gg} (= R_{gg\to ggg}$ in equilibrium) depend again on $\sigma_{gg\to ggg}$. This problem is solved by a selfconsistent, iterative computation. Inspecting Fig.5.1 we see that the collision rates are proportional to the temperature, which indicates that the $< v_{rel}\sigma >$ are inversely proportional to T^2. This behaviour stems from the fact that the cross section $\sigma_{gg\to gg}$ and $\sigma_{gq\to gq}$ depend mainly on $1/m_D^2$ and the cross section $\sigma_{gg\to ggg}$ and $\sigma_{gg\to q\bar{q}}$ mainly on $1/s$. Furthermore we realize that the collision rate of the three-body processes is in the same order as the rate of two-body gluon collisions.

We now come to some numerical details when simulating the parton equilibration in a fixed box. As shown in Appendix D, the computations of σ_{23} and

I_{32} over momentum space are reduced to a four- (D.9) and a two-dimensional (D.13) integration respectively. Even then, the computations are still time-consuming when σ_{23} and I_{32} have to be calculated for every gluon doublet and triplet in cells, since the number of integrations is proportional to n^2 and n^3 respectively (n being the total gluon number in an individual cell). In order to reduce the computing time, one first thinks of tabulating σ_{23} as well as I_{32}. In simulations we then make interpolations using these tabulated data sets. This gives a convenient way for obtaining σ_{23} because the underlying integral depends on only two parameters, m_D^2/s and $\Lambda_g\sqrt{s}$, as mentioned in Appendix D. The same data sets have been used for calculating σ_{23} in thermal equilibrium as shown in Fig.5.1. In contrast to the case for σ_{23}, I_{32} depends on five parameters (see Appendix D). A tabulation of I_{32} is thus crude due to the limitation of the storage, which leads to large errors by interpolations. Therefore we decide to calculate I_{32} in simulations using the Monte Carlo algorithm VEGAS [PTVF 92] with low computing expense (2 iterations and 100 function calls). Furthermore, in order to reduce the computing time we employ the method as explained in chapter 3: Instead of evaluating probabilities of all possible collisions, we choose randomly $\mathcal{N}$ out of the possible doublets or triplets, since in our case the transition probabilities of any channel are in fact very small within one time step. The corresponding collision probabilities are amplified accordingly to be

$$P_{22} \to P_{22}\frac{n(n-1)/2}{\mathcal{N}_{22}}, \quad P_{23} \to P_{23}\frac{n(n-1)/2}{\mathcal{N}_{23}}, \quad P_{32} \to P_{32}\frac{n(n-1)(n-2)/6}{\mathcal{N}_{32}}. \tag{5.7}$$

The choices of $\mathcal{N}_{22}$, $\mathcal{N}_{23}$ and $\mathcal{N}_{32}$ are arbitrary. In the following simulations we set $\mathcal{N}_{22} = \mathcal{N}_{23} = \mathcal{N}_{32} = n$.

The initial condition for the box calculations is taken by sampling multiple minijet production in heavy ion collisions at RHIC energy $\sqrt{s} = 200$ GeV, which was discussed in the last chapter in detail. The parameter p_0 is set here to be 2 GeV. We consider gluons stremming from a central rapidity region $y \in [-0.5 : 0.5]$ as the only initial parton species, since at the central rapidity region the partons with small x dominate and these are almost gluons. The initial number of gluons is assumed to be 500, about 3 times larger than that of gluon jets at RHIC. The momentum spectrum of the gluons has a power-law behaviour and thus initially the parton system is strongly out of equilibrium. The primary minijets produced in a real high energy heavy ion collision are distributed within a thin disc due to the Lorentz contraction. Instead of such a space-time configuration discussed in the previous chapter, we assume a homogeneous spatial distribution of partons in the box for simplicity. This allows us to still use a static cell configuration. In the following studies we are interested in the way of how thermalization of different parton species proceeds and also interested in the timescales of kinetic and chemical equilibration.

The size of the box is set to be 3 fm $\times$ 3 fm $\times$ 3 fm and the box is divided into equal cells. The length of a cell is set to be 1 fm. These settings are tuned as that there will be enough gluons (about 15) in each cell during the whole evolution. (For quarks strong statistic fluctuation occurs at the beginning of the evolution due to the initial lack of quarks.)

We employ a constant coupling of $\alpha_s = 0.3$ in the rest of this chapter for evaluating the screening masses and the cross sections. The screening masses m_D^2 and m_q^2 are calculated dynamically according to (5.1) and (5.2). The integrations are computed as

$$\int \frac{d^3p}{(2\pi)^3\, p}\, f \to \frac{1}{V} \sum_i \frac{1}{p_i}\,, \tag{5.8}$$

where the sum runs over all particles in a volume V, which should be, in general, small in order to maintain the local homogeneity. Since the initial position of partons is distributed homogeneously, we extend the sum over all particles in the fixed box.

The gluon collision rate, which will be employed for evaluating σ_{23} and I_{32}, can be obtained from the calculated collision probabilities, since the sum of the probabilities of all possible collisions gives the average total collision number within the current time step. We then have

$$R_{gg\to f} = \frac{\sum_i P_i^{gg\to f}}{\frac{1}{2} N_g \Delta t}\,, \qquad f = gg, q\bar{q}, ggg, \tag{5.9}$$

$$R_{ggg\to gg} = \frac{\sum_i P_i^{ggg\to gg}}{\frac{1}{2} N_g \Delta t} \tag{5.10}$$

and

$$R_{gq\to gq} = \frac{\sum_i P_i^{gq\to gq}}{N_g \Delta t}\,, \tag{5.11}$$

where the sums run over possible particle doublets or triplets in the individual cells and also over all cells. N_g denotes the total gluon number in the box. On the other hand, the $P_i^{gg\to ggg}$ and $P_i^{ggg\to gg}$ depend again on σ_{23} and I_{32} respectively. Therefore, a correct calculation for σ_{23} and I_{32} as well as $P_i^{gg\to ggg}$ and $P_i^{ggg\to gg}$ should be a selfconsistent, iterative computation. However, since such computations are too time-consuming, we employ the gluon collision rate, obtained at the last time step, to calculate σ_{23} and I_{32} within the current time step.

When the parton system becomes fully equilibrated at the later evolution, the final values of gluon and quark number should be given by

$$N_g^{eq} = \nu_g \frac{T^3}{\pi^2} V\,, \tag{5.12}$$

$$N_q^{eq} = 2\nu_q \frac{T^3}{\pi^2} V\,, \tag{5.13}$$

where $\nu_g = 2 \times 8$ and $\nu_q = 2 \times 3 \times n_f$ are the degeneracy factors of a gluon and quark respectively. The factor 2 in (5.13) indicates the sum of quark and antiquark. Employing the relation

$$E = 3(N_g^{eq} + N_q^{eq})T\,, \tag{5.14}$$

which holds in thermal equilibrium, we obtain the final temperature

$$T = \left(\frac{E}{V}\frac{\pi^2}{3(\nu_g + 2\nu_q)}\right)^{\frac{1}{4}}\,. \tag{5.15}$$

The total energy E can be determined by the specified initial momentum distribution of minijets (4.1). Considering only up and down quarks ($n_f = 2$) we get a final temperature of about 430 MeV and thus $m_D^2 \approx 0.7\text{GeV}^2$ and $m_q^2 \approx 0.1\text{GeV}^2$ for $\alpha_s = 0.3$.

Fig.5.2 shows time evolutions of the gluon and quark number. 60 independent realizations are collected to obtain sufficient statistics. We see that the time evolution of the gluon number has two stages. At first the gluon number increases rapidly to a maximum and then relaxes towards its equilibrium value on a slower scale. The quark number starts from zero because of the initial absence of quark species and increases smoothly towards its equilibrium value. The gluon and quark number do reach their final values simultaneously. These behaviours of $N_g(t)$ and $N_q(t)$ reveal the well-known scenario of two-stage chemical equilibration: The gluon system equilibrates at first as if no quarks were there and then cools down gradually by producing quark-antiquark pairs until the quarks reach the equilibrium. Such two-stage equilibration could also happen in a real high energy heavy ion collision [S 92].

Next we compare the equilibrium values of gluon and quark number of Fig.5.2 with the analytical values which one would expect directly from the initial conditions. The final temperature in one individual run can be obtained by inserting the total amount of energy into expression (5.15). Averaged over 60 runs we have $< T >= 427.84$ MeV. Inserting the averaged temperature into (5.12) and (5.13) gives $< N_g^{eq} >= 428$ and $< N_q^{eq} >= 643$. The values extracted from Fig.5.2 are $N_g = 430$ and $N_q = 640$. We see that the agreements are pretty good, which demonstrates that our new cascade algorithm is indeed very successful in keeping the detailed balance even for the considered complexity of employing pQCD motivated cross sections. We also calculate the equilibrium number of gluons when no quarks are considered ($n_f = 0$). In the present situation this is $\bar{N}_g^{eq} = 852$, which is somewhat greater than the maximum of gluon number read off from Fig.5.2, since in the latter case gluons are already lost due to the production of quark-antiquark pairs starting at the beginning of the evolution.

In Fig.5.3 we depict the energy distributions of the partons (gluons and quarks) at different times. The initial ($t = 0$ fm/c) distribution possesses a

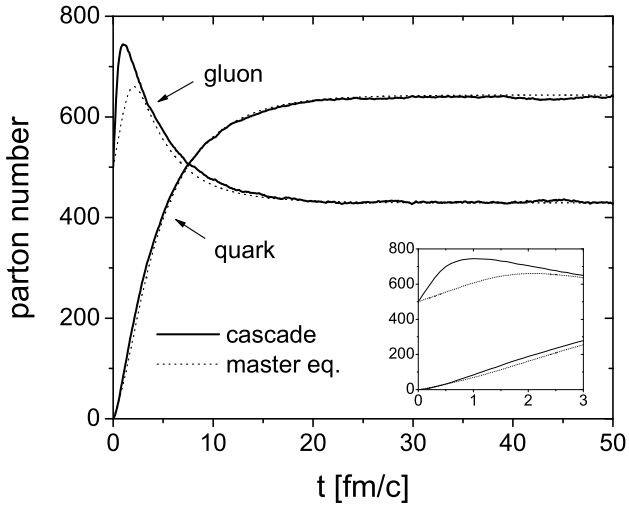

Figure 5.2: Time evolution of the gluon and quark number in box calculations. We consider here gluons and quarks with two flavors as parton species. Collision processes are the elementary two-body parton-parton scatterings and three-body processes $gg \leftrightarrow ggg$ in leading order of perturbative QCD. The coupling is assumed to be a constant of $\alpha_s = 0.3$. The initial momentum distribution of particles is taken from the minijets production in central rapidity interval $y \in (-0.5 : 0.5)$ in a nucleon-nucleon collision at RHIC energy $\sqrt{s} = 200$ GeV. The initial particles are gluons and distributed homogenously in the box. The size of the box is 3 fm $\times$ 3 fm $\times$ 3 fm and the box is divided into equal cells. The length of a cell is 1 fm. The initial gluon number is set to be 500. The results are obtained from an average over 60 runs. The dotted curves show the results solving a set of rate equations (5.19) and (5.20).

cutoff at $E = p_0 = 2$ GeV and is highly nonthermal. Immediately after the onset of interactions, soft gluons with smaller energy do emerge by the process $gg \to ggg$ and thermalize very quickly. We see that even at 0.3 fm/c the energy distribution for partons with smaller energy than 2 GeV is almost exponential. The hard particles with larger energy are still out of equilibrium. There is still a hump at 2 GeV. This hump will vanish gradually and at 2 fm/c the total distribution becomes exponential. One can refer to this stage as the onset of kinetic equilibration. The energy distribution at a final time of $t = 50$ fm/c is also depicted in Fig.5.3. We have compared this spectrum to the analytical form eq. (2.5) with the averaged temperature $< T >= 427.84$ MeV obtained from the initial input. (The analytical distribution is not shown in Fig.5.3.) The agreement is very good.

To study the kinetic equilibration in more detail, we calculate the time

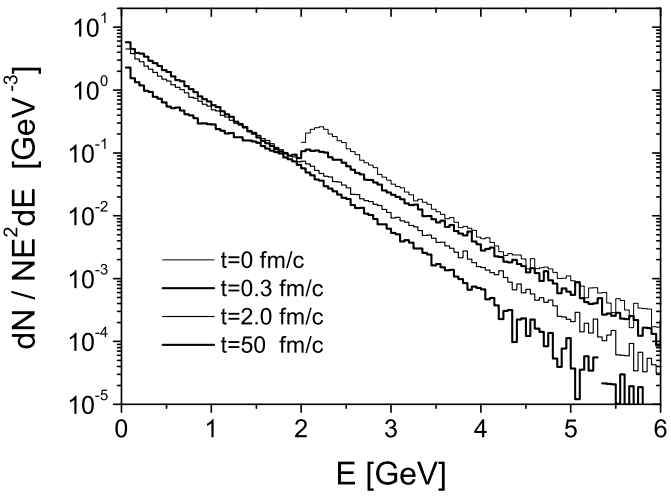

Figure 5.3: Energy distributions at different times from the same calculation as in Fig.5.2.

evolutions of the momentum anisotropy

$$\frac{2 < p_z^2 >_g}{< p_T^2 >_g}(t)\,, \qquad \frac{2 < p_z^2 >_q}{< p_T^2 >_q}(t) \tag{5.16}$$

for gluons and quarks, which are shown in Fig.5.4. We see that the momentum of the gluons and quarks becomes isotropic at almost same time of about $1-2$ fm/c which is just the timescale when the energy spectrum gets exponential, as shown in Fig.5.3. However, if one looks at the time evolutions of the effective temperatures in Fig.5.5, which are defined as $T_g(t) := E_g(t)/3\,N_g(t)$ and $T_q(t) := E_q(t)/3\,N_q(t)$, one notices that between 0 fm/c and 10 fm/c the temperature of quarks is lower than the one of gluons. The reason is that the quarks stem mainly by the $gg \to q\bar{q}$ quark pair production and the cross section $\sigma_{gg\to q\bar{q}}$ is inversely proportional to s. Therefore, when the quark production is still more dominant compared to the annihilation process, more quark-antiquark pairs with smaller energies are produced than those with larger energies, compared to the equilibrated Boltzmann distribution. Correspondingly, there would be a slight suppression in the energy spectrum of quarks at high energy and in the energy spectrum of gluons at low energy during the ongoing chemical equilibration. It takes time for the gluon-quark mixture to obtain an identical temperature via the gluon-quark interactions. This identical, final temperature is extracted from Fig.5.5, $T_g = T_q = 429$ MeV, and agrees perfectly with the expectation of $< T >= 427.84$ MeV.

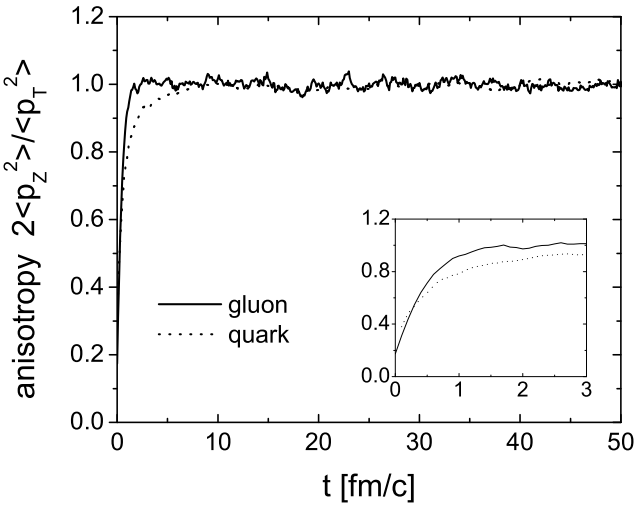

Figure 5.4: Time evolution of the momentum anisotropy for gluons and quarks from the same calculation as in Fig.5.2.

The parton fugacity is defined as follows

$$\lambda_g(t) := \frac{N_g(t)}{\tilde{N}_g^{eq}(t)} \quad \text{and} \quad \lambda_q(t) := \frac{N_q(t)}{\tilde{N}_q^{eq}(t)}\,, \tag{5.17}$$

where

$$\tilde{N}_g^{eq}(t) := \nu_g \frac{T_g^3(t)}{\pi^2} V \quad \text{and} \quad \tilde{N}_q^{eq}(t) := 2\nu_q \frac{T_q^3(t)}{\pi^2} V\,. \tag{5.18}$$

In the upper panel of Fig.5.6 the time evolutions of the fugacity are depicted for gluons and quarks by the solid curves. We see that while the gluons approach the chemical equilibrium at about 3 fm/c, the quarks do equilibrate later at 20 fm/c. These time-scales agree well with those when the collision rates of $gg \to ggg$ and $gg \to q\bar{q}$ process become same as the rates of their backreaction, respectively, as shown in the lower panel of Fig.5.6 by the solid curves where the corresponding absolute collision numbers counted within a time interval of $\Delta t = 0.1$ fm/c about t are depicted. The two-stage chemical equilibration is clearly demonstrated in Fig.5.6.

In Fig.5.7 we show the gluon collision rates per particle (upper panel) and the corresponding cross sections $< v_{rel}\sigma >$ (lower panel). The collision rates per particles are obtained by counting the collision events within a time interval of $\Delta t = 0.1$ fm/c at t and then divided by the particle number (or half of the particle number for collisions with identical incoming particles) at the same time. Since $R = n < v_{rel}\sigma >$, dividing the collision rates per particle by the corresponding particle densities gives the cross section $< v_{rel}\sigma >$. From Fig.5.7

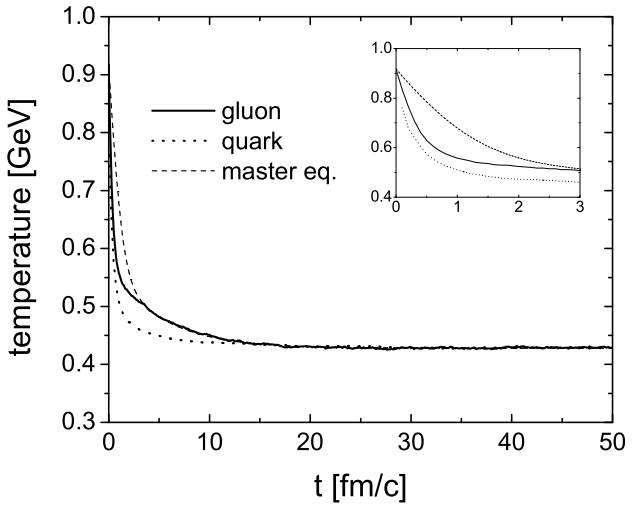

Figure 5.5: Time evolution of the temperature for gluons and quarks from the same calculation as in Fig.5.2.

we see that the quantities approach the final values gradually. Comparing these final values with the analytical results read off from Fig.5.1 at the final temperature gives perfect agreements. (Note that the analytical results are $R = 0.630$, 0.585, 0.0981 and 0.390 fm^{-1}, $< v_{rel}\sigma >= 0.4$, 0.368, 0.0617 and 0.164 mb for $gg \to ggg$, $gg \to gg$, $gg \to q\bar{q}$ and $gq \to gq$ processes respectively.) Furthermore, we notice from the small window in Fig.5.7, which depicts the results from 0 to 3 fm/c, that the cross sections for $gg \to ggg$, $gg \to gg$ and $gq \to gq$ processes are very large at the beginning of the evolution. This is due to the undersaturation of partons which leads to a smaller sceening masses. In Fig.5.8 the time evolutions of the screening masses are shown. Also here, the agreements of the extracted equilibrium values from the figures with the analytical values (5.6) are perfect. For $gg \to q\bar{q}$ process, however, the cross section is still small at the beginning of the evolution. The reason is that the cross section for this channel has only logarithmical dependence on the quark screening mass, i.e. $\sigma_{gg\to q\bar{q}} \sim \frac{1}{s}\ln(1 + \frac{s}{4m_q^2})$.

Now we turn to describe the chemical equilibration using a set of rate equations. The evolution of the parton numbers is governed by the master equations

$$\dot{N}_g = \dot{N}_{coll}^{gg\to ggg} - \dot{N}_{coll}^{ggg\to gg} - 2\dot{N}_{coll}^{gg\to q\bar{q}} + 2\dot{N}_{coll}^{q\bar{q}\to gg}, \quad (5.19)$$

$$\dot{N}_q = 2\dot{N}_{coll}^{gg\to q\bar{q}} - 2\dot{N}_{coll}^{q\bar{q}\to gg}, \quad (5.20)$$

where the dot denotes the derivation of time. Note that N_q is the sum of

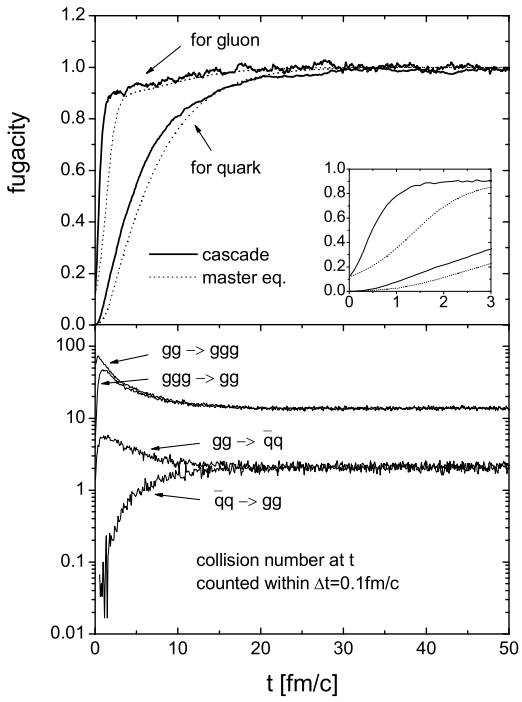

Figure 5.6: Time evolution of the fugacity for gluons and quarks from the same calculation as in Fig.5.2 (upper panel). Collision numbers counted with a time interval of $\Delta t = 0.1$ fm/c about t for different channels from the same calculation as in Fig.5.2 (lower panel).

quarks and antiquarks. $\dot{N}^i_{coll}$ are the collision rates

$$\dot{N}^{gg\to ggg}_{coll} = \frac{N_g^2}{2} < v_{rel}\,\sigma_{gg\to ggg} > \frac{1}{V}\,, \tag{5.21}$$

$$\dot{N}^{ggg\to gg}_{coll} \approx \lambda_g \frac{N_g^2}{2} < v_{rel}\,\sigma_{gg\to ggg} > \frac{1}{V}\,, \tag{5.22}$$

$$\dot{N}^{gg\to q\bar{q}}_{coll} = \frac{N_g^2}{2} < v_{rel}\,\sigma_{gg\to q\bar{q}} > \frac{1}{V}\,, \tag{5.23}$$

$$\dot{N}^{q\bar{q}\to gg}_{coll} = n_f \left(\frac{N_q}{2\,n_f}\right)^2 < v_{rel}\,\sigma_{q\bar{q}\to gg} > \frac{1}{V}\,, \tag{5.24}$$

where in (5.22) equality is only valid when assuming that the system is in kinetic equilibrium. One can also easily realize from Appendix C that $\sigma_{q\bar{q}\to gg}/\sigma_{gg\to q\bar{q}} = 32/9n_f$, in which $\sigma_{gg\to q\bar{q}}$ sums over all the final states with different flavors. For the given initial values, $N_g = 500$, $N_q = 0$ and $\lambda_g = 0.12$, and taking the equilibrium values for the cross sections we solve the master equations (5.19)

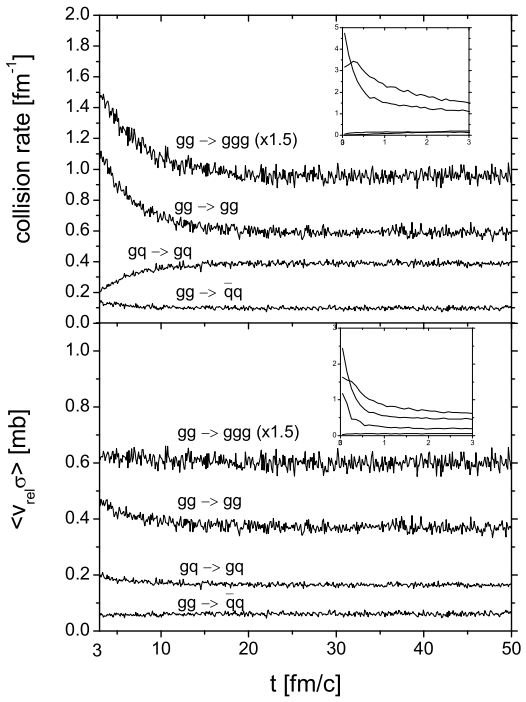

Figure 5.7: Time evolution of the collision rates per particle (upper panel) and the cross sections (lower panel) for different channels. The results are obtained from the same calculation as in Fig.5.2.

and (5.20) numerically employing the simple Euler method. After each time step we compute the parton fugacities according to (5.17) and (5.18), where we assume $T_g(t) = T_q(t) = E/3(N_g(t) + N_q(t))$. E is obtained from the initial condition. The results are depicted in Fig.5.2, Fig.5.5 and the upper panel of Fig.5.6. We see that at late times the simple master equations do describe the same chemical equilibration as the Boltzmann equations did. At early times the results based on the solution of the master equations are clearly underestimated due to the fact that the cross sections and thus the collision rates at early times are actually larger than the final equilibrium values. However, more surprisingly, the quark numbers in Fig.5.2, obtained by solving the Boltzmann equations and the master equations, show almost the same time evolutions.

From the present study of creating QGP in a box some speculations are made when we consider parton evolution in a real ultrarelativistic heavy ion collision. (1) Two-stage equilibration is a good scenario describing parton thermalization in high energy heavy ion collisions. (2) The cross section $\sigma_{gg\to ggg}$ is in the same order as $\sigma_{gg\to gg}$ and thus the $gg \leftrightarrow ggg$ processes should play

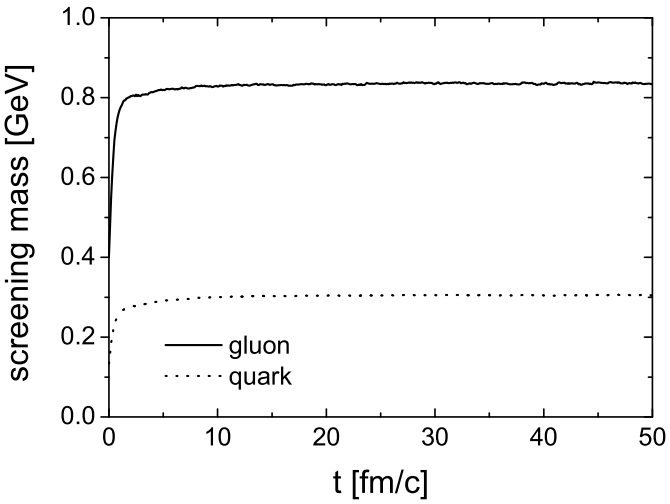

Figure 5.8: Time evolution of the screening mass for gluons and quarks from the same calculation as in Fig.5.2.

an important role in chemical and as well as kinetic equilibration. Analyses based on a full $3+1$ dimensional transport simulation of the parton evolution after a high energy heavy ion collision will be presented in the next chapter.

Chapter 6

Full $3+1$ dimensional operation of the parton cascade for central Au+Au collisions at RHIC: kinetic and chemical equilibration

As motivated in the introduction, the perfect agreement of the recent RHIC data on elliptic flow parameter v_2 with the predictions from the hydrodynamical model indicates that a thermalized system of quarks and gluons is produced at RHIC. One the other hand, the parton cascade simulations employing $2 \to 2$ pQCD interactions failed to demonstrate the onset of thermalization. It is suggested that $2 \leftrightarrow 3$ processes are more responsible to equilibration and should be included in transport simulations. In chapter 2 and 3 we have presented a new parton cascade including such inelastic collisions. Covariance and convergence of the numerical algorithm have been demonstrated. In the previous chapter the correct implementations of $gg \leftrightarrow ggg$ processes are confirmed for an example of parton evolution in a fixed box. In this chapter we take the step forward to simulate the space time evolution of partons produced in a central Au+Au collision at maximal RHIC energy $\sqrt{s} = 200$ GeV by means of the well tested stochastic collision algorithm. The simulation is performed in the center of mass frame of the colliding nuclei. For the present and first exploratory study we include only the pQCD motivated gluonic interactions $gg \leftrightarrow gg$ and $gg \leftrightarrow ggg$ in the dynamical evolution. Simulations with all parton degrees of freedom will be postponed to a sequent study.

6.1 Cell configuration

To be able to apply the stochastic method to simulate the full collision sequences, we divide the space into appropriate cells. The individual cell structure has to be considered selfconsistently to be well suited to the details of the dynamical evolution of the parton system. Since it is a priori not clear whether the parton evolution is invariant under Bjorken boost, a configuration with constant division in space-time rapidity, $\Delta\eta$ =constant, as chosen in chapter 3 when simulating one dimensional expansion of a thermal system in a tube, is here not really reliable. The cell structure should be refreshed every time step to adapt to the dynamical parton evolution. In principle, one dimensional expansion is still a good approximation for the whole parton evolution for the first few fm/c after a central nucleus-nucleus collision. We thus still employ a static cell configuration in the transverse plan: Cells are transversely set as squares with a length of 0.5 fm. Longitudinally, space is divided into Δz bins, where each bin contains about the same number of test particles. This ensures the same statistics for each bin and automatically adapts to the density profile of the evolving parton system. This dynamical structuring begins at the center of the fireball and then proceeds to the very outside. Test particles from the far outside are not included into the cell configuration, because there the density distribution is too inhomogeneous. Instead, we then consider only elastic scatterings among these partons treated via the geometrical method. To obtain sufficient statistics, one has to tune the test particle number in each bin to be large enough: It turns out that a number of 20 test particles on average in each cell is sufficient during the first $4 \sim 5$ fm/c. However, in the region with lower particle density, especially in the transversal surface, there are not enough test particles. If the test particle number in a cell is less than a certain cutoff, which is set to be 4 in the simulations, we treat test particles in this cell again only by means of elastic scatterings with the geometrical method. How fine the longitudinal bins would be, depends on N_{test}, the number of test particles per real particle. We set $N_{test} = 60$ in the simulations. In total, this leads to an equivalent division of roughly equally sized bins in space-time rapidity with $\Delta\eta \sim 0.2$, as shown in Fig.6.1 where the structure of longitudinal bins in space-time rapidity is depicted for progressing time. This structure is extracted from one simulation for a central Au+Au collision at RHIC energy. Other results obtained from the same simulation are presented in the next section. In Fig.6.1 one also sees a 'zigzag' pattern. That is due to the random shift of the cell structure by a small amount in the longitudinal (as well as transversal) direction after every time step, in order to avoid that particles belong to the same cell for too long time, as discussed in chapter 3.

Besides this fine mesh of cells we also have to choose a sufficiently small time step to prevent a too strong change of the spatial configuration in each local cell. In the simulations, this time step is time dependent and is determined

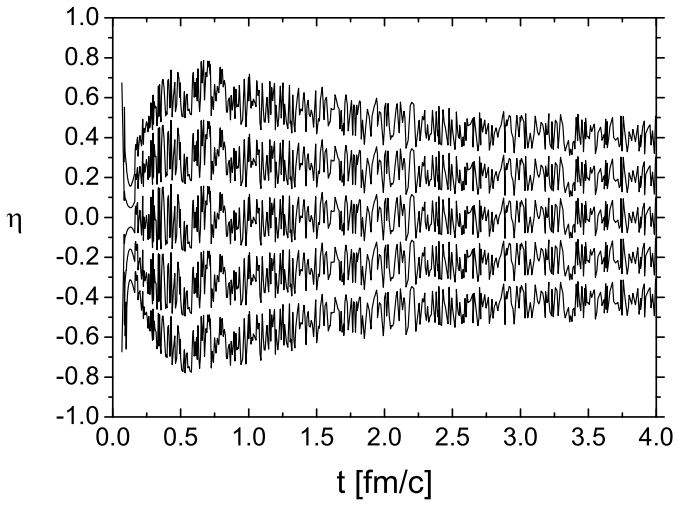

Figure 6.1: Structure of longitudinal bins in space-time rapidity. The structure is extracted from one simulation for a central Au+Au collision. In this figure, only the structure of longitudinal bins in the region $\eta \in [-0.8 : 0.8]$ is depicted.

to be the one fifth of the smallest occurring cell length. For the case that a collision probability turns out to be greater than 1, all operations done within the current time step are redone with an appropriately chosen smaller time step.

6.2 Assumptions and Results I

6.2.1 Assumptions

We calculate the dynamical screening mass m_D^2 in a similar way as done for the box calculations in chapter 5 [W 96]

$$m_D^2 = 16\pi\alpha_s \int \frac{d^3p}{(2\pi)^3\, p}\, N_c\, f_g \approx 16\pi\alpha_s N_c \frac{1}{V} \sum_i \frac{1}{p_i}\,. \tag{6.1}$$

The evaluation is carried out (quasi-)locally. V denotes the volume of a local region and the sum runs over all test particles in the region. The presence of the cell structure makes it reasonable to calculate the screening mass in each cell. However, the statistical uncertainty due to fluctuations is still large, since there are at maximum $20 \sim 30$ test particles in one individual cell, and thus an extraction of the particle phase space density f is not precise. If one assumes that the expansion in the first few fm/c is mainly longitudinal, and

further, that the transverse parton distribution is homogeneous over a large transversal area, one can extend the sum in (6.1) over a more broader region compared to the individual cell. In the simulations we consider a volume V as a cylinder with a radius of 6 fm in the individual Δz-bin. Within each bin m_D^2/α_s is assumed to be transversely constant. This approximation will lead to an underestimate of m_D^2/α_s in the very central area and an overestimate in the outside area when the transverse flow builds up, since within the same Δz-bin the particles moving with larger transverse velocity have larger energy and thus make a smaller contribution to the sum in (6.1) than the particles moving with smaller transverse velocity. The radius is a parameter which we set to be roughly equal to the radius of a Au nucleus. It turns out that the influence of this parameter on the screening mass is still quite sensitive at least for late times. A future improvement will be to simulate the parton evolution within a parallel ensemble technique, which will give the possibility to locally extract the particle phase space density more precise.

The coupling α_s is assumed to be

$$\alpha_s(Q^2) \approx \alpha_s(s) = \frac{12\,\pi}{(33 - 2\,n_f)\,\ln(s/\Lambda_{QCD}^2)} \tag{6.2}$$

for individual collisions, where s denotes the invariant mass of a particular colliding system of two or three particles. We set the quark flavour n_f to be 3 and Λ_{QCD} to be 200 MeV. In general, Q^2 in (6.2) stands for the momentum transfer in collision such as in deep inelastic scattering. For many-body collisions, however, the scale Q^2 is not unambiguous.

The gluon collision rate R_g, which will be employed to determine the effectively incorporated Landau-Pomeranchuck-Migdal (LPM) suppression in the $gg \leftrightarrow ggg$ processes by means of a low-momentum cutoff, is evaluated locally in cells

$$R_g = R_{gg\to gg} + R_{gg\to ggg} + R_{ggg\to gg}\,, \text{ where}$$

$$R_{gg\to f} = \frac{\sum_i P_i^{gg\to f}}{\frac{1}{2}N_g\Delta\tau}\,, \quad f = gg, ggg \qquad \text{and} \tag{6.3}$$

$$R_{ggg\to gg} = \frac{\sum_i P_i^{ggg\to gg}}{\frac{1}{2}N_g\Delta\tau}\,. \tag{6.4}$$

The P_is denote the respective individual collision probabilities. The sum over P_i gives the mean number of collisions occurring during a time step Δt in a cell with N_g gluons. $\Delta\tau$ denotes the corresponding time interval in the comoving frame $\Delta\tau = \Delta t/\gamma$, where $\gamma = 1/\sqrt{1 - v^2/c^2}$ and v is the collective velocity of the moving cell. For a cell with about 20 gluons there are in total 200 individual possible $gg \to gg$ and $gg \to ggg$ collisions each and 1200 possible $ggg \to gg$ collisions. The statistics is high enough to ensure evaluations of

the collision rates in local cells to be sufficiently precise, in contrast to the calculation of the screening mass. Still a problem remains, which is that the calculation of the collision probability for a $ggg \to gg$ process by a two dimensional integral is time-consuming. To reduce the computing time we have to take the following approximation, which has already been applied for the box calculations in chapter 5: We randomly choose about 20 gluon triplets instead of the total 1200 combinations and compute the amplified collision probabilities (5.7). Therefore the statistical fluctuation of the collision rate $R_{ggg\to gg}$ is stronger than that of the others. Also, when extracting the velocity of an individual space element we encounter the same difficulty of insufficient statistics as explained by calculating the screening mass. We assume that all the cells in a Δz-bin have the same longitudinal velocity

$$v = \frac{V \int \frac{d^3p}{(2\pi)^3} \frac{p_z}{E} f}{V \int \frac{d^3p}{(2\pi)^3} f} \approx \frac{1}{N_g} \sum_i \frac{p_{iz}}{E_i}, \tag{6.5}$$

where the sum runs over the test particles within a cylinder with a radius of 6 fm in the considered Δz-bin, and N_g denotes the gluon number in the cylinder. The transverse component of the velocity is set to be zero. In principle, this assumption can be corrected when a parallel computing device is employed for achieving considerable higher statistics. Then one is able to look for and calculate transverse flow of each individual cell more accurately.

6.2.2 Results I

We now present first numerical results obtained for the time evolution of the gluons produced in a central Au+Au collision at RHIC energy $\sqrt{s} = 200$ GeV. The initial conditions for the cascade are the multiple minijets with $p_T > p_0 = 2$ GeV produced in the collision. No formation time is introduced here for the minijets. As mentioned in Chapter 2, a $2 \to n$ collision with $n > 2$ can be realized within the geometrical method. However, the difficulty of the geometrical method lies in the consistent realization of the back reaction $n \to 2$. At this point the stochastic method shows its advantage in contrast, although the realization of $ggg \to gg$ process is time-consuming as explained before. If the multiplication processes ($gg \to ggg$) are dominant compared to the back reactions in the initial phase of the gluon expansion, then a cascade simulation including $gg \leftrightarrow gg$ and $gg \to ggg$ collisions employing the geometrical method [SM 02] would be an alternative for studying the parton evolution in heavy ion collisions. To see whether this consideration is reasonable, we carry out simulation with $gg \leftrightarrow gg$ and $gg \to ggg$ processes (but within the stochastic method). In both simulations the number of the test particles is set to be $N_{test} = 60$. In order to further focus on the importance of the inelastic channels to the evolution, to the thermalization and to the potential onset of nearly ideal

hydrodynamical behaviour of the partonic system, we also perform simulations for comparison only with pure elastic scatterings among the gluons. Since in this case no gluons will be produced during the evolution, more test particles are needed to build for a fine cell structure. We set $N_{test} = 240$. All results are obtained by an average over 30 independent realizations.

Rapidity distributions

Fig.6.2 and Fig.6.3 show the particle number distributions per unit rapidity versus the space-time rapidity and the momentum rapidity at the times 0.2, 0.5, 1.0, 2.0, 3.0 and 4.0 fm/c, respectively, obtained from the simulation of a central Au+Au collision at RHIC energy including pQCD $gg \leftrightarrow gg$ and $gg \leftrightarrow ggg$ interactions. The time interval of the overlapping for the two Au

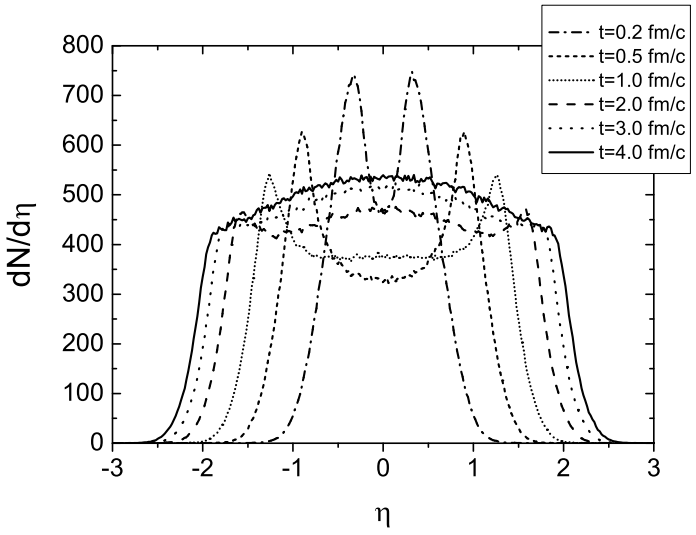

Figure 6.2: Gluon number distribution versus space-time rapidity at the time $t = 0.2$, 0.5, 1.0, 2.0, 3.0 and 4.0 fm/c during the expansion in a real, fully 3-D central Au+Au collision with pQCD $gg \leftrightarrow gg$ and $gg \leftrightarrow ggg$ interactions at the maximal RHIC energy.

nuclei is about 0.17 fm/c. Therefore, the first extraction at 0.2 fm/c is just after the end of the production of the primary partons (or minijets). In Fig.6.2 one sees a noticeable spreading of the $dN/d\eta$ distribution with progressing time. The reason is that the initially produced partons are distributed within a very small longitudinal region due to the Lorentz contraction of the Au nuclei. Their momentum rapidities, however, have a wider distribution, as can be seen in Fig.6.3. The spreading of the space-time rapidity distribution continues until its width reaches a comparable magnitude with that of the momentum rapidity

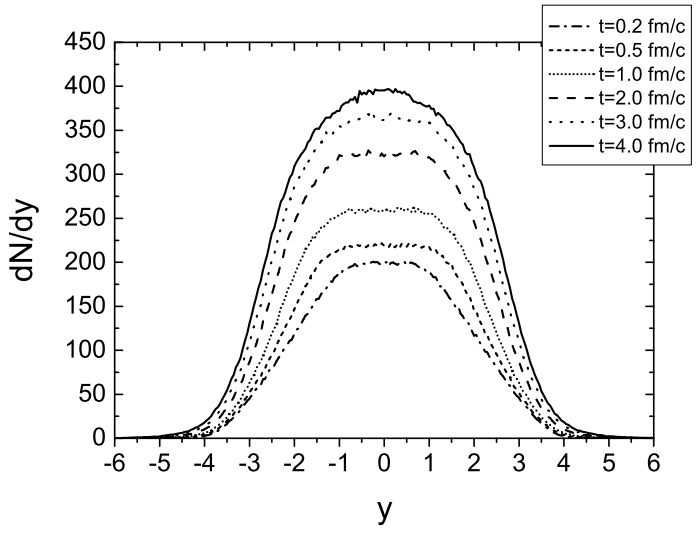

Figure 6.3: Gluon number distribution versus momentum rapidity at the time $t = 0.2$, 0.5, 1.0, 2.0, 3.0 and 4.0 fm/c during the expansion.

distribution. For the special case of a simple non-interacting free streaming system, the $dN/d\eta$ distribution will then have exactly the same shape as the dN/dy distribution at late times. In the present case we see that at 4 fm/c the width of space-time rapidity distribution is about 4.2 and approaches nearly the width of the distribution of the momentum rapidity being about 5. It can be clearly seen that the spreading of the $dN/d\eta$ distribution indeed slows down at late times. In the central space-time rapidity region the gluon density first decreases due to this spreading, and then increases because of the ongoing gluon production via the $gg \to ggg$ process. The gluon multiplication is most clearly demonstrated by inspecting the momentum rapidity distributions in Fig.6.3, where for instance at $y = 0$ the gluon number is twice amplified until 4 fm/c. Moreover, at late times the net gluon production slows down, which implies the completion of the ongoing chemical equilibration. Of course, from the momentum rapidity distributions it is difficult to recognize any evidences for kinetic equilibrium. To investigate whether the system indeed does thermalize or not, one needs more detailed analyses in sufficiently local regions. We will present the results in next subsection.

Fig.6.4 shows the momentum rapidity distributions of the transverse energy (upper panel) and the total energy (lower panel) at the different times during the expansion. While the distributions would not change during an evolution like free streaming, we see in Fig.6.4 the decrease of the transverse energy and the energy transport from the center towards the higher rapidity due to the longitudinal work done by the potential pressure. This gives first significant

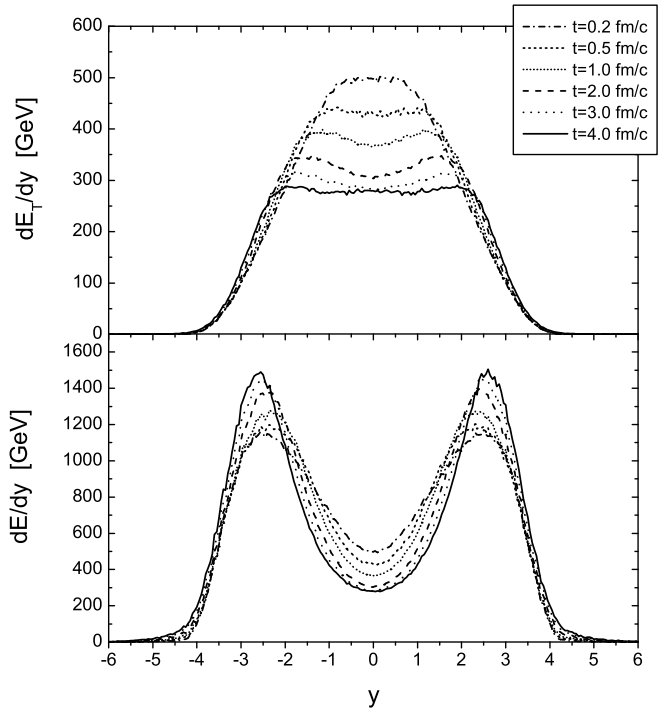

Figure 6.4: Momentum rapidity distributions of the transverse energy (upper panel) and the total energy (lower panel) of gluons at the time t = 0.2, 0.5, 1.0, 2.0, 3.0 and 4.0 fm/c during the expansion.

indications of (partial) hydrodynamical behaviour. In addition, we note that when comparing Fig.6.3 with the upper panel of Fig.6.4, the shape of the latter clearly looks more alike one dimensional Bjorken expansion than that for the particle number distribution. Hence, one can not really conclude whether simple Bjorken expansion of constant dE_T/dy and dN/dy manifests or not.

Thermalization in the 'central region'

In the following we study possible gluon thermalization in the 'central region' being defined as a longitudinally expanding cylinder located in the middle of the expanding system. The radius of the cylinder is fixed to be 1.5 fm and its length is $\Delta\eta = 1.0$ from -0.5 to 0.5. In view of the possible buildup of transverse flow, one could consider a cylinder with varying radius which is comparable with the longitudinal length. On the other hand, however, the statistics within such cylinder would be very low at early times. Since the analysis of transverse flow, which we want to address next, shows that the

transverse flow velocity is not large close to the central region even at time of 4 fm/c, the above choice with fixed radius is a reasonable compromise.

In Fig.6.5 we depict the time evolution of the gluon density and energy density in the central region by the solid curves. The dotted and dashed curves

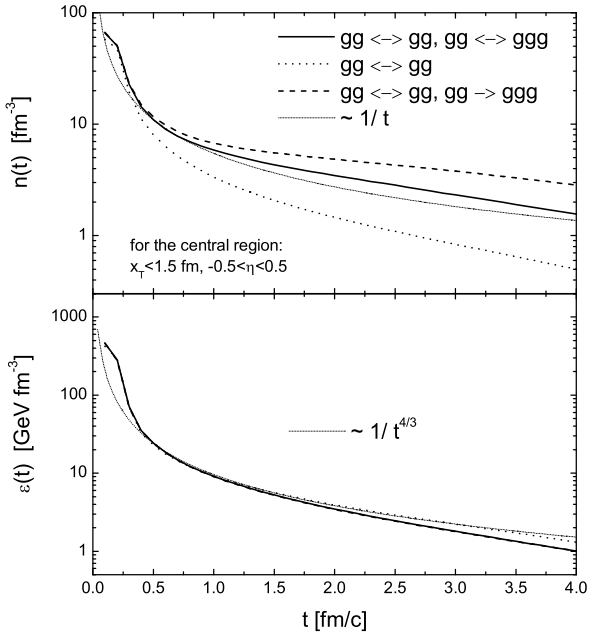

Figure 6.5: Time evolution of the gluon density and energy density in the central region: radial transverse extension $x_T < 1.5$ fm and $\eta \in [-0.5 : 0.5]$ for a central Au+Au collision at the maximal RHIC energy. The short-dotted curves denote the ideal hydrodynamical limit of one dimensional Bjorken-type expansion with a fixed intercept at time $t = 0.5$ fm/c. The dotted and dashed curves show, respectively, the results obtained from simulations with only elastic gluon scatterings and with $gg \leftrightarrow gg$, $gg \rightarrow ggg$ (without $ggg \rightarrow gg$) collisions.

show, respectively, the results obtained from simulations with only elastic gluon scatterings and with $gg \leftrightarrow gg$, $gg \rightarrow ggg$ (without $ggg \rightarrow gg$) collisions. We see that the densities are very high at early times. An implementation of the formation time for gluons (see chapter 4) will reduce the densities. The results will be shown later. In Fig. 6.5 we have also plotted there by the short-dotted curves for comparison with the standard Bjorken behaviour $n \sim 1/t$ and $\epsilon \sim 1/t^{4/3}$ with a fixed intercept at time $t = 0.5$ fm/c. Compared to that one clearly recognizes that the particle number density extracted from the simulation including complete elastic and inelastic collisions decreases more *slowly* (with an exponent of about -0.7) due to the net particle production.

The decrease of the particle number density extracted from the simulation without the annihilation processes $ggg \to gg$ slows down further, while for the simulation with only elastic collisions the partilce number density decreases more fast. The differences in the particle number density between the three simulations are not small. On the other hand, most interestingly, the energy density extracted from the three simulations more or less exactly follows the form which one would expect from ideal Bjorken hydrodynamics. Although the standard relation $P = \epsilon/3$ is all what enters into ideal hydrodynamical evolution for massless constituents, irrespective whether the system is chemically saturated or not, we have to note that the agreement shown in the lower pannel of Fig.6.5 with the ideal hydrodynamics could be an accident. As we will realize later, the elastic gluonic scatterings alone cannot drive the system into kinetic equilibrium. Therefore no ideal fluid can be built up in the simulation with only $gg \leftrightarrow gg$ collisions.

Moreover, we see from Fig.6.5 that at 4 fm/c the energy density is still 1 GeV fm^{-3}. Thus the parton picture of particle interactions is valid for the first 4 fm/c in a central Au+Au collision at RHIC. After that hadronization should occur and the system is then possibly in a parton-hadron 'mixed phase'.

Fig.6.6 shows the spectra of transverse momentum in the central region at different times during the expansion. The boldfaced histogram, which has a

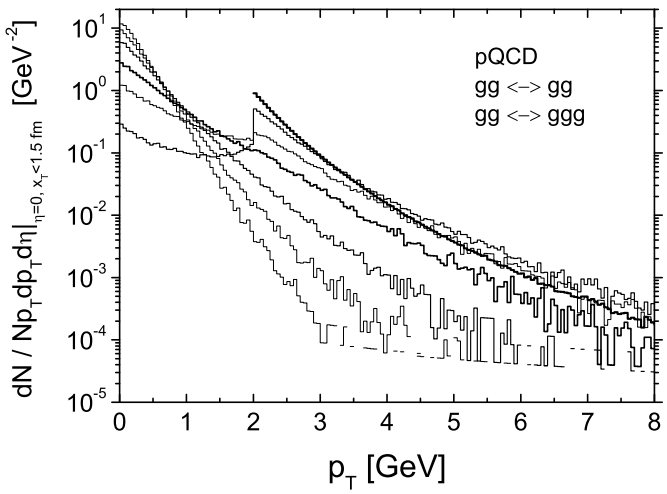

Figure 6.6: Transverse momentum spectrum in the central region at different times (t = 0.2, 0.5, 1, 2, 3 and 4 fm/c from second upper to lowest histogram) during the expansion. The most-upper and boldfaced histogram with a lower cutoff at $p_T = 2$ GeV denotes the spectrum of the primary gluons (minijets).

lower cutoff at 2 GeV, depicts the initial distribution of the primary gluons

(minijets). The spectrum possesses a typical power-law behaviour. Already at 0.2 to 0.5 fm/c a tremendous population of the soft gluons below 2 GeV has taken place. However, still a remedy of the edge at 2 GeV in spectra is visible. The 'edge' vanishes at about 1 fm/c and the distributions become nearly exponential and progressingly steepen at the later times 2, 3 and 4 fm/c. The ongoing steepening of the spectra in time represents a further strong indication of a (quasi-)hydrodynamical expansion of an almost kinetically equilibrated system with decreasing temperature.

In contrast, Fig.6.7 depicts the spectra of the transverse momentum obtained from the simulation with only elastic scatterings. The population of

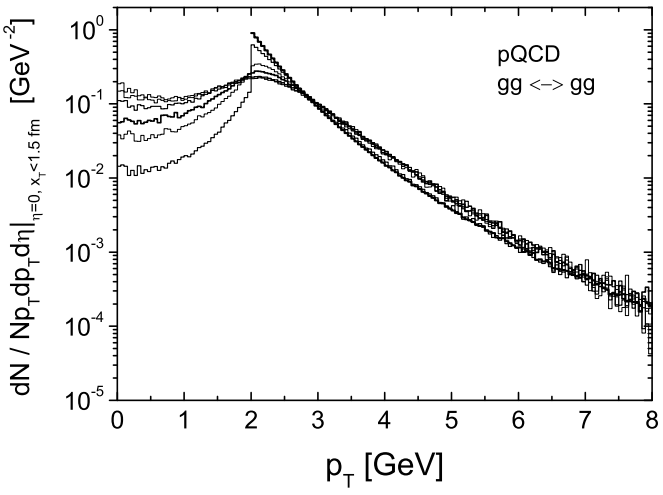

Figure 6.7: Transverse momentum spectrum in the central region extracted from the simulation with only elastic collisions at different times. The most-upper and boldfaced histogram with a lower cutoff at $p_T = 2$ GeV denotes the spectrum of the primary gluons (minijets). According to the increase of the population of the soft gluons below 2 GeV, the other histrograms present the spectrum at times 0.2, 0.5, 1.0, 2.0, 3.0 and 4.0 fm/c respectively.

the soft gluons below 2 GeV is rather low and the distributions at large p_T are only slightly altered. Indeed gluons with highest momenta get more populated. It is obvious that the gluon system is not thermalized during the expansion in this case.

We do not show the p_T spectra extracted from the simulation without the $ggg \to gg$ collisions, since the spectra are similar as plotted in Fig.6.6. The only difference is that the spectra are more steep at late times, because the stronger net gluon production leads to the stronger cooling. Also in this case

we expect a fully kinetic equilibration of gluons in the central region during the expansion.

To study kinetic equilibration in more detail, we first concentrate on the momentum anisotropy $< p_T^2 > /2 < p_z^2 >$. For an ideal, one dimensional boost-invariant hydrodynamical expansion the value of the anisotropy extracted within a region $\eta \in [-\Delta\eta/2, \Delta\eta/2]$ is given by

$$\frac{< p_T^2 >}{2 < p_z^2 >} = \frac{\int_{-\tilde{z}}^{\tilde{z}} dz \int d^2p_T dy \, E \, p_T^2 \, e^{-\frac{p_\perp \cosh(y-\eta)}{T(\tau)}}}{2 \int_{-\tilde{z}}^{\tilde{z}} dz \int d^2p_T dy \, E \, p_z^2 \, e^{-\frac{p_\perp \cosh(y-\eta)}{T(\tau)}}} = \frac{\int_0^{\Delta\eta/2} d\eta \, (\cosh\eta)^{2/3}}{6 \int_0^{\Delta\eta/2} d\eta \, (\cosh\eta)^{8/3} - 5 \int_0^{\Delta\eta/2} d\eta \, (\cosh\eta)^{2/3}}, \qquad (6.6)$$

where $\tilde{z} = t \tanh(\Delta\eta/2)$. The expression (6.6) depends only on the longitudinal length of the local region where the momentum anisotropy is extracted, and goes to 1 in the limit $\Delta\eta \to 0$. In the central region with $\Delta\eta = 1$, the anisotropy is equal to 0.65 for an ideal expansion. In Fig.6.8 the time evolution of the momentum anisotropy extracted from the present simulations is depicted by the solid curve. Compared with the thermal value (0.65), the

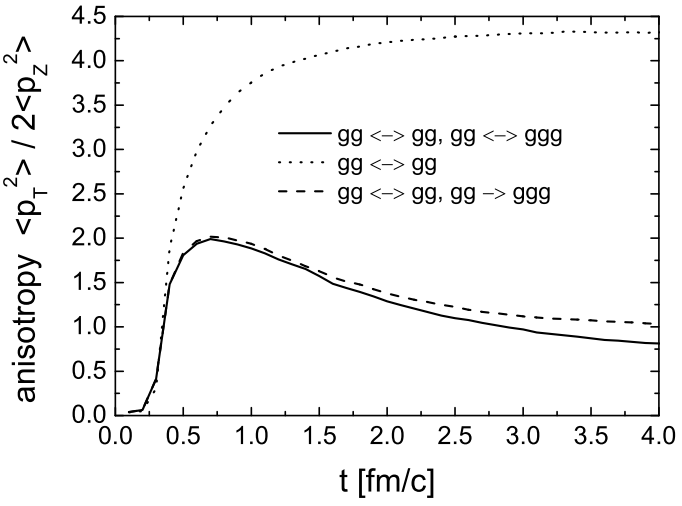

Figure 6.8: Time evolution of the momentum anisotropy extracted in the central region. The solid curve shows the result from the simulation with full dynamics, while the dotted and dashed curves depict, respectively, the results from the simulation with only elastic scatterings and with $gg \leftrightarrow gg$, $gg \to ggg$ (without $ggg \to gg$) collisions.

curve (with $gg \leftrightarrow gg$, $gg \leftrightarrow ggg$) in Fig.6.8 shows first a significant increase

during a short time 0.6 fm/c and then a smooth relaxation to that thermal value. The early increase of the momentum anisotropy is due to the initial p_T cutoff, $p_T > 2$ GeV, and the fact that the primary gluons with large longitudinal momentum also have large rapidity and thus move rapidly out of the central space-time rapidity region. The following decrease of the anisotropy unambiguously implies the ongoing persistence of kinetic equilibration. The reason why the anisotropy is still slightly larger than the thermal value is due to the fact that particles with larger p_T equilibrate later, as also seen from the p_T spectra in Fig.6.6. From that particular analysis, quantitatively, the gluon system becomes approximately fully equilibrated at 2.5 fm/c. On the other hand, as just stated, the clear bending over at a time of 0.75 fm/c signals that the strong thermalization has already started at that time, as one also notices from the onset of the pronounced exponential behaviour at a similar time as seen in Fig.6.6. Inspecting again the time evolution of the energy density shown in the lower panel of Fig. 6.5, the almost agreement with the standard Bjorken behaviour $\epsilon \sim 1/t^{4/3}$ gives another evidence that the system in the central region behaves nearly as an ideal fluid.

As seen in Fig.6.8, the momentum anisotropy extracted from the simulation with only elastic scatterings saturates at much higher value than 1 at late times. This is a further argument to demonstrate that there is no kinetic equilibration in this case. The comparison shows that the inelastic collisions play the essential role on driving the system into kinetic equilibrium. However, we remark that in the full dynamics with the inelastic channels, the contribution of the elastic scatterings to kinetic equilibration should be significantly larger than that in the simulation with purely $gg \leftrightarrow gg$ collisions, because in the full dynamics we have more gluons due to the radiation and the ongoing chemical equilibration leads to larger screening mass of gluons and thus larger scattering angle for elastic collisions. In Fig.6.8 we also recognize the ongoing kinetic equilibration in the simulation without the $ggg \rightarrow gg$ collisions. The slightly slowdown of the decrease of the momentum anisotropy, when compared with that for the simulation with complete inelastic channels, indicates a smaller rate of total inelastic collisions.

The rapid diffusion of the high-energy particles out of the central region at the beginning of the expansion also explains the dramatic decrease of the gluon density, energy density (both shown in Fig.6.5) and the effective temperature $T = \epsilon/3n$ at early times, which is shown in the upper panel of Fig.6.9 by the solid curve. The further decrease of the temperature until 200 MeV at 4 fm/c is due to the fact that work is done by the pressure and also due to the ongoing production of gluons. For simple free streaming the effective temperature would be constant over the whole time, just like the case in the simulation with only elastic collisions (dotted curves). To characterize the time dependence of the temperature we assume that the temperature behaves like

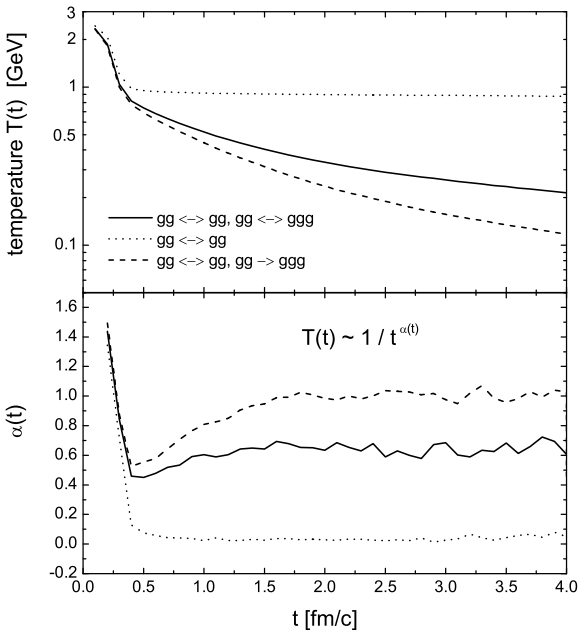

Figure 6.9: Time evolution of the effective temperature (upper panel) and the exponent describing the cooling of the system (lower panel) in the central region. The curves are arranged in the same way as in Fig.6.8.

$T \sim 1/t^{\alpha}$ with a time dependent exponent. $\alpha(t)$ is shown in the lower panel of Fig.6.9 by the solid curve. We see that the exponent is almost constant, about 0.6, at late times and is roughly double the size of 1/3, which one expects for an ideal, one dimensional boost-invariant expansion. This is mainly due to the further production of gluons and also might indicate the buildup of transverse flow. In the simulation without $ggg \to gg$ collisions the temperature deceases the fastest with an exponent of 1 due to stronger particle production. Since detailed balance is ignored in this case, the gluon fugacity, depicted in Fig.6.10 in a way similar as in chapter 5 (see eq.(5.17)), becomes much higher than 1 at late times. This demonstrates the importance of the back reactions. Those are absolutely essential for chemical equilibration. For the simulation with full dynamics chemical equilibration is still not fully achieved until 4 fm/c.

We conclude that starting from a special, yet highly nonthermal initial condition a gluon plasma, even not fully thermalized, may form at 1 fm/c in a central Au+Au collision at RHIC energy and its ongoing evolution in bulk behaves (quasi-)hydrodynamically. Of course, this reasoning will depend crucially on the initial conditions chosen. If we would only double the number of initial gluons, thermalization should occur faster. Indeed, our initial gluon

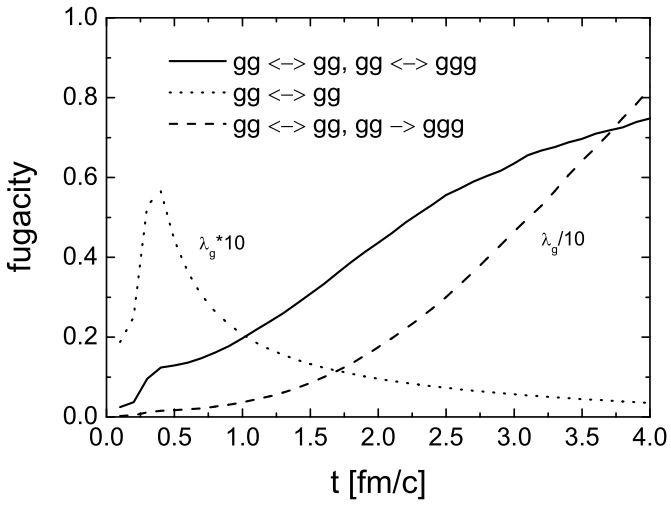

Figure 6.10: Time evolution of the gluon fugacity extracted in the central region. The curves are arranged in the same way as in Fig.6.8.

number is lower compared to other studies in the literature [MG 02, EKRT 00], where a factor of $4-6$ more initial gluons is assumed. This will then clearly imply that full gluon equilibration within a consistent pQCD approach can have a full realization at RHIC. A detailed study, addressing various initial conditions for the gluon number, i.e. different forms of minijet productions or color glass condensate initial conditions, will be presented in the later sections.

Fig.6.11 shows the time evolution of the cross sections which are first calculated as ensemble averages over all the possible doublets in a cell and then averaged over all the cells within the central region. As $< v_{rel} > \approx 1$ in the central region, the collision rates of the $gg \leftrightarrow gg$ and $gg \rightarrow ggg$ are obtained by $R = n < v_{rel}\sigma > \approx n < \sigma >$ respectively. We have compared these collision rates with those counted directly from the simulation and have seen nice agreements. The increase in time of the two cross sections is due to the fact that the cross sections are inversely proportional to the screening mass squared and the latter is proportional to the temperature squared. One sees that $\sigma_{gg\rightarrow gg}$ is always larger than $\sigma_{gg\rightarrow ggg}$. For kinetic equilibration, however, not only a large total cross section but also large scattering angle are essential for a possible fast thermalization. In other word, the transport cross section [MG 02]

$$\sigma_t = \int d\sigma \, \sin^2\theta_{cm} = \int d\theta_{cm} \frac{d\sigma}{d\theta_{cm}} \sin^2\theta_{cm} \tag{6.7}$$

is the key quantity controlling the ongoing of the equilibration by given particle density n. θ_{cm} denotes the scattering angle in the center of mass frame of the

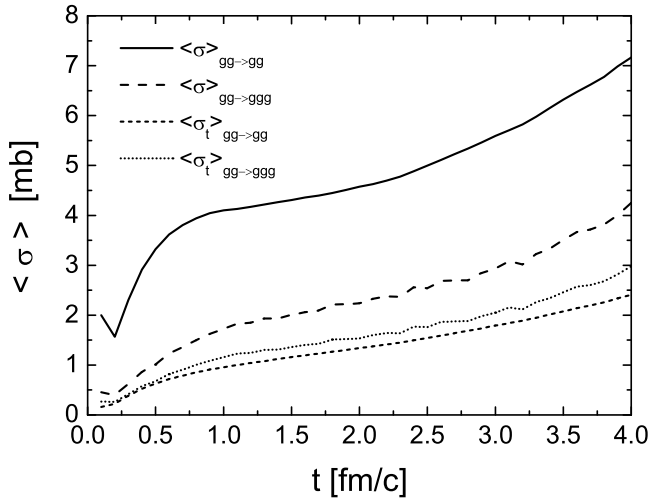

Figure 6.11: Time evolution of the averaged cross section and the averaged transport cross section in the central region. The solid and dashed (short dashed and short dotted) curves depict the averaged cross sections (transport cross sections) for the $gg \to gg$ and $gg \to ggg$ processes respectively.

colliding particles. For a $gg \to ggg$ process each outgoing particle has its own scattering angle. In this case we modify (6.7) by $(\sin^2\theta_1 + \sin^2\theta_2 + \sin^2\theta_3)/3$ instead of $\sin^2\theta_{cm}$. The averaged transport cross sections are shown in Fig.6.11 by the short dashed and short dotted curves. Taking into account that at late times the collision rate of the $ggg \to gg$ is comparable with the rate of the $gg \to ggg$ process, one realizes that the inelastic processes are actually the dominant processes driving the system to kinetic equilibrium. This represents an important finding of the investigation.

Following the expression of the differential cross section one knows that the gluon elastic collisions favour small angle scatterings. That is the reason why the parton evolution simulated with only pQCD elasctic interactions resembles a free streaming, although the collision rate in this case is actually not small. The transport cross sections in Fig.6.11 indicate that the angular distribution of the inelastic collisions is more moderate than that of the elastic collisions. As can be realized from the differential cross sections expressed in Appendix C and D, the angular distribution of the elastic scatterings depends on m_D^2/s, while it depends on m_D^2/s and $\lambda_g\sqrt{s}$ for the inelastic collisions. In Fig.6.12 we depict the angular distributions of the $gg \to gg$ and $gg \to ggg$ scatterings for the parameters $m_D^2/s = 0.05$ and $\lambda_g\sqrt{s} = 4$. The distributions are calculated according to the differential cross sections. The two parameters are chosen from an intermediate situation within the simulation. We see that while the

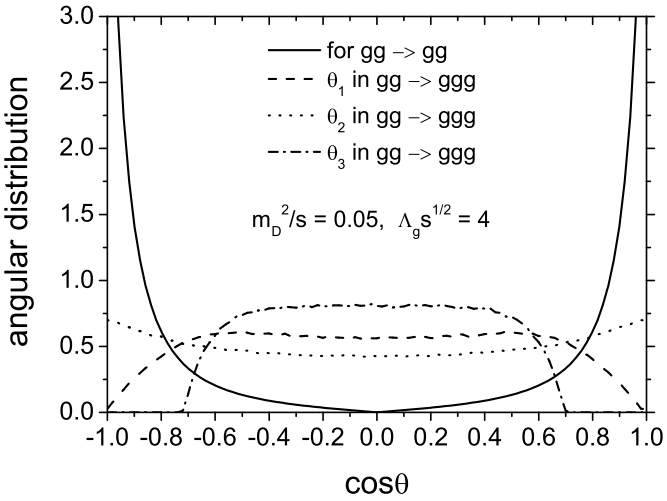

Figure 6.12: Angular distribution of the scattering processes $gg \to gg$ (solid curve) and $gg \to ggg$ for a representative situation during the gluon evolution. θ_3 denotes the scattering angle of the radiated gluon and its radiation partner has the angle θ_2. The distributions are computed with the parameters $m_D^2/s = 0.05$ and $\lambda_g\sqrt{s} = 4$ extracted in the central region at an intermediate time during the evolution.

angular distribution of the elastic collisions clearly shows forward scatterings as expected, the angular distribution of the inelastic collisions is surprisingly almost isotropic. The reason for this behaviour is due to the effective LPM cutoff being implemented. For a larger $\lambda_g\sqrt{s}$ the $gg \leftrightarrow ggg$ processes would also favour the more the small angle scatterings. Notice that θ_3 denotes the angle of the radiated gluon and thus possesses also a cutoff in its distribution due to the incorporation of the LPM suppression of low momentum gluon emissions.

We note that when comparing the cross sections calculated in thermal equilibrium (see Fig.5.1), the cross sections $\sigma_{gg\to gg}$ and $\sigma_{gg\to ggg}$ extracted from the dynamical runs are $2-5$ times larger at later times. This is because first α_s had been fixed to 0.3 in Fig. 5.1 and in the cascade simulation the running coupling is computed according to (6.2). In Fig.6.13 we depict the ensemble averaged running coupling $<\alpha_s>$ extracted within the central region during the gluon evolution. By the averaging only possible collisions are taken into account. Since $gg \to ggg$ collisions with small s are often kinematically forbidden due to the LPM effect, the averaged running coupling for $gg \to ggg$ process is smaller than that for elastic process. For both cases it turns out that $<\alpha_s>$ increases almost linearly in time from 0.2 at 0.2 fm/c to 0.87 (elastic)

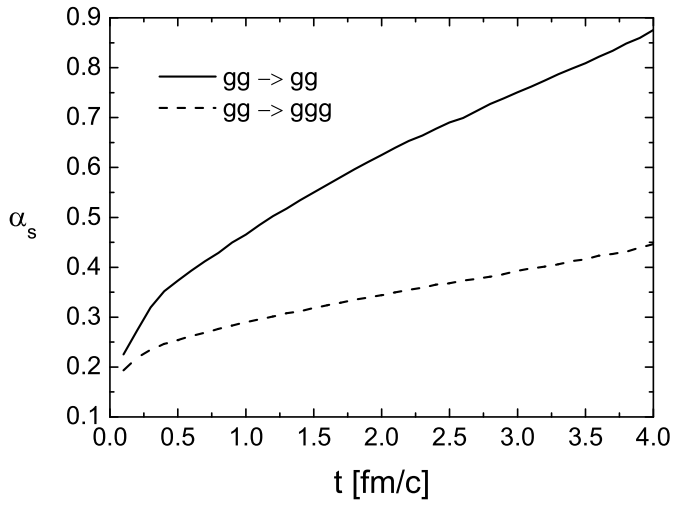

Figure 6.13: Time evolution of the averaged running coupling $< \alpha_s >$. The solid and dashed curves show the results obtained by averaging $gg \to gg$ and $gg \to ggg$ processes respectively.

or 0.45 (inelastic), respectively, at 4 fm/c, which is larger than 0.3. Second, the screening mass is appreciably smaller in the dynamical calculation as the gluons are not fully saturated in its occupation number. Both effects add up to the difference.

The time evolution of m_D^2/α_s, the gluon screening mass squared over the running coupling, is depicted in Fig.6.14 by the solid curve. Assuming that gluons in the central region are in kinetic equilibrium, one has

$$\frac{m_D^2}{\alpha_s} = \frac{24}{\pi}\lambda_g T^2 \tag{6.8}$$

according to (5.6) with $n_f = 0$. Using the extracted gluon fugacity (Fig.6.10) and temperature (Fig.6.9) we depict (6.8) in Fig.6.14 to make a comparison with the result from the cascade simulation. One expects agreement of two curves from some time when the gluon system in the central region reaches kinetic equilibrium. However, the figure shows that the two curves are always parallel and the value of m_D^2/α_s is 30 per cent smaller than expected. This is due to the assumption, given at the beginning of this section, that m_D^2/α_s is computed by an average over a large region with a transverse radius of 6 fm. As mentioned, this assumption underestimates m_D^2/α_s. An improvement will be given later in section 6.4.

As seen in the previous chapter, simple rate equations can also successfully describe the chemical equilibration of partons in a fixed box. Therefore

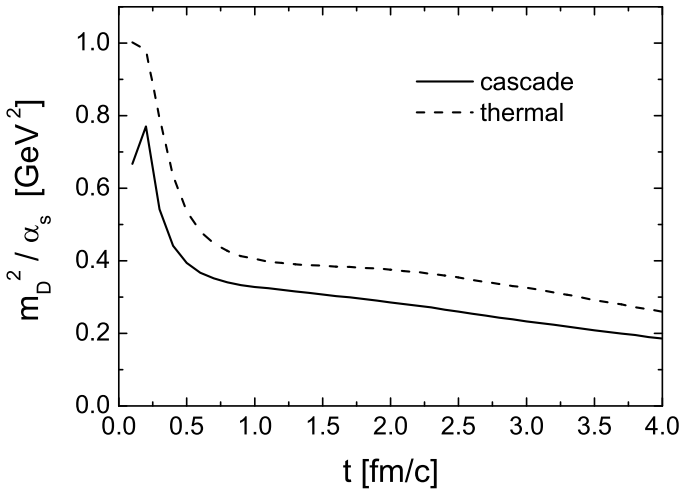

Figure 6.14: The time evolution of m_D^2/α_s. The solid curve shows the result from the cascade simulation, while the dashed curve shows the result when kinetic equilibrium is assumed.

it is interesting to solve rate equations for partons in a Au+Au collision at RHIC and then to compare the chemical equilibration with our cascade results. Such calculations have been performed by Biro et al. in [BDMTW 93]. In Fig.6.15 we show the scaled collision rates versus the gluon fugacity. The solid curves show the results extracted in the central region from the cascade simulation for $gg \to gg$, $gg \to ggg$ and $ggg \to gg$ process from upper to lowest curves. The dotted curves show the results from a similar calculation as in [BDMTW 93]. As mentioned in Appendix D, the calculation of the cross section $\sigma_{gg\to ggg}$ in [BDMTW 93] is not absolute correct. The lower dotted curve in Fig.6.15 depicts the exact result after corrections. There is small difference when comparing with the original plot, Fig.2 in [BDMTW 93]. (Note that $R_3 = R_{gg\to ggg}/2$ in the reference.) In their calculation the mean free path of gluon is computed by $\Lambda_f^{-1} = R_{gg\to gg} = \sigma_{gg\to gg}\, n_g$ and the LPM effect is modeled by $\Theta(k_\perp \Lambda_f - 2\cosh y)$. That is different from the modeling in our cascade simulation, where we apply $\Theta(k_\perp \Lambda_g - \cosh y)$ and $\Lambda_g^{-1} = R_{gg\to gg} + R_{gg\to ggg} + R_{ggg\to gg}$. Comparing the collision rates from the cascade simulation we realize that $R_{gg\to gg}$ is always larger than $R_{gg\to ggg} + R_{ggg\to gg}$ and thus the gluon emission is more suppressed in the analysis by Biro et al. than in our investigation. This is the first reason for the difference between the $gg \to ggg$ collision rates. Second, the running coupling is set to be 0.3 in [BDMTW 93], which is smaller than that in the cascade simulation (see Fig.6.13). Furthermore, as shown in Fig.6.14, the screening mass calculated dynamically in the simulation is smaller

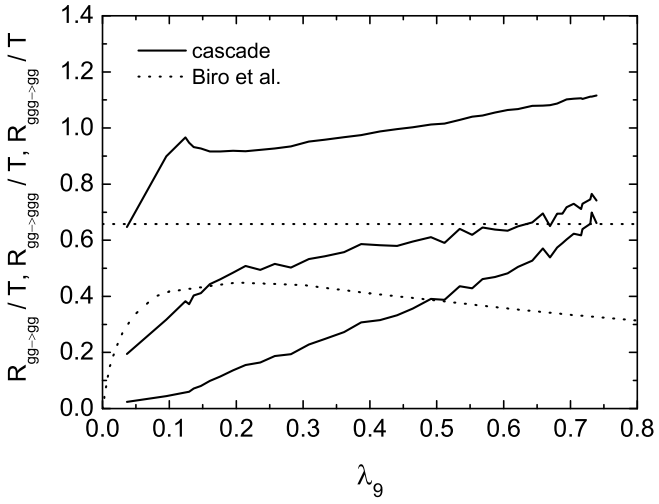

Figure 6.15: The scaled collision rates versus the gluon fugacity. The solid curves show the results for $gg \to gg$, $gg \to ggg$ and $ggg \to gg$ process (from upper to lowest curves), extracted in the central region from the cascade simulation. The dotted curves show the results for $gg \to gg$ and $gg \to ggg$ process (from upper to lower curves), obtianed from a similar calculation as in [BDMTW 93].

than that should be due to the assumption. The three effects lead to the differences between the solid and dotted curves in Fig.6.15. It is then obvious that the chemical equilibration will go faster in our simulation than in the analysis by Biro et al.. Note that the initial values for the temperature and fugacity in [BDMTW 93] are $T = 0.57$ GeV and $\lambda_g = 0.09$ at $t_{iso} = 0.31$ fm/c and in our calculation the temperature decreases to the value of 0.57 GeV at about $t = 0.8$ fm/c and at this time the fugacity reaches a value of 0.15 (see Fig.6.9 and Fig.6.10). These values are not very different. However, when comparing the time evolution of the gluon fugacity shown in Fig.3 in [BDMTW 93] with the cascade result depicted in Fig.6.10, one finds a difference of a factor of 3. This value is too large to be explained by the different collision rates alone. The second reason is that also $gg \leftrightarrow q\bar{q}$ processes are included in the analysis employing the rate equations, while quark dynamics has not been considered in the present cascade simulations. Finally, the relation $\epsilon \sim \tau^{-4/3}$ used in [BDMTW 93], which follows the assumption of one dimensional hydrodynamical expansion, is only approximately established in the cascade simulation (see Fig.6.5).

Transverse Evolution

In the previous subsection we have seen that in the central region thermalization is achieved during the expansion. It is therefore reasonable to expect that thermalization would also be established within a larger transverse region beyond the central region and a transverse flow, as a hydrodynamical behaviour, would be then built up at some time during the parton evolution. To give definite answers for such qualitative considerations we investigate now the transverse evolution of gluons in the central unit space-time rapidity $\eta \in [-0.5 : 0.5]$. Results presented below are obtained from the simulations, which have already been performed for the investigations in the previous subsection. Moreover, until now we have assumed that in a central Au+Au collision at RHIC energy the initial expansion of gluons is mainly longitudinal and thus the dependence of the setups for calculating the screening mass and velocities of a moving space element on a possible transverse flow is completely neglected in the simulations. In this subsection we will inspect whether this assumption is justified.

Fig.6.16 shows the transverse profiles of the gluon number at different times during the expansion by the solid curves. The dashed curves depict the results

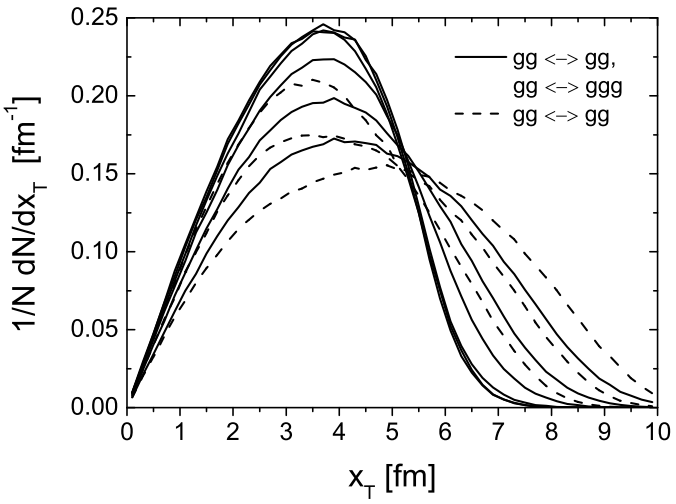

Figure 6.16: Transverse profile of the gluon number. The solid curves, from that with smallest width to that with largest width, depict the results from the simulation including both elastic and inelastic pQCD gluonic interactions at the times 0.2, 0.5, 1.0, 2.0, 3.0 and 4.0 fm/c respectively. The dashed lines depict the results from the simulation with only the elastic collisions at 2.0, 3.0 and 4.0 fm/c.

from the simulation with only elastic collisions. One sees that until 1 fm/c

the transverse profile does not change very much. The system seems to be transversely at rest in the initial stage. Thereafter the profile becomes broader and broader with progressing time, which indicates the ongoing transverse expansion. One can also recognize that in the simulation with only the elastic collisions the gluon system expands stronger.

To study the collective motion of a medium, one has to first determine the space elements, for which velocities will then be calculated. In the central unit space-time rapidity region we divide the transverse plan into rings due to the symmetry of the expansion: the central ring has a radius of $R_1 = 1.5$ fm and the distance between the other neighboring rings is set to be $\Delta R = 1$ fm. The transverse velocity v_T in an individual ring is computed as the mean radial velocity of gluons in the locally fixed ring. Fig.6.17 shows the time evolution of the transverse velocities during the expansion. The lines, from the lowest

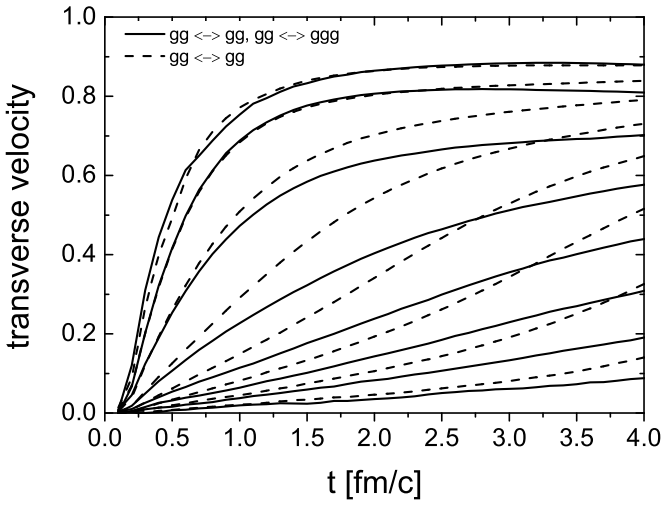

Figure 6.17: Time evolution of the transverse velocity within the central unit space-time rapidity. The lines, from the lowest to the uppermost, depict the transverse velocities extracted in the central to the outermost ring, respectively. The central ring has a radius of $R_1 = 1.5$ fm and the distance between the other neighboring rings is set to be $\Delta R = 1$ fm. The solid lines denote the results from the simulation including both elastic and inelastic pQCD gluonic interactions, while the dashed lines denote the results from the simulation with only the elastic collisions.

to the uppermost, depict the transverse velocities extracted in the central to the outermost ring respectively. The solid lines denote the results from the simulation including both elastic and inelastic pQCD gluonic interactions, while the dashed lines denote the results from the simulation with only the

elastic collisions. We see that the transverse velocities, starting from zero due to the initially random sampling for the transverse momentum of the particles, increase during the expansion. According to the analyses in the central region in the previous subsection, one can definitely conclude that the time evolution of the transverse velocities in the simulation including only the elastic collisions just results from the free streaming of the particles and cannot indicate any hydrodynamical flow, since no pressure exists in this case. Compared to that, the transverse expansion of gluons in the simulation with full dynamics, except the very outer region, seems to be much 'viscouser', which is also observed in Fig.6.16. It shows that if the transverse flow is being built up during the evolution, it will take some time. Whether this behaviour really results from the hydrodynamics needs detailed investigation via comparisons between ideal two dimensional hydrodynamical expansion and free streaming. This is beyond the scope of the present study. On the other hand, since the hydrodynamical behaviour has been seen in the central region as the continuous steepening in time of the nearly exponential p_T spectra, it is reasonable to believe that hydrodynamical flow has been built up in the transverse direction. We will confirm this consideration later. From Fig.6.17 one can also recognize that for the transverse region with radius $R < 4$ fm the flow is actually not big.

To study thermalization in the transverse direction beyond the central region, one has to go to the co-moving frame of the individual ring. The number and energy density in the rings can be formulated as Lorentz scalars according to

$$n = U^\mu N_\mu \,, \quad \epsilon = U_\mu T^{\mu\nu} U_\nu \,, \tag{6.9}$$

and can be calculated in any frame. N^μ and $T^{\mu\nu}$ denote, respectively, the particle four-flow and the energy-momentum tensor. U^μ is the four-velocity of a ring and defined as $U^\mu = N^\mu/\sqrt{N^\nu N_\nu}$. Employing the expressions (F.7) in Appendix F we extract U^μ, N^μ and $T^{\mu\nu}$ from the simulation and then calculate n and ϵ. For instance, we obtain $U^\mu = (1, v_T, \mathbf{0})/\sqrt{1 - v_T^2}$ and $n = \sqrt{1 - v_T^2}\, N/V$ (N being the gluon number in the ring with a volume of V), which one can also receive by simple Lorentz transformation. Fig.6.18 shows the local number and energy densities versus the position of the rings at different times during the parton evolution. The results are obtained from the simulation with full gluonic interactions. We see that within the radius of the gold nucleus ($x_T < 6$ fm) the densities decrease for the progressing time due to the 3D expansion. Comparing the number densities to the energy densities, one can recognize that the energy densities decrease stronger than the number densities, which indicates the dissipation done by the pressure. Beyond the radius of the nucleus we see increasing number densities and also increasing energy densities at late times as well due to the transverse expansion. When assuming that the confinement-deconfinement transition occurs roughly at $\epsilon \approx 1\,\mathrm{GeVfm}^{-3}$, then the partons out of the central region will hadronize gradually before the final

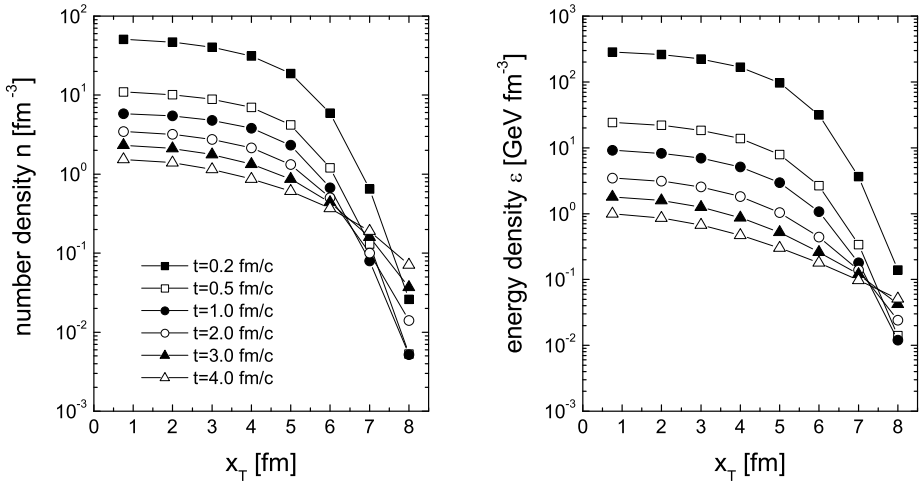

Figure 6.18: Local number and energy densities versus the position of the rings at the times 0.2, 0.5, 1.0, 2.0, 3.0 and 4.0 fm/c.

time 4 fm/c, as seen in the right part of Fig.6.18. Their interactions thereafter should be hadronic. However, the phenomenon of hadronization has not been implemented in the present study. In the simulations presented the particles interact still via the partonic cross sections, although they are in the region with energy density lower than 1 GeVfm^{-3}.

In Fig.6.19 we show the collision rates extracted in the rings at different times. Comparing the collision rates $R_{gg\to gg}$ for $gg \to gg$ process with the number densities (left part of Fig.6.18), we see the almost same patterns, which indicates that the cross section for $gg \to gg$ collision does not vary much in the transverse plan. This is in fact true because m_D^2/α_s is assumed to be constant everywhere in the transverse plan. In contrast, the collision rates $R_{gg\to ggg}$ for $gg \to ggg$ process are even larger at lower particle densities. That is mainly due to the LPM effect taken in the calculation of the cross section for $gg \to ggg$ process: Where the mean free path of gluons is large or the collision rate is small (note that $R_{gg\to gg}$ is the dominant part), the probability for a $gg \to ggg$ process becomes large. The complicated pattern in the right part of Fig.6.19 shows the nontrival, non-linear behaviour of gluon radiation with the LPM effect.

Since, as realized in the previous subsection, the inelastic collisions are dominant processes for thermalization, the results of the collision rates in Fig.6.19 indicate that thermalization should be also achieved in the region within $x_T \leq 5$ fm. In Fig.6.20 we show the momentum anisotropy (left panel) and the gluon fugacity (right panel) versus the transverse position of the rings

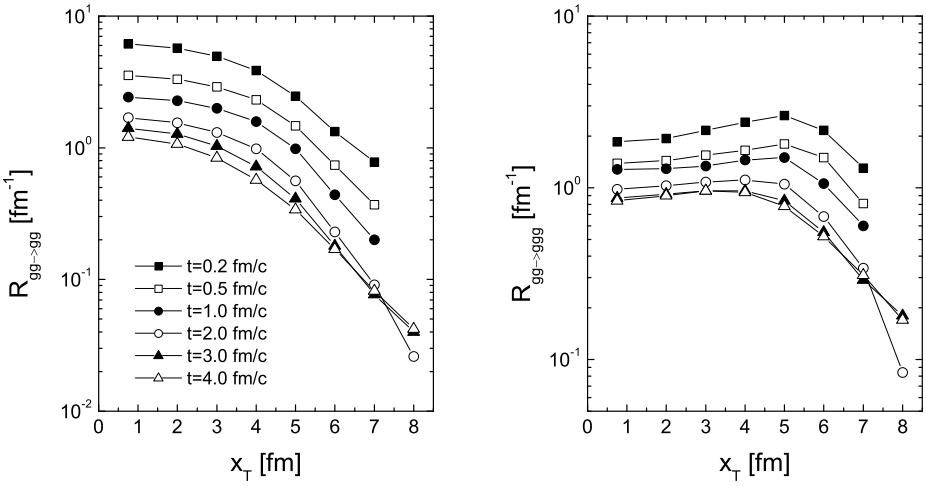

Figure 6.19: Collision rates for $gg \to gg$ and $gg \to ggg$ processes in the rings at the times 0.2, 0.5, 1.0, 2.0, 3.0 and 4.0 fm/c.

at different times. The transverse momenta of particles in the rings are now

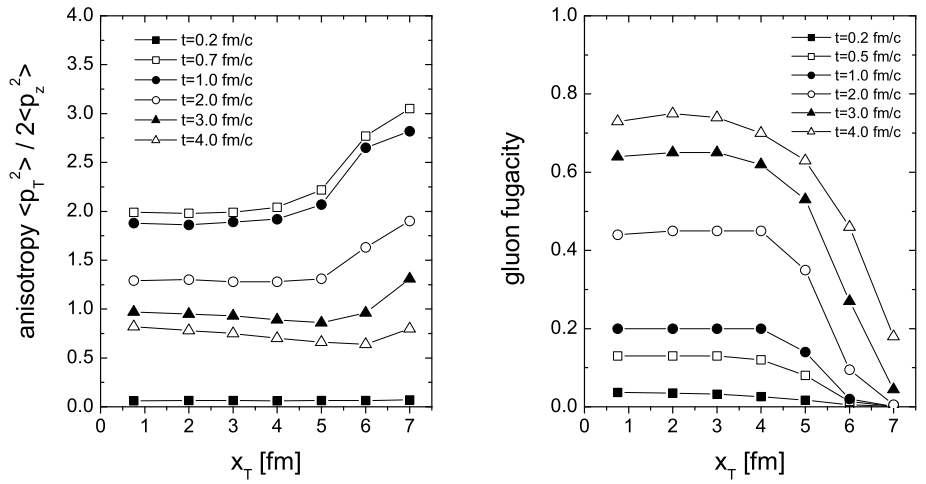

Figure 6.20: Momentum anisotropy and gluon fugacity versus position of the locally fixed rings at the times $t = 0.2$, 0.5 (0.7 in left panel), 1.0, 2.0, 3.0 and 4.0 fm/c.

obtained by Lorentz transformation with corresponding transverse velocity.

From the left panel of Fig.6.20 one sees that the momentum anisotropies in all rings start with very small values at the beginning, reach maxima at about 0.7 fm/c and then decrease below 1 at the final time of 4 fm/c. It seems that at the end kinetic equilibration is achieved even in the outermost ring at $x_T = 7$ fm. This can not be explained intuitively by the argument via the collision rate. We therefore inspect, and show in Fig.6.21, spectra of the transverse momentum in the ring positioned at $x_T = 5$ fm, which corresponds to the edge of the gold nucleus, and in the outermost ring at $x_T = 7$ fm. One can clearly

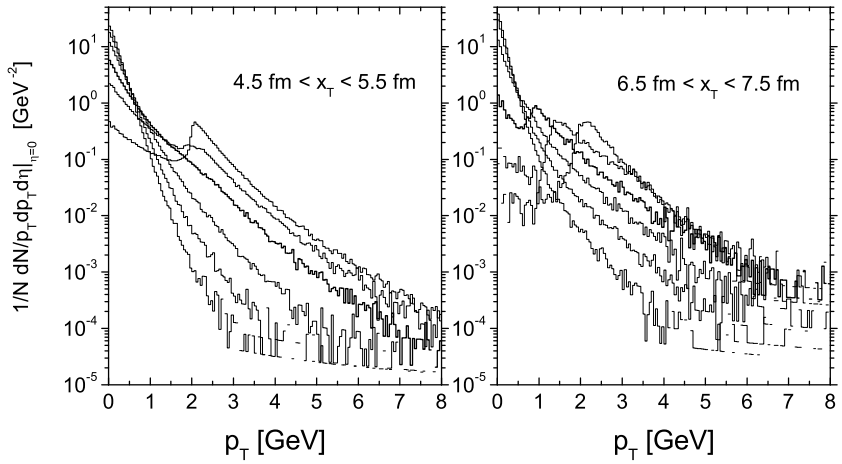

Figure 6.21: Transverse momentum spectrum in the transverse rings at $x_T = 5$ fm (left panel) and at $x_T = 7$ fm (right panel) at different times ($t = 0.2$, 0.5, 1.0, 2.0, 3.0 and 4.0 from most-upper to lowest histogram).

recognize that the spectra in the ring at $x_T = 5$ fm resemble those shown in Fig.6.6 for the central region, except for slight deviation from the straight line at higher p_T. This shows that kinetic equilibration is indeed achieved in the transverse region within a radius of a gold nucleus. When viewing the left panel of Fig.6.20 again, we realize that the anisotropies for the rings below 5 fm (including 5 fm) possess almost the same values at each stage of the expansion, which indicates that the large portion of the gluon matter becomes kinetically equilibrated at the same time. The spectra in the outermost ring, however, do not show kinetic equilibration and hydrodynamical behaviour. We clearly see the shift of the initial spectrum at the early times (0.2, 0.5 and 1.0 fm/c) simply due to the Lorentz boost. Particles with high p_T stream out of the ring and this leads to the further decrease of the spectrum at high p_T. In the right panel of Fig.6.20 we depict the gluon fugacities versus the position of the rings at different times. We see the same characteristic as for kinetic equili-

bration: Chemical equilibration occurs simultaneously at about 3 fm/c within the region of $0 < x_T < 4 - 5$ fm and in contrast gluons are very undersaturated in the outermost region. Different from kinetic equilibration for which the collision rates per particle is responsible, chemical equilibration depends on the absolute net production events. Despite the decreasing profile of the number density in Fig.6.18, the inceasing profile of $R_{gg\to ggg}$ until 5 fm, shown in Fig.6.19, gives the reason for the simultaneous chemical equilibration in a large transverse region. The temperature in the rings, depicted in Fig.6.22, shows a decreasing profile from the cental to outer region ($0 < x_T < 5$ fm) of the thermalized matter. This resembles the profile of the gluon number density

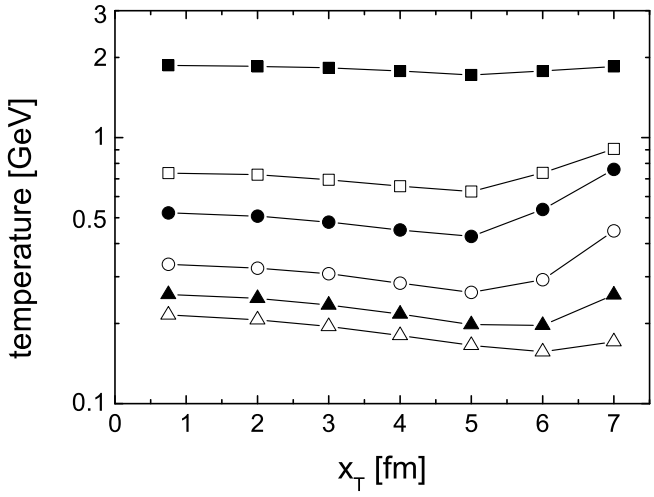

Figure 6.22: Effective temperature versus position of the rings at different times. Symbols are arranged in the same way as in the right panel of Fig.6.20.

(see Fig.6.18).

Finally, we show in Fig.6.23 the time evolution of the transverse energy per unit momentum rapidity at midrapidity for the three cases compared also in Fig.6.5. We see that the transverse energy decreases in the simulation including pQCD elastic and inelastic interactions and in the simulation including only elastic and $gg \to ggg$ scatterings. The unaltered behaviour of the transverse energy in the simulation including only pQCD elastic scatterings indicates again that in this case the parton evolution resembles free streaming. In contrast to the cooling of the temperature, to which the production of gluons also contributes, the decrease of the transverse energy within a unit rapidity is purely due to the longitudinal work done by the pressure! This is the most pronounced indication for nearly ideal hydrodynamical behaviour. Expected from the Bjorken-type ideal hydrodynamics, where one assumes that the colli-

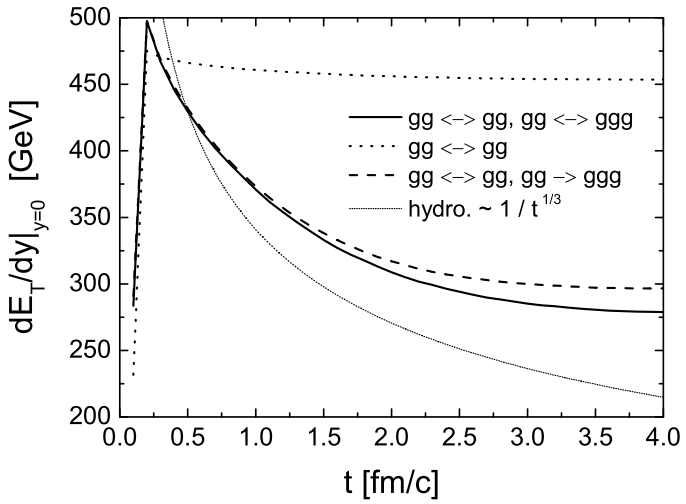

Figure 6.23: Time evolution of the transverse energy per unit momentum rapidity at midrapidity. The curves are arranged in the same way as in Fig.6.5.

sion rate is so high that the mean free path of gluons is much smaller than the macroscopical scale of length, the transverse energy behaves like $E_T \sim t^{-1/3}$. When inspecting again the collision rates in Fig.6.19, the condition for a possible ideal hydrodynamical motion is only perfectly fulfilled at early times. At the late stage, the collision rate becomes small and the expansion should then be described by the viscous hydrodynamics. Therefore a smaller amount of longitudinal work is performed. This explains the slowdown of the decrease of the transverse energy with progressing time. Moreover, as stated in [KHHET 01], the transverse flow will lead to an enhancement of the transverse energy. This, however, cannot be recognized straightforwardly in Fig.6.23.

Jet-Quenching

Jet-quenching is one of the most prominent suggested signatures for an existance of a deconfined partonic matter at the early stage of a heavy ion collision [G 90]. Measurement on the p_T spectrum of hadrons at RHIC showed a significant suppression of the spectrum at high p_T, compared with that obtained by the adding up independent events of binary nucleon-nucleon collisions. This indicates the formation of a medium, across which particles lose their energy due to radiations. However, hadronization could occur within the fireball, so that high p_T hadrons might lose their energy further when acrossing the dense hadron medium [GGX 03]. Applying the present parton cascade we can analyse the particle p_T suppression in the parton phase. In Fig.6.24 we present

the p_T spectra at different times within the unit central momentum rapidity integrated over the whole transverse region. Comparing the spectra in Fig.6.24

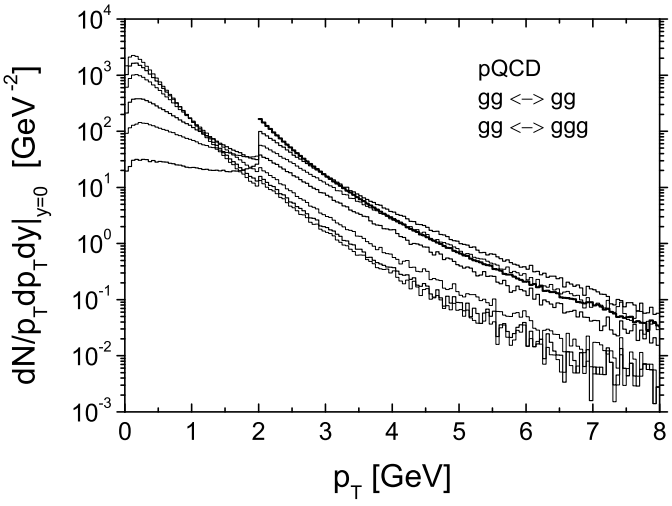

Figure 6.24: Transverse momentum spectrum in the unit central momentum rapidity ($y \in [-0.5 : 0.5]$ at different times (t = 0.2, 0.5, 1.0, 2.0, 3.0 and 4.0 fm/c from second upper to lowest histogram). The most-upper and boldfaced histogram with a lower cutoff at p_T = 2 GeV denotes the spectrum of the primary gluons (minijets).

with those in Fig.6.6, we see that there is no full global thermalization over whole transverse region until 4 fm/c. Also the buildup of transverse flow should contribute. At least for the lower momenta we see an exponential shape and a clear steepening at the later stages. Part of the minijet spectra, of course, survives as those gluons might escape directly from the outer region without interactions and thus becomes unaltered at the later times. Fig.6.24 also demonstrates the potential energy loss of gluons due to the Bremsstrahlung process. The new developed parton cascade offers an alternative possibility to investigate the phenomenon of the jet quenching in a more quantitative way based on a full $3+1$ dimensional treatment of the geometry. To be able to compare the numerical results with the experimental data one has to model the mechanism of the hadronization and include further hadronic interactions. A detailed analysis is again one of possible future projects. However, one can make an estimate based on the result depicted in Fig.6.24. The ratio of the final spectrum to the primary one manifests the amount of the energy loss in the partonic phase. From Fig.6.24 one can recognize a ratio of about 0.1 at higher p_T. When including further energy loss in the hadron gas, the ratio will be even smaller. However, the experiments at RHIC [JQ 03] shows that

the measured ratio of the final hadronic p_T spectrum to the scaled one from a nucleon-nucleon collision is $0.2 - 0.3$ at high p_T. The reason of the stronger energy loss compared to the data is mainly due to the higher collision rate of $gg \leftrightarrow ggg$ processes in the simulation, especially in the outer transverse region where pQCD interactions still exist, although the density might be so small that the hadronization should occur there and partonic processes are no longer valid (see Fig.6.18 and Fig.6.19). Note that the $gg \rightarrow gg$ processes contribute only slightly to the Jet-Quenching, since the scattering angle in such processes is always small.

6.2.3 Summary and Discussions

We now summarize the findings obtained from the first simulations for central Au+Au collisions at RHIC energy employing the new 3+1 dimensional parton cascade. The initial conditions are assumed to be generated by independent minijets with $p_T > p_0 = 2$ GeV. With this choice it is demonstrated that kinetic equilibration is driven mainly by the inelastic processes and is achieved on a scale of 1 fm/c in the central space-time rapidity region and overall within the transverse extension of the gold nucleus. The further evolution of the expanding gluonic matter then shows almost an ideal hydrodynamical behaviour. Our results also indicate the buildup of a hydrodynamical flow in the transverse direction by inspecting the transverse velocity. In addition, full chemical equilibration of the gluons follows on a longer timescale of about 3 fm/c.

There are still some uncertainties to be discussed.

1.) In the implementation of the space-time production of minijets, it is assumed that partons become immediately on-shell and thus interactive when the (semi-)hard nucleon-nucleon collisions occur. Therefore, during the head-on-head overlapping of two nuclei produced partons with larger momentum rapidity (or larger longitudinal velocity) are more or less stopped by partons with smaller rapidity. The further expansion of the parton system resembles then the Landau-type expansion in which particles are extremely stopped as that the whole system is first at rest after the overlapping. On the other hand, the Bjorken-type expansion is the most assumed one, in which at time t each piece of the system moves with a velocity of z/t, where z denotes the position of the individual piece. One can introduce an additional formation time for every minijets to model the off-shell propagation of the freed partons. This will change the initial situation to be similar as for the Bjorken-type expansion. Whether the inclusion of the formation time for the initial partons may affect our main findings, will be answered in section 6.3 by comparisons between results from numerical simulations with and without the formation time.

2.) At the beginning of this section we have assumed that there is no trans-

verse flow for the first few fm/c of the expansion. Based on this assumption we made computation for the screening mass within a large transverse region and for the collision rates ignoring the transverse velocity of the considered cell. However, as the cascade results showed, the transverse flow is actually built up during the first 4 fm/c. The ignoring of the transverse flow leads first to an underestimated screening mass in the central region, as verified in Fig.6.14, and an overestimate for the outer transverse region. Therefore, the rate of the $gg \to gg$ process should be smaller in the central region and larger in the outer region when compared with Fig.6.19. Second, all rates have to be amplified by the additional transverse boost. Note that it is difficult to make an estimate for the rate of the $gg \leftrightarrow ggg$ processes due to the complicated dependence on the LPM effect. In section 6.4 we will correct the calculation for the screening mass and the collision rates and present results from the second run of the cascade simulation.

3.) In the present simulation we have set the cut-off parameter for the initial minijets to be $p_0 = 2$ GeV. This is a very conservative assumption. A smaller value of p_0 as used in [EKRT 00] would lead to $4-6$ times larger initial parton number and thus faster thermalization. In section 6.5 we will investigate in more detail the timescales of thermalization in dependence on p_0 applying the second setup of the parton cascade presented in section 6.4. The final transverse energy per unit rapidity will be compared with RHIC data to manifest the appropriate value of p_0. In addition, we will briefly discuss thermalization of gluons with the color glass condensate as the initial condition in section 6.6.

4.) The pQCD interactions with quarks have not been included in the present simulation. We leave this as a future project.

6.3 Result II: inclusion of formation time

In this section we will first show results from a similar simulation as performed in the previous section, but now including the formation time for the initial minijets. The implementation of the formation time has already been outlined at the end of chapter 4: The produced partons are assumed to propagate freely without interactions within the time span $\Delta t_f = \cosh y \, \Delta\tau_f \approx \cosh y \cdot 1/p_T$. Secondly, in subsection 6.3.2 we present simulations including only elastic collisions with isotropic, instead of pQCD based, and large cross section. We compare the results with those already obtained employing physically motivated pQCD cross sections to demonstrate the importance of including the inelastic $gg \leftrightarrow ggg$ interactions. Furthermore, we discuss also for this case the differences between results from simulations with and without the formation time for the initial partons.

6.3.1 Simulation with pQCD motivated cross sections

In Fig.6.25 we compare the time evolutions of the gluon number density, the energy density and the temperature for the central region, extracted from the simulations with and without the formation time for the initial partons. The

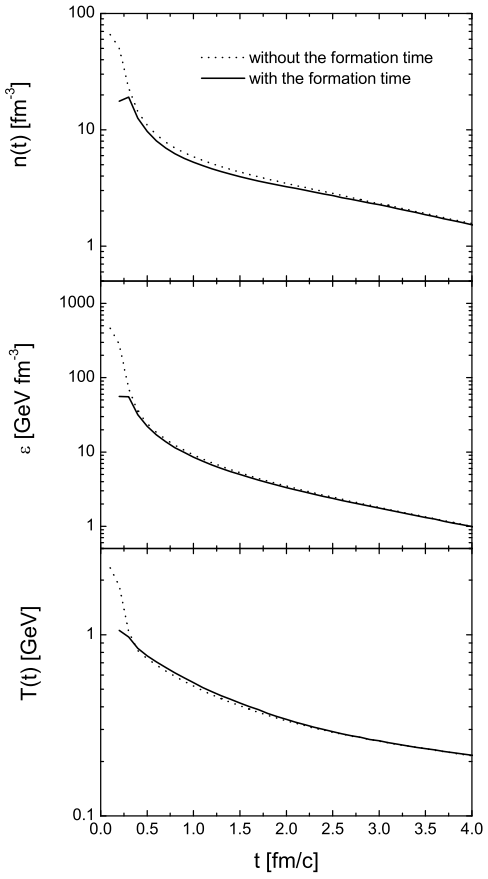

Figure 6.25: Time evolution of the gluon number density, the energy density and the temperature for the central region. The solid (dotted) lines depict the results extracted from the simulation with (without) the formation time.

latter have been already shown in Fig.6.5 and Fig.6.9 in the previous section. Remember that the central region is defined as a cylinder with $\eta \in [-0.5 : 0.5]$ and $x_T < 1.5$ fm. We have to note that the results depicted in Fig.6.25 denote the amounts for the on-shell gluons at respective time. The still off-shell propagating gluons are not taken into account. The comparisons show that the implementation of the formation time for the initial gluons strongly reduces the densities at early times: $n \sim 20$ fm^{-3} and $\epsilon \sim 50$ GeV fm^{-3} before 0.3 fm/c. After that time the results for the number and energy density with and without the formation time are nearly identical throughout the subsequent

evolution. It shows that even if the densities are very high at very early times with no formation time, interactions are not strong enough to fully stop the gluons with high momentum rapidity. These gluons rather stream freely within the first $0.3 - 0.4$ fm/c. When including the formation time for the initial minijets, the gluon number is highly undersaturated at early times. This, on the other hand, leads to a much smaller screening mass and thus larger cross sections. The results of the collision rates show finally that in the case with the formation time we actually obtain an enhanced collision rate for the elastic process and almost the same collision rates for $gg \leftrightarrow ggg$ processes, when compared to those from the simulation without the formation time. It is therefore clear that the inclusion of the formation time does not slow down kinetic and also chemical equilibration too much. We do not show the results for the p_T spectra, the momentum anisotropy and the gluon fugacity. They are almost identical as the results from the simulation without the formation time, except for some differences at the very early times. These, however, do not affect our findings for thermalization in the previous section.

6.3.2 Simulation with isotropic, large elastic cross section

In the previous section we have already seen that elastic collisions make smaller contribution to thermalization compared to inelastic collisions. In principle, kinetic equilibration can be achieved by elastic scatterings alone, if ad hoc the transport cross section is chosen sufficiently large. To demonstrate this we carry out simulations with *isotropic* $2 \leftrightarrow 2$ collisions and a large and constant total cross section of $\sigma_{22} = 30$ mb. The corresponding transport cross section is thus 20 mb. Such extreme conditions of an assumed large opacity in $2 \leftrightarrow 2$ reactions have been used in [MG 02] to study the possible buildup of elliptic flow. We set the test particle number to be $N_{test} = 240$ in the simulations. All results shown below are averaged over 30 independent realizations.

Fig.6.26 depicts the momentum rapidity distribution of the gluon number at different times from the simulations with isotropic elastic collisions and without (left panel) and with (right panel) the formation time. One can clearly see that in the simulation without the formation time gluons are strongly, but not fully, stopped during the time span of the overlapping of the two nuclei, when comparing the distribution at $t = 0.2$ fm/c with that for the primary minijets. This initial stopping slows down the sequent longitudinal expansion and the energy transport outwards. The latter can be recognized by comparing the distributions at the final time $t = 4.0$ fm/c, obtained from the two simulations: Without the formation time the plateau of the distribution possesses a larger value and a smaller width. The still plateau shape of the final distribution in the simulation without the formation time indicates that

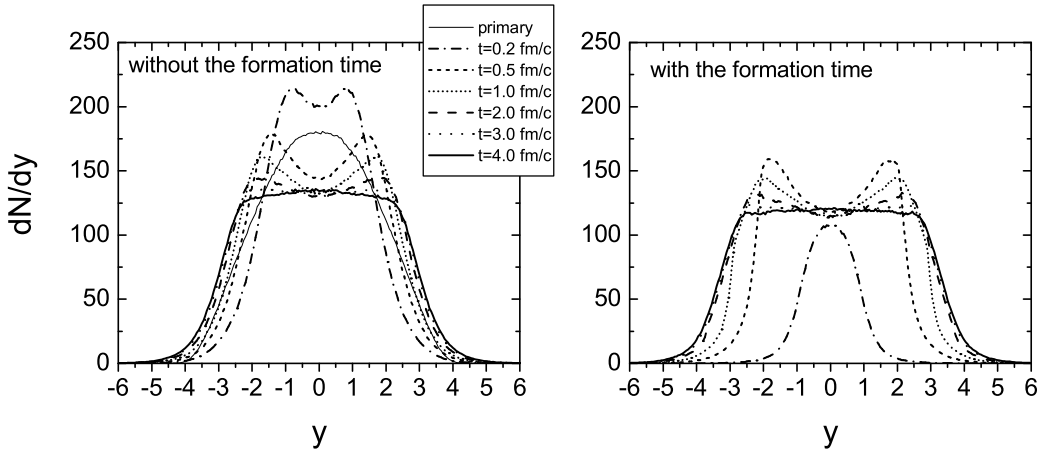

Figure 6.26: Gluon number distribution versus momentum rapidity at the time $t = 0.2$, 0.5, 1.0, 2.0, 3.0 and 4.0 fm/c. The thin solid curve in the left panel depicts the distribution of the primary produced gluons (minijets).

despite the stopping the early situation of the minijets resembles that for a Bjorken expansion. On the other hand, it shows that the 30 mb cross section is still not large enough to make a condition for a perfect Landau expansion.

However, the choice of the 30 mb should be sufficient for a complete kinetic equilibration. Fig.6.27 shows the p_T spectra in the central region at different times. Indeed we observe fast equilibration. The spectra at 0.5 fm/c in both cases are thermal. At the later times the distributions become more and more steeper, which indicates the cooling down of the system due to (quasi-)hydrodynamical expansion. Moreover, the spectrum, extracted from the simulation with no formation time, becomes exponential already at 0.2 fm/c, and the slopes of the distributions are always smaller than those obtained from the simulation with the formation time. These show that the initial stopping makes kinetic equilibration faster and leads to a larger deposit of energy in the local central region. The same can also be seen from the time evolution of the temperature in the central region, depicted in Fig.6.28. In the simulation with the formation time the exponent describing the cooling of the temperature, $\alpha(t)$, is nearly constant from 1 to 3 fm/c and meets exactly the value of the ideal Bjorken-type hydrodynamical expansion, 1/3. In the simulation with no formation time $\alpha(t)$ is slightly higher. The difference is due to the fact that earlier equilibration builds up earlier transverse flow. In Fig.6.29 we show the time evolution of the transverse velocities of the local rings, defined in the previous section (see Fig.6.17). Indeed the transverse flow in the simulation without the formation time is stronger during the expansion. Futhermore, the results depicted in Fig.6.29 are almost identical with those shown in Fig.6.17, obtained from the simulation with pQCD elastic and in-

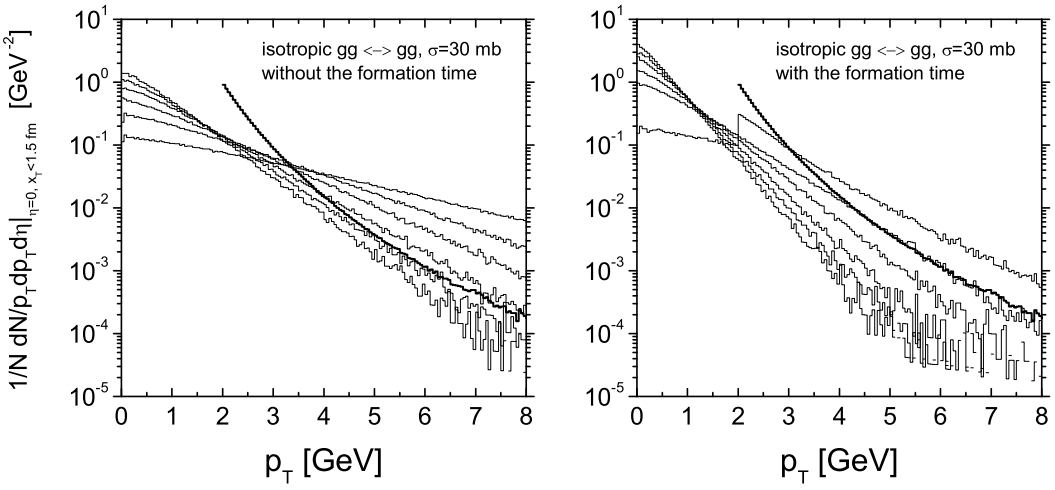

Figure 6.27: Transverse momentum spectrum in the central region extracted from the simulation with isotropic elastic scatterings and a large cross section of $\sigma = 30$ mb at different times ($t = 0.2$, 0.5, 1.0, 2.0, 3.0 and 4.0 fm/c from second upper to lowest histogram). The most-upper and boldfaced histogram with a lower cutoff at $p_T = 2$ GeV denotes the spectrum of the primary gluons (minijets). Left (right) panel: spectra from the simulation without (with) the formation time.

elastic interactions. This manifests that both pathes, pQCD or isotropic and large cross section, resemble (quasi-)hydrodynamical behaviour.

All the results shown above demonstrate that for the given extreme conditions the gluon system equilibrates indeed rapidly and then expands nearly hydrodynamically according to the ideal Bjorken scenario. However, of course, the constant and isotropic cross section can not be further motivated. In addition, following that particular evolution, the system would stay for a rather long time in a hot, but very dilute and undersaturated (in its gluon number) deconfined state (see Fig. 6.26). Contrary, in the more realistic situation with inelastic collisions included, the temperature drops much more dramatically (compare Fig.6.9 and Fig.6.28) and the system would stay only until $t \approx 4$ fm/c in a pure deconfined state, being then (nearly) fully saturated in the gluonic degrees of freedom, and will then hadronize.

6.4 Result III: with new setup

Now we turn to the second point in the discussions given at the end of section 6.2. There we pointed out that it turns out from the first simulations that the determination for an averaged screening mass over a large transverse region is

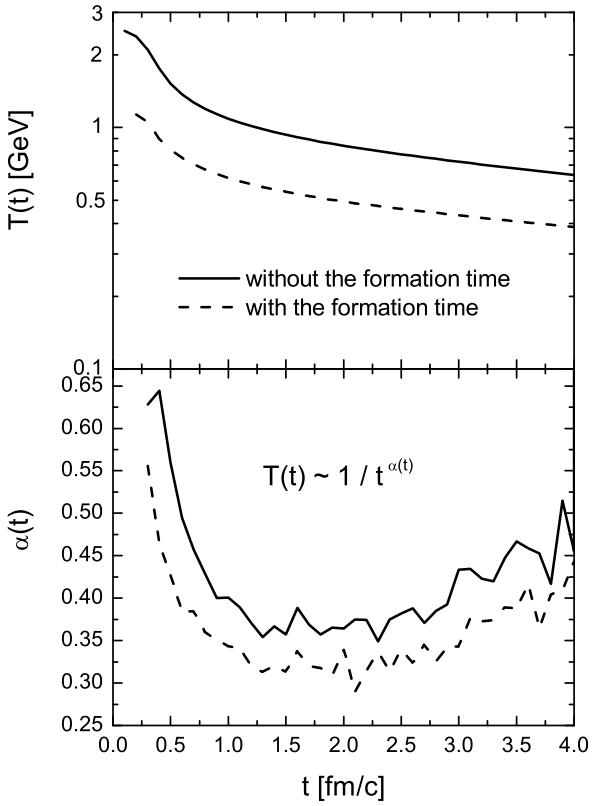

Figure 6.28: Time evolution of the effective temperature (upper panel) and the exponent describing the cooling of the system (lower panel) in the central region. The solid (dashed) curves depict the results obtained from the simulations without (with) the formation time.

a rather crude choice. One should, in principle, take the locality of the screening mass and the transverse flow into account. On the other hand, a change in screening mass would modify the cross sections and might thus influence the onset of thermalization. In the following we introduce improvements concerning local incorporation of the screening mass and the transverse flow and investigate again thermalization of gluons by performing new simulations.

To be specific we divide transverse plan in each Δz-bin into rings: from center to outer the first ring has a region of $0 < x_T < 1.5$ fm (x_T being the transverse radius), and the next rings have a width of 1 fm in transverse radius. For instance, the second ring possesses a region of 1.5 fm $< x_T <$ 2.5 fm. The rings are regarded as local region, where, as the first improvement, the screening mass will be evaluated, i.e., the volume V in (6.1) denotes now the volume of a ring and the sum runs over all test particles in the ring. We

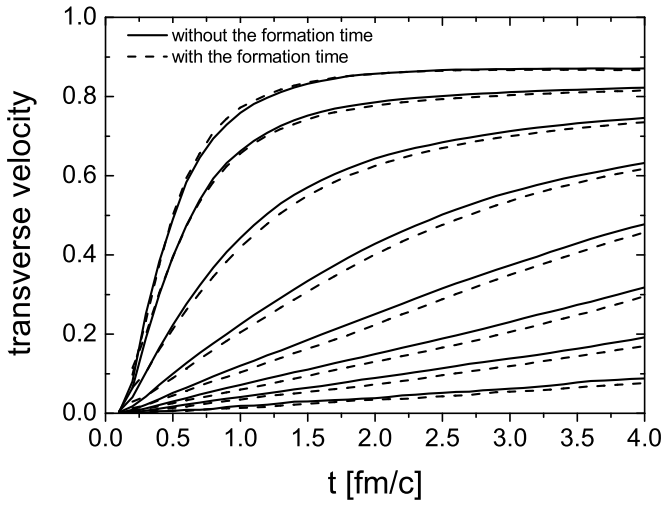

Figure 6.29: Time evolution of the transverse velocity within the central unit space-time rapidity. The lines are arranged as in Fig.6.17.

notice that such ring structure is based on the symmetry of central collisions and is not valid any more for non-central collisions. The choice for the width of rings depends on the locality on the one hand and on the required statistics on the other hand. Secondly, since local collision rates of all channels, which will be applied to model the LPM effect by $\Lambda_{LPM} = 1/R_{all\ channals}$ in $gg \leftrightarrow ggg$ processes, are until now evaluated in individual cells, large fluctuations in Λ_{LPM} arise in cells with small number of test particles. In order to reduce this fluctuation, we take the averaged value, $1/ < R_{all\ channals} >$, over all the cells within individual rings. Moreover, transverse velocities of rings, v_T, are taken into account for calculating $\Delta\tau = \Delta t\sqrt{1 - v_z^2 - v_T^2}$ in (6.3) and (6.4). In future investigations for non-central collisions, one has to find a clever way to calculate Λ_{LPM} locally without large numerical fluctuations.

With the new and more realistic setup we perform again simulations for parton evolution in central Au+Au collisions at RHIC energy. Formation time for the initial partons is included. Cell configuration is the same as for the first simulations. The number of test particles is still set to be $N_{test} = 60$. All results below are obtained by averaging over 30 independent realizations.

6.4.1 Screening mass

Fig.6.30 shows the local screening mass squared divided by the running coupling, averaged in the rings within the central unit space-time rapidity region

($\eta \in [-0.5 : 0.5]$) from the new simulation, versus the position of the rings. Different symbols denote the times at which the quantity is extracted. We see

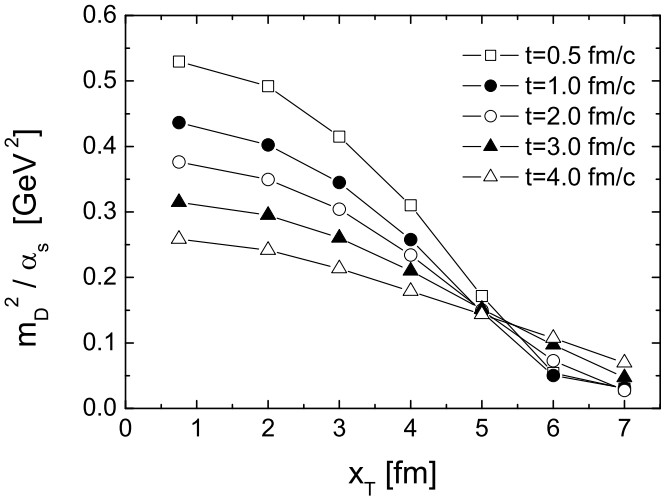

Figure 6.30: Averaged screenings mass squared over the running coupling versus the position of the transverse rings at different times. The quantity is extracted in the rings within the central unit space-time rapidity region ($\eta \in [-0.5 : 0.5]$).

that there is indeed a strong variation of the screening mass in the transverse direction. Averaging m_D^2/α_s in Fig.6.30 over the region of $0 < x_T < 6$ fm gives almost the same values as those evaluated in the first simulations, when compared with Fig.6.14. From Fig.6.30 we also recognize that the time behaviour of m_D^2/α_s is moderate from the central to the outer region. Remember that in kinetic equilibrium m_D^2/α_s is proportional to $\lambda_g T^2$ (see eq. (6.8)) with overall increasing fugacity λ_g and decreasing temperature T. Therefore, it seems that the amplification factor of the fugacity in the outer region is larger than that in the central region due to the initially different gluon occupations.

We compare the screening mass extracted from the simulation with the analytical one obtained for an assumed kinetically equilibrated gluon plasma, $\lambda_g m_{Deq}^2 = \lambda_g \alpha_s 24 T^2/\pi$ (see (6.8)), where T and λ_g are achieved in the corresponding rings and will be shown later. Such comparison has been made in Fig.6.14. Fig.6.31 depicts now the ratio of the screening mass squared to the analytical value. In the left panel we show the time evolution of the ratio obtained in the central region. We see that the ratio from the new simulation (solid curve) increases to a maximum of 1.16 at 1 fm/c and then decreases smoothly to 1.08 at the final time. The bending over at 1 fm/c implies the onset of the kinetic equilibration. The result from the first simulation (dashed

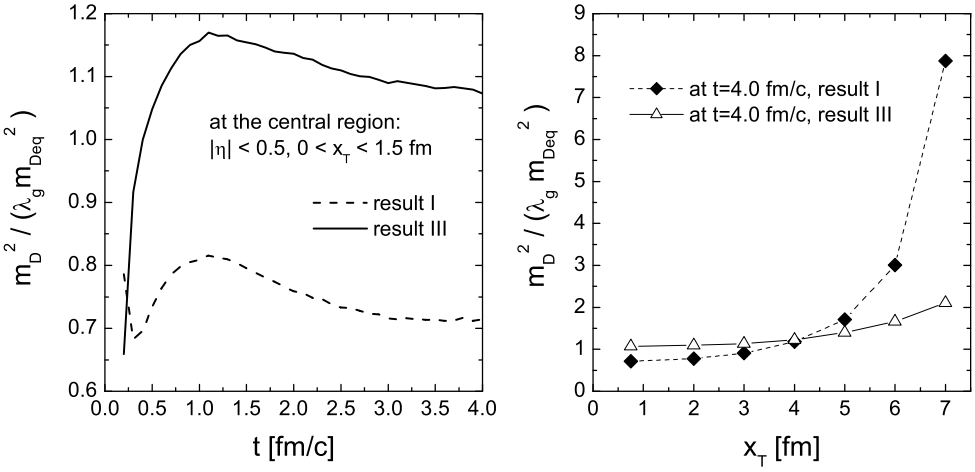

Figure 6.31: Left panel: time evolution of the ratio of the screening mass squared extracted in the central region from the simulations to the analytical value when assuming a kinetically equilibrated gluon plasma. The solid (dashed) curve shows the result from the new (first) simulation. In addition, the dashed curve corresponds Fig.6.14. Right panel: transverse profile of the ratio extracted within the central unit space-time rapidity interval at the final time 4 fm/c, compared with the result obtained from the first simulation.

curve) shows almost the same pattern as the new one, but with much smaller value than 1 due to the average over large transverse region. The transverse profiles of the ratio within the central unit space-time rapidity interval at the final time 4 fm/c are depicted in the right panel of Fig.6.31. For the result from the new simulation (open triangle) the increase in the transverse direction, from 1 at the central region to 2 at the outermost region, indicates the slowdown of the kinetic equilibration in the outer region. The power-law behaviour of the initial minijets gives rise to a larger final screening mass than the thermal value, if kinetic equilibrium is not fully achieved at the end. In contrast, the increase of the ratio from the first simulation (solid diamond) stems mainly from the average of the screening mass. It shows that the screening mass at the very outer region was much overestimated in the first simulation.

6.4.2 Thermalization

The more realistic calculation of the screening mass in local region gives rise to changes in collision rate, and hence may affect the findings about thermalization of gluons in the first simulation (see section 6.2) of central Au+Au

collision at RHIC energy.

Fig.6.32 shows the collision rates per particle, extracted in the transverse rings within the central unit space-time rapidity region, versus the position of the rings. Different symbols denote the results at different times during

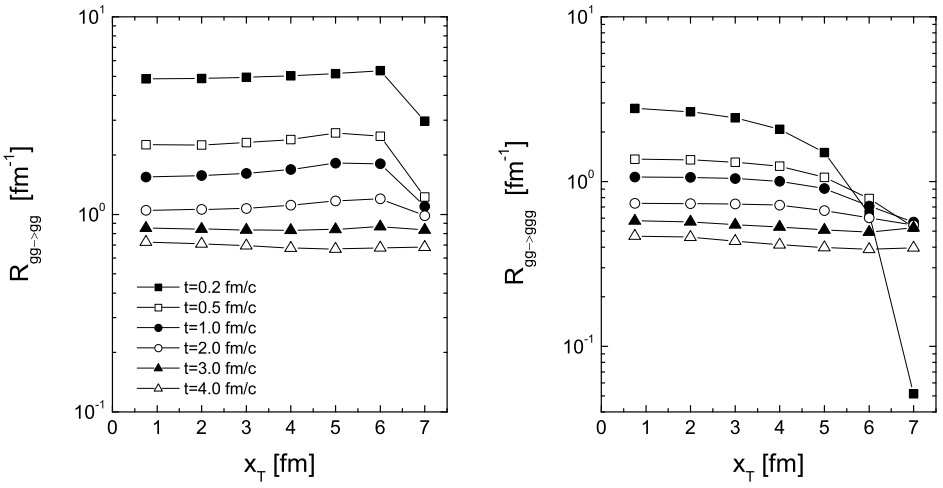

Figure 6.32: Collision rates per particle versus the position of the tranverse rings at different times. Left panel: collision rate for elastic scattering. Right panel: collision rate for inelastic $gg \to ggg$ interaction. The collision rates are extracted in the transverse rings within the central unit space-time rapidity region.

the expansion. Comparing the collision rates obtained in the new simulation (Fig.6.32) with those obatined in the first simulation (Fig.6.19), one recognizes first that R_{22} has a different profile. At every time stage, the collision rate R_{22} in the new simulation possesses almost the same value over large transverse region. In contrast, the profile of R_{22} in the first simulation decreases more strongly in the transverse direction. This difference stems from the different computation of the screening mass in both simulations: In the first simulation the screening mass is assumed to be constant transversely. Thus the transverse profile of R_{22} corresponds exactly to the profile of the gluon density. In the new simulation the screening mass is calculated locally also in the transverse region, which results in a decreasing transverse profile (see Fig.6.30). This then leads to an increasing profile of the averaged elastic cross section, which together with the decreasing gluon density gives the final profile shown in the left panel of Fig.6.32. Ideally, when the system is in kinetic equilibrium, R_{22} will be directly proportional to the temperature [BDMTW 93], which has a much moderater transverse profile than the gluon density ($n \sim T^3$). Second,

when comparing the absolute values of R_{22} in both simulations, we see that at every time stage the two curves, which connect the values of the collision rate in the rings and represent the transverse profiles in both simulations, cross each other. Especially, in the central region ($x_T < 1.5$ fm), R_{22} has a smaller value (a reduction of about 30%) in the new simulation than that in the first simulation due to a larger screening mass.

The influence on the inelastic collision rate R_{23} due to the change of the screening mass is complicated and not trivial, since there are two counteracting contributions to R_{23}. On the one hand, like R_{22}, a larger (smaller) screening mass decreases (increases) the cross section and thus R_{23} as well. On the other hand, reduced (enhanced) collision rate (R_{22} is the dominant term) corresponds to larger (smaller) mean free path of gluon and thus increases (decreases) the cross section and R_{23} due to the LPM effect. Comparing R_{23} obtained in both simulations (Fig.6.19 versus Fig.6.32), we see that R_{23} possesses a flatter transverse profile in the new simulation than that in the first simulation. The absolute values of R_{23} within the transverse extension of a Au nucleus are almost the same in both simulations in the initial expansion stage before 1 fm/c. Thereafter the collision rates, obtained in the new simulation, reduce $20 - 50\%$ at the late times, when compared with those in the first simulation. This will obviously slow down kinetic and chemical equilibration.

Fig.6.33 depicts the momentum anisotropy (left panel) and the gluon fugacity (right panel) versus the position of the transverse rings, where the quantities are obtained. Different symbols denote the different times, at which the results are extracted. Comparing the results in both simulations, Fig.6.20 versus Fig.6.33, we recognize only a slight slowdown of kinetic equilibration in the new simulation (compare for instance the results at 2 fm/c, open circles). We have also inspected, but not plotted here, the p_T spectra in the local rings. The same as shown in Fig.6.6 and Fig.6.21, in the central region the p_T spectrum becomes almost exponential at $1 - 2$ fm/c and its slope steepens further with progressing time, which indicates hydrodynamical behaviour of the expanding gluon system with decreasing temperature. In the outermost region ($x_T = 7$ fm), despite the decreasing momentum anisotropy, the final p_T spectrum possesses still a power-law form and implies that an onset of kineic equilibrium does not occur in the outermost region. We conclude that in spite of reduced collision rates of about 30% on average at late times, compared with those obtained in the first simulation, the onset of kinetic equilibrium within 5 fm in transverse plan slows down only slightly at $1 - 2$ fm/c. Furthermore, when comparing the gluon fugacities in Fig.6.20 and Fig.6.33 it turns out that chemical equilibration also slows down by about 15% in the new simulation.

Not only for $gg \to ggg$ process but also for the back reaction, their collision rates reduce in the new simulation. The net gluon production, however, is only slightly reduced within the central space-time rapidity region. This can

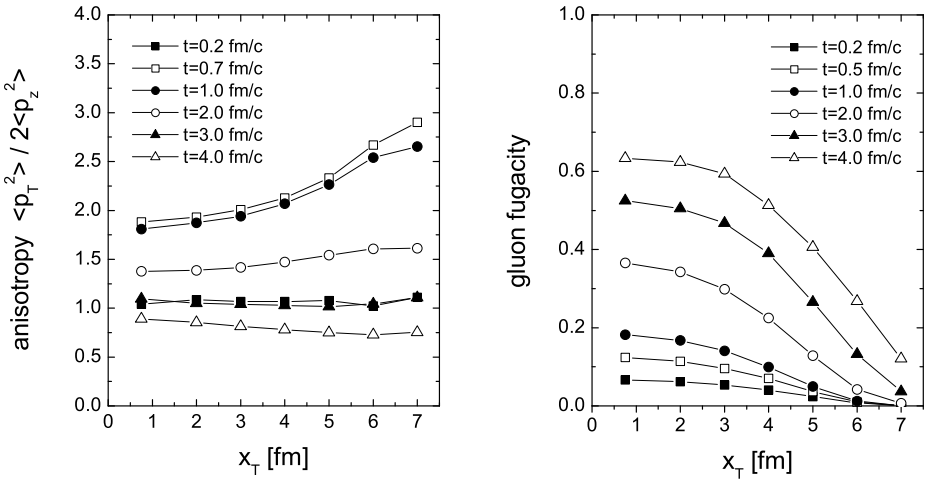

Figure 6.33: Momentum anisotropy and gluon fugacity versus position of the locally fixed rings at the times $t = 0.2$, 0.5 (0.7 in left panel), 1.0, 2.0, 3.0 and 4.0 fm/c.

be further realized by comparing the number density of gluons in the local rings, extracted in the first and new simulation (Fig.6.18 versus Fig.6.34, left panels). We see that especially in the central region, the number densities in both simulations are almost identical at late times, 2.32 fm^{-3} (first simulation) vs. 2.14 fm^{-3}(new simulation) at 3 fm/c and 1.54 fm^{-3} vs. 1.49 fm^{-3} at 4 fm/c. Corresponding the slower chemical equilibration in the new simulation, the effective temperature in the central region should be numerically larger than that obtained in the first simulation at late times. In addition, this is consistent with the fact that reduced collisions perform smaller amount of (longitudinal) work and thus slow down the cooling. The consideration is verified by comparison between Fig.6.22 and the right panel of Fig.6.34, 0.257 GeV vs. 0.268 GeV at 3 fm/c and 0.215 GeV vs. 0.223 GeV at 4 fm/c in the central region. We notice that the differences are too small to be read off from the figures. However, since the defined fugacity (see (5.17) and (5.18)) is proportional to n/T^3, therefore the small differences in number density and temperature result in a larger difference of about 15% in fugacity at the final time.

We summarize this section: A new setup of the parton cascade has been made for a more realistic calculation of the screening mass and also taking the transverse expansion into account. These changes in the setup result in reduction of the collision rates, especially in the central region, by $20 - 50\%$ at late times. Surprisingly, this has only slight influence on the onset of ki-

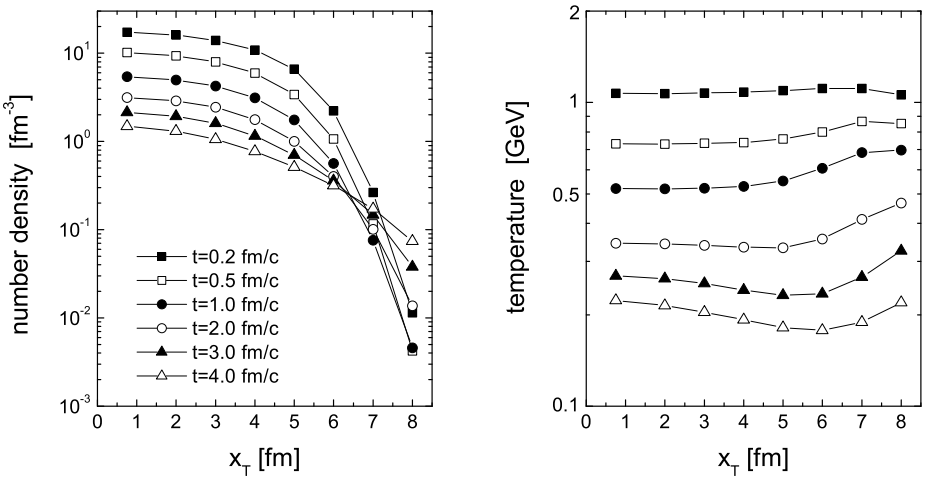

Figure 6.34: Left panel: number density of gluons in local transverse rings versus the position of the rings at time 0.2, 0.5, 1.0, 2.0, 3.0 and 4.0 fm/c. Right panel: effective temperature in local rings versus the position of the rings at different times.

netic equilibrium, compared with the results in the first simulation. Chemical equilibration slows down by 15%. In addition, the transverse expansion of gluons in the central space-time rapidity region, observed (not shown) in the new simulation, is very similar as that in the first simulation.

From now we regard this new setup including formation time of initial minijets as the default setup for the parton cascade.

6.5 Result IV: variation of the p_T cutoff for minijets

The findings for thermalization of gluons in heavy ion collisions, presented in the previous sections for Au+Au collisions at RHIC energy, depend crucially on the chosen initial conditions of partons. Intuitively, a denser system of gluons may achieve faster thermalization than a dilute system. In addition, hadron number and total energy after freezeout also depend on the initial values of partons. Obtained from the simulation in section 6.4, the gluon number and the total transverse energy within $|y| < 0.5$ are, respectively, $dN_g/dy|_{y=0} = 352$ and $dE_T/dy|_{y=0} = 272$ GeV at the final time 4 fm/c. If the number of final state hadrons is simply assumed to be equal to that of gluons before hadroniza-

tion ('parton-hadron-duality'), i.e. at 4 fm/c, then the charged-particle multiplicity will be $dN_{ch}/dy|_{y=0} \approx 2/3 * dN_g/dy|_{y=0} = 235$. In contrast, the experiments at RHIC at $\sqrt{s} = 200$ GeV obtained $dN_{ch}/dy|_{y=0} = 625 \pm 55$ [BRAHMS 02] and $dE_T/dy|_{y=0} = 620 \pm 33$ GeV [STAR] for the 5% most central events. The differences are factors of more than two. Remember that in the performed simulations the initial conditions are considered as multiple minijets with transverse momentum larger than some cutoff p_0 which is assumed to be 2 GeV until now. This has been a rather conservative assumption for the initial minijets. 'Soft' partons with $p_T < p_0$, which are produced by the non-perturbative part of nucleus-nucleus interaction and also contribute the entropy production, are completely neglected. These soft partons may stem from the color glass condensate (CGC) [MV 94] and can also be included in the transport simulation [BV 01], when they are freed from the color field. In next section we will perform simulation with initial gluons from CGC. In principle, one should combine the soft gluons from CGC and hard gluons from minijets production to give a more realistic initial condition for partons after a heavy ion collision. The final results after parton evolution with such initial condition is thus appropriate for comparisons with the experimental data. We leave this interesting topic for the future investigations. For the moment, p_0 is a phenomenological parameter. The number and the transverse energy of minijets increase when p_0 decreases.

In another idea within a saturation picture of quarks and gluons in phase space, presented by Eskola et al. [EKRT 00], the authors assumed that performing the computation at a saturation momentum, $p_0 = p_{sat}$, gives an estimate of the effect from all momentum scales, both above and below p_{sat}. At RHIC energy they got $p_{sat} = 1.13$ GeV and $dN_g/dy|_{y=0} = 1373$ for corresponding initial minijets, and estimated the final charged particle multiplicity $dN_{ch}/dy|_{y=0} \approx 870$ and $dE_T/dy|_{y=0} \approx 660$ GeV by assuming *immediate* thermalization and adiabatic expansion. Compared with the experimental data, the calculations met the value of the transverse energy, but overestimated the final particle multiplicity by 30%. One also notices that the number of initial gluons for $|y| < 0.5$ at p_{sat} is $6 - 7$ times larger than that at $p_0 = 2$ GeV. Immediate thermalization might be a naive assumption, particularly for chemical equilibration. However, the onset of thermalization depends essentailly on the collision rate which is the multiplication of the number density and cross section. The latter decreases for increasing number density due to the incerasing screening mass. Therefore, one needs explicit verification for the quick thermalization at small p_0. This strongly motivates us to apply the developed parton cascade to inspect the timescale of thermalization and final freezeout values of N_{ch} and E_T in dependence on the parameter p_0. In the following we present results from simulations with different value of p_0 employing the default setup. All results are obtained by averaging 30 independent realizations.

In Fig.6.35 we depict the gluon numbers of the primary produced minijets within $|y| < 0.5$ by solid diamonds for $p_0 = 2.0$, 1.5, 1.4 and 1.3 GeV. One

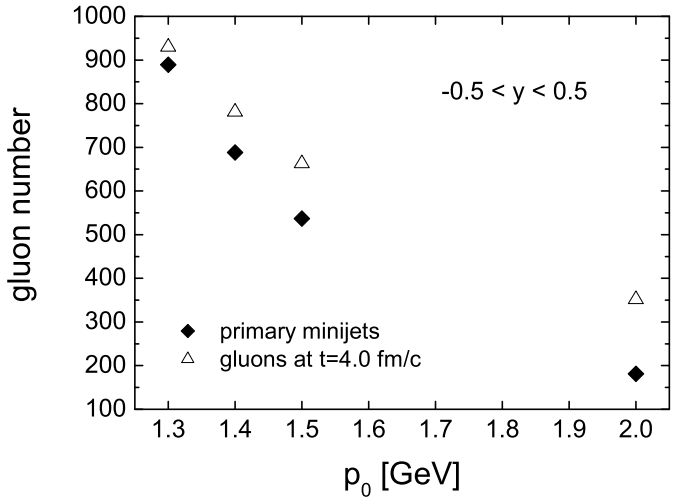

Figure 6.35: Particle number within $|y| < 0.5$ of initial minijets (solid diamonds) and of gluons at time 4 fm/c (open triangles) in simulations using different p_0, the cutoff for minijets production.

sees that the number increases for decreasing p_0. The computation is slightly different than that performed by Eskola et al. in [EKRT 00], since we use different parton distribution function and do not include any nuclear effects (see chapter 4). However, such uncertainty will not affect the final results very much. In Fig.6.35 we also show the gluon numbers at the final time 4 fm/c (open triangles) after the parton expansion simulated by the cascade. The particle enhancement indicates that even at $p_0 = 1.3$ GeV the gluons are still undersaturated. However, the enhancement is weaker for smaller p_0, which implies larger initial fugacity at smaller p_0. Using the simple convertation from gluons to hardons, $N_{ch} = 2/3 * N_g$, we achieve $dN_{ch}/dy|_{y=0} \approx 620$ at $p_0 = 1.3$ GeV. This value meets the RHIC data. We will come back to this point when discussing the final transverse energy. A technical thing remains. Due to the larger initial number of gluons at smaller p_0 we vary the number of test particles in the simulations respectively: $N_{test} = 40$ for $p_0 = 1.5$ GeV, $N_{test} = 35$ for $p_0 = 1.4$ GeV and $N_{test} = 30$ for $p_0 = 1.3$ GeV,

We now investigate the dependence of the onset of thermalization on the scale p_0. As mentioned before, the collision rate is essential for kinetic and also chemical equilibration. In Fig.6.36 we show the collision rates per particle of elastic and inelastic scatterings in dependence on p_0. The collision rates are extracted in the central region, $|\eta| < 0.5$ and $x_T < 1.5$ fm, at different times. We

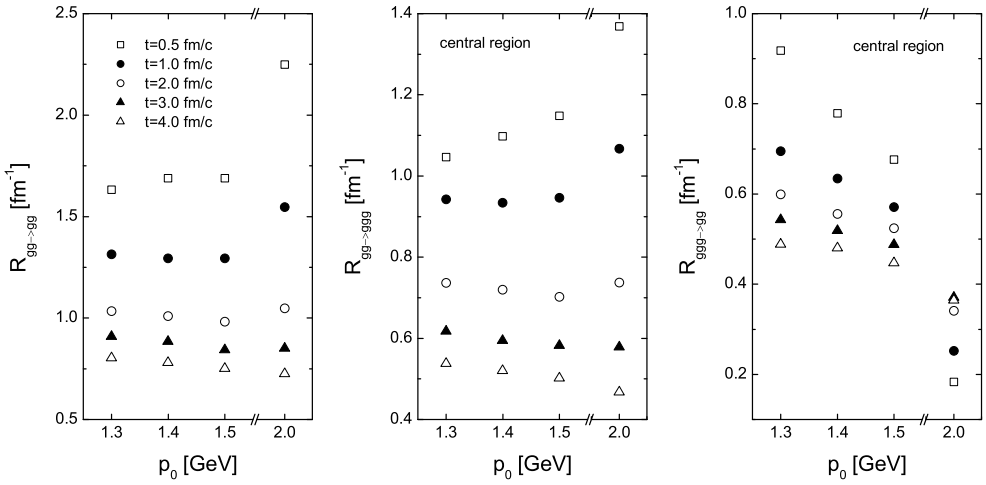

Figure 6.36: Collision rates in the central region at the time $t = 0.5$, 1.0, 2.0, 3.0 and 4.0 fm/c from the simulations with different p_0.

see that at every time stage, except $t = 0.5$ fm/c, $R_{gg\to gg}$ are almost the same at different p_0. It is not surprising, since at kinetic equilibrium $R_{gg\to gg}$ is proportional to temperature and has very weak dependence on the gluon fugacity, as discussed in section 6.4 to explain the almost constant behaviour of $R_{gg\to gg}$ within large transverse region. Especially at the late times one recognizes that $R_{gg\to gg}$ decreases with increasing p_0, which indicates its dependence on temperature, since the gluon system produced with smaller p_0 is denser and thus hotter. At $t = 0.5$ fm/c, especially for $p_0 = 2$ GeV, the initial smaller screening mass (due to the small fugacity) leads to quite large $R_{gg\to gg}$. In contrast to $R_{gg\to gg}$, the dependence of $R_{gg\to ggg}$ on p_0 is not trival due to the complex of the screening and LPM effect. However, as observed in Fig.6.36, $R_{gg\to ggg}$ possesses almost the same behaviour as $R_{gg\to gg}$, except for the absolute values. For $ggg \to gg$ process the collision rate is much larger at smaller p_0, especially at initial stage of the expansion. This is due to the larger initial gluon density (or fugacity) at smaller p_0 according to $R_{ggg\to gg} \approx \lambda_g R_{gg\to ggg}$. The total inelastic collision rate, which dominates the kinetic equilibration, increases for decreasing p_0. Therefore, faster kinetic equilibration will be achived at smaller p_0. However, the difference in the total inelastic collision rate at every time is maximal 20%. We thus do not expect superior fast kinetic equilibration at the smallest p_0. Furthermore, comparing the absolute values of $R_{gg\to ggg}$ and $R_{ggg\to gg}$ in Fig.6.36, one recognizes faster onset of chemical equilibration at smaller p_0.

To find out the timescales of the onset of thermalization in the central

region, we depict in Fig.6.37 the time evolutions of the momentum anisotropy extracted from the simulations employing different p_0s. We clearly see faster

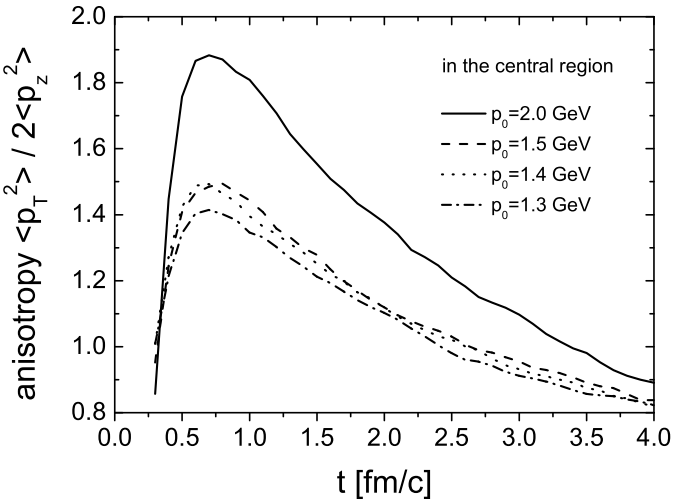

Figure 6.37: Time evolution of the momentum anisotropy in the central region in the simulations employing $p_0 = 2.0$, 1.5, 1.4 and 1.3 GeV.

kinetic equilibration at smaller p_0. Quantitatively, the system achieves fully kinetic equilibrium (when the momentum anisotropy becomes 1) at $t = 3.3$ fm/c for $p_0 = 2.0$ GeV and at $t \approx 2.4$ fm/c for $p_0 = 1.5 - 1.3$ GeV. As realized from the first simulation in section 6.2, gluons with smaller energy equilibrate faster than gluons with larger energy. Therefore, the timescales given denote the averaged values. Moreover, further uncertainty also arises, for instance, from the definition of the particular geometry for the central region. When comparing the timescales of the onset of fully kinetic equilibrium at $p_0 = 2.0$ GeV and $p_0 = 1.3$ GeV, one recognizes a difference of $30 - 40\%$, which is larger than the difference of 20% in the collision rate. This shows that including more soft minijets, between 1.3 GeV $< p_T <$ 2.0 GeV, leads to more efficient equilibration. The difference of kinetic equilibration in the simulations using $p_0 = 2.0$ GeV and $p_0 = 1.3$ GeV, which is shown in the momentum anisotropy, should also be found consistently in p_T spectra at the central region. These are depicted in Fig.6.38 at different times. When comparing especially the specta at $t = 2.0$ fm/c (the boldfaced histogram) from both simulations, one can recognize (with a ruler for instance) that for $p_0 = 2.0$ GeV the slope of the spectrum varies significantly within $p_T < 3$ GeV, while for $p_0 = 1.3$ GeV the spectrum is almost a straight line. This implies that in the simulation employing $p_0 = 1.3$ GeV the gluons in the central region become fully equilibrated at 2.0 fm/c, whereas at the same time the equilibration is

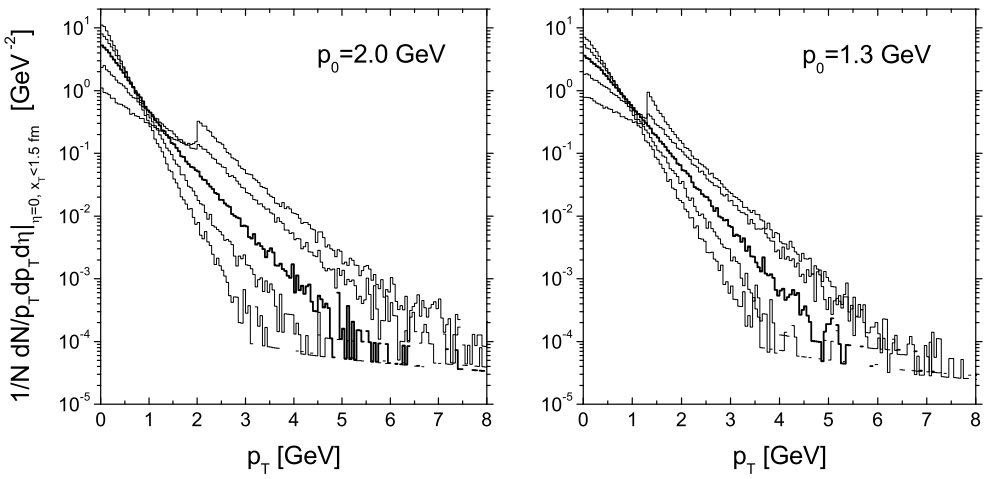

Figure 6.38: p_T spectrum in the central region at the time t = 0.5, 1.0, 2.0, 3.0 and 4.0 fm/c (from most-upper to lowest histogram). The distributions are extracted from the default simulations using $p_0 = 2.0$ GeV (left panel) and $p_0 = 1.3$ GeV (right panel).

still going on in the simulation using $p_0 = 2.0$ GeV. The finding is consistent with the results on momentum anisotropy (see Fig.6.37).

In order to demonstrate the dependence of chemical equilibration on the scale p_0, we show the time evolutions of the gluon fugacity in the central region in the left panel of Fig.6.39. We see faster chemical equilibration in the simulation with smaller p_0. This is mainly due to the larger initial value of fugacity at smaller p_0. For instance, it is larger than 1 at $p_0 = 1.3$ GeV. However, instead of a smooth equilibration, we notice first that for smaller p_0 the gluon fugacity decreases strongly at the initial stage of expansion, even for the case that the initial fugacity is smaller than 1, and then increases smoothly to the final value. To explain the early decrease we assume a Bjorken expansion of an initially thermal system. We have then $n \sim \lambda_g T^3$ with $\lambda_g(t_0) = 1$. It is obvious that the decrease of the number density starts with $n \sim 1/t$. In contrast, the temperature has a slower decrease in a viscous expansion, when compared with the ideal hydrodynamics, in which T decreases as $t^{-1/3}$. Therefore, even in this assumed ideal case the fugacity decreases at the beginning of the expansion. How strong the decrease will be, depends on viscosity or collision rate. For instance, there is only a slight decrease in the $1+1$ dimensional (tube) calculation performed for a Bjorken initial condition in section 3.3.3 of chapter 3 (see Fig.3.17), since there the initial collision rate is about 60 times larger than those in the present cases (compare the upper panel of Fig.3.16

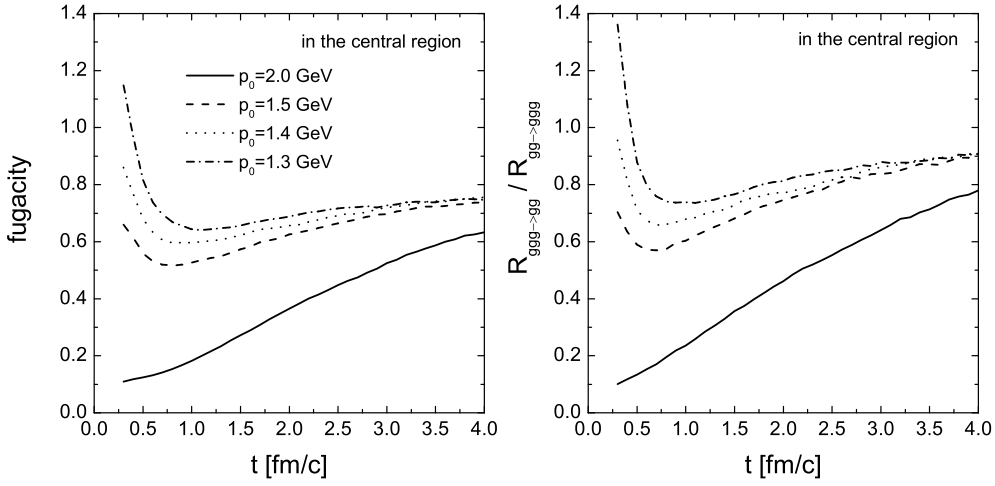

Figure 6.39: Left panel: time evolution of the gluon fugacity. Right panel: time evolution of the ratio of the annihilation and production rate, $R_{ggg\to gg}/R_{gg\to ggg}$. Results are obtained in the central region from default simulations employing the different cutoffs p_0.

with Fig.6.36). The following particle production will then slow down the decrease of the number density and on the other hand make a faster decrease of the temperature, which will lead to a smooth increase of λ_g to 1. Therefore, the behaviours of the fugacity for $p_0 = 1.5$, 1.4 and 1.3 GeV, shown in left panel of Fig.6.39, arise from the viscous expansion of gluons. Secondly, we see that at small p_0 the fugacity converges at the final time to a value of 0.75, but not 1. This is due to the particular geometrical choice of the central region ($\eta \in [-0.5 : 0.5]$ and $x_T < 1.5$ fm). The extension in space-time rapidity makes the central region not exactly local. The same effect has been taken into account for analysing the results from the simulation for a longitudinal expansion with a boost-invariant and thermal initial condition in chapter 3. There we have corrected the fugacity by a multiplication of a factor of $a_T^3/a_n = 1.18$ (see eq.(3.19) and the definition of the factors in eq.(3.13)-eq.(3.15)). Multiplying the fugacity shown in the left panel of Fig.6.39 by this factor (although the expansion is not exactly the Bjorken-type), the convergent value at small p_0 is corrected to be 0.9. This is identical with the final value of the ratio of the annihilation and production rate, $R_{ggg\to gg}/R_{gg\to ggg}$, which is depicted in the right panel of Fig.6.39. We note that $R_{ggg\to gg} = \lambda_g R_{gg\to ggg}$ is valid at kinetic equilibrium and contrary to the extracted fugacity, $R_{ggg\to gg}/R_{gg\to ggg}$ is insensitive to the geometry of the local region. As a conclusion, for small p_0 the system is near chemical equilibrium during the whole expansion, although

there is still 10% deficiency to reach fully chemical equilibrium at the final time 4 fm/c. The deficiency may stem from technical simplification for implementing $ggg \to gg$ collisions. Remember (see subsection 6.2.1) that for sampling $ggg \to gg$ collisions we choose randomly n instead of correct $n^3/6$ triplets (n being the number of test particles in an individual cell), in order to reduce the computing time. To give a quantitative prediction for this uncertainty, further detailed analysis should be done.

Fig.6.40 shows the time evolution of number density and effective temperature ($T = \epsilon/3n$) of gluons, extracted in the central region. One recognizes

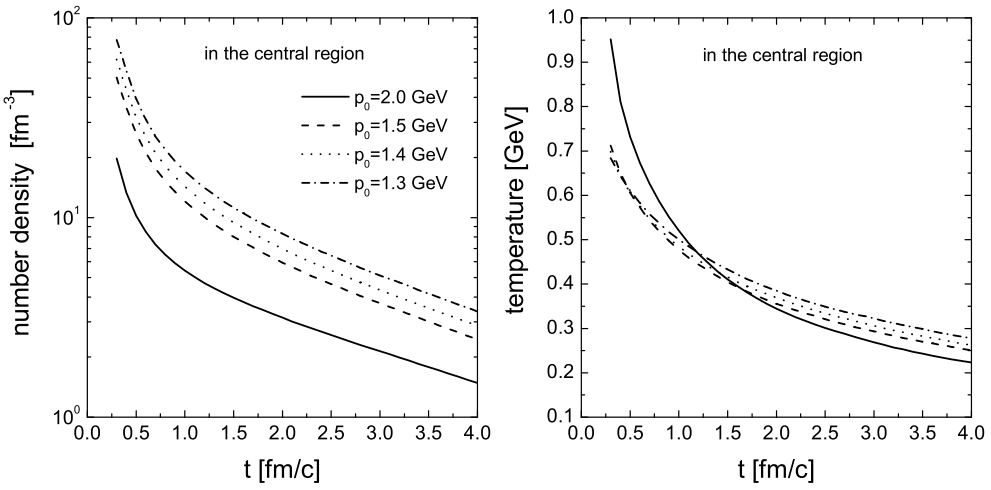

Figure 6.40: Time evolution of number density (left panel) and effective temperature (right panel) of gluons, extracted in the central region from simulations employing different cutoffs p_0.

that the number density of gluons in the central region is larger for smaller p_0. Comparing the temperatures from the simulations with the different p_0s, we see first that the decrease of the temperature slows down with decreasing p_0. This is due to the weaker net production of gluons in the simulation with smaller p_0, since there the gluon fugacity is always large during the expansion (see left panel of Fig.6.39). The exponent describing the decrease of the temperature in time, $T \sim t^{-\alpha}$, is initially small for small p_0s, $\alpha \approx 0.25$ at $t = 0.3$ fm/c, and increases most linearly in time to 0.5 at $t = 4$ fm/c. The value of the exponent α is around 1/3 in the time span of $1 - 2.5$ fm/c, which indicates that when the gluon system becomes thermalized, it evolves according to a one dimensional, nearly ideal hydrodynamical expansion. The further increase of α at the late times is due to the onset of the transverse flow. Secondly, while the effective temperature (or energy per particle) of the initial minijets

is smaller for smaller p_0, it becomes large at the late stage of the parton evolution when the system is at equilibrium. This verifies the basic law of the thermodynamics: Denser system has higher temperature according to $n \sim T^3$. At the final time $t = 4$ fm/c, we obtain $n = 3.38(1.48)$ fm^{-3} and $T = 278(223)$ MeV for $p_0 = 1.3(2.0)$ GeV respectively, which demonstrates that a larger life time of the gluon plasma will be achieved in the simulation with smaller p_0.

Since the number of minijets increases for decreasing p_0, the initial transverse energy increases too, as shown for the central unit rapidity in the left panel of Fig.6.41 by the solid diamonds. The open triangles denote the final

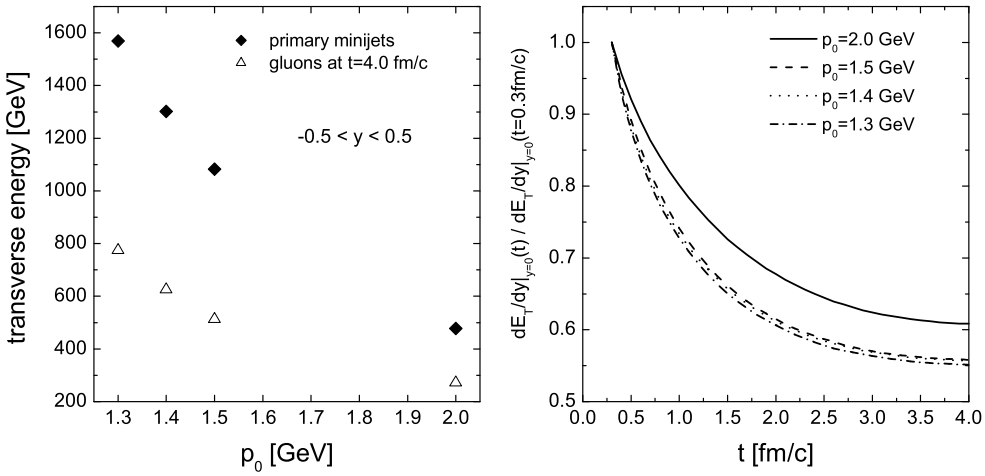

Figure 6.41: Transverse energy within $|y| < 0.5$ of initial minijets (solid diamonds) and of gluons at time 4 fm/c (open triangles) in simulations using different cutoffs p_0.

transverse energies at the time 4 fm/c. The decrease of the transverse energy is due to the longitudinal work done by the pressure. We see, especially from the right panel of Fig.6.41 depicting the normalized transverse energies, that the decrease is stronger in the simulation using smaller p_0, which shows that more longitudinal work is done at smaller p_0. This is consistent with the results that the total collision rate is always larger at smaller p_0, which is previously shown in Fig.6.36 for the central region. Note that the finding about the total collision rate is also true (not plotted in figure) for the other transverse regions. The strong decrease of the transverse energy occurs at the beginning of the expansion. At the late stage when the collision rate becomes small, the decrease of E_T slows down. In addition, the transverse flow which is built up earlier in denser system may increase the transverse energy [KHHET 01]. Therefore, the results are consistent with the expectation of more and more

slowly decreasing transverse energy. However, it is surprising that the $E_T(t)$ obtained in the simulations with different p_0 go to constant almost at the same time.

Inspecting the absolute values of E_T at the final time in the left panel of Fig.6.41, we see that the value at $p_0 = 1.4$ GeV meets the experimental data. At the same p_0 the roughly estimated final number of charged hadrons (see Fig.6.35) is $dN_{ch}/dy|_{y=0} \approx 2/3 * dN_g/dy|_{y=0} = 521$ with a deficiency of 16% to the experimental data. However, one should notice that at $t = 4$ fm/c there is still 10% deficiency to the full chemical equilibrium (see the right panel of Fig.6.39). Therefore, the particle production may continue in the partonic or the hadronic phase. Moreover, the inclusion of quarks will also increase the final particle multiplicities. The latter will be investigated in the future.

We summarize the findings obtained in this section. We have performed simulations for parton evolution at RHIC using different p_0, the p_T-cuttoff for minijets production. Due to the increase of the number of initial minijets at decreasing p_0 the gluon system becomes denser at smaller p_0. On the other hand, in the denser system the screening mass becomes larger so that the cross sections of $gg \to gg$ and $gg \to ggg$ interactions become smaller. In total, the collision rates $R_{gg\to gg}$ and $R_{gg\to ggg}$ are insensitive to p_0. However, the total collision rate is larger at smaller p_0 due to more $ggg \to gg$ collisions in denser system. This leads to rapider kinetic equilibration, $1 - 2$ fm/c at $p_0 = 1.3 - 1.5$ GeV, while at those p_0s the full chemical equilibration is almost achieved after the minijets production. We have also found that the decrease of the transverse energy per unit rapidity is much stronger at smaller p_0, which indicates stronger hydrodynamical expansion. If one compares roughly the final multiplicity and the final transverse energy per unit rapidity with the experimental data, one finds that minijets production with $p_0 = 1.4$ GeV gives an appropriate initial condition at RHIC.

6.6 Result V: Color Glass Condensate as initial conditions

As realized from the previous sections, the forming and the lifetime of a (quark) gluon plasma depend strongly on the initial conditions of partons produced immediately after a nucleus-nucleus collision. Until now we have assumed that minijets production are the initial conditions which are computable by the theory of pQCD. A more recent, prominent suggestion of the initial condition is the so-called 'color glass condensate'(CGC) [MV 94], which represents a non-perturbative solution of the Yang-Mills equation and is described by a bulk scale Q_s, the momentum scale at which gluon distributions saturate. In this section we study thermalization of gluons which initially come from a color

glass condensate. For the initial gluon distribution we employ an idealized form given by Mueller [M 00]. Analysis using the recently achieved initial distributions [HN 04] will be presented in the future studies. We have to mention that using the initial condition from [M 00] Bjoraker and Venugopalan [BV 01] have investigated kinetic equilibration of gluons in the subsequent evolution by means of a non-linear Landau equation. They considered only $2 \to 2$ small angle scattering processes and found out that full kinetic equilibrium was not achieved until 10 fm/c. The convergence to isotropic momentum distributions was very slow. Taking these results as guideline, we will see whether the inclusion of $2 \leftrightarrow 3$ processes leads to a much rapider thermalization.

In [BV 01] the initial single particle distribution $f(x,p)$ is given by

$$f(x,p) = \frac{c}{\alpha_s N_c} \frac{1}{\tau_f} \delta(p_z) \Theta(Q_s^2 - p_T^2) \,, \tag{6.10}$$

where $N_c = 3$ for SU(3) and $c = 1.3$ is a parameter. For RHIC one assumes Q_s to be 1 GeV and the corresponding formation time, at which gluons become on-shell, to be $\tau_f = 0.4$ fm/c $\sim 1/Q_s$. We see that the initial condition is boost-invariant, but highly anisotropic, with the produced partons having zero longitudinal momentum p_z. This is certainly an idealization based on the CGC model of infinite thin nuclei. Integrating (6.10) gives (see also [BV 01]) the initial number density

$$\frac{1}{\pi R^2} \frac{dN_g}{d\eta}(\tau_f) = c \frac{N_c^2 - 1}{4\pi^2 \alpha_s N_c} Q_s^2 \,. \tag{6.11}$$

R denotes here the transverse radius and is set to be 6 fm. With $\alpha_s = 0.3$ we obtain $dN_g/d\eta(\tau_f) = 830$ for the initial gluons. The following evolution of gluons is described by the default parton cascade employing $N_{test} = 50$. All results presented below are averaged over 10 independent realizations.

In Fig.6.42 we depict the gluon number distribution of space-time rapidity (left panel) and of momentum rapidity (right panel) at different times. While the distributions $dN/d\eta$ and dN/dy are quite different in the simulations applying the minijets as the initial conditions (compare Fig.6.2 and Fig.6.3), we see that the two distributions in Fig.6.42 have similar shape at the same times. This is due to the different initial correlations between η and y. In the present case (6.10) it is $\eta = y$. Since particles are formed in the lab-frame at $t_0 = \tau_f \cosh(\eta = y)$, the distributions $dN/d\eta$ and dN/dy have the same widths at the same times. On the other hand, diffusion of particles towards higher momentum rapidity is also clearly seen in the right panel of Fig.6.42. Moreover, we observe the decrease of the gluon number overall in the rapidity region. In the regions of smaller $|\eta|$ or $|y|$, where gluons are formed earlier, the decrease is stronger. However, the decrease slows down and ceases at sometime during the expansion. All these indicate an initially oversaturated

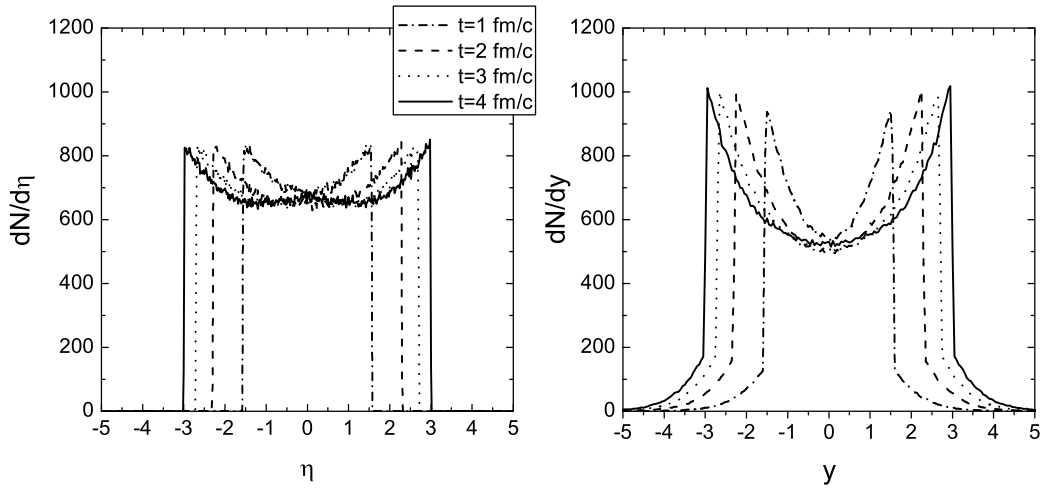

Figure 6.42: Gluon number distribution of space-time rapidity (left panel) and of momentum rapidity (right panel) at time $t = 1$, 2, 3 and 4 fm/c.

system, which is going to chemical equilibrium by annihilating particles in the subsequent evolution. To give a verification, we calculate the initial gluon fugacity. Convolving energy E to the particle distribution (6.10) and integral over the momentum space give the initial energy density

$$\frac{1}{\pi R^2}\frac{dE_g}{d\eta}(\tau_f) = c\,\frac{N_c^2-1}{4\pi^2\alpha_s N_c}\,\frac{2}{3}\,Q_s^3\,. \tag{6.12}$$

Thus the initial effective temperature is $T(\tau_f) = \epsilon/3n = 2/9 * Q_s$. We obtain then

$$\lambda_g(\tau_f) = \frac{n}{n_{eq}} = \frac{\frac{dN}{\pi R^2\tau_f d\eta}}{2(N_c^2-1)\frac{T^3}{\pi^2}} = \frac{9^3}{4^3}\,\frac{c}{\alpha_s N_c \tau_f Q_s}\,. \tag{6.13}$$

For RHIC $\lambda_g(\tau_f) = 8$. So the initial gluons are indeed 'oversatuated' in this thermodynamical interpretation.

We now concentrate on the central region: $|\eta| < 0.5$ and $x_T < 1.5$ fm. Fig.6.43 shows the time evolution of the number and energy density of gluons by the solid lines, compared with the results from ideal hydrodynamics (dotted lines) and from the free streaming (dashed line). Note that for the given initial conditions the time evolutions of the number density from ideal hydrodynamics and from the free streaming are exactly the same, $\sim t^{-1}$, while it is different for the energy density, i.e. $\sim t^{-4/3}$ in the hydrodynamical limit versus $\sim t^{-1}$ for the free streaming. We see that the decrease of the number density in the simulation employing the CGC initial condition is stronger, especially

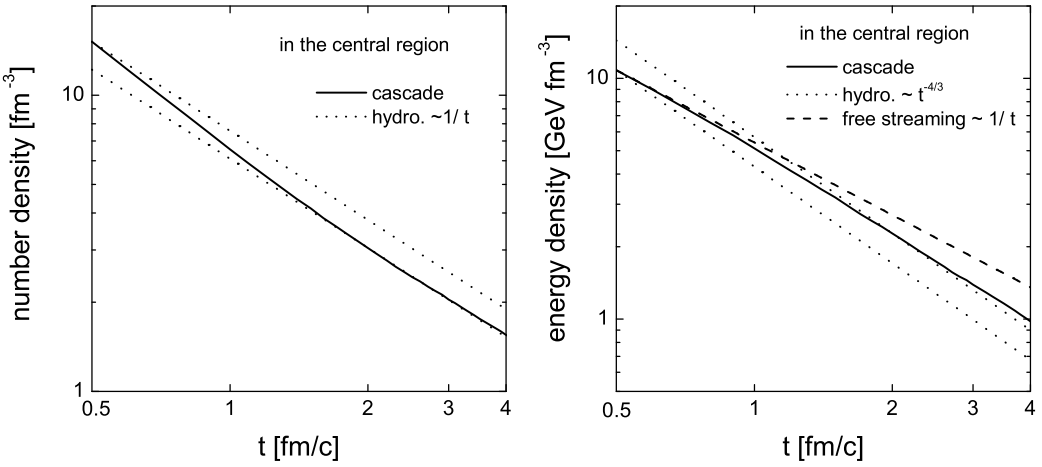

Figure 6.43: Time evolution of number density (left panel) and energy density (right panel) in the central region. The dotted and dashed lines depict, respectively, the results from ideal hydrodynamics with fixed intercepts at 0.5 and 2.0 fm/c and from the free streaming.

at the early times, than that from ideal hydrodynamics due to the particle annihilations mentioned before. From 2 fm/c the line agrees well with the ideal hydrodynamical limit, which implies the onset of full chemical equilibrium around 2 fm/c in the central region. Inspecting the energy density, we also see the agreement between the results from the cascade simulation and the ideal hydrodynamics from 2 fm/c. These are strong indications for a near ideal hydrodynamical behaviour in the following expansion. We also recognize that at the very beginning of the evolution the energy density decreases slowly. It seems that the viscosity at the early times is large.

The effective temperature in the central region is shown in Fig.6.44. We see an increase at the early times until 1.0 fm/c. This is mainly due to the strong decrease of the number density at the beginning of the expansion. We also see that the time evolution of the temperature after 2 fm/c is again near ideal hydrodynamical behaviour, when compared with the ideal hydrodynamical limit with a fixed intercept at 2 fm/c.

To follow the ongoing kinetic equilibration in the central region, we depict the transverse momentum spectrum at different times in Fig.6.45. The initial distribution at 0.4 fm/c is at high non-equilibrium. At 1 fm/c one can still recognize the edge at 1 GeV. The spectrum at 2 fm/c has already a thermal shape. One also sees that the slope of spectrum at 4 fm/c is larger than that at 2 fm/c, which corresponds the cooling demonstrated in Fig.6.44. We therefore

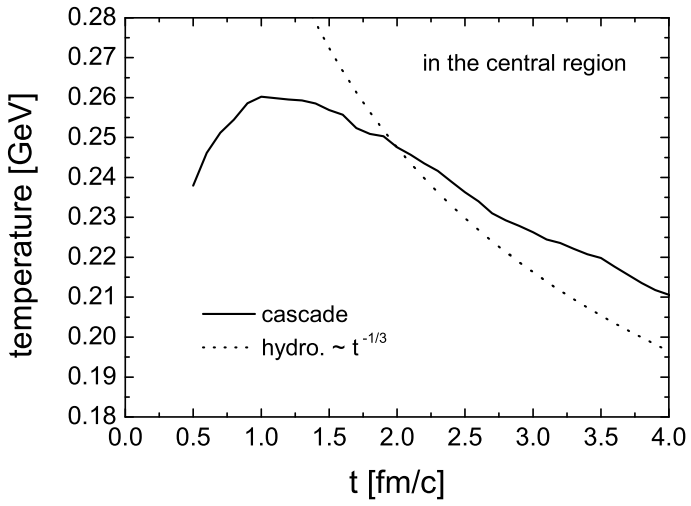

Figure 6.44: Time evolution of effective temperature in the central region. The dotted line depicts the result from ideal hydrodynamics with a fixed intercept at 2 fm/c.

expect that the system becomes full kinetic equilibrated at $1-2$ fm/c. To show that the momentum is getting isotropic, we extract the fraction $< p_T^2 > /2 < p_z^2 >$ as a function of time in the central region. The result is depicted in the left panel of Fig.6.46. We see that the value of the anisotropy is very high at the early times. It is initially infinite due to the highly non-isotropic initial distribution of gluons having $p_z = 0$. However, the decrease towards 1 is indeed rather rapid. At 2 fm/c the momentum distribution becomes fully isotropic and this time denotes thus the scale of the onset of full kinetic equilibrium. We have to note that the result of the anisotropy is not insensitive to the particular choice of the local region. Detailed analysis on the uncertainty should be done. In contrast, chemical equilibration can be described by the ratio of the inelastic collision rates, $R_{ggg\to gg}/R_{gg\to ggg}$, which is exactly equal to the fugacity at kinetic equilibrium and is insensitive to the geometry of the local region, as mentioned in the previous section. The time evolution of the ratio is depicted in the right panel of Fig.6.46. As have been calculated, the initial fugacity is $8 > 1$. Thus there are more particle annihilations than productions at the early times, as seen in the right panel of Fig.6.46. At 1.5 fm/c the ratio reaches 1 and stays at 1 from this time on, which demonstrates that from 1.5 fm/c the system is in full chemical equilibrium in the central region. Thermalization of gluons from CGC has been studied parametrically in the 'bottom-up' picture [BMSS 01]. The authors found that in the limit $Q_s >> \Lambda_{QCD}$, thermalization occurs at $\tau \sim \alpha_s^{-13/5} Q_s^{-1}$. Extracting α_s in

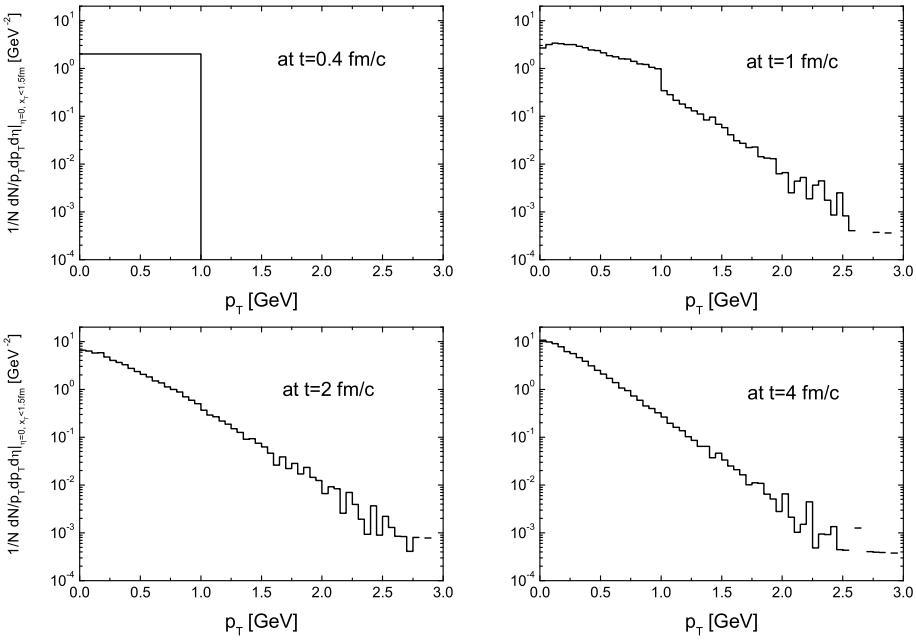

Figure 6.45: Transverse momentum spectrum in the central region at time 0.4, 1.0, 2.0 and 4.0 fm/c.

the central region from our cascade simulation ($\alpha_s \approx 0.43$ is almost constant in time corresponding small variance of the temperature, see Fig.6.44), and inserting it into the above formula, we obtain $\tau \sim 1.8$ fm/c. Our result lies within this range. Detailed study on the 'bottom-up' picture will be done in the future.

Finally, we show in Fig.6.47 the time evolution of the transverse energy per unit momentum rapidity at midrapidity, compared with the ideal hydrodynamical limit with a fixed intercept at 0.5 fm/c. The decrease of E_T at the early times is slightly stronger than that from ideal hydrodynamics. Therefore the longitudinal work done by pressure is not the only reason for the decrease of the transverse energy. Remember that the initial gluons have zero p_z in their local frames. Thus any changes towards the isotropy of the momentum distribution will then lead to particle diffusion to higher or lower momentum rapidities. Since particles with smaller rapidity are formed earlier, one obtains in total a diffusion of gluons to higher rapidities. This contributes the additional decrease of E_T at the beginning of the expansion. After a time of 0.5 fm/c the diffusion seems to cease. The decrease of E_T is then mainly due to the longitudinal work, which is less performed in the subsequent evolution when the collision rate becomes smaller. We also see that both the final (at 4 fm/c)

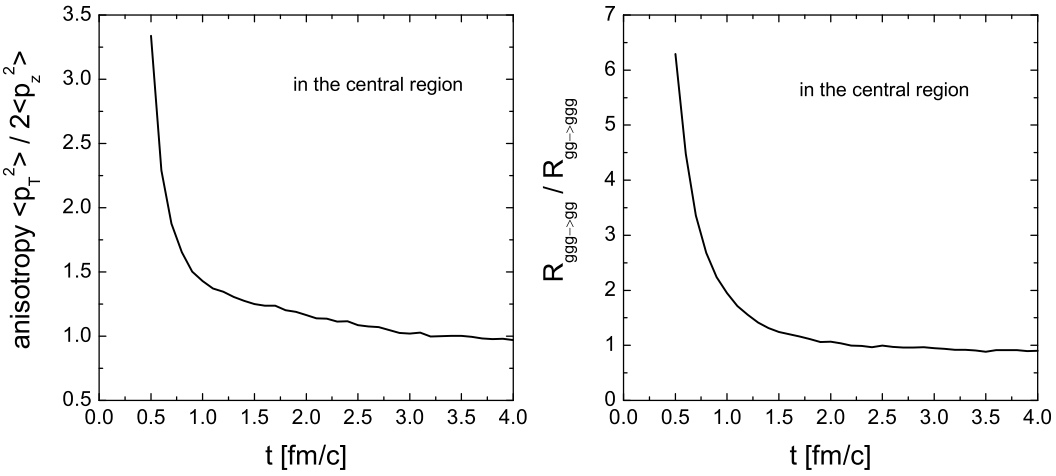

Figure 6.46: Left panel: time evolution of anisotropy $< p_T^2 > /2 < p_z^2 >$ in the central region. Right panel: time evolution of ratio of collision rates $R_{ggg \to gg}/R_{gg \to ggg}$ in the central region.

and initial value of dE_T/dy at midrapidity are smaller than the experimental data at RHIC, $dE_T/dy|_{y=0} = 620 \pm 33$ GeV. Therefore, CGC alone does not give the appropriate initial conditions at RHIC. One should combine this with the high p_T minijets.

In this section we have studied thermalization of gluons with an initial condition from color glass condensate, which was already applied in [BV 01]. Contrary to the result of large timescale of thermalization in [BV 01], we have found that a more rapid thermalization is achieved at $1.5 - 2$ fm/c when inelastic pQCD motivated interactions among gluons are included. Analysis with recently obtained initial gluon distributions will follow.

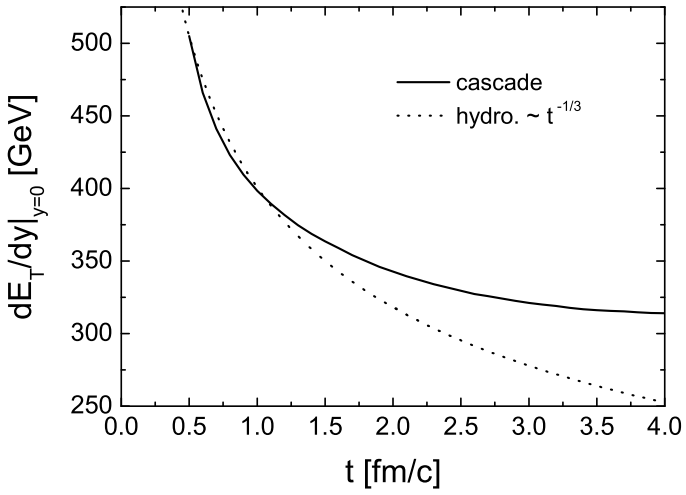

Figure 6.47: Time evolution of the transverse energy per unit momentum rapidity at midrapidity (solid line). The dotted line denotes the ideal hydrodynamical limit with a fixed intercept at 0.5 fm/c.

Chapter 7

Summary and Outlook

We have investigated thermalization of gluons in central Au+Au collisions at the maximum RHIC energy employing a new $3+1$ dimensional (pQCD inspired) relativistic transport simulation solving the kinetic on-shell Boltzmann equations for partons. The development of the new cascade represents the basis for the present and future studies concerning parton evolution in high-energy heavy ion collisions. An important feature of this cascade is that besides binary $2 \leftrightarrow 2$ scatterings, inelastic $2 \leftrightarrow 3$ processes are implemented for the first time. The numerical emphasis is put on the extension of the stochastic collision algorithm for the back reaction $3 \rightarrow 2$, which is treated fully consistently within this scheme. Different from any geometrical concept, this collision algorithm is based on the handle of collision rates in the divided spatial local regions (see chapter 2). Although the development specifically aims at a simulation of the parton evolution in an ultrarelativistic heavy ion collision, the presented algorithm will certainly have more potential applications beyond the scope of this study. Also the standard geometrical collision algorithm (based on the geometrical intepretation of cross section) has been discussed in detail. In particular, we find that for the case that the mean free path of particles is in the same order as or comes below the interaction length, which is always true in a very energetic (and dense) high-energy heavy ion collision, the results from the simulations employing the geometrical method have shown several unphysical numerical artifacts which appear only weakly in the simulations (with the same number of test particles N_{test}) employing the stochastic method. Especially in the study of frame independence in chapter 3, we have seen that with same N_{test} results from the simulations using the geometrical method show much stronger frame dependence than those from the simulation using the stochastic method. The convergence of the numerical solution in the geometrical scheme for $N_{test} \rightarrow \infty$ turns out to be not as efficient as it does in the simulations when employing the stochastic method.

The operation of the newly developed cascade has been demonstrated by

investigating gluon thermalization for a central Au+Au collision at RHIC energy. Interactions among gluons are described by pQCD. We have applied the screening mass to regularize the infra-red divergence of the pQCD cross sections. The suppression of gluon radiation with small p_T (and the back reaction) due to the Landau-Pomeranchuck-Migdal (LPM) effect is taken into account by introducing a p_T cutoff for the radiated gluons. To demonstrate the correct implementations of $gg \leftrightarrow ggg$ processes (and $gg \leftrightarrow q\bar{q}$ as well), we have performed simulations in a fixed box to show the detailed balance between gluons and quarks in thermal equilibrium. The numerical results from the simulations of parton evolution at RHIC have been presented in chapter 6. Main conclusions are listed below.

1.) Starting initially from a nonthermal system made up of minijets (with cutoff $p_T > p_0 = 2$ GeV), the gluons in the expanding center equilibrate kinetically on a timescale of 2 fm/c and evolve further according to (quasi-)hydrodynamics. The system cools down due to the hydrodynamical expansion and ongoing gluon multiplication. The gluons are initially strongly undersaturated. Full chemical equilibration follows on a longer timescale of about $3-4$ fm/c. Compared with the case of free streaming, transverse flow seems to be built up during the parton expansion at RHIC. Thermalization in the transverse region slows down with increasing distance of the local region to the center. Within a transverse radius of a gold nucleus, ~ 5 fm, the timescale of thermalization varies only by 15%. In the outer region with $x_T > 5$ fm gluons come mainly from the surface of the fireball and are almost non-interacting. We have observed a decrease of the transverse energy per unit momentum rapidity at midrapidity of a factor 1.7, which is definitely due to the longitudinal work performed by the pressure and thus strongly indicates an early buildup of pressure at RHIC.

2.) The results in 1.) do not change significantly when including a phenomenological formation time given by the uncertainty relation for the initial gluons.

3.) We have studied the contribution of the elastic and inelastic collisions to kinetic equilibration. It turns out that the inelastic scatterings are the main responsible processes driving the system to equilibrium. Without any inelastic collision channel, the collective behaviour observed nowadays at RHIC can not be generated, unless one uses an unrealistic large cross section (or equivalently a large gluon density) to mimic a strongly interactive gluon system [MG 02]. We have also realized that the angular distribution of the $gg \leftrightarrow ggg$ processes is almost isotropic during the expansion. This leads to larger transport cross section compared with the elastic scatterings.

4.) With smaller p_T-cutoff for the minijets production, $p_0 = 1.5 - 1.3$ GeV, simulations for parton evolution at RHIC have been performed. We obtained moderately rapider kinetic equilibration at $1-2$ fm/c at smaller p_0, while at those small cutoffs full chemical equilibration is almost achieved after the

minijets production. The decrease of the transverse energy per unit rapidity is considerably stronger at smaller p_0, which indicates stronger hydrodynamical expansion. Comparing roughly the final multiplicity and the final transverse energy per unit rapidity with the experimental data, we found that minijets production at $p_0 = 1.4$ GeV would give an appropriate initial condition at RHIC.

5.) We have studied thermalization of gluons with an initial condition from color glass condensate at RHIC. Contrary to the result of large timescale of thermalization in [BV 01], where the same initial condition has been used, we found that a rapider thermalization is achieved at $1.5 - 2$ fm/c when inelastic interactions among gluons are included.

All together, inelastic gluonic interactions can account for fast equilibration of deconfined matter.

There are a lot of interesting investigations and numerical improvements in plan. Some of them are already pointed out in the previous chapters. We now discuss them in more detail.

As claimed in the introduction, the RHIC data on the elliptic flow in semi-central Au+Au collisions showed large values. These can be explained as a consequence of early buildup of pressure in the parton phase and a rapid thermalization, since the calculations applying ideal hydrodynamics at the very beginning of the expansion fitted the experimental data. However, pQCD inspired transport simulations [MG 02] did not yield reasonable values of v_2, unless one uses an unrealistic large cross section. On the other hand, in [MG 02] only elastic gluonic collisions are considered. As argued in [SS 01], elastic scatterings alone cannot drive the parton system, created at RHIC, to equilibrium. The present study showed that the inclusion of inelastic $gg \leftrightarrow ggg$ makes equilibration more efficiently. The indication of an early thermalization and the hydrodynamical behaviour during the subsequent expansion, which is one of the main findings from the first study concerning RHIC physics, gives strong motivation for exploring elliptic flow using the new kinetic parton cascade. Can the inelastic interactions generate the seen elliptic flow v_2? The study is in progress [X 05]. Particularly, one has to find a way to calculate the local screening mass and local mean free path for modeling the LPM effect with low statistic fluctuations.

Our results showed that although a strongly interacting QGP might exist at RHIC, the mean free path of gluons in the evolution is still not very much smaller than the macroscopical scale of length, like the longitudinal extension of the plasma. Therefore, if any thermal state is created, the further expansion of the system should be rather better described by viscous than ideal hydrodynamics. It is interesting to compare the present calculations with some fixed and specified hydrodynamical initial conditions directly with calculations based on *viscous* relativistic hydrodynamics [M 02], either assuming Bjorken

boost invariance within an expanding tube or for full 3+1 dimensions. Such a comparison can tell how viscous the QGP really turns out to be at RHIC. However, the input for the calculation applying viscous hydrodynamics, the viscosity, has to be first extracted from the cascade simulation. One thus needs to understand in detail how viscosity establishes in a microscopical transport model [F 05].

Jet-quenching is one of the most prominent suggested signatures for an existance of a deconfined partonic matter at the early stage of a heavy ion collision. Measurement on the p_T spectrum of hadrons at RHIC showed a significant suppression of the spectrum at high p_T, compared with that obtained by the adding up independent events of binary nucleon-nucleon collisions. This indicates the formation of a medium, across which particles lose their energy due to radiations. The phenomenon of jet quenching or electromagnetic radiation can be studied systematically within the new transport scheme and has been also observed in the present analysis (see Fig.6.24). We see that gluons lose more energy than what is measured for hadrons at RHIC. It was discussed in subsection 6.2.2 that the reason for the stronger jet-quenching may be due to the still occurrence of $gg \leftrightarrow ggg$ collisions on the surface of the fireball in spite of a lower energy density than the critical value, ~ 1 GeV fm^{-3}. This should be inspected in more detail. Futhermore, how do the screening and LPM effect influence energy loss? This also has to be explored in further investigations [Fo 05].

In heavy ion collisions at energies higher than the RHIC energy one would expect quicker thermalization of partons, since more partons are freed in the first moment after the collision. On the other hand, at high energies it is often assumed that the initial distribution of gluons is given by the saturation scenario or color glass condensate [MV 94] and is described by the saturation scale Q_s. This initial distribution is far from thermal equilibrium. In addition, the strong coupling α_s decreases at high energies, which would make thermalization harder to achieve. In [BMSS 01] Baier et al. showed that, in the limit $Q_s >> \Lambda_{QCD}$ corresponding to very large nuclei and/or very high collision energy, thermalization occurs relatively fast at $\tau \sim \alpha_s^{-13/5} Q_s^{-1}$. The authors claimed the way thermalization occurs: At first large amount of soft gluons are produced by the emission process. These soft gluons then quickly equilibrate and form a thermal bath. The thermal bath then draws energy from the hard gluons until full thermalization is achieved. This 'bottom-up' picture and the parametrical behaviour of thermalization should be studied employing the present parton cascade [E 05]. How likely is this picture for true coupling constants and not parametrically small ones at RHIC and LHC?

Moreover, quarks will be included in simulations. Numerical implementations are straightfoward. We are then able to study the thermalization of quarks and more interesting, the heavy quark production during the parton

evolution. Also the dilepton and direct photon production can be investigated systematically with the new parton cascade.

The newly developed parton cascade provides a powerful tool for exploring the possibility of a rapid thermalization and an early buildup of pressure in the parton phase considering various initial conditions. On the other hand, a best way to prove theoretical considerations is to compare their results with the experimental data. Therefore, it is desired to perform simulations following the whole process, which may happen in heavy ion collisions, from initial conditions for partons to freezeout of hadrons [ZKLL 00], in order to be able to make comparisons with the RHIC data of hadronic constituents. It is our attempt to develop such event generator in the future by including hadronization of partons [W 05] and subsequent hadron cascade.

When applying the stochastic collision algorithm and the lattice-like discretization in space, the exact solution of the Boltzmann equation will be obtained in the limit $\Delta V \to 0$, $\Delta t \to 0$ and $N_{test} \to \infty$. We have shown the convergence of results from 1+1D cascade simulations in a fixed tube by decreasing longitudinal grid size dz (or $d\eta$) and increasing the number of test particles at the same time. The provement of convergence in the 3+1D simulations for RHIC has to be done. Especially one may worry about acausal effects due to larger signal velocity than c in cells if the mean free path of particles is less than the grid size. It is indeed the case for the transverse propagation at the initial stage, where the mean free path of gluons is 2 times smaller than the constant transverse grid size $dx = dy = 0.5$ fm. The situation is more drastic when we use a 30 mb cross section for mimicing a strongly interacting system. In this case the mean free path of gluons at the initial stage is 10 times smaller than the transverse grid size. To explore whether the acausal effect makes large numerical artifact, we carry out simulation for the extreme case of large cross section employing half of the default transverse grid size and 4 times enhanced N_{test} (to keep the same statistics in cells). In Fig.7.1 we depict the time evolutions of the number and energy density of gluons extracted in the central region from the simulation with $dx = dy = 0.25$ fm and $N_{test} = 960$ by the dotted lines, compared with the results with the default settings, depicted by the solid lines. We do not recognize any visible difference between the solid and dotted lines. Although the mean free path $(1/n\sigma)$ is still smaller than $dx = dy = 0.25$ fm at the initial stage, it decreases to 0.25 fm at about 2 fm/c. Therefore, if there are some effects, deviations should be seen from this time. The fact that the results from the simulations with different transverse grid size are identical indicates that the acausal effects seem to be not sensitive to the grid size when the system is uniformly distributed in space. Detailed study should be done further to confirm this consideration. In addition, we want to understand how viscosity, heat conductivity and particle diffusion are numerically affected by the scale of non-vanishing cell length [CH 02, F 05].

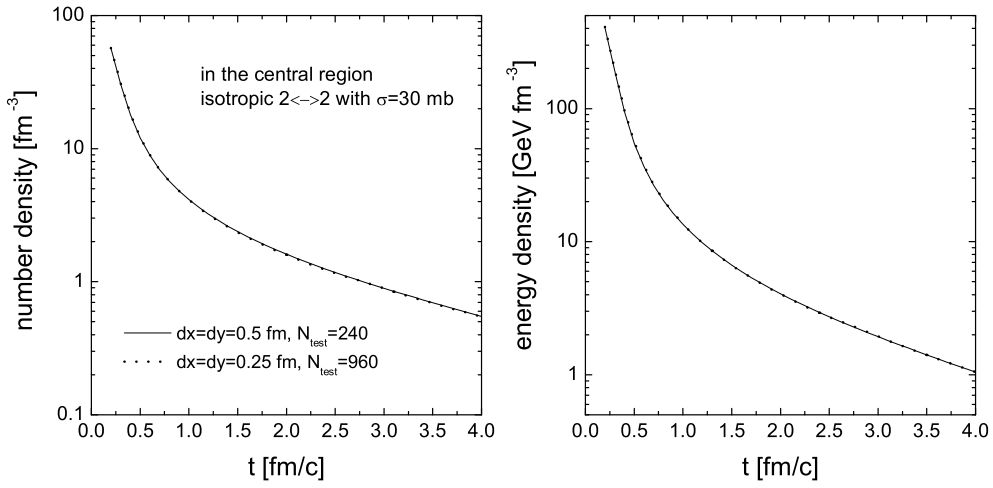

Figure 7.1: Time evolution of the number (left panel) and energy (right panel) density extracted in the central region from the simulation with $dx = dy = 0.25$ fm and $N_{test} = 960$ by the dotted lines, compared with the results with the default settings $dx = dy = 0.5$ fm and $N_{test} = 240$, depicted by the solid lines.

Finally, the technique of the parallel programing is needed to improve the practical operation of the cascade. With this technique quantities like the screening mass can be calculated and incorporated more precisely and quantum effects like the Pauli-blocking and Bose enhancement can be then implemented straightforwardly.

Things have only get started. There is still a lot to do.

Appendix A

Collision times in the geometrical method

Within the algorithm implementing the geometrical picture collisions occur if the considered particles approach each other and their *closest* distance is less than the interaction length $\sqrt{\sigma/\pi}$. This criterion will be inspected in the center of mass frame of the colliding particles. Suppose that $\hat{r}_i = (t_i, \mathbf{r}_i)$, $\hat{p}_i = (E_i, \mathbf{p}_i)$ and $\hat{r}'_i = (t'_i, \mathbf{r}'_i)$, $\hat{p}'_i = (E'_i, \mathbf{p}'_i)$, $i = 1, 2$, are the space-time coordinates and four momenta of two particles in the lab frame and in their c.m. frame respectively. Defining $H = (\hat{r}_2 - \hat{r}_1) \cdot (\hat{p}_1 + \hat{p}_2)$, one has in the c.m. frame: $t'_1 > t'_2$ if $H < 0$ and $t'_1 \leq t'_2$ if $H \geq 0$. For the case $t'_1 > t'_2$ (otherwise we change the indices of the particles) the two particles will approach each other if $\hat{p}_2^2 \, [\hat{p}_1 \cdot (\hat{r}_2 - \hat{r}_1)] - (\hat{p}_1 \cdot \hat{p}_2) \, [\hat{p}_2 \cdot (\hat{r}_2 - \hat{r}_1)] < 0$. The closest distance of the colliding particles in the c.m. frame is

$$\Delta r'_s = \sqrt{-f - \frac{a^2 \, d + b^2 \, c - 2 \, a \, b \, e}{e^2 - c \, d}} \,, \tag{A.1}$$

where

$$\begin{aligned} a &= (\hat{r}_2 - \hat{r}_1) \cdot \hat{p}_1 \,, \quad b = (\hat{r}_2 - \hat{r}_1) \cdot \hat{p}_2 \,, \\ c &= \hat{p}_1^2 \,, \quad d = \hat{p}_2^2 \,, \quad e = \hat{p}_1 \cdot \hat{p}_2 \,, \\ f &= (\hat{r}_2 - \hat{r}_1)^2 \,. \end{aligned} \tag{A.2}$$

If $\Delta r'_s < \sqrt{\sigma/\pi}$, the particles will collide at the same time $t'_{c1} = t'_{c2}$ at the closest distance in the c.m. frame. Making Lorentz transformation back to the lab frame gives

$$t_{c1} = t_1 - E_1 \, \frac{a \, d - b \, e}{e^2 - c \, d} \,, \quad t_{c2} = t_2 + E_2 \, \frac{b \, c - a \, e}{e^2 - c \, d} \,. \tag{A.3}$$

We call t_{c1} and t_{c2} the collision times. Due to the spatial separation, the two collision times have, in general, different values, $t_{c1} \neq t_{c2}$. This means that

one of the particles reacts later within the same collision. The transformed space coordinates at the collision times are correspondingly denoted by $\mathbf{r}_{c1}$ and $\mathbf{r}_{c2}$. The new momenta of the particles are sampled in the c.m. frame according to the given differential cross section and then transformed to the lab frame, which are denoted by $\mathbf{p}_{c1}$ and $\mathbf{p}_{c2}$. We thus label the particles with $(t_{ci}, \mathbf{r}_{ci})$ and $(E_{ci}, \mathbf{p}_{ci})$, $(i = 1, 2)$, and keep the labels until their next respective collisions. For example, t_1 denotes the time when the last collision of particle 1 occurs. It is kinematically possible that the case $t_1 < t_{c1} < t_2 < t_{c2}$ occurs. Such a collision sequence is not causal, because at t_{c1} when the particle 1 experiences the collision with the particle 2, the particle 2 is just on the way to its last collision with some other particle. To forbid those collisions we add an additional criterion: The collision times t_{c1} and t_{c2} should be greater than t_1 as well as t_2. Illustratively, the additional criterion means that during the time interval $|t_1 - t_2|$, the particle, which will change its trajectory later (it is the particle 2 in the example), is not considered for dynamics for that particular interval.

In the following we are interested in the probability distribution of the difference of collision times, $\Delta t_c := |t_{c1} - t_{c2}|$, in a thermal system of massless particles. In this case we have $c = d = 0$. If $t_1 \neq t_2$ (e.g. $t_1 < t_2$), the particle with smaller time (t_1) can propagate freely to the larger time (t_2), which does not give any effect on the whole evolution due to the additional criterion. Thus we obtain

$$\Delta t_c = r_{12} \left| \frac{u_1 + u_2}{1 - \tilde{u}} \right| . \tag{A.4}$$

r_{12} denotes $|\mathbf{r}_2 - \mathbf{r}_1|$ and $u_i = \cos\alpha_i$, $\tilde{u} = \cos\theta$, where α_i is the angle between $\mathbf{p}_i$ and $\mathbf{r}_2 - \mathbf{r}_1$ and θ is the angle between $\mathbf{p}_1$ and $\mathbf{p}_2$. Since $\tilde{u}$ relates u_i according to $\tilde{u} = \sqrt{1-u_1^2}\sqrt{1-u_2^2}\cos(\phi_1 - \phi_2) + u_1\, u_2$, where ϕ_i is the polar angle of $\mathbf{p}_i$ around $\mathbf{r}_2 - \mathbf{r}_1$, (A.4) can be now expressed by $\Delta t_c = r_{12}\, F(u_1, u_2, \phi)$ with $\phi := \phi_1 - \phi_2$. One obtains the probability distribution of Δt_c by the integral

$$\begin{aligned} P(\Delta t_c) &= \int_{-1}^{1} du_1 \int_{-1}^{1} du_2 \int_0^{2\pi} d\phi \int_0^{R} dr_{12} \\ &\quad \times P(r_{12}, u_1, u_2, \phi)\, \delta(\Delta t_c - r_{12} F)\, \Theta(\sqrt{\sigma/\pi} - \Delta r'_s) \\ &= \int_{-1}^{1} du_1 \int_{-1}^{1} du_2 \int_0^{2\pi} d\phi \\ &\quad \times P(r_{12}, u_1, u_2, \phi)|_{r_{12} = \Delta t_c / F} \frac{1}{F(u_1, u_2, \phi)}\, \Theta(\sqrt{\sigma/\pi} - \Delta r'_s) \,, \end{aligned} \tag{A.5}$$

where $P(r_{12}, u_1, u_2, \phi)$ is the multiple probability distribution. Note that it is easy to realize that $\Delta r'_s$ can also be expressed as a function of r_{12}, u_1, u_2 and ϕ. Since r_{12}, u_1, u_2 and ϕ are independent variables, $P(r_{12}, u_1, u_2, \phi)$ can be factorized, $P(r_{12}, u_1, u_2, \phi) = P(r_{12})P(u_1)P(u_2)P(\phi)$. For a thermal system we have $P(u_i) = 1/2$, $P(\phi) = 1/2\pi$ and $P(r_{12}) = 3r_{12}^2/R^3$, where R serves as a

normalization factor and is set to be much larger than the interaction length. We realize that the probability distribution (A.5) depends only on the size of the total cross section. For a constant cross section we calculate the integral in (A.5) numerically. Fig.A.1 shows the results for $\sigma = 10$ mb and $\sigma = 30$ mb. The distribution has a larger width for larger cross section. We also calculate the mean value of Δt_c and obtain $< \Delta t_c >= 0.24$ fm/c for $\sigma = 10$ mb and $< \Delta t_c >= 0.41$ fm/c for $\sigma = 30$ mb.

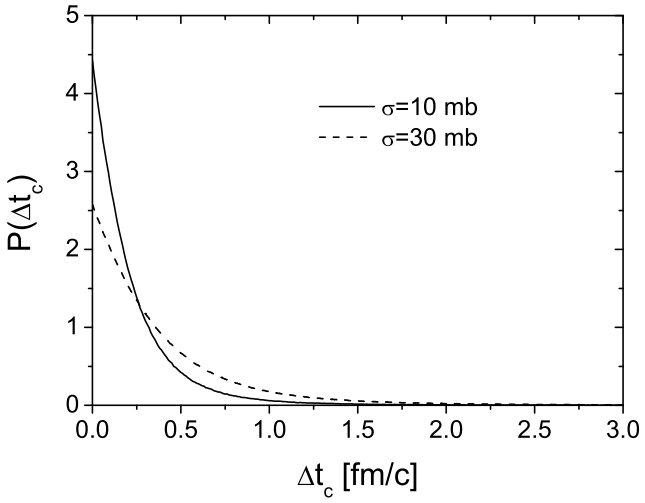

Figure A.1: Probability distribution of difference in 'collision times' within the geometrical collision algorithm. In the calculations a thermal system is assumed and the cross section is set to be a constant.

Appendix B

Optimization of the computing time within the geometrical method

Consider a system with N particles in total. To get the next collision, $N(N-1)/2$ operations have to be carried out to get all the ordering times for each particle pair and $N(N-1)/2-1$ comparisons have to be made to obtain the particle pair which collides next. Then these two particular particles propagate freely until the two respective collision times when the respective momenta will be sampled according to the differential cross section. The same procedure will be repeated as long as needed. Since the operation number in each step is proportional to N^2, the computing time increases strongly with increasing particle number and increasing collision number. However, a large amount of operations are obviously futile, because after the update of two colliding particles only the ordering times of particle pairs which involve one of the two updated particles are indeed needed. Therefore only $2(N-2)$, but not $N(N-1)/2$, operations are necessary if one, in principle, wants to save all the ordering times from the last step. This, of course, reduce the computing time enormously. On the other hand, however, a large storage for those ordering times would be required. For an optimization we thus do not store all the ordering times, but only do store for each particle the informations of its possible next collision: the ordering time and the collision partner. We need therefore $2N$, instead of $N(N-1)/2$, memory places. The next collision will be obtained by comparing the marked and stored ordering times. In a next step we compute only the ordering times of the last colliding particles with the other particles ($2(N-2)$ operations) and compare them with the other stored times, respectively, to obtain the new informations of the next collision for each particle. The 'worst' case then occurs when the next collision partner of a particle is one of the last colliding particles. In this case the stored informations

for this particle are out of use and one has to compute the ordering times of the considered particle with all the other particles (additional $N-3$ operations). Fortunately those cases do not happen frequently in practice. We note that our prescription is different from the optimization used by Zhang in his parton cascade [Z 98], which follows the fact that particles which are far away from each other most probably do not collide as next pair. In this algorithm the space was divided into cells and only particles from the same cell and the neighboring cells may collide next within the geometrical method.

Appendix C

Parton-Parton scattering cross sections

Differential pQCD parton-parton cross sections in leading order of α_s have been calculated in [ORG 78]. For elastic gluon scattering the differential cross section reads

$$\frac{d\sigma^{gg\to gg}}{dt} = \frac{9\pi\alpha_s^2}{2s^2}(3 - \frac{tu}{s^2} - \frac{su}{t^2} - \frac{st}{u^2}) \,, \tag{C.1}$$

where s, t and u are the Mandelstam variables. $-t$ is equal to the momentum transfer squared

$$-t = q^2 = \frac{s}{2}(1 - \cos\theta) \,, \tag{C.2}$$

where θ denotes the scattering angle in the c.m. frame of colliding partons. For small angle scatterings the momentum transfer is approximately equal to its transverse component $q_\perp$. Therefore we have $-t \approx q_\perp^2$. Since the differential cross section (C.1) diverges at small t (and also at small u due to the symmetry of identical particles), (C.1) can be expressed approximately as

$$\frac{d\sigma^{gg\to gg}}{dq_\perp^2} \approx \frac{9\pi\alpha_s^2}{(q_\perp^2)^2} \,. \tag{C.3}$$

We regularize the infrared sigularity in (C.3) employing the Debye mass and obtain

$$\frac{d\sigma^{gg\to gg}}{dq_\perp^2} = \frac{9\pi\alpha_s^2}{(q_\perp^2 + m_D^2)^2} \,. \tag{C.4}$$

The other approximate differential cross sections are achieved in the same way and read as follows:

$$\frac{d\sigma^{gq\to gq}}{dq_\perp^2} = \frac{2\pi\alpha_s^2}{(q_\perp^2 + m_D^2)^2} \,, \tag{C.5}$$

$$\frac{d\sigma^{gg\to q\bar{q}}}{dq_\perp^2} = \frac{\pi\alpha_s^2}{3s(q_\perp^2 + m_q^2)} \,, \tag{C.6}$$

$$\frac{d\sigma^{qq\to qq}}{dq_\perp^2} = \frac{16\pi\alpha_s^2}{9(q_\perp^2+m_D^2)^2}\,, \tag{C.7}$$

$$\frac{d\sigma^{qq'\to qq'}}{dq_\perp^2} = \frac{d\sigma^{q\bar{q}\to q\bar{q}}}{dq_\perp^2} = \frac{8\pi\alpha_s^2}{9(q_\perp^2+m_D^2)^2}\,, \tag{C.8}$$

$$\frac{d\sigma^{q\bar{q}\to gg}}{dq_\perp^2} = \frac{64\pi\alpha_s^2}{27s(q_\perp^2+m_q^2)}\,, \tag{C.9}$$

$$\frac{d\sigma^{q\bar{q}\to q'\bar{q}'}}{dt} = \frac{4\pi\alpha_s^2}{9s^2}\,\frac{t^2+u^2}{(s+4m_q^2)^2}\,, \tag{C.10}$$

where m_D^2 and m_q^2 denote, respectively, the Debye mass for gluons and for quarks. In the last expression $-t$ is not replaced by $q_\perp^2$, since $q\bar{q} \to q'\bar{q}'$ processes do not favour small angle scatterings. Employing the fomulas (C.4) - (C.10) the total cross sections can be obtained analytically by integration. (C.4) - (C.10) also then dictates how to sample new momenta for particles after an occurring collision.

Appendix D

Cross section for $gg \leftrightarrow ggg$ processes

For the multiplication process $gg \to ggg$, the Gunion-Bertsch formula [GB 82] is used for the matrix element squared in leading order of pQCD, and modified by implementing the Debye screening mass. This is

$$|\mathcal{M}_{gg\to ggg}|^2 = \left(\frac{9g^4}{2}\frac{s^2}{(\mathbf{q}_\perp^2+m_D^2)^2}\right)\left(\frac{12g^2\mathbf{q}_\perp^2}{\mathbf{k}_\perp^2[(\mathbf{k}_\perp-\mathbf{q}_\perp)^2+m_D^2]}\right), \qquad \text{(D.1)}$$

where $g^2 = 4\pi\alpha_s$, and $\mathbf{q}_\perp$ and $\mathbf{k}_\perp$ are, respectively, the transverse component of the momentum transfer and that of the momentum of radiated gluon in the c.m. frame of the colliding gluons. In this section we will give the derivations of the cross section $\sigma_{gg\to ggg}$ and $I_{ggg\to gg}$ defined in section 2.2 by an integral of the scattering amplitude given in (D.1) over momentum space.

Employing usual convention, the total cross section for a $gg \to ggg$ process is defined as

$$\begin{aligned}\sigma_{gg\to ggg} &= \frac{1}{2s}\int \frac{d^3p_1'}{(2\pi)^3 2E_1'}\frac{d^3p_2'}{(2\pi)^3 2E_2'}\frac{d^3p_3'}{(2\pi)^3 2E_3'} \\ &\quad \times|\mathcal{M}_{12\to 1'2'3'}|^2(2\pi)^4\delta^{(4)}(p_1+p_2-p_1'-p_2'-p_3'), \qquad \text{(D.2)}\end{aligned}$$

where p_1, p_2, p_1', p_2' and p_3' are the four momenta and all momenta are expressed in the c.m. frame of the two colliding gluons. We assume that $3'$ denotes the radiated gluon. Integrating over d^3p_2' gives

$$\begin{aligned}\sigma_{gg\to ggg} &= \frac{1}{256\pi^5 s}\int \frac{d^3p_1'}{E_1'}\frac{d^3p_3'}{E_3'}\,|\mathcal{M}_{12\to 1'2'3'}|^2\,\delta((p_1+p_2-p_1'-p_3')^2) \\ &= \frac{1}{256\pi^5 s}\int d^2q_\perp dy_1' d^2k_\perp dy\,|\mathcal{M}_{12\to 1'2'3'}|^2\,\delta(F), \qquad \text{(D.3)}\end{aligned}$$

where y_1' and y denote the momentum rapidity of $1'$ and $3'$ respectively and

$$F = (p_1+p_2-p_1'-p_3')^2$$

$$
\begin{aligned}
= \; & s - 2\sqrt{s}q_\perp \cosh y_1' - 2\sqrt{s}k_\perp \cosh y + 2q_\perp k_\perp \cosh y_1' \cosh y \\
& + 2\mathbf{q}_\perp \cdot \mathbf{k}_\perp - 2q_\perp k_\perp \sinh y_1' \sinh y \,. \qquad \text{(D.4)}
\end{aligned}
$$

Further integration over y_1' gives

$$
\sigma_{gg\to ggg} = \frac{1}{256\pi^5 s} \int d^2q_\perp d^2k_\perp dy \, |\mathcal{M}_{12\to 1'2'3'}|^2 \sum \frac{1}{\left|\frac{\partial F}{\partial y_1'}\right|_{F=0}} \,, \qquad \text{(D.5)}
$$

where all the solutions of $F = 0$ contribute to the sum. The corresponding differential cross section has the form

$$
\frac{d\sigma_{gg\to ggg}}{d^2q_\perp d^2k_\perp dy} = \frac{1}{256\pi^5 s} \, |\mathcal{M}_{12\to 1'2'3'}|^2 \sum \frac{1}{\left|\frac{\partial F}{\partial y_1'}\right|_{F=0}} \,. \qquad \text{(D.6)}
$$

This is different than in [BDMTW 93], where the authors ignored the factor $\sum 1/\left|\frac{\partial F}{\partial y_1'}\right|_{F=0}$. However, to make the correct implementation of the detailed balance for $gg \leftrightarrow ggg$ processes, one should take the exact fomula of the cross section. Expressing $d^2q_\perp$ and $d^2k_\perp$ in polar coordinates and integrating one of the two angles, one obtains

$$
\int d^2q_\perp d^2k_\perp dy \;\to\; \pi \int dq_\perp^2 dk_\perp^2 dy \int_0^\pi d\phi \,, \qquad \text{(D.7)}
$$

where ϕ denotes the angle between $\mathbf{q}_\perp$ and $\mathbf{k}_\perp$.

We now turn to determine the integral boundaries for (D.7). At first, the energies of the three particles in the final state can not be greater than $\sqrt{s}/2$ because of the energy conservation. (Note that the total energy is equal to $\sqrt{s}$.) We then have the upper boundaries for $q_\perp^2$ and $k_\perp^2$: $q_\perp^2 < s/4$ and $k_\perp^2 < s/4$. Secondly, $k_\perp$ and y will be further constrained by $\Theta(k_\perp \Lambda_g - \cosh y)$ due to the Laudau-Pomeranchuk suppression (compare section 5). This leads to a lower cutoff for $k_\perp$: $k_\perp > 1/\Lambda_g$. For given $q_\perp$ and $k_\perp$, the constraints for $\cosh y$ are

$$
\cosh y \le k_\perp \Lambda_g \quad \text{and} \quad \cosh y = \frac{E_3'}{k_\perp} \le \frac{\sqrt{s}}{2k_\perp} \,. \qquad \text{(D.8)}
$$

Thus the upper boundary of y, denoted by y_m, is the smaller one among $Arcosh(k_\perp \Lambda_g)$ and $Arcosh(\sqrt{s}/2k_\perp)$. Finally we have

$$
\sigma_{gg\to ggg} \sim \int_0^{s/4} dq_\perp^2 \int_{1/\Lambda_g^2}^{s/4} dk_\perp^2 \int_{-y_m}^{y_m} dy \int_0^\pi d\phi \cdots \,. \qquad \text{(D.9)}
$$

This integral actually scales with s, $\sigma_{gg\to ggg} = \bar{\sigma}/s$, where

$$
\bar{\sigma} \sim \int_0^{1/4} d\bar{q}_\perp^2 \int_{1/\bar{\Lambda}_g^2}^{1/4} d\bar{k}_\perp^2 \int_{-y_m}^{y_m} dy \int_0^\pi d\phi \cdots \qquad \text{(D.10)}
$$

with $\bar{q}_\perp^2 = q_\perp^2/s$, $\bar{k}_\perp^2 = k_\perp^2/s$, $\bar{\Lambda}_g = \Lambda_g\sqrt{s}$ and $\bar{m}_D^2 = m_D^2/s$. $\bar{\sigma}$ depends on two parameters: $\bar{\Lambda}_g$ and $\bar{m}_D^2$. We evaluate the above integral numerically using the Monte Carlo integration routine VEGAS [PTVF 92]. For any sampled point $(\bar{q}_\perp^2, \bar{k}_\perp^2, y, \phi)$ one has to solve y_1' for $F = 0$ in (D.4). If there is no solution, then the chosen point is out of the kinematic region and thus has no contribution to the integral. Thus the equation $F = 0$ serves as a further constraint for the kinematic region of collisions.

For the annihilation process $ggg \to gg$, the analogous quantity as $\sigma_{gg\to ggg}$, which sums all the possible final states, is $I_{ggg\to gg}$ defined via

$$I_{ggg\to gg} = \frac{1}{2}\int \frac{d^3p_1'}{(2\pi)^3 2E_1'}\frac{d^3p_2'}{(2\pi)^3 2E_2'}|\mathcal{M}_{123\to 1'2'}|^2(2\pi)^4\delta^{(4)}(p_1+p_2+p_3-p_1'-p_2')\,, \tag{D.11}$$

where the factor $1/2$ takes the identical gluons $1'$ and $2'$ into account and

$$|\mathcal{M}_{123\to 1'2'}|^2 = \frac{1}{\nu_g}|\mathcal{M}_{1'2'\to 123}|^2\,, \tag{D.12}$$

where $\nu_g = 2\times 8$ is the gluon degeneracy factor. Since $I_{ggg\to gg}$ is invariant under Lorentz transformations, we evaluate the integral in the rest frame of the three incoming particles. Therefore it is $p_1+p_2+p_3 = (\sqrt{s}, \mathbf{0})$. Integrating over d^3p_2' in (D.11) we find

$$\begin{aligned} I_{ggg\to gg} &= \frac{1}{16\pi^2}\int \frac{d^3p_1'}{E_1'}\,|\mathcal{M}_{123\to 1'2'}|^2\,\delta((p_1+p_2+p_3-p_1')^2) \\ &= \frac{1}{16\pi^2}\int dE_1'\,d\cos\theta\,d\phi\,E_1'|\mathcal{M}_{123\to 1'2'}|^2\,\delta(s-2\sqrt{s}\,E_1') \\ &= \frac{1}{64\pi^2}\int_{-1}^{1} d\cos\theta\int_0^{2\pi} d\phi\,|\mathcal{M}_{123\to 1'2'}|^2\,, \end{aligned} \tag{D.13}$$

where the solid angle $(\cos\theta, \phi)$ defines the orientation of $\mathbf{p}_1'$ ($\mathbf{p}_2' = -\mathbf{p}_1'$ because of the energy-momentum conservation). We now express $q_\perp$, $k_\perp$ and $\mathbf{q}_\perp\cdot\mathbf{k}_\perp$ in $|\mathcal{M}_{123\to 1'2'}|^2$ with the solid angle and momenta of the incoming gluons. To do that one has to specify the fussion process $2\to 1$. There are in total 6 combinations. Each combination contributes to $I_{ggg\to gg}$. One of them is

$$123\to 1'2' \quad\hat{=}\quad (\mathrm{a})\,23\to 2^*\,\text{and}\,(\mathrm{b})\,12^*\to 1'2'$$

and $\mathbf{p}_3$ corresponds to $(\mathbf{k}_\perp, y)$. In this particular case one can establish a coordinate system in momentum space whose Z-axis coincides with the orientation of $\mathbf{p}_1$. We find out (after a direct but lengthy calculation)

$$q_\perp = E_1\sin\theta \tag{D.14}$$

$$k_\perp = E_3\sqrt{1-(\sin\gamma\,\sin\theta\,\cos\phi+\cos\gamma\,\cos\theta)^2} \tag{D.15}$$

$$\mathbf{q}_\perp\cdot\mathbf{k}_\perp = E_1E_3\,(\sin\gamma\,\sin\theta\,\cos\theta\,\cos\phi-\cos\gamma\,\sin^2\theta)\,, \tag{D.16}$$

where γ denotes the angle between $\mathbf{p}_1$ and $\mathbf{p}_3$, and $(\cos\theta, \phi)$ is, as defined before, the solid angle of $\mathbf{p}_1'$. Due to the Laudau-Pomeranchuk suppression $\Theta(k_\perp \Lambda_g - \cosh y)$ and $\cosh y = E_3/k_\perp$ we obtain the kinematic region for the $ggg \to gg$ process

$$k_\perp \geq \sqrt{\frac{E_3}{\Lambda_g}}\,. \tag{D.17}$$

In analogy to $\sigma_{gg\to ggg}$, $I_{ggg\to gg}$ also scales with s, $I_{ggg\to gg} \sim \bar{I}/s$, where $\bar{I}$ depends on five parameters, namely $E_1/\sqrt{s}$, $E_3/\sqrt{s}$, γ, $\Lambda_g\sqrt{s}$ and m_D^2/s.

Appendix E

Monte Carlo Samplings

E.1 Monte Carlo Sampling of momentum and position for initial particles

E.1.1 Minijets

The momenta of the minijets (partons with $p_T > p_0 = 2$ GeV) are sampled according to the differential jet cross section

$$\frac{d\sigma_{jet}}{dp_T^2 dy_1 dy_2} = K \sum_{a,b} x_1 f_a(x_1, p_T^2) x_2 f_b(x_2, p_T^2) \frac{d\sigma_{ab}}{d\hat{t}}\,, \tag{E.1}$$

where p_T^2, y_1 and y_2 are, respectively, the transverse momentum and the momentum rapidities of produced partons and the sum runs over all incoming parton species. f_a and f_b denote the parton distribution function in the two colliding nucleons (proton or neutron). In principle, one can employ the 'rejection method' [PTVF 92] to smaple p_T^2, y_1 and y_2 directly. However, this method is not convenient in this case, since the distribution (E.1) is very pronounced at $p_T = p_0$ and $y_1 = y_2$. Therefore, we at first calculate $d\sigma_{jet}/dp_T^2$ at a series of points of p_T^2 by integrating y_1 and y_2 numerically and then sample p_T using the 'transformation method' [PTVF 92] with interpolation. The samplings for y_1 and y_2 with given p_T are carried out employing the rejection method. One obtains the longitudinal momentum via $p_z = p_T \sinh y$ and obtains $p_x = p_T \cos\theta$, $p_y = p_T \sin\theta$ with uniformly sampled θ. Species of the produced partons, gluon or quark with flavor, are determined according to the corresponding contributions in the sum in (E.1).

The sampling of the space-time coordinates of partons follows the geometry of the overlapping of the two colliding nuclei

$$\frac{d < N_{parton} >}{d^2 x_{T1}\, dz\, dt} \sim n_A(\mathbf{x}_{T1}, z - v\,t)\, n_A(\mathbf{x}_{T1}, z + v\,t)\,, \tag{E.2}$$

where n_A denotes the nuclear density which is parametrized using the Woods-Saxon distribution (4.8). Analogous to the sampling of momentum, we compute dN_{parton}/dt at a series of time by integrating the space coordinates numerically and then sample t using the transformation method with interpolation. Finally we sample the space coordinates at t via the rejection method.

When introducing an additional formation time for every partons modeling the off-shell propagation, the virtual partons do not interact and move with speed of light during the individual formation time, $\Delta t_f = \cosh y \Delta\tau \approx \cosh y \cdot 1/p_T$.

E.1.2 Bjorkens initial condition

The Bjorken-type boost invariant initial conditions [B 83] reads

$$\frac{dN}{d^3x\, d^3p}(\tau_0) = f(\mathbf{x}, \mathbf{p}, \tau_0) = e^{-\frac{p_\perp \cosh(y-\eta)}{T(\tau_0)}}, \tag{E.3}$$

where τ_0 denotes the initial proper time. At first we sample η by its uniform distribution within given region at the starting time τ_0. We then obtain the time and longitudinal position of the particle

$$t_0 = \tau_0 \cosh\eta, \quad z_0 = \tau_0 \sinh\eta\,. \tag{E.4}$$

The transverse positions x_0 and y_0 are sampled uniformly. Finally we determine the initial momentum according to the thermal distribution (E.3) at τ_0 for given η and $T(\tau_0)$.

E.2 Monte Carlo Sampling of momenta for outgoing particles

Momenta of outgoing particles are sampled in the rest frame of the incoming particles. Their momentum in the lab frame is obtained by Lorentz transformations.

E.2.1 $2 \leftrightarrow 2$ processes

In the rest frame the energy of each particle is $\sqrt{s}/2$. The only to be sampled quantity is the solid angle $(\cos\theta, \phi)$. The scattering angle θ is samlped according to the differential cross section and the polar angle ϕ is sampled uniformly within $[0, 2\pi]$.

Since the pQCD differential cross sections (C.4) - (C.10) can be integrated analytically, we can perform samplings for $q_\perp$ (or $\cos\theta$) using the 'transformation method' [PTVF 92] from a uniform probability distribution. For isotropic

collisions we sample the scattering angle θ according to the uniform distribution of $\cos\theta$.

E.2.2 $gg \leftrightarrow ggg$ processes

As shown in Appendix D, the differential cross section for a $gg \to ggg$ process has the form

$$\frac{d\sigma_{gg\to ggg}}{dq_\perp^2 dk_\perp^2 dy d\phi} \sim \frac{1}{(q_\perp^2+m_D^2)^2}\frac{q_\perp^2}{k_\perp^2[(\mathbf{k}_\perp-\mathbf{q}_\perp)^2+m_D^2]}\sum\frac{1}{\left|\frac{\partial F}{\partial y_1'}\right|_{F=0}}, \qquad \text{(E.5)}$$

where ϕ denotes the angle between $\mathbf{q}_\perp$ and $\mathbf{k}_\perp$. We then first sample $q_\perp$, $k_\perp$, y and ϕ according to (E.5). Since the differential cross section can not be integrated analytically, one can not make samplings by means of the transformation method, as done for $2 \to 2$ processes. Instead, we employ the 'rejection method' [PTVF 92].

To make enough efficient samplings, we want to find out a special function of $q_\perp$, $k_\perp$, y and ϕ, which should be always greater than the right hand side of (E.5) at every point set ($q_\perp$, $k_\perp$, y, ϕ) in the kinematic region and, more important, can be integrated out analytically over $q_\perp$, $k_\perp$, y and ϕ. Such a function is called as a *comparison function*. If one has the comparison function, one can first use the transformation method to generate the random numbers according to the comparison function. Then one needs a further uniform sampling between zero and the value of the comparison function at the particular sampled point. If this random number is less than the value of the real distribution (right hand side of (E.5)) at the sampled point, then we accept this sampling, if not, we reject this sampling and start a next trial. One possible choice of the comparison function is

$$\frac{1}{q_\perp^2+m_D^2}\,\frac{1}{k_\perp^2}\,\frac{1}{m_D^2}\,m\,, \qquad \text{(E.6)}$$

where m denotes a constant with a sufficient large value, which is greater than $\sum 1/\left|\frac{\partial F}{\partial y_1'}\right|_{F=0}$ in (E.5) at every point in the possible kinematic region. Since, unfortunately, one can not obtain the upper limit for $\sum 1/\left|\frac{\partial F}{\partial y_1'}\right|_{F=0}$, the value of m is an empirical number.

We have to note that for an individual sampling one has to solve the equation $F = 0$ (D.4). Therefore one also obtains y_1' the momentum rapidity of the particle $1'$, at the same time when $q_\perp$, $k_\perp$, y and ϕ are sampled. One sampling remains: The direction of $\mathbf{q}_\perp$ is sampled uniformly in the transverse plan being perpendicular to the scattering axis. Finally we obtain the momenta of the outgoing particles

$$\mathbf{p}_{1\perp}' = -\mathbf{q}_\perp\,, \quad p_{1z}' = q_\perp \sinh y_1' \qquad \text{(E.7)}$$

$$\mathbf{p}'_{3\perp} = \mathbf{k}_\perp\,, \quad p'_{3z} = k_\perp \sinh y \tag{E.8}$$
$$\mathbf{p}'_2 = -(\mathbf{p}'_1 + \mathbf{p}'_3)\,. \tag{E.9}$$

For a $ggg \to gg$ process the solid angle $(\cos\theta, \phi)$ is sampled again by using the rejection method. We find

$$\begin{aligned}\frac{dI_{ggg\to gg}}{d\cos\theta\, d\phi} &\sim \frac{1}{(q_\perp^2 + m_D^2)^2}\frac{q_\perp^2}{k_\perp^2[(\mathbf{k}_\perp - \mathbf{q}_\perp)^2 + m_D^2]} \\ &< \frac{1}{q_\perp^2 + m_D^2}\frac{\Lambda_g}{E_3}\frac{1}{m_D^2} = \frac{1}{E_1^2(1-\cos^2\theta) + m_D^2}\frac{\Lambda_g}{E_3}\frac{1}{m_D^2}\,,\end{aligned} \tag{E.10}$$

where we have employed the constraint (D.17) and the identity (D.14) for the particular example presented in Appendix D.

E.2.3 Isotropic $2 \leftrightarrow 3$ processes

A $2 \to 3$ process, $12 \to 1'2'3'$, is assumed to be composed of a two-body scattering $12 \to 1'2^*$ and a decay $2^* \to 2'3'$, where 2^* denotes an intermediate state with an invariant mass of $m^* = \sqrt{E_*^2 - \mathbf{p}_*^2}$. We employ the formula for the phase space integrations of [BK 73] and obtain the differential cross section of an isotropic collision

$$\frac{d\sigma_{23}}{d\Omega_1 dm_*^2 d\Omega_2} \sim \lambda^{\frac{1}{2}}(s, 0, m_*^2) \int dE'_2\, \frac{E'_2}{E_* - E'_2}\, \delta(f(E'_2))\,, \tag{E.11}$$

where $\Omega_1 = (\cos\theta_1, \phi_1)$ denotes the solid angle of $\mathbf{p}'_1$ with respect to the collision axis, and $\Omega_2 = (\cos\theta_2, \phi_2)$ denotes the solid angle of $\mathbf{p}'_2$ with respect to $\mathbf{p}_*$, and

$$f(E'_2) = E_* - E'_2 - \sqrt{p_*^2 + E'^2_2 - 2p_* E'_2 \cos\theta_2}\,, \tag{E.12}$$
$$\lambda(s, m_1^2, m_2^2) = s^2 - 2s(m_1^2 + m_2^2) + (m_1^2 - m_2^2)^2\,. \tag{E.13}$$

The integral over E'_2 in (E.11) gives

$$\frac{d\sigma_{23}}{d\Omega_1 dm_*^2 d\Omega_2} \sim \frac{(s - m_*^2)m_*^2}{(E_* - p_* \cos\theta_2)^2}\,. \tag{E.14}$$

Ω_1, m_*^2 and Ω_2 are the to be sampled quantities. From (E.14) we realize that the differential cross section does not depend on Ω_1 and ϕ_2. Thus they are sampled uniformly. Integral over Ω_1 and Ω_2 gives the probability distribution for m_*^2. It is simply proportional to $s - m_*^2$. We sample m_*^2 by employing the transformation method. For given Ω_1 and m_*^2 the momenta of $1'$ and 2^* are fully determined due to the energy-momentum conservation. Now (E.14) just represents the probability distribution of $\cos\theta_2$ for a given Ω_1 and m_*^2. Its numerical sampling is straightforward.

Sampling for an isotropic $3 \to 2$ process is more trivial, since just one solid angle is to be sampled and its probability distribution is uniform.

Appendix F

Relativistic Hydrodynamics

We review briefly the theory of relativistic hydrodynamics. Details can be found in [W 72] and [GLW 80]. We consider here a *perfect fluid*, which is defined as having at each point a velocity $\mathbf{v}$, such that an observer moving with this velocity sees the fluid around him as isotropic. This will be the case if the mean free path between collisions is much smaller compared with the scale of lengths used by the observer. Otherwise viscosity becomes important and one has a imperfect fluid.

For a perfect fluid the energy-momentum tensor takes the form

$$T^{\mu\nu} = (\epsilon + p)\, U^\mu U^\nu - p\, g^{\mu\nu}\,, \tag{F.1}$$

where U^μ denotes the four-velocity of the fluid with $U_\mu U^\mu = 1$ and $U^\mu = (1,0,0,0)$ in the rest frame of the fluid element. ϵ and p are, respectively, the energy density and pressure measured in the rest frame. The motion of the fluid is governed by the equations of conservation of energy and momentum

$$\partial_\nu T^{\mu\nu} = 0 \tag{F.2}$$

and of the particle number

$$\partial_\mu N^\mu = 0 \tag{F.3}$$

with $N^\mu = n\, U^\mu$, the particle four-flow (n being the particle density in the rest frame).

Assuming a one dimensional, boost-invariant expansion of the fluid with $U^\mu = (t,0,0,z)/\tau$ [B 83], one obtains from (F.2)

$$\frac{d\epsilon}{d\tau} = -\frac{\epsilon + p}{\tau}\,. \tag{F.4}$$

For a perfect, ultrarelativistic fluid the equation of state reads $p = \epsilon/3$. Therefore one obtains the energy density

$$\epsilon(\tau) = \epsilon(\tau_0)\left(\frac{\tau_0}{\tau}\right)^{4/3} \tag{F.5}$$

by sovling (F.4) and then the temperature and the particle density

$$T(\tau) = T(\tau_0)\left(\frac{\tau_0}{\tau}\right)^{1/3}, \quad n(\tau) = n(\tau_0)\frac{\tau_0}{\tau} \tag{F.6}$$

using the thermaldynamical relations.

The macroscopic quantities like the particle density, the energy density and the hydrodynamical velocity can be defined with the help of the *distribution function*, $f(x,p)$,

$$N^\mu(x) = \int \frac{d^3p}{(2\pi)^3 E}\, p^\mu\, f(x,p)\,, \quad T^{\mu\nu}(x) = \int \frac{d^3p}{(2\pi)^3 E}\, p^\mu\, p^\nu\, f(x,p) \tag{F.7}$$

$$n = U_\mu N^\mu\,, \quad \epsilon = U_\mu T^{\mu\nu} U_\nu\,. \tag{F.8}$$

$f(x,p)\Delta^3x\Delta^3p$ gives the averaged number of particles which at the time t are situated in the volume Δ^3x about $\mathbf{x}$ with momenta in Δ^3p about $\mathbf{p}$. The definition of the hydrodynamical velocity is, however, ambiguous. We choose the Eckart's definition $U^\mu = N^\mu/\sqrt{N^\nu N_\nu}$. After this definition the hydrodynamical velocity is the mean partilcle velocity. If the system is in equilibrium, like in the case of the perfect fluid, the distribution function takes the form

$$f^{eq}(x,p) = \exp\left(\frac{-p^\mu U_\mu}{T}\right)\,. \tag{F.9}$$

Especially for the case of the one dimensional, boost-invariant expansion one has

$$f^{eq}(x,p) = \exp\left(\frac{-p_T\,\cosh(y-\eta)}{T}\right)\,. \tag{F.10}$$

Inserting (F.9) in (F.7) and (F.8) gives, independently on the choice of the definition of U^μ,

$$n = \frac{T^3}{\pi^2}\,, \quad \epsilon = 3\,n\,T \tag{F.11}$$

when the particles in the fluid are massless.

Using the distribution function one can easily obtain the quantities like the momentum distribution dN/d^3p, the rapidity distribution dN/dy and $dN/d\eta$ at time t. For instance,

$$\frac{dN}{d^3p}(t) = \int d^3x\, f(x,p)\,. \tag{F.12}$$

The question now is what about the quantities at τ. In general one has to use the Cooper-Frye formula [CF 74]

$$E\frac{dN}{d^3p} = \int d\Sigma_\mu p^\mu\, f(x,p)\,, \tag{F.13}$$

where Σ^μ specifies the 3D hypersurface on which the momentum distribution is measured. For a fixed t it takes $d\Sigma^\mu = (d^3x, 0, 0, 0)$ and for a fixed τ $d\Sigma^\mu = (\tau\cosh\eta, 0, 0, -\tau\sinh\eta)d\eta d^2x_T$ [GPZ 97].

Bibliography

[B 83] J.D. Bjorken, *Phys. Rev.* D **27**, 140 (1983).

[B 84] G. Baym, *Phys. Lett.* B **138**, 18 (1984).

[B 89] H. Babovsky, *Eur. J. Mech.* B **8**, 41 (1989).

[BDMTW 93] T.S. Biro, E. van Doorn, B. Müller, M.H. Thoma, and X.-N. Wang, *Phys. Rev.* C **48**, 1275 (1993).

[BK 73] E. Byckling and K. Kajantie, *Particle Kinematics* (John Wiley and Sons, 1973).

[BMGMN 00] V. Börchers, J. Meyer, S. Gieseke, G. Martens, and C.C. Noack, *Phys. Rev.* C **62**, 064903 (2000).

[BMS 03] S.A. Bass, B. Müller and D.K. Srivastava, *Phys. Lett.* B **551**, 277 (2003).

[BMSS 01] R. Baier, A.H. Mueller, D. Schiff and D.T. Son, *Phys. Lett.* B **502**, 51 (2001).

[BRAHMS 02] I.G. Bearden et al. [BRAHMS Collaboration], *Phys. Rev. Lett.* **88**, 202301 (2002).

[BV 01] J. Bjoraker and R. Venugopalan, *Phys. Rev.* C **63**, 024609 (2001).

[C 02] W. Cassing, *Nucl. Phys.* A **700**, 618 (2002).

[CF 74] F. Cooper and G. Frye, *Phys. Rev.* D **10**, 186 (1974).

[CH 02] S. Cheng et al., *Phys. Rev.* C **65**, 024901 (2002).

[CP 75] J.C. Collins and M.J. Perry, *Phys. Rev. Lett.* **34**, 1353 (1975).

[DB 91] P. Danielewicz and G.F. Bertsch, *Nucl. Phys.* A **533**, 712 (1991).

[DG 85] P. Danielewicz and M. Gyulassy, *Phys. Rev.* D **31**, 53 (1985).

[E 05] A. Ec, diploma thesis.

[EKL 89] K.J. Eskola, K. Kajantie and J. Lindfors, *Nucl. Phys.* B **323**, 37 (1989).

[EKRT 00] E.J. Eskola, K. Kajantie, P.V. Ruuskanen, K. Tuominen, *Nucl. Phys.* B **570**, 379 (2000); E.J. Eskola, P.V. Ruuskanen, S.S. Räsänen, K. Tuominen, *Nucl. Phys.* A **696**, 715 (2001).

[EKS 99] E.J. Eskola, V.J. Kolhinen, C.A. Salgado, *Eur. Phys. J.* C **9**, 61 (1999).

[F 05] J. Fiedler, diploma thesis.

[Fo 05] O. Fochler, diploma thesis.

[G 90] M. Gyulassy, *Phys. Lett.* B **243**, 432 (1990); M. Gyulassy, X.-N. Wang, *Phys. Rev. Lett.* **68**, 1470 (1992).

[G 92] K. Geiger, *Phys. Rev.* D **46**, 4965 (1992); *Phys. Rev.* D **46**, 4986 (1992).

[GB 82] J.F. Gunion and G. Bertsch, *Phys. Rev.* D **25**, 746 (1982).

[GCG 98] J. Geiss, W. Cassing, C. Greiner, *Nucl. Phys.* A **644**, 107 (1998).

[GGBCM 99] J. Geiss, C. Greiner, E.L. Bratkovskaya, W. Cassing, U. Mosel, *Phys. Lett.* B **447**, 31 (1999).

[GGJ 88] S. Gavin, M. Gyulassy, A. Jackson, *Phys. Lett.* B **207**, 257 (1988).

[GGX 03] K. Gallmeister, C. Greiner and Z. Xu, *Phys. Rev.* C **67**, 044905 (2003); W. Cassing, K. Gallmeister, C. Greiner, *Nucl. Phys.* A **735**, 277 (2004).

[GL 01] C. Greiner, S. Leupold, *J. Phys. G* **27**, L95 (2001).

[GLW 80] S.R. de Groot, W.A. van Leeuwen and Ch.G. van Weert, *Relativistic Kinetic Theory: Principles and Applications* (North Holland, Amsterdam, 1980).

[GM 92] K. Geiger and B. Müller, *Nucl. Phys.* B **369**, 600 (1992).

[GPZ 97] M. Gyulassy, Y. Pang, B. Zhang, *Nucl. Phys.* A **626**, 999 (1997).

[GRV 95] M. Glück, E. Reya, A. Vogt, *Z. Phys.* C **67**, 433 (1995).

[HN 04] T. Hirano and Y. Nara, nucl-th/0404039.

[HW 96] H. Heiselberg, X.N. Wang, *Nucl. Phys.* B **462**, 389 (1996); H. Heiselberg, X.N. Wang, *Phys. Rev.* C **53**, 1892 (1996).

[JQ 03] J. Adams et al. [STAR Collaboration], *Phys. Rev. Lett.* **91**, 172302 (2003); I. Arsene et al. [BRAHMS Collaboration], *Phys. Rev. Lett.* **91**, 072305 (2003); S.S. Adler et al. [PHENIX Collaboration], *Phys. Rev.* C **69**, 034910 (2004).

[K 02] F. Karsch, *Lect. Notes Phys.* **583**, 209 (2002); C. Bernard et al., *Phys. Rev.* D **55**, 6861 (1997).

[KBHMP 95] G. Kortemeyer, W. Bauer, K. Haglin, J. Murray, and S. Pratt, *Phys. Rev.* C **52**, 2714 (1995).

[KDCDN 84] T. Kodama, S.B. Duarte, K.C. Chung, R. Donangelo, and R.A.M.S. Nazareth, *Phys. Rev.* C **29**, 2146 (1984).

[KHHET 01] P.F. Kolb, U. Heinz, P. Huovinen, K.J. Eskola and K. Tuominen, *Nucl. Phys.* A **696**, 197 (2001).

[KHHH 01] P.F. Kolb, P. Huovinen, Ulrich W. Heinz and H. Heiselberg, *Phys. Lett.* B **500**, 232 (2001); P. Huovinen, P.F. Kolb, Ulrich W. Heinz, P.V. Ruuskanen and S.A. Voloshin, *Phys. Lett.* B **503**, 58 (2001).

[KLL 87] K. Kajantie, P.V. Landshoff, and J. Lindfors, *Phys. Rev. Lett.* **59**, 2527 (1987).

[KLS 91] J. Kapusta, P. Lichard, D. Seibert, *Phys. Rev.* D **44**, 2774 (1991).

[KM 81] K. Kajantie, H.I. Miettinen, *Z. Phys.* C **9**, 341 (1981).

[KMR 86] P. Koch, B. Müller, J. Rafelski, *Phys. Rep.* **142**, 167 (1986).

[L 93] A. Lang, H. Babovsky, W. Cassing, U. Mosel, H.G. Reusch, and K. Weber, *J. Comp. Phys.* **106**, 391 (1993).

[M 86] L.D. McLerran, *Rev. Mod. Phys.* **58**, 1021 (1986).

[M 00] A.H. Mueller, *Nucl. Phys.* B **572**, 227 (2000).

[M 02] A. Muronga, *Phys. Rev. Lett.* **88**, 062302 (2002); A. Muronga, *Heavy Ion Phys.* **15**, 337 (2002); A. Muronga, *Phys. Rev.* C **69**, 034903 (2004).

[MG 00] D. Molnar and M. Gyulassy, *Phys. Rev.* C **62**, 054907 (2000).

[MG 02] D. Molnar and M. Gyulassy, *Nucl. Phys.* A **697**, 495 (2002).

[MR 82] B. Müller and J. Rafelski, *Phys. Rev. Lett.* **48**, 1066 (1982).

[MS 86] T. Matsui and H. Satz, *Phys. Lett.* B **178**, 416 (1986).

[MSSG 89] R. Mattiello, H. Sorge, H. Stöcker, W. Greiner, *Phys. Rev. Lett.* **63**, 1459 (1989).

[MV 94] L.D. McLerran and R. Venugopalan, *Phys. Rev.* D **49**, 2233 (1994); L.D. McLerran and R. Venugopalan, *Phys. Rev.* D **49**, 3352 (1994).

[ORG 78] J.F. Owens, E. Reya, and M. Glück, *Phys. Rev.* D **18**, 1501 (1978).

[PHENIX 03] S.S. Adler et al. [PHENIX Collaboration], *Phys. Rev. Lett.* **91**, 182301 (2003).

[PTVF 92] W.H. Press, S.A. Teukolsky, W.T. Vetterling and B.P. Flannery, *Numerical Recipes in C* (Cambridge University Press, 1992).

[RHIC 00] www.bnl.gov/RHIC/

[S 80] E.V. Shuryak, *Phys. Rep.* **61**, 71 (1980).

[S 92] E. Shuryak, *Phys. Rev. Lett.* **68**, 3270 (1992).

[SM 02] G.R. Shin and B. Müller, *J. Phys. G* **28**, 2643 (2002); *J. Phys. G* **29**, 2485 (2003).

[SS 01] J. Serreau and D. Schiff, JHEP **0111**, 039 (2001).

[STAR 04] J. Adams et al. [STAR Collaboration], *Phys. Rev. Lett.* **92**, 052302 (2004); *Phys. Rev. Lett.* **92**, 062301 (2004).

[STAR] J. Adams et al. [STAR Collaboration], nucl-ex/0407003, to be published in Physical Review C.

[UA1] G. Arnison et al. [UA1 Collaboration], *Phys. Lett.* **123B**, 115 (1983); *Phys. Lett.* **132B**, 214 (1983); *Nucl. Phys.* B **309**, 405 (1988).

[UA2] P. Bagnaia et al. [UA2 Collaboration], *Phys. Lett.* **138B**, 430 (1984).

[VPKH 88] R. Vogt, M. Prakash, P. Koch, T.H. Hansson, *Phys. Lett.* B **207**, 263 (1988).

[W 72] S. Weinberg, *Gravitation and Cosmology: Principles and Applications of the General Theory of Relativity* (John Wiley and Sons, 1972).

[W 82] C.-Y. Wong, *Phys. Rev.* C **25**, 1460 (1982).

[W 96] S.M.H. Wong, *Nucl. Phys.* A **607**, 442 (1996).

[W 05] Q. Wang et al., working in progress.

[WG 91] X.N. Wang and M. Gyulassy, *Phys. Rev.* D **44**, 3501 (1991).

[WMGPS 89] G. Welke, R. Malfliet, C. Gregoire, M. Prakash and E. Suraud, *Phys. Rev.* C **40**, 2611 (1989).

[Wo 96] S.M.H. Wong, *Phys. Rev.* C **54**, 2588 (1996).

[X 05] Z. Xu, working in progress.

[XS 94] Li Xiong and E.V. Shuryak, *Phys. Rev.* C **49**, 2203 (1994).

[Z 98] B. Zhang, *Comput. Phys. Commun.* **109**, 193 (1998).

[ZGP 98] B. Zhang, M. Gyulassy, and Y. Pang, *Phys. Rev.* C **58**, 1175 (1998).

[ZKLL 00] B. Zhang, C.M. Ko, B.A. Li and Z. Lin, *Phys. Rev.* C **61**, 067901 (2000).

[ZP 97] B. Zhang, and Y. Pang, *Phys. Rev.* C **56**, 2185 (1997).

Deutsche Zusammenfassung

Ein Nukleon enthält *Quarks*, die zu den elementaren Bausteinen der Materie zählen. Quarks wechselwirken mit einander über den Austausch von *Gluonen*. Diese *starke* Wechselwirkung zwischen Quarks und Gluonen wird durch die Theorie der *Quantenchromodynamik* (QCD) beschrieben. Außerdem kommen Quarks und Gluonen nicht als isolierte Teilchen in der Natur vor, sondern sind immer in Hadronen gefangen (*Confinement*). Dies bedeutet zum Beispiel, daß in einem aus Nukleonen gebildeten Atomkern Quarks und Gluonen aus einem Nukleon nicht in die Nachbarnukleonen wandern können. Ein Atomkern stellt eine nukleare Materie dar. Andererseits sagt die Theorie der QCD für sehr hohe Dichte und Temperatur einen Phasenübergang von Kernmaterie in ein Plasma aus Quarks und Gluonen, das sogenannte *Quark Gluon Plasma* (QGP) [CP 75], voraus. Insbesondere zeigen die numerischen QCD Gitterrechnungen [K 02] einen rapiden Anstieg der Energiedichte bei einer Temperatur von $T \sim 170$ MeV. Dies weist auf einen Phasenübergang hin. Die Energiedichte bei der kritischen Temperatur ist ~ 1 GeV/fm^3, was etwa 10 mal größer als die in einem Atomkern ist. Nach der Urknalltheorie (*Big Bang*) sollte ein QGP im jungen Universum kurz nach der Explosion entstanden haben. Im Labor wird Kernmaterie in hochenergetischen Kern-Kern-Kollisionen erhitzt und komprimiert, so daß man annimmt, daß die benötigte hohe Energiedichte für einen Phasenübergang erreicht werden kann. In den letzten 30 Jahren wurden mehrere Beschleunigerexperimente der Kern-Kern-Kollisionen konstruiert und durchgeführt. Die Einschußenergie steigt kontinuierlich von einer Experimentgeneration zu der nachfolgenden. Die zur Zeit höheste Energie beträgt $\sqrt{s} = 200$ AGeV (im Schwerpunktsystem der kollidierenden Kerne) am Relativistic Heavy Ion Collider (RHIC) [RHIC 00] in den USA, der seit Jahr 2000 im Betrieb ist. Nach einer Abschätzung, die auf der Bjorken-Formel [B 83] beruht, soll in der Anfangsphase der Kollision am RHIC eine Energiedichte von ca. $20 - 30$ GeV/fm^3 erreicht werden, die hoch genug ist, um ein QGP zu erzeugen. QCD Voraussagen über neue Physik unter extremen Bedingungen hoher Temperatur und Dichte können am RHIC geprüft werden. Experimentelle Daten, die bisher analysiert worden sind, zeigen aufregende neuartige Phänomene. Eines davon, elliptischer Fluß, wird später in dieser Zusammenfassung näher diskutiert. Ferner möchten wir erwähen, daß in dem Zukunft-

sprojekt am Large Hadron Collider (LHC) am CERN in der Schweiz die Kolliderenergie eine Ordnung höher sein wird als die RHIC-Energie. Die Voraussetzung für die Erforschung des aufgelösten (deconfined) Zustands der QCD Materie ist noch besser gegeben am LHC.

Stellen wir uns zuerst das Geschehen schematisch dar, das in einer Kern-Kern-Kollision stattfinden könnte. Im ersten Moment nach der Kollision werden Quarks und Gluonen, die ursprunlich in den Nukleonen eingesperrt sind, befreit. Das System von strark welselwirkenden Quarks und Gluonen wird schnell zum thermischen Gleichgewicht geführt und ein QGP entsteht. Das erzeugte QGP expandiert dann hydrodynamisch in Raum und Zeit bis die Energiedichte oder Temperatur zu dem kritischen Punkt fällt. Dann beginnen Quarks und Gluonen sich zu Hadronen zu kombinieren. Es wird eine gemischte Phase geben, die aus Quarks, Gluonen und Hadronen besteht. Nach der Vollendung der Hadronisierung existiert ein Hadron-Gas, das weiter expandiert, bis das System auseinander fällt und entkoppelt. Die einzelnen Teilchen werden dann im Detektor registriert. Es zeigt sich, daß eine Kern-Kern-Kollision ein komplexer Prozeß ist und ein QGP, wenn es existieren würde, nur als ein temporärer Zustand der QCD Materie in der Kollision erscheinen wird. Deswegen muß die Suche nach QGP durch Analyse hadronischer und elektromagnetischer Signaturen wie zum Beispiel die Erhöhung der Seltsamkeit, J/ψ Unterdrückung oder Jet-Quenching [M 86, S 80, MR 82, KMR 86, MS 86, KM 81, KLS 91, G 90] erfolgen. Diese Effekte würden auftreten, wenn ein thermisches System aus Quarks und Gluonen, ein QGP, vorliegt. Auf der anderen Seite können die möglichen QGP-Signaturen auch teilweise aus der hadronischen Phase der Kollision hervorgerufen werden [MSSG 89, GCG 98, GL 01, GGJ 88, VPKH 88, GGBCM 99, GGX 03]. Um eine eindeutige Signatur eines QGP to finden, sollte man nach neuartigen Phänomenen suchen, die in der früheren Phase der Kollision entstehen können. Der sogenannte elliptische Fluß v_2 ist eine solche 'frühe Signatur' des QGP. In der folgenden Darstellung

$$\frac{dN_h}{dp_T^2 dy d\phi} = \frac{dN_h}{dp_T^2 dy}\,\frac{1}{\pi}\,(1 + 2\,v_1\,\cos\phi + 2\,v_2\,\cos 2\phi + \cdots)\,,$$

ist v_2 definiert als der zweite harmonische Koeffizient der Fourier-Entwicklung in dem Azimutwinkel der gemessenen Hadronen-Verteilung. Der Parameter v_2 bezeichnet das Quadrupolmoment und wird daher nicht verschwinden, wenn eine räumliche Anisotropie in der Reaktionszone vorliegt, die in einer nicht-zentralen Kollision realisiert wird. Der Grund dafür, daß der elliptische Fluß v_2 als eine 'frühe Signatur' des QGP gilt, ist folgender: Wenn ein QGP mit hohem Druck in einem nicht-zentralen Kern-Kern-Stoß erzeugt wird, existiert ein vom Azimutwinkel abhängiger Druckgradient. Dieser drückt die Teilchen so, daß die räumliche Symmetrie wieder hergestellt wird. Dabei wird die anfängliche räumliche Asymmetrie in die Impuls-Anisotropie der Teilchen transportiert.

Dies soll in der Impulsabhängigkeit von v_2 beobachtet werden. Zweitens wird v_2 hauptsächlich in den frühen Zeiten, d.h. in der Quark-Gluon-Phase, erzeugt, weil die räumliche Asymmetrie zu diesen Zeiten am größten ist. Fig.1.1 zeigt die Meßdaten von v_2 am RHIC für mehrere Hadronen [PHENIX 03, STAR 04] im Vergleich zu den theoretischen Voraussagen, die auf den hydrodynamischen Modellen [KHHH 01] beruhen. Die perfekten Übereinstimmungen unter 1.5 GeV/c deuten auf eine frühe Herstellung des Drucks und eine schnelle Thermalisierung des Systems von Quarks und Gluonen hin. Es zeigt ferner ein stark wechselwirkendes (mit kleiner Viskosität) QGP. Man kann auch sehen, daß die gemessenen v_2 bei hohen p_T saturieren, während das hydrodynamische Modell einen weiteren Anstieg voraussagt. Dies zeigt, daß das Verhalten der Teilchen mit hohem p_T nicht hydrodynamisch beschrieben werden kann.

Trotz des Erfolges bei den Voraussagen von elliptischem Fluß durch die hydrodynamischen Modelle ist es wichtig zu wissen, ab welcher Zeit die hydrodynamische Annahme gilt. Dabei fragt man nach dem Zeitpunkt, zu dem das Quark-Gluon-System sich vollständig im thermodynamischen Gleichgewicht befindet, da das primäre System weit von jeglichem thermodynamischen Gleichgewicht entfernt ist. Um diese wichtige Frage zu beantworten, wurden zahlreiche theoretische Studien mit der Anwendung der QCD durchgeführt, die entweder auf der Relaxationsnäherung [B 84, HW 96, W 96, Wo 96] oder auf den 3+1 dimensionalen Monte Carlo Kaskadensimulationen [GM 92, Z 98, MG 00, BMGMN 00, BMS 03] zur Lösung der Boltzmann-Gleichung basieren. Während die Relaxationsnäherung nur gilt, wenn sich das System nah an dem Gleichgewicht befindet, eignet sich eine Monte Carlo Kaskadensimulation für alle Situationen. Auch das hydrodynamische Verhalten eines thermischen Zustands kann prinzipiell damit beschrieben werden. Es ist daher essentiell, Kaskadensimulationen für die Beschreibung einer Kern-Kern-Kollision anzuwenden, um eine quantitative Voraussage über den Zeitpunkt der Herstellung des thermodynamischen Gleichgewichts and auch über das Verhalten der weiteren Evolution des QGP zu erzielen. In dieser Dissertation entwickeln wir eine neue Kaskadesimulation für 'on-shell' Partonen (Quarks und Gluonen), die partonkinetische Evolution in einer energetischen Schwerionenreaktion untersucht.

Zuerst werfen wir einen Rückblick auf die von anderen Gruppen entwickelten Parton-Kaskade-Modelle. Die erste Parton-Kaskade, VNI [GM 92], entwickelt von Geiger und Müller, beschrieb die 'off-shell' Dynamik der Partonen unter der Anwedung der störungstheoretischen Wirkungsquerschnitte der QCD (pQCD) für die binären $2 \leftrightarrow 2$ Reaktionen und Emissions- und Absorptionsprozesse $1 \leftrightarrow 2$. Die Partonen propagieren nicht nur in der Raum-Zeit und im Impulsraum sondern auch in ihrer Virtualität, die den 'off-shell' Charakter des Partons beschreibt. In ihrer Simulation für eine zentrale Au+Au Kollision mit der RHIC-Energie fanden sie, daß ein thermisches QGP nach einer Zeit von

$\tau \approx 1.8$ fm/c formiert wird [G 92]. Das potentielle hydrodynamische Verhalten in der weiteren Parton-Evolution wurde aber nicht demonstriert. Außerdem ist ihre konzeptionelle Formulierung der 'off-shell' Propagation nicht klar vom Standpunkt der Quantenkinetik. Vor kurzem haben Molnar and Gyulassy die Erzeugung des elliptischen Flußes am RHIC [MG 02] mit der Anwendung ihrer on-shell Parton-Kaskade, MPC [MG 00] (eine verbesserte Version von ZPC [Z 98]), untersucht. Dabei wurden nur die binären elastischen Reaktionen eingeführt. In ihrer Analyse kann der frühe Druck nur ausgebildet werden, wenn ein viel größerer als pQCD motivierter Wirkungsquerschnitt benutzt wird. Außerdem ist bekannt [SS 01], daß die elastischen $gg \leftrightarrow gg$ Stöße allein nicht in der Lage sein werden, das System zum thermodynamischen Gleichgewicht zu führen. Dies würde bedeuten, daß das kollektive Flußverhalten, das am RHIC beobachtet wurde, nicht durch pQCD beschrieben werden könnte. Auf der anderen Seite spielen die inelastischen Reaktionen die entscheidende Rolle im Bild der sogenannten 'bottom-up' Äquilibrierung [BMSS 01]. Es ist anschaulich klar, daß die inelastischen Reaktionen nicht nur für das chemische Gleichgewicht [BDMTW 93] verantwortlich sind, sondern auch zu einer schnellen kinetischen Äquilibrierung [XS 94, BV 01] beitragen. Dies gibt uns eine (aber nicht alle) wichtige Motivation, einen konsistenten Algorithmus zur Simulation der Stoßprozesse zu entwickeln, der auch für die inelastischen Reaktionen wie $2 \leftrightarrow 3$ geeignet ist.

Eine weitere Motivation für die Entwicklung einer neuen Parton-Kaskade inklusive $gg \leftrightarrow ggg$ Prozesse besteht darin, daß in den meisten bisher entwickelten Kaskaden der Wirkungsquerschnitt der elastischen Stöße geometrisch interpretiert wird, und es unheimlich schwierig ist, dieses Konzept auf die Behandlung eines $3 \rightarrow 2$ Stoßes zu übertragen. Das ist auch der Grund, warum die Rolle der $gg \leftrightarrow ggg$ Prozesse in der thermischen Äquilibrierung bisher noch nicht quantitativ untersucht werden kann. Die Entwicklung eines konsistenten Algorithmus' inklusive $2 \leftrightarrow 3$ Prozesse stellt eine Herausforderung dar und bildet den technischen Teil der vorliegenden Arbeit.

In Kapitel 2 wird ein neuer Algorithmus, insbesondere geeignet für die Behandlung der $2 \leftrightarrow 3$ Prozesse, vorgestellt. Dieser Algorithmus wurde in [B 89, L 93] für $2 \rightarrow 2$ Stöße vorgeschlagen und in [DB 91, C 02] auch für bestimmte, aber nicht allgemeine, $2 \leftrightarrow 3$ Prozesse benutzt. Anders als die geometrische Interpretation des Wirkungsquerschnitts, bindet dieser Algorithmus direkt an die Reaktionsrate und beschreibt den Vorgang der Stöße in einer stochastischen Art und Weise: Man bestimmt die individuellen Reaktionen im Subvolumen und in einem Zeitschritt durch Würfelung nach der entsprechenden Reaktionswahrscheinlichkeit. In diesem Kapitel wird dieser stochastische Algorithmus verallgemeinert. Das funktioniert nun für alle Übergangsmatrixelemente ohne jegliche Näherungen. Auch der übliche geometrische Algorithmus wird in diesem Kapitel zum Vergleich mit dem stochastischen Algorithmus

präsentiert.

Eine besondere Eigenschaft der neuen Parton-Kaskade mit der Anwendung des stochastischen Algorithmus' liegt darin, daß der Raum in die Subvolumina zerlegt wird, in denen die Würfelungen der Stoßereignisse erfolgen. Dieses in der Praxis nicht verschwindende Subvolumen bricht die absolute Lorentz-Invarianz der Boltzmann-Gleichung und wird zu der möglichen Frameabhängigkeit der Observable führen. In Kapitel 3 wird die Frameabhängigkeit für den Fall einer eindimensionalen Bjorken-Typ Expansion eines Systems mit hoher Dichte in einem Rohr untersucht. Man stellt fest, daß für hinreichend kleines Subvolumen die Frameabhängigkeit der Observable minimal ist, und die Konvergenz zur exakten Lösung der Boltzmann-Gleichung viel schneller erfolgt wird in der Simulation mit der Anwendnung des stochastischen Algorithmus' als die in der Simulation mit der Anwendnung des geometrischen Algorithmus'. Dies zeigt, daß der stochastische Algorithmus besonders für die Beschreibung dynamischer Entwicklung des Systems mit hoher Dichte geeignet ist.

Nach detaillierten Testen des neuen Stoß-Algorithmus' konstruieren wir eine neue Parton-Kaskade zur Beschreibung der Parton-Evolution am RHIC inklusive $gg \leftrightarrow gg$ und $gg \leftrightarrow ggg$ Reaktionen, wobei die inelastischen pQCD Prozesse erstmalig in die Simulation eingeführt wurden. Die Anfangsbedingung der primären Partonen wird durch die sogenannte 'Minijets'-Produktion aus semi-harten binären Nukleon-Nukleon-Streuungen bestimmt. Details über die 'Minijets'-Produktion findet man in Kaptel 4. Als erste Anwendnung der neuen Parton-Kaskade wird in Kapitel 5 die thermische Äquilibrieung in einer Box simuliert. Man stellt fest, daß das chemische Gleichgewicht auch für die komplizierten Bremsstrahlungsprozesse $gg \leftrightarrow ggg$ mit dem Landau-Pomeranchuck-Migdal Effekt erreicht wird. Dies zeigt die korrekte Operation der neuen Kaskade.

Wir zeigen die numerischen Ergebnisse aus den Simulationen der Parton-Evolution am RHIC in Kapitel 6. In der Studie wird die Dynaymik von Quarks nicht berücksichtigt. Die Hauptresultate sind unten kurz zusammengefaßt.

1.) Mit den Minijets, deren transversaler Impuls größer als $p_0 = 2$ GeV ist, als Anfangsbedingung, ist das primäre System nicht im Gleichgewicht. Nach einer Zeit von 2 fm/c erreicht das Gluon-System im Zentrum der Kollision das kinetische Gleichgewicht und expandiert hydrodynamisch weiter. Da die primären Gluonen untersaturiert sind, sinkt die Temperatur nicht nur wegen der hydrodynamischen Expansion sondern auch wegen der Gluonen-Emission. Vollständiges chemisches Gleichgewicht folgt nach einer längeren Zeit von $3-4$ fm/c. Vom Kollisionszentrum weg, in die transversale Richtung innerhalb des Radius' des Goldkerns werden die Äquilibrierungen bis zum 15% verlangsamt. Außerhalb des Radius' des Goldkerns stammen die Gluonen meistens aus der Oberfläche des Feuerballs und sind frei von der starken Welchselwirkung. Wir

haben gesehen, daß die transversale Energie in der Mittelrapidität ca. 1.7-fach gesunken ist. Dies ist ein starker Hinweis auf eine frühe Herstellung des Drucks am RHIC.

2.) Die einzelnen Beiträge der elastischen und inelastischen Reaktionen zur Herstellung des kinetischen Gleichgewichts werden untersucht. Man stellt fest, daß die inelastischen Stöße die wesentlichen verantwortlichen Prozesse sind, die das System ins Gleichgewicht treiben. Ohne die inelastischen Kanäle kann das kollektive Verhalten am RHIC nicht erzeugt werden, außer man nimmt einen unrealistisch größeren Wirkungsquerschnitt an.

3.) Simulationen mit kleinerem Schnittpunkt p_0 für die Minijets-Produktion werden durchgeführt. Mit sinkendem p_0 steigt die Anzahl der primären Gluonen, so daß ein immer dichteres System vorliegt. Man findet heraus, daß in der Simulation mit kleinerem $p_0 = 1.3 - 1.5$ GeV eine schnellere kinetische Äquilibrierung nach einer Zeit von $1 - 2$ fm/c stattfindet. Für solche kleine p_0s wird das chemische Gleichgewicht fast von Anfang an herstellt. Man sieht auch eine starkere Abnahme der transversalen Energie in der Mittelrapdität mit kleinerem p_0. Dies deutet auf eine stärkere und längere hydrodynamische Expansion in der Simulation mit kleinerem p_0 hin. Wenn man den Endwert der transversalen Energie per Rapidität mit den experimentellen Daten vergleicht, findet man, daß die Minijets-Produktion mit $p_0 = 1.4$ GeV eine passende Anfangsbedingung nach einer Au+Au Kollision am RHIC darstellt.

4.) Eine Anfangsbedingung aus sogenanntem 'Color Glass Condensate' am RHIC wird angenommen. Im Vergleich mit der Rechnung in [BV 01], wo nur elastische Stöße berücksichtigt wurden, findet eine viel schnellere thermische Äquilibrierung von Gluonen in unserer Simulation nach ca. $1.5 - 2$ fm/c statt.

Als Ausblick nennen wir einige interessante Fragestellungen, die wir weiter untersuchen wollen. Als erstes wollen wir die Erzeugung des elliptischen Flußes v_2 in einer semi-zentralen Kern-Kern-Kollision verstehen. Der Hinweis einer relativ schnellen Herstellung des Gleichgewichts des Systems von Quarks und Gluonen, was ein Hauptergebnis der vorliegenden Arbeit ist, signalisiert, daß das Anwachsen von v_2 auch durch den Einschluß der inelastischen Reaktionen erfolgen kann. Zweitens, wenn das Parton-System thermalisiert, entwickelt sich dieses hydrodynamisch in Raum und Zeit. Dieses Verhalten wird im allgemeinen durch die Viskos-Hydrodynamik beschrieben. Es ist interessant, die Kaskaden-Simulation mit dem Resultat aus der Viskos-Hydrodynamik zu vergleichen. Dann weiß man, wie viskos das QGP am RHIC sein wird. Außerdem kann das Phänomen von Jet-Quenching, der Energieverlust der Partonen durch Bremsstrahlung, mit der Anwendung der neuen Parton-Kaskade systematisch untersucht werden. Im Bild der 'bottom-up' Äquilibrierung [BMSS 01] gaben die Autoren eine parametrische Zeitskala der vollständigen Thermalisierung von $\tau \sim \alpha_s^{-13/5} Q_s^{-1}$ an, wenn ein Color Glass Condensate als Anfangsbedingung bei einer Kern-Kern-Kollision mit sehr hoher Energie angenommen

wird. Dabei ist Q_s die Skala für die Gluonen-Sättigung. Es ist auch interessant, dieses parametrische Verhalten der Äquilibrierung mit Hilfe der neuen Kaskade zu überprüfen. Ferner können die Dynamik von Quarks und Hadronisierungsprozesse in die Simulation einbezogen werden.

Danksagung

An dieser Stelle möchte ich all denen danken, die mich während meiner Promotionszeit unterstützt haben und die zum Gelingen dieser Arbeit beigetragen haben.

An erster Stelle danke ich Prof. Dr. Ulrich Mosel für die Aufnahme in sein Institut und sein stetes Interesse am Fortgang dieser Arbeit. Aufgrund seiner Föderung konnte ich an zahlreichen Konferenzen und Workshops teilnehmen.

Mein herzlicher Dank geht an Prof. Dr. Carsten Greiner für die interessante Themenstellung sowie seine intensive Betreuung und ständige Diskussionsbereitschaft. Ich habe nicht nur von seinen breiten Physikkenntnissen und kritischer Denkweise profitiert, sondern auch vieles von seiner menschlichen Seite gelernt. Bei den wissenschaftlichen Diskussionen hat er immer große Geduld und Sachlichkeit gezeigt, besonders wenn ich meine Gedanken wegen der sprachlichen Schwierigkeiten nicht genau ausdrücken konnte. Ich danke ihm für seiner Ermunterung zur Entwicklung des numerischen Modells. Auch für das Korrekturlesen dieser Arbeit gilt ihm mein Dank.

Ich möchte meinem Freund, Dr. Frank Daniel Steffen, für seine freundschaftliche Unterstützung und den wissenschaftlichen Austausch danken. Ein großes Dankeschön gilt Dr. Gunnar Martens, von dem ich in vielen Diskussionen viel gelernt habe und von dessen C++ Kenntnissen ich viel profitiert habe. Ich danke Dr. Kai Gallmeister für seine Diskussionsbereitschaft und viele Hinweise.

Ich danke Prof. Dr. Dr. Wolfgang Cassing für sein Interesse an dieser Arbeit und die Diskussionsbereitschaft.

Besonderer Dank geht an Frank Frömel für seine ständige Hilfsbereitschaft bei der PC Betreuung. Christoph Keil und Frank Frömel sei für den guten Computerservice und für die funktionierende Wasti-Anlage am Institut gedankt.

Ein Dankeschön gilt Elke Jung für ihre effektive administrative Hilfe. Ich danke den Mitgliedern des Institutes, insbesondere meinen Zimmerkollegen, für die stets gute Stimmung.

Abschließend möchte ich meinen Eltern für ihre permanente moralische Unterstützung danken.